UNIVERSITY OF PRETORIA
DEPARTMENT OF CIVIL ENGINEERING

THE INFLUENCE OF FOOTING STIFFNESS ON THE BEHAVIOUR OF SURFACE STRIP FOUNDATIONS ON SAND

August 2015

© University of Pretoria

THE INFLUENCE OF FOOTING STIFFNESS ON THE BEHAVIOUR OF SURFACE STRIP FOUNDATIONS ON SAND

HUGO EDUARD LEMMEN

A project dissertation submitted in partial fulfilment of the requirements for the degree of
MASTER OF ENGINEERING (STRUCTURAL ENGINEERING)
In the
FACULTY OF ENGINEERING
UNIVERSITY OF PRETORIA

August 2015

© University of Pretoria

DISSERTATION SUMMARY

THE INFLUENCE OF FOOTING STIFFNESS ON THE BEHAVIOUR OF SURFACE STRIP FOUNDATIONS ON SAND

HUGO EDUARD LEMMEN

Supervisor:	Professor E.P. Kearsley
Co-Supervisor:	Professor S.W. Jacobsz
Department:	Civil Engineering
University:	University of Pretoria
Degree:	Master of Engineering (Structural Engineering)

Foundation systems are some of the most widely used structures in civil engineering. The design thereof is governed by two failure mechanisms, either bearing capacity failure or settlement failure. Generally, the governing mechanism is settlement failure. In order to accurately predict the settlement of a foundation system, the exact material properties of all the various constituents of the system are required. However, due to the complexity of the interaction problem, assumptions have been introduced in the design of foundations to simplify the process. To govern against shear failure of a footing, structural engineers increase the thickness thereof. However, there is no limit to the extent with which this increase can be made. In order to obtain an economic design, the optimum thickness of a footing for a certain set of soil parameters should be obtained.

The main objectives of this study is to determine whether the settlement, deflection and contact stress distribution of a footing on cohesionless sand can be predicted as a function of the stiffness's of the footing and sand. Centrifuge model tests were conducted on seven aluminium footings and one reinforced concrete footing, all with an equivalent 4.5 m × 4.5 m plan area. The tests were conducted on dense, cohesionless sand. The settlement and deflection data were captured with the use of particle image velocimetry, whereas the stress distribution was captured with the use of Tekscan™ pressure sensors.

The main conclusions drawn from the study are as follows. The relative stiffness of the foundation system affects the deflection and contact stress distribution beneath the footing. The contact stress distribution beneath stiff footings are uniform. A decrease in the flexibility of a footing results in

© University of Pretoria

curvature of the footing during loading, which reduces the contact stress at the footing edges. The behaviour of the initially stiff concrete footings change to flexible at the onset of cracking, with the load distribution changing from uniform to a distribution reducing linearly towards the edge. Finally it was concluded that the results obtained from the aluminium footings could be used to predict the settlement, deflection and contact stress distribution beneath a footing.

© University of Pretoria

DECLARATION

I, the undersigned hereby declare that:

- I understand what plagiarism is and I am aware of the University's policy in this regards;
- The work contained in this dissertation is my own original work;
- I did not refer to work of current or previous students, lecture notes, handbooks, or any other study without proper referencing;
- Where other people's work has been used this has been properly acknowledged and referenced;
- I have not allowed anyone to copy any part of my dissertation;
- I have not previously in its entirety or in part submitted this dissertation at any university for a degree.

_____

HUGO EDUARD LEMMEN

29071799

16 August 2015

© University of Pretoria

ACKNOWLEDGEMENTS

The writing and completion of this dissertation would not have been possible without the assistance, guidance and support of several individuals. I would like to show sincere gratitude to the following:

- My supervisor, Prof Kearsley for her excellent guidance, dedication and financial support. The hours and wisdom she provided me with were of immense value.
- My co-supervisor, Prof Jacobsz, for contributing valuable and irreplaceable ideas.
- Mr Derick Mostert for all his assistance with experimental procedures.
- The lab personnel at the University of Pretoria for their assistance:
    - Mr. Johan Scholtz
    - Mr. Jaco Botha
    - Mr. Rikus Kock
- Hugo and Anné Lemmen, my parents, who always supported, encouraged and believed in me.
- To my partner, Carmen Coetzee, for all her care, encouragement and motivation throughout the entire project.

© University of Pretoria

TABLE OF CONTENTS

© University of Pretoria

© University of Pretoria

© University of Pretoria

© University of Pretoria

LIST OF FIGURES

PAGE

© University of Pretoria

© University of Pretoria

© University of Pretoria

© University of Pretoria

LIST OF TABLES

PAGE

© University of Pretoria

LIST OF SYMBOLS

ε_x	=	Horizontal strain of sand
ε_y	=	Vertical strain of sand
γ	=	Unit weight of soil
γ'	=	Effective soil unit weight
ν	=	Poisson's ratio of soil
ω	=	Radial velocity
ρ_{pixel}	=	PIV precision error
φ	=	Mobilised friction angle
φ'_{cv}	=	Critical state friction angle
φ'_{p}	=	Peak strength friction angle
π	=	Pi
ψ	=	Angle of dilation
σ	=	Normal stress on the shearing plane
σ_y	=	Average vertical stress increase in sand
τ	=	Shear strength
ξ_{crit}	=	Critical crack length
A	=	Empirical constant
B	=	Width of the footing
c	=	Soil cohesion
d	=	Thickness of the raft foundation
D	=	Embedment depth
D_R	=	Soil relative density
D_{50}	=	Median grain size
E	=	Modulus of elasticity of material
E_b	=	Young's modulus of the raft foundation
E_s	=	Secant stiffness modulus of the soil
EI	=	Stiffness of footing
FEM	=	Finite element modelling
g	=	Gravitational acceleration of centrifuge
G	=	Gravitational acceleration
I	=	Inertia around neutral axis through width of footing
I_R	=	Relative dilatancy index
IDT	=	Inductive displacement transducer
K_s	=	System stiffness
l	=	Length of the raft foundation
L	=	Length of the PIV patch
M	=	Moment present at specific point of footing
N_c	=	Bearing capacity factor
N_q	=	Bearing capacity factor
N_γ	=	Bearing capacity factor
p'	=	Mean normal effective stress
PIV	=	Particle image velocimetry
q_{norm}	=	Nominal bearing pressure
Q	=	Empirical constant
r	=	Radius of centrifuge arm
R	=	Empirical constant
s	=	Displacement in PIV analysis
v	=	Velocity
V_a	=	Arch mechanism variable
V_d	=	Beam mechanism variable
x	=	Distance along width of footing

© University of Pretoria

y	=	Distance to neutral axis of footing
z	=	Vertical deflection of footing

Deflection	=	Transverse displacement under transverse loading
Foundation system	=	Combination of footing and underlying soil
Sensel	=	Individual sensor of Tekscan™ pressure sensor
Settlement	=	Downward movement of footing during loading

© University of Pretoria

1 Introduction

1.1 Background

A foundation system consists of the combination of the soil supporting a structure and the footing that spreads the imposed load of the structure over a soil area that is large enough to form a stable system. The most important aspects to consider in the design of a foundation system are ultimate bearing capacity and serviceability settlement (Aiban and Znidarčic, 1995), with the settlement performance of the system generally being the governing factor. When a foundation system is designed it is difficult to accurately determine the material properties of the soil in the system, whereas the properties of the materials used to construct the footing in a foundation system can be quantified fairly accurately.

To simplify the design of a foundation system, structural engineers often model the material behaviour of the soil as a spring system with a constant spring stiffness. The use of the spring model delivers fairly accurate settlement and deflection results when relatively small strains are present within the soil mass (Conniff and Kiousis, 2007). The spring model system cannot accurately predict any inelastic material behaviour caused by loading and it can thus not be used to model the ultimate bearing capacity of a foundation system. It also cannot consider compatibility of strains below and adjacent to the foundation.

The current design procedure used by structural engineers takes neither the size nor the stiffness of footings into account, possibly resulting in the overdesign of large footings. Although the thickness of a footing is often increased to improve the shear performance, there is no limit to the extent with which the thickness can be increased. To obtain the most economical foundation design there should be an optimum footing thickness for a given soil stiffness which needs to be determined.

The extent to which an increase in the footing thickness can improve the performance of a foundation system should be investigated. The effect of footing stiffness on the settlement of and stress distribution beneath the footing must be established. Research is required to determine whether the current design assumptions used by structural engineers are valid or over conservative for relatively large strip footings.

© University of Pretoria

1.2 Objective of the Study

The objective of this study is to determine the effect of footing stiffness on the soil-structure interaction of a footing on cohesionless sand. The study specifically focuses on the settlement behaviour and the deflected shapes of the footings. The effect of footing stiffness on not only the contact stress distribution at the soil-structure interface, but also the displacement of the soil beneath the footing due to load application is investigated.

1.3 Scope of the Study

Centrifuge modelling was used to determine the effect of footing stiffness on the interaction between the footing and the underlying soil. The scope of the study is limited to laboratory testing of physical models of surface strip footings on dry cohesionless silica sand with a relative density of approximately 70%. A number of aluminium and one reinforced concrete footing with a prototype base area of 4.5 m × 4.5 m were considered in the study. This size was kept constant and was representative of a section of a relatively large single strip footing. Determining the effect of varying the footing size on the soil-structure interaction falls beyond the scope of this study.

Settlement data of the footings was recorded with inductive displacement transducers, as well as photographically. The contact stress distribution at the soil-structure interface was recorded with the use of the Tekscan™ system. Displacement of the soil beneath the footing was measured photographically (using particle image velocimetry (PIV) (White et al., 2003) equipment).

Although seven aluminium footings were tested, only one reinforced concrete footing was tested to compare the behaviour of the reinforced concrete with that of aluminium. Establishing the effect of reinforced concrete footing depth and steel reinforcing content fall outside the scope of this study.

Plane-strain conditions were considered in all analyses. It was assumed that the displacements as observed through the centrifuge strongbox window is representative of the typical movement of the soil and the footing under the applied line loads.

© University of Pretoria

1.4 Methodology

The methodology used to achieve the objectives of this study was as follows:

- A literature review was conducted to obtain background knowledge on surface foundations, failure of soil in foundation systems, failure of concrete footings, the relative stiffness of a foundation system along with geotechnical centrifuge modelling and particle image velocimetry. The information obtained in the literature contributed towards the design of the experimental model.
- An experimental procedure was developed to investigate the effect of footing stiffness on the settlement and deflection of the footing, as well as the contact stress distribution at the soil-structure interface. Eight model footings were tested underlain by a 300 mm thick layer of silica sand in a geotechnical centrifuge while the load, displacement and contact stress under the footing were recorded. Throughout the test, photos were taken to record the movement and deflection of the footings. The experiment was designed to be able to investigate the mentioned factors simultaneously.
- The data from the experimental work was analysed to determine the effect of the footing stiffness on the settlement, deflection and contact stress distribution behaviour of each individual footing.
- Finally, the horizontal and vertical displacement of the soil beneath the footings were analysed to determine whether the stiffness of the footings and, in effect the deflection thereof, had an influence on the displacement of the soil.

1.5 Organisation of the Report

The report consists of the following chapters and appendices:

- **Chapter 1** serves as an introduction to the report, briefly discussing the topic considered and reasons as to why the research was conducted. The chapter also highlights the objective, scope and methodology followed in carrying out the research described in the report.
- **Chapter 2** contains an overview of the applicable literature regarding this study. The review contains literature on surface foundations, failure of soil and concrete in foundation systems, relative stiffness of foundation systems, geotechnical centrifuge modelling and particle image velocimetry.
- **Chapter 3** contains a discussion on the experimental work conducted. The chapter includes the design of the experimental model, information on the instrumentation used during the study, as well as the experimental procedure followed in each test.

© University of Pretoria

- **Chapter 4** discusses the results obtained from the experimental work. The chapter presents the settlement and deflection data of the footings, the contact stress distribution at the soil-structure interface and the displacement of the soil beneath the footings and the results are discussed.
- **Chapter 5** presents the conclusions reached as well as recommendations for further study.
- **Chapter 6** presents the references used throughout this study.
- **Appendix A** contains the calibration of the force transducer.
- **Appendix B** contains the calibration of all the inductive displacement transducers used in the study.
- **Appendix C** contains all the load settlement data from the inductive displacement transducer settlement recorded in this study.
- **Appendix D** contains the PIV settlement data of all the stiff footings not shown in Chapter 4.
- **Appendix E** contains the PIV deflection data of all the stiff footings not shown in Chapter 4.
- **Appendix F** contains the Tekscan^{TM} pressure data of all the stiff footings not shown in Chapter 4.

© University of Pretoria

2 Literature Review

2.1 Introduction

The design and analysis of foundation systems need to be conducted in a way that the soil-structure interaction can be considered in a sophisticated manner to produce accurate results, but still remain relatively simple for practical applications (Morfidis and Avramidis, 2002).

The basis on which reinforced concrete footings or slabs are designed was first pioneered by Westergaard (1925). Through the study of concrete pavements, he presented a mathematical model to compute the stresses in a concrete slab by assuming that the slab acts as an isotropic, homogeneous, elastic solid and that all the subgrade reaction forces are perfectly vertical and proportionate to the size of the slab. He assumed that the subgrade was an elastic medium, where the stiffness of the subgrade can be considered as the force which will cause unit deflection if it was spread over a unit area (Beckett, 1995). Westergaard (1937) also proposed a measure of the stiffness of the subgrade compared to the stiffness of the foundation, termed the radius of relative stiffness. The work done by Westergaard has been refined over the years through analytical models and experimental procedures and it still remains the basis of a large number of current design procedures.

For the design of footings from a structural engineer's point of view, the footing is considered as a rigid body on top of an elastic medium. This leads to the assumption that the vertical settlement of the footing on the elastic medium must have a planar distribution, because a rigid structure remains planar when it settles. The planar distribution theory is based on the assumption that the ratio of pressure to settlement remains constant and that the stress distribution below the rigid footing is uniform. However, these assumptions are not necessarily true, as experimental studies have shown that soil exhibits a certain amount of plastic behaviour, footings have a finite stiffness and the distribution of pressures below a footing varies with time. The pressure distribution in the soil is a function of the type of soil as well as the stiffness of the footing and superstructure (Algin, 2007).

Currently, the design of footings is based on an iterative process where the initial size of the footing required relies on the educated guess of an engineer. The size of the footing is then checked to see whether it satisfies the serviceability conditions and that the bearing capacity of the soil is not exceeded. As soon as the size of the footing has been confirmed as adequate, the reinforcement and depth of the footing are determined to ensure that it has adequate flexural, shear and punching shear strength to resist the applied loading conditions (Algin, 2007).

© University of Pretoria

The current design procedure for surface footings does not take the stiffness of either the footing or the soil into account, but rather focuses on the strength of the reinforced concrete and the allowable bearing capacity of the soil. The strength and behaviour of the footing is also considered to remain constant regardless of the loads applied to it. To investigate the effect of the stiffness on the settlement and deflection behaviour of a large surface footing, various parameters need to be considered as discussed in this chapter.

The design of foundations, as well as the contact stress distribution at the soil-structure interface of the foundations are discussed. This is followed by the various aspects which have an influence on the soil-structure interaction. Failure of the foundation can occur through either the failure of the soil or the failure of the footing as discussed in this chapter.

The effect of the stiffness on the settlement and deflection behaviour of a surface footing was investigated experimentally using physical modelling. Due to certain limitations of small scale tests conducted in laboratories under normal gravitational loads, the experiments were conducted in a geotechnical centrifuge, therefore a short introduction to centrifuge modelling is included in the chapter.

When the centrifuge tests were conducted, a large amount of measuring equipment and techniques were used to track various important aspects of this study. The most important measuring technique used in the experimental work is particle image velocimetry (PIV) (White et al., 2003) and therefore a discussion of the method is included in this chapter. At the very end of the chapter, a summary of the most important aspects discussed throughout the chapter is included.

2.2 Surface Footings

Reinforced concrete footings are extensively used in engineering practise. When analysing and designing footings, the interaction between the soil and the reinforced concrete structure poses a number of challenges from both the soil and structural elements as outlined by Camp and Assadollahi (2013) below. The first two aspects represent soil-related factors and the other, structural requirements:

- The footing must support the superstructure in a stable and safe manner.
- The footing must provide stability against excessive settlement or against bearing capacity failure.
- The footing must have adequate shear and moment capacities in its short and long directions.
- The foundation system cannot exceed its bearing capacity.
- The design of the footing with the reinforcing must meet strict design requirements.

© University of Pretoria

The design of reinforced concrete footing involves a trial and error procedure, where the initial dimensions are selected by the engineer, checked against the relevant code requirements and altered until a satisfactory design in terms of ultimate and serviceability limit states is achieved (Pisanty and Gellert, 1972). For a wide variety of reinforced concrete footings, the dominant mechanism engineers design for is the resistance of the footing to punching shear failure, similar to that of flat concrete slabs. Therefore, it is assumed that sufficient structural depth at the column will provide adequate shear, diagonal tension as well as bending moment capacity (Pisanty and Gellert, 1972). However, the majority of footings are overdesigned redundant systems and a more efficient design method needs to be employed (Baumann and Weisgerber, 1983).

The modern design procedure of reinforced concrete structures is based on ultimate limit state equilibrium analysis. The volume of concrete and amount and length of reinforcement required is determined based on the flexural, as well as the shear strength of the concrete, through which potential crack planes can form. In the design of reinforced concrete footings, adequate safety margins need to be applied to both the shear and flexural components of the structure (Leshchinsky, 2001).

For the design of a foundation system, the strength of the footing as well as the soil has to be considered. Although the strength of the steel and concrete used for the reinforced concrete is easily determined and controlled, the strength of the soil on which the footing is constructed is more challenging to accurately quantify. Due to the non-homogeneity of naturally occurring soils, the use of laboratory tests might be unreliable to predict actual behaviour and properties of the soil. Unfortunately properties of the soil used to determine the permissible bearing capacity value for the design of reinforced concrete footings is generally determined with the minimal values obtained from either field or laboratory testing (Wei et al., 2012).

2.2.1 Foundation Design

The majority of footings are analysed and designed using the Winkler hypothesis, where the soil is modelled as a continuous system of non-connected discrete springs. Due to the simplicity of the Winkler model, it is used extensively to solve soil-structure interaction problems and has produced accurate results in most cases (Morfidis and Avramidis, 2002). The Winkler approach yields relatively accurate results if the structure does not yield at any point. However, it becomes less applicable if the load keeps on increasing beyond yielding (Baumann and Weisgerber, 1983). The Winkler method is a very basic simplification of the behaviour of the soil under loading conditions (Morfidis and Avramidis, 2002).

© University of Pretoria

To determine whether the use of linear Winkler springs results in accurate analysis of foundation systems, De Beer (1948) did a series of tests to determine the soil-structure interaction of a steel beam on a sand subgrade. He determined that the more flexible the beam became, the more the bending moments in the footing differed from the bending moments predicted with the use of the Winkler stiffness model. Müller and O'Sullivan (1999) experimented with the use of photoelastic methods to determine the bending moment in the footings tested on sand. They concluded that the use of the linear Winkler assumptions led to more conservative predictions with an increase in flexibility.

In the 21st century footings are mostly designed with the use of finite element modelling (FEM), as the use of FEM in engineering has become common practise. For simple structures the use of FEM is not necessary, and the benefits of FEM disappear, leaving a simple hand calculation much more time-efficient (Brooker, 2006). The process of FEM has simplified the design of structures, although there are some limitations to the use of the software, as well as the accuracy thereof. The most important limitation for footing design is the material modelling of the soil and concrete and the assumptions that are incorporated by the designer in the choice of soil and concrete behaviour. All the limitations of FEM, such as the boundary conditions, loading conditions and material properties will not be discussed in detail in this section, as they are not relevant to this study.

Wei et al. (2012) analysed the effect of design parameters on the accuracy of nonlinear finite element analysis and highlighted one important aspect that needs to be considered with the soil-structure interaction problem. When modelling footings on granular material with finite elements, structural engineers typically model either a perfectly smooth footing or a perfectly rough footing. This means that no horizontal shear stresses are allowed at the footing base for a smooth footing or that no horizontal sliding is allowed between the footing and the soil for a rough footing. However, a footing is cast by pouring the concrete directly on the soil surface, which acts as the bottom formwork. This causes the footing surface to be sufficiently rough to resist the majority of slip tendencies (Wei et al., 2012).

2.2.2 Stress Distribution beneath Surface Foundations

Soil-structure interaction is the process where the movement of the structure directly influences the response behaviour of the soil and the soil movement has an influence on the behaviour of the structure (Hallak, 2012). As load transfer occurs between the footing and the soil, the foundation moves, causing internal forces to change within the structure and creating a soil-structure interaction. The significance of this interaction is important for both dynamic and static loading conditions. The most important aspect of the soil-structure interaction is the contact stress distribution beneath the footing (Conniff and Kiousis, 2007).

© University of Pretoria

In Section 2.2.1 attention was given to the use of the Winkler springs method by structural engineers to design footings. The general assumption of a uniform pressure distribution beneath a footing, shown in Figure 2-1, would be valid for an infinitely stiff footing placed on top of a perfectly elastic soil comprising of springs. This is however not possible as soil is not realistically represented by a collection of springs and the required thickness resulting in a footing that is infinitely stiff would not be economical (Robberts and Marshall, 2010).

The distribution of contact stresses below a typical footing on a sand and cohesive soil can also be seen in Figure 2-1 (Mosley and Bungey, 1987). The sand particles on the edge of the footing are displaced laterally when a load is applied to the footing, relieving a portion of the stress. In a cohesive soil such as clay, shear stresses develop at the edges of the footing, adding to the bearing capacity of the clay (Robberts and Marshall, 2010).

The relationship between the stiffness of the footing and the soil controls the contact stress distribution beneath the footing (Aiban and Znidarčic, 1995; Arnold et al., 2010), which can also vary with time. Robberts and Marshall (2010) concluded that the errors made in the calculation of the forces exerted on the footing is relatively small and are compensated for with the use of adequate safety factors.

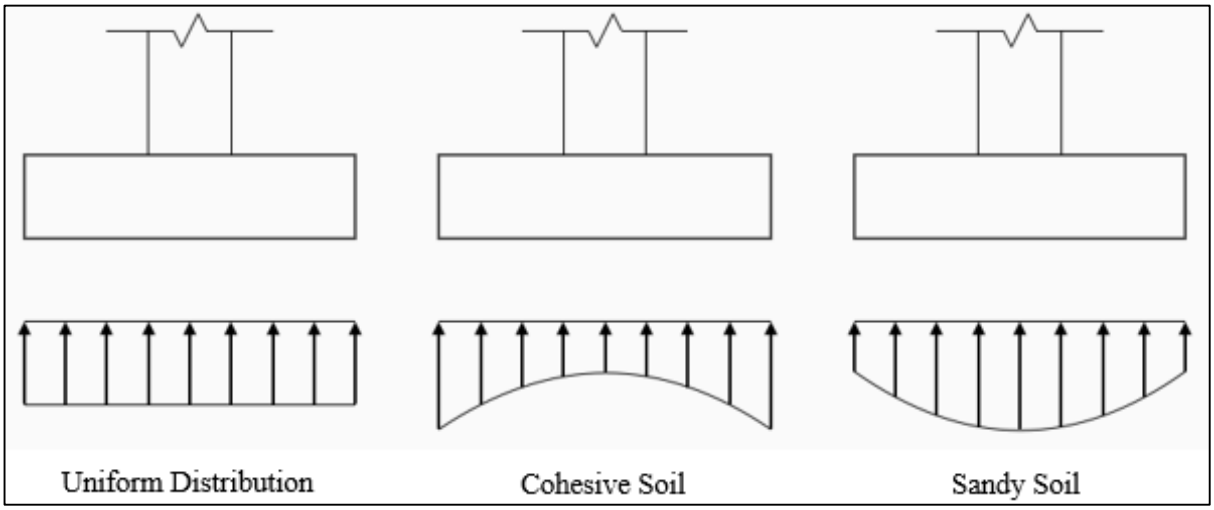

Figure 2-1 Stress beneath a sandy soil and cohesive soil (Mosley and Bungey, 1987)

Leshchinsky and Marcozzi (1990) conducted small-scale model tests to determine the effect of the footing stiffness on the bearing capacity of the soil, by subjecting a flexible and rigid footing to loading on the same dense sand. They found that the contact stress distribution for a flexible footing differed from that of a rigid footing, as can be seen in Figure 2-2. As the rigid footing is loaded, large stress concentrations develop at the edge of the footing, causing local failure of the soil at the edge of the footing as the soil is stressed beyond its peak strength. For a flexible footing the stress is more evenly

© University of Pretoria

distributed, leading to an almost uniform shear strength mobilization and subsequent peak strength along most of the failure surface. Leshchinsky and Marcozzi (1990) believed that reducing the footing stiffness would lead to an increase in the load-bearing capacity of the system, but also concluded that the reduced stiffness would lead to increased deflection of the footing in the soil.

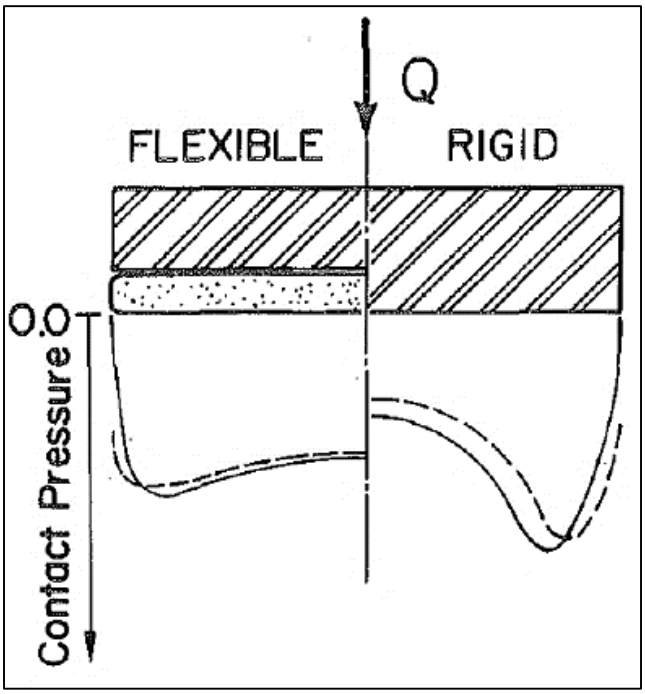

Figure 2-2 Difference in stress beneath a flexible and rigid footing (Leshchinsky and Marcozzi, 1990)

By changing the flexibility of the footing and in effect changing the pressure distribution shape, it is important to remember that the integral of the pressure over the area of the footing needs to be constant for a given load and cannot alter as a results of flexure or contact loss if the same load is applied (Dempsey and Li, 1989). The relationship between the stiffness of the footing relative to the stiffness of the soil plays an important role in the stress distribution beneath a footing. Excessive stresses applied to the soil can lead to failure thereof. Therefore, the mechanisms of soil failure are discussed in the next section.

2.3 Soil Failure in Foundations

Failure of a foundation can be due to two factors: excessive settlement of the foundation, or bearing capacity failure of the underlying soil. According to Knappett and Craig (2012), the following limits for the design of foundations apply and should not be exceeded. They are divided into two categories, namely ultimate limit states, which are discussed in points 1 to 4 and serviceability limit states, which are discussed in points 5 and 6:

© University of Pretoria

1. Bearing capacity failure due to shear failure of the soil.
2. Loss of stability as a result of the formation of a slip surface that forms beneath the footing.
3. Failure due to sliding of the footing subjected to an inclined loading.
4. Failure of the foundation system, failure of the footing or failure of the superstructure due to excessive settlement of the foundation.
5. Excessive settlement.
6. Unwarranted vibration causing unacceptable settlement or soil liquefaction.

2.3.1 Bearing Capacity

Bearing capacity is the maximum pressure which can be applied to the soil with a footing without causing the soil to experience shear failure (Knappett and Craig, 2012). According to White et al. (2008), the field of bearing capacity problems remain an area of continued research. There is still no consensus on the following factors:

- Choice of the appropriate factors to be used in the bearing capacity equations.
- Methods to be used to determine the correct friction angle of the granular material for the calculation of the bearing capacity.
- A definitive method to capture the correct 'scale effect' observed in small-scale testing that is performed under 1 G loads which causes a different behaviour to the small-scale tests performed within a geotechnical centrifuge or full-scale testing.

Bearing capacity calculations are based on the superposition method presented by Terzaghi (1943), where the various load and soil strength parameters such as friction angle, cohesion, surface surcharge and self-weight are presented as non-dimensional bearing capacity factors N_c, N_q and N_γ (Manoharan and Dasgupta, 1995). The common bearing capacity formula proposed by Terzaghi (1943) is shown in Equation 2-1:

$$q_f = cN_c + \gamma DN_q + 0.5\gamma BN_\gamma \qquad \text{(Equation 2-1)}$$

Where:

c	=	Soil cohesion
γ	=	Unit weight of soil
D	=	Embedment depth
B	=	Width of the footing
N_c	=	Bearing capacity factor
N_q	=	Bearing capacity factor
N_γ	=	Bearing capacity factor

© University of Pretoria

The bearing capacity equation is a superposition of three individual equations relating to different parts of the bearing capacity problem. Each bearing capacity factor (N_c, N_q and N_γ) is dependent on the mobilised friction angle (φ) of the soil (Knappett and Craig, 2012).

The first factor N_c, is due to the shear strength of the soil, the second factor N_q, is due to the surcharge pressure and the third factor N_γ, is related to the self-weight of the soil beneath the foundation (Knappett and Craig, 2012). A schematic depicting the width (B) and the embedment depth (D) of the footing used in Terzaghi's equation is shown in Figure 2-3 (Craig, 2004).

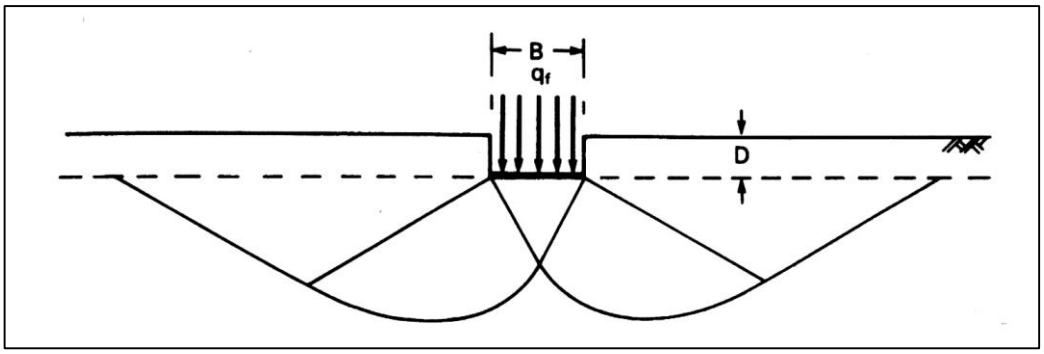

Figure 2-3 Variables used in Terzaghi's equation (Craig, 2004)

The first two bearing capacity factors are relatively easy to quantify and are largely agreed upon by the geotechnical engineering community. The bearing capacity factors N_c and N_q of a granular soil are derived from the principle of rigid-perfectly plastic theory (Perkins and Madson, 2000). The values for the bearing capacity factors can be determined using Equations 2-2 and 2-3, proposed by Prandtl (1921) and Reisner (1924) respectively:

$$N_q = e^{(\pi \tan\varphi)} \tan^2(45° + \varphi/2) \qquad \text{(Equation 2-2)}$$

$$N_c = (N_q - 1)\cot\varphi \qquad \text{(Equation 2-3)}$$

Where:

φ = Mobilised friction angle
N_c = Bearing capacity factor
N_q = Bearing capacity factor

The third bearing capacity factor (N_γ) is semi empirical and more complex to quantify, with extensive research still being conducted. The main concern regarding the bearing capacity factor N_γ is not the formulas used to calculate the factor, but rather the mobilised friction angle that should be used in the equations (White et al., 2008). This is explained further in Section 2.3.1.2. The two most common methods to solve this factor is to use Equation 2-4 proposed by Meyerhof (1963) or Equation 2-5 proposed by Hansen (1968).

© University of Pretoria

$$N_\gamma = 1.8(N_q - 1)\tan\varphi \qquad \text{(Equation 2-4)}$$

$$N_\gamma = (N_q - 1)\tan(1.4\varphi) \qquad \text{(Equation 2-5)}$$

Where:

φ = Mobilised friction angle
N_q = Bearing capacity factor
N_γ = Bearing capacity factor

The bearing capacity equation proposed by Terzaghi, shown in Equation 2-1 and the subsequent iterations of the equation are all dependent on a variety of assumptions discussed earlier. Another limitation is the fact that it was proposed for a strip foundation in 2D, making the application in 3D conditions difficult (Knappett and Craig, 2012). The complications involved with 3D calculations are considered too extensive for practical use and the 2D solution has been accepted as the general equation to calculate the bearing capacity in design codes. However, to compensate for different shapes of footings, semi-empirical shape factors have been introduced by various authors. The most simplified of these factors are presented by Craig (2004) as indicated in Table 2-1.

Table 2-1 Shape factors used for Terzaghi's bearing capacity equation (Craig, 2004)

Shape Factor	Square Footing	Circular Footing	Rectangular Footing
s_c	1.2	1.2	1 + 0.2B/L
s_q	1.2	1.2	1 + 0.2B/L
s_γ	0.8	0.6	1 - 0.2B/L

The bearing capacity equation proposed by Terzaghi is therefore altered and the proposed equation as indicated by Knappett and Craig (2012) is shown in Equation 2-6:

$$q_f = cN_c s_c + \gamma D N_q s_q + 0.5\gamma B N_\gamma s_\gamma \qquad \text{(Equation 2-6)}$$

Other factors that can have an influence on the Terzaghi equation are load inclination factors and depth factors. Michalowski and You (1998) determined mathematically through the use of a lower bound analysis that the effect of eccentric loading can be taken into account by using a reduced effective size of the foundation as proposed by Meyerhof (1953). As only vertical loading is investigated in this study, these factors are not relevant and will therefore not be considered further. However, various other factors that can have an influence on the bearing capacity of a foundation system are discussed in the next section.

© University of Pretoria

2.3.1.1 Bearing Capacity Factors

In order for the bearing capacity formula to give reasonably accurate results, the bearing capacity factors proposed in the formula needs to be given accurate values in line with the deformation characteristics of the soil, as well as the size of the loaded area (Terzaghi, 1955). A limitation of the Terzaghi method is the assumption that the increase in bearing capacity is linear. However, since the material behaviour of the soil is non-linear, errors are introduced into the calculation of the bearing capacity. Despite shortcomings, practising engineers still prefer to use this method due to the simplicity thereof (Manoharan and Dasgupta, 1995).

Bearing capacity calculations for a foundation system on sand are still not well understood due to the difficulty in calculating the bearing capacity factor N_γ (Dijkstra et al., 2013). Difficulty to accurately predict the bearing capacity of a foundation system on a granular soil is due to the nonlinear strength of the soil and the progressive failure phenomenon (Perkins and Madson, 2000).

According to Aiban and Znidarčic (1995), a large variety of methods can be used to perform ultimate bearing capacity calculations such as limit analysis, limit equilibrium, slip-line and finite element analysis. However, the variation in the results obtained from these methods is large. Various researchers have tried to reduce the uncertainty of the bearing capacity factor N_γ, predominately with the use of the method of characteristics. This method is based on the assumption of associated flow, as required by the plasticity formulation, which can over-estimate the bearing capacity of sands (Dijkstra et al., 2013). One common characteristic of all the methods is the assumption of perfect plasticity of the materials, which has been shown to be a conservative assumption (Aiban and Znidarčic, 1995).

In the following sections several factors and mechanisms that can result in a foundation system's bearing capacity to differ from that predicted using Terzaghi's equation are explained in detail. The influence of these factors illustrates the complexity of the soil-structure interaction problem.

2.3.1.2 Progressive Failure and Shear Band Formation of Soil

Progressive failure of a soil is the phenomenon where the plastic strains that occur within a soil mass is non-uniform, therefore the mobilised shear strength of the soil is different at various points within the soil mass as the slip surface starts to develop (Conte et al., 2013). Due to the progressive failure of soils, certain points or sections within the soil mass have a larger shear strain than other, which are known as shear bands (Conte et al., 2013).

© University of Pretoria

It is assumed that the stress-strain behaviour of a soil can be classified as rigid perfectly-plastic, therefore the peak strength of the soil is mobilised simultaneously within the soil mass along the slip surface (Kotake et al., 2004). However, a number of experimental results have indicated that when the peak stresses are reached within the soil, failure does not occur immediately within the soil mass.

Conte et al. (2013) evaluated the bearing capacity equation proposed by Terzaghi analytically through the use of FEM. They assumed that when failure of the soil occurred, it occurs simultaneously along the entire slip surface which developed below the footing. However, their experimental results indicated that the failure process is progressive and that the plastic strains below the footing are mobilized non-uniformly. Therefore, the soil strength is not mobilized equally at all the points in the slip surface.

Aiban and Znidarčic (1995) illustrated the principle of progressive failure experimentally through centrifuge testing of three aluminium footings. As can be seen below in Figure 2-4, their experimental results indicate that after the peak stress is reached (point A), for a footing loaded vertically at its centre point, the deflection of the footing increases slightly whilst the stress beneath the footing decreases sharply (point B). This is followed by a relatively constant stress level with an increase in the deflection, up to point C, where after the stress level reduces dramatically with an increase in the deflection up to point D. After this point, the slip surface was almost fully formed and the deflection increased under constant stress. The x-axis in Figure 2-4 represents deflection divided by the width of the footing, known as normalised settlement.

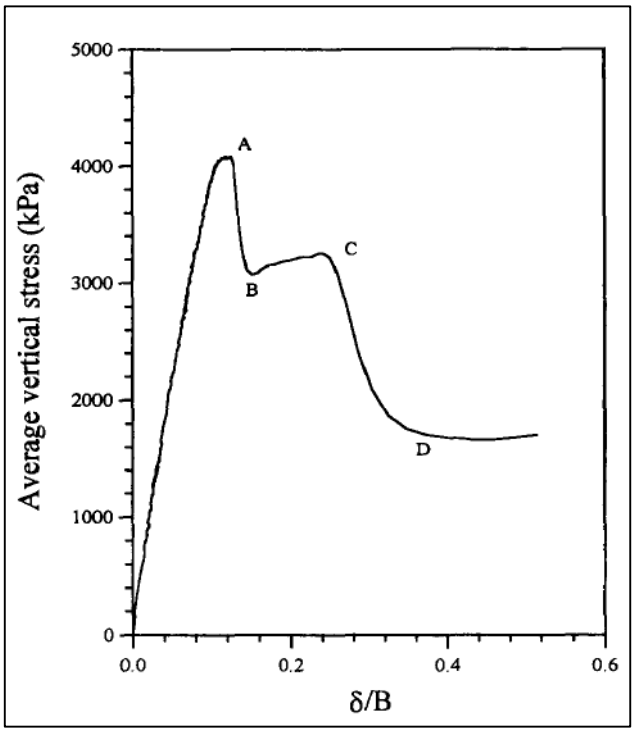

Figure 2-4 Progressive failure of soil example (Aiban and Znidarčic, 1995)

© University of Pretoria

When considering soils with strain-softening behaviour, such as dense sands, shear bands develop within the soil as it is stressed (Conte et al., 2013). When the stress is increased further after the development of the shear bands, the soil strength is reduced from peak strength to a critical state within the band. Due to the redistribution of the stresses within the soil, the shear band develops throughout the soil until a slip surface forms which eventually causes the collapse of the foundation system. The strength of the soil located in the slip surface at the moment of collapse is larger than the critical state, but lower than the peak strength of the soil (Conte et al., 2013).

According to Perkins and Madson (2000), as the load applied to the footing increases, the shearing strength in the soil is not mobilised at the same rate at all points within the slip surface. Soil particles with the highest strain will be mobilized first for shear strength, with the shear strength of the rest of the soil mass further mobilized when the strain increases. Due to this occurrence, the shear strength along the slip surface is not equal at all points and only a certain portion of the soil mass along the slip plane contributes towards the shear strength of the soil mass. This is dependent on the peak friction angle of the soil. The remaining soil mass contributes a smaller shear strength dependent on either a constant volume, residual or critical state friction angle (Perkins and Madson, 2000).

Conte et al. (2013) confirmed the process described by Perkins and Madson (2000) through their analytical analysis of the bearing capacity of a footing on a granular soil with FEM. As illustrated in Figure 2-5, the friction angle is not constant across the entire width of the slip surface (indicated as a white circular strip). The section closest to the footing (located at the top left of the figure) experiences a critical state friction angle (φ'_{cv}), the section a bit further away from the footing experiences a friction angle between the critical state and peak friction angle (φ'_{p}) and the section furthest away from the footing experiences a peak friction angle of the soil. It is therefore clear from their analysis that the mobilised friction angle varies along the width of the slip zone.

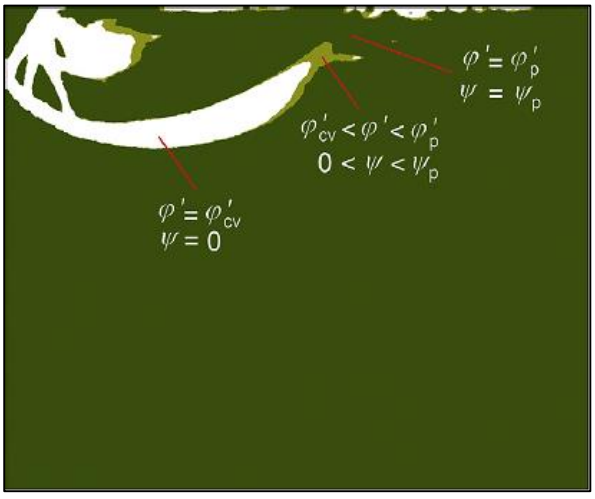

Figure 2-5 Variation in mobilised friction angle along slip surface (Conte et al., 2013)

© University of Pretoria

(a) Factors Affecting Progressive Failure and Shear Band Development

It is clear from the preceding text that progressive failure occurs within a granular soil. Perkins and Madson (2000) postulated that the process of progressive failure is dependent on two counteracting circumstances:

- As progressive failure is a result of the non-uniformity of the mobilised friction angle along the slip plane, it becomes more prominent as the width of the footing increases.
- However, as progressive failure is also defined by the difference between the peak and residual mobilised friction angle, it becomes more prominent when the width of the footing decreases (Perkins and Madson, 2000).

The soil's strength-dilatancy relationship (dependent on the characteristics of the particular soil, such as type and density, as well as the footing geometry) is responsible for determining which process would be dominant.

A few authors have proposed factors affecting the progressive failure process. White et al. (2008) conducted centrifuge tests on a flat and two conical circular foundations to determine the effect of the footing shape on the bearing capacity of the foundation system. From their experimental work they found that the effects of brittleness and progressive failure are more evident in dense soil. Perkins and Madson (2000) analytically assessed the work done by other authors to find a better approximation of the bearing capacity of a foundation system by considering the strength dilatancy relationship of the soil. With their analysis, they found that the process of progressive failure becomes more noticeable with an increase in the foundation width, as well as increasing the confinement of the soil mass.

The occurrence of shear bands within a soil mass is part of the mechanism of progressive failure and has a large influence on the mechanical behaviour of the soil. Gajo et al. (2007) explained that a considerable amount of experimental and analysis work had been carried out on the formation of strain localizations or shear bands and their influence on the mechanical behaviour of the soil. Most of the work focused on the occurrence of the shear bands, particularly the strain conditions when the bands occur and their orientation. The reasons for the occurrence of shear bands are discussed, followed by some of the work by different authors postulating various factors that contributes to the occurrence of shear bands and concluding with experimental evidence of the shear band formation.

Liu et al. (2005) stated that shear bands can be formed through either the formation of stress concentration, local inhomogeneities or any mechanism that could degrade the strength of the soil at a certain point, or through the variation from a smooth deformation pattern due to the instability of the inelastic behaviour of the soil. These mechanism are similar to progressive failure, as shear banding is part of the progressive failure mechanism for a granular material.

© University of Pretoria

Zhang et al. (2013) determined through discrete element modelling that both the sliding and rolling of the sand particles cause energy to dissipate within the soil mass. As the energy changes within a small section where the elastic strain increase is still occurring, shear bands start to form. With an increase in the load applied to the soil, the rolling, sliding and combined shear of the particles form the shear bands (Zhang et al., 2013).

Researchers have suggested that the occurrence of shear bands can be attributed to a wide variety of factors. Zhang, et al (2013) postulated that the rolling resistance of granular materials (due to the irregular size, shape and surface roughness of the individual particles) can be responsible for various soil characteristics, including enhanced dilatancy and shear strength, as well as shear band formation. Gajo et al. (2007) found mathematically that the elastic anisotropy plays an important role in the development of localization effects under triaxial conditions, with a smaller effect observed under biaxial conditions.

Gajo et al. (2007) observed that when an elastic-plastic material model for soil is used, the elastic portion is of limited importance due to the fact that the elastic strains of the soil is quickly replaced with plastic strains at the stresses and loads used in most laboratory tests. In order to study the evolution of elastic stiffness and anisotropy which can contribute to the early formation of shear bands, very subtle experimental work is required which have only become available with modern testing techniques (Gajo et al., 2007). From the preceding text regarding shear bands, it is clear that there is no consensus on the mechanisms or the factors that affect the mechanisms, with further research required if the mechanism is to be incorporated in designs.

The majority of experimental measurements concerning shear band formation have been conducted under plane-strain conditions (Hasan and Alshibli, 2010). A few suggestions regarding analysis of shear bands have been proposed. During analysis with FEM, Conte et al. (2013) found that the failure mechanism of a granular soil with progressive failure can be modelled with the use of a non-local elasto-viscoplastic constitutive model together with a Mohr-Coulomb yield function, which reduces the shear strength parameters of the soil with accumulated deviatoric plastic strain. Although the exact method used to determine the progressive failure mechanism and subsequent shear band formation by Conte et al. (2013) falls beyond the scope of the study, their method yielded fairly realistic results with respect to the formation of shear. In Figure 2-6, stage E demonstrates the formation of the slip surface as well as shear bands from the corner of the footing (footing is located at the top left), while stage F illustrates how both the mechanisms developed further with an increase in the load applied to the soil.

© University of Pretoria

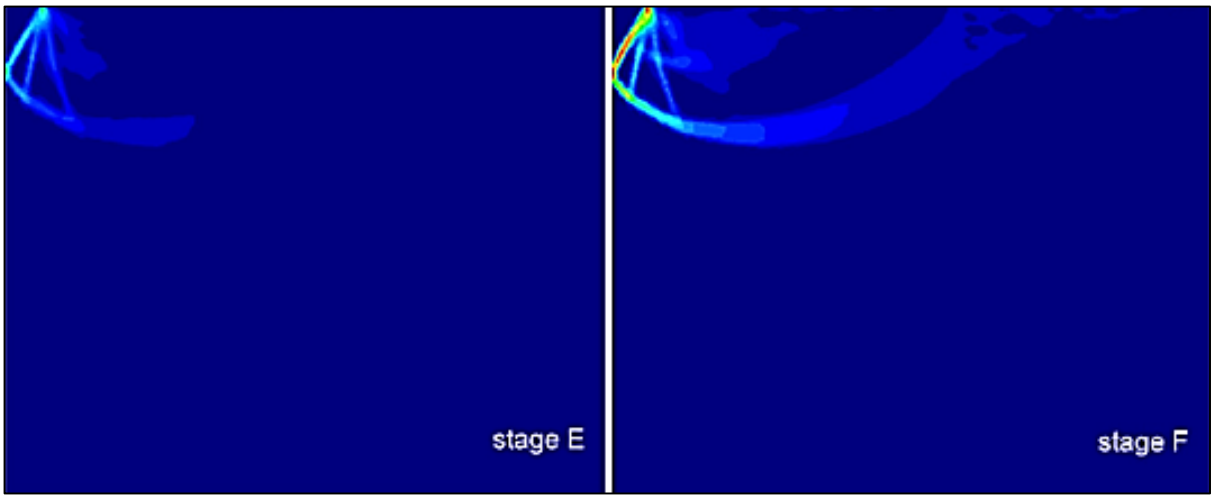

Figure 2-6 Shear band formation shown during finite element analysis (Conte et al., 2013)

(b) Mobilised Shear Strength

To calculate the bearing capacity factor N_γ, the mobilised friction angle of the soil is required. The friction angle determined through laboratory testing is highly dependent on the testing procedure used, as a different friction angle is obtained through different testing procedures (triaxial, plane strain, etc.), which result in a different shear band formation mechanism. Leshchinsky and Marcozzi (1990) noted that the use of friction angles obtained from direct shear tests as opposed to triaxial tests, yielded larger friction angles (approximately 6-8° higher for dense sand with low confinement pressures), but also produced better correlation with the experimental results for plane-strain problems.

Approaching the problem using traditional methods of bearing capacity calculations, Spasojevic and Cabarkapa (2012) illustrated that with the traditional Mohr-Coulomb failure criterion, the friction angle is considered to remain constant regardless of the load applied, therefore the shear strength increases linearly as a function of the normal stress, as shown in Equation 2-7.

$$\tau = \sigma \tan\varphi \qquad \text{(Equation 2-7)}$$

Where:

τ = Shear strength
σ = Normal stress on the shearing plane
φ = Mobilised friction angle

Experimental evidence has shown that this relationship is not valid due to the stress dependency of the mobilised friction angle of the soil. The variation in the mobilised friction angle of the soil can be attributed to non-uniform sliding friction, particle rearrangement and particle crushing at different pressure levels within the soil mass (Spasojevic and Cabarkapa, 2012). Experimental evidence

© University of Pretoria

illustrating a failure envelope is presented in Figure 2-7 by Spasojevic and Cabarkapa (2012). The secant friction angle (usually obtained with triaxial tests) which remain constant regardless of the load applied to the soil is shown alongside experimental observations of the true failure envelope of the soil, clearly illustrating the variability of the friction angle with an increase in the stress level.

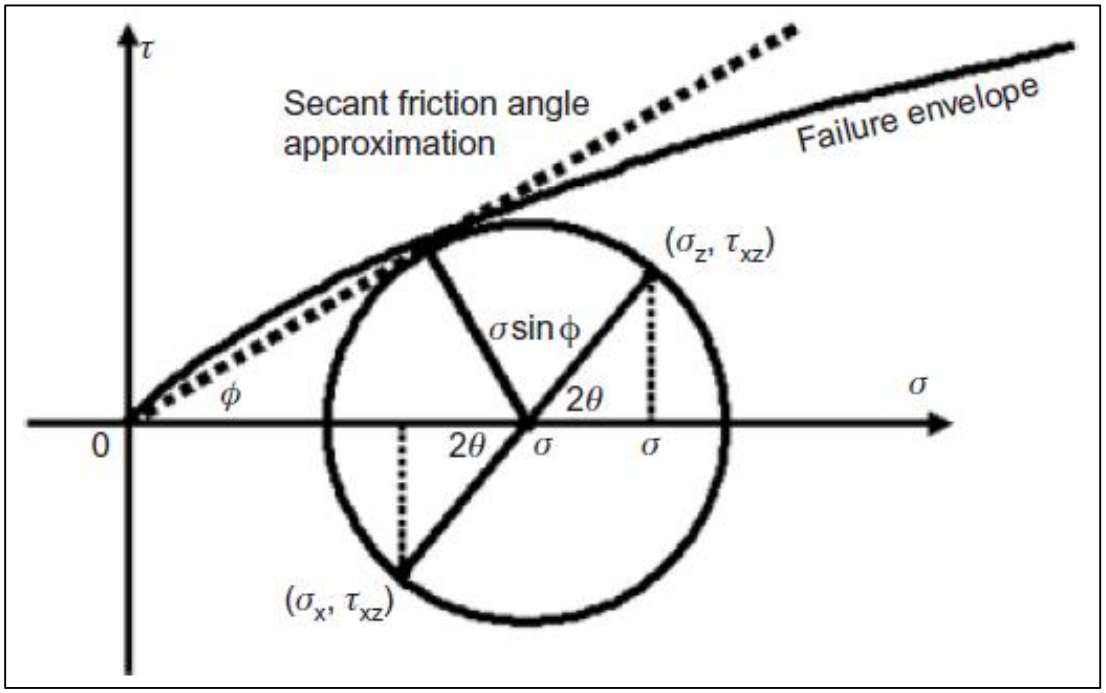

Figure 2-7 Difference between actual and predicted failure envelope of soils (Spasojevic and Cabarkapa, 2012)

With the variation in friction angle due to increased stress in mind, various authors have proposed methods to incorporate the variable friction angle into the calculation of the bearing capacity of a foundation system. The peak friction angle of the soil is a function of the rate at which the soil dilates in shear (Perkins and Madson, 2000), therefore the dilation of soil during loading has a large influence on the occurrence of progressive failure and shear banding. Dilation of a soil occurs when the volume of the soil increases during shearing (Knappett and Craig, 2012).

To compensate for the strength-dilatancy effect of soils, Bolton (1986) examined the strength-dilatancy relationship of a soil by considering data from 17 different sands tested in either axisymmetrical or plane-strain conditions. Bolton's (1986) analyses led to a re-expression of an equation developed by Rowe (1962) in terms of the peak and constant volume friction angles, as well as the dilation angle at peak strength (φ'_p). The dilation angle of the soil at peak shear strength is a function of the relative density of the soil (D_r) and the mean effective stress confinement (p'), therefore Bolton (1986) suggested empirical Equations 2-8 and 2-9.

© University of Pretoria

$$\varphi'_p = \varphi'_{cv} + AI_R \qquad \text{(Equation 2-8)}$$

Where:

φ'_p	=	Peak effective stress friction angle
φ'_{cv}	=	Critical state effective stress friction angle
A	=	Empirical constant
I_R	=	Relative dilatancy index

The constant A in Equation 2-8 is an empirical constant proposed by Bolton, with a value of 3 for triaxial tests, or 5 for a plane-strain tests. The value I_R is termed the relative dilatancy index, determined using Equation 2-9.

$$I_R = D_R(Q - \ln p') - R \qquad \text{(Equation 2-9)}$$

Where:

D_R	=	Soil relative density
Q	=	Empirical constant
p'	=	Mean normal effective stress
R	=	Empirical constant

Constants Q and R are both empirical constants, with Q = 10 and R = 1, providing the most accurate results. Bolton (1986) suggested that the equations are only valid for soils with a relative dilatancy index larger than zero, indicating that the equations are not valid for sands of low density. Provided the sand is dense enough, the only parameters required to solve Bolton's equations are the relative density of the sand and the critical state friction angle, eliminating the need for triaxial testing of undisturbed sand samples. The mean stress level required in Bolton's equation can be determined by using the De Beer's (1967) formula shown in Equation 2-10, which is a function of the mobilised friction angle of the soil.

$$p' = \left(\frac{1}{1+\tan^2\varphi}\right)\left(\frac{1}{1+\sin^2\varphi}\right)\frac{q_{norm} + 3\gamma' D}{4} \qquad \text{(Equation 2-10)}$$

Where:

p'	=	Mean normal effective stress
φ	=	Operational friction angle
q_{norm}	=	Nominal bearing pressure
γ'	=	Effective soil unit weight
D	=	Embedment depth

The equations shown above gives an indication of the methods used by various researchers to incorporate the dilatancy and variable friction angle into the calculation of the bearing capacity of a foundation system. These equations form the basis of the procedures proposed by various authors, such as Perkins and Madson (2000) or White et al. (2008). The research conducted by these authors highlight the importance of the effect of dilatancy and variable friction angle on the bearing capacity of foundation systems. The precise details of these procedures fall beyond the scope of this study.

© University of Pretoria

(c) Properties of Shear Bands

Although the mechanism of occurrence and the analytical approach to incorporate shear bands are not agreed upon yet and still require further research, the properties of the shear bands have been identified to some extent by various researchers. Modern experimental techniques allow delicate testing of soil samples, combined with the utilization of computers enabling researchers to study the shear bands within soil samples. Properties of the shear bands that have been determined to date are discussed further.

In the context of foundation failure, the study of strain localization is an important aspect, as localization can be a precursor of sudden failure. The behaviour of the soil within the shear bands play an important role in the stability and deformation of footings (Desrues and Viggiani, 2004). The size and orientation of these shear bands are dependent on the material properties, geometry of the sample, boundary conditions imposed, as well as loading conditions (Liu et al., 2005). According to Hasan and Alshibli (2010), as a soil specimen fails when peak loading occurs under plane-strain conditions, the failure occurs along a well-defined shear band or multiple shear bands, dependent on the boundary conditions.

Figure 2-8 represents results obtained from discrete element modelling by Liu et al. (2005), indicating the formation and location of shear bands within their 3D soil specimen. They concluded that strain localization takes place in all tests containing granular materials, with the location and directions of the bands dependent on the type of test being conducted.

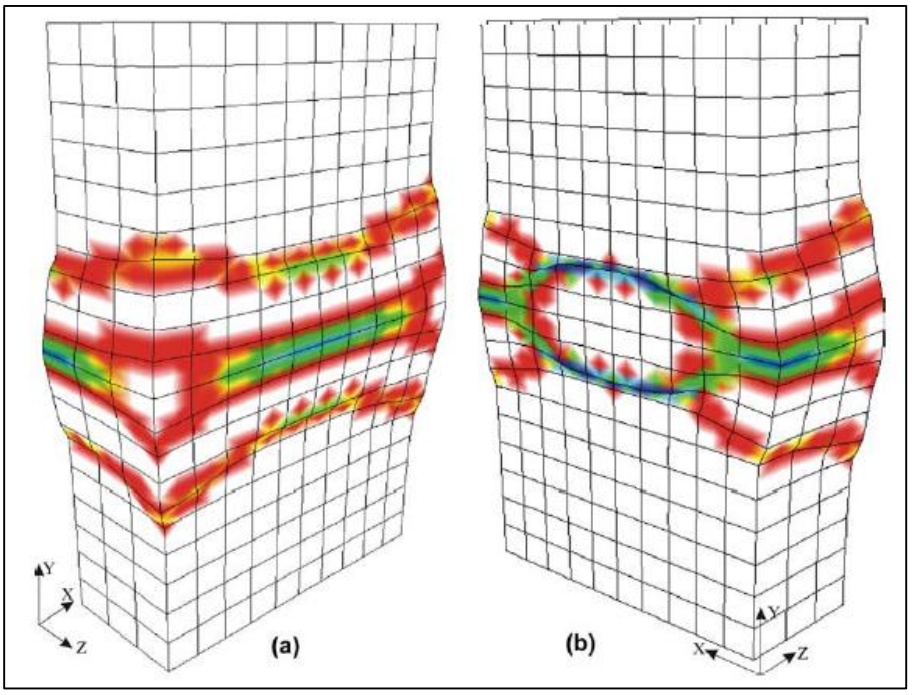

Figure 2-8 Shear band formation in a discrete numerical modelling model (Liu et al., 2005)

© University of Pretoria

The use of photoelastic methods have become more popular due to the increased quality of digital cameras as well as increased computational power readily available to engineers. Muir Wood (2012) used a simple shear apparatus to conduct various photoelastic tests to determine the physical properties of the shear bands. Figure 2-9 indicates shear band formation seen by Muir Wood (2012) with photoelastic experimental techniques. Muir Wood (2012) determined that the width of shear bands are approximately 10 D_{50} - 20 D_{50} for narrowly graded soils, with natural sands showing slightly larger shear bands due to the increased interlocking of the particles. When shear bands start to form patterns, the size of the shear bands increase to approximately 40 D_{50}.

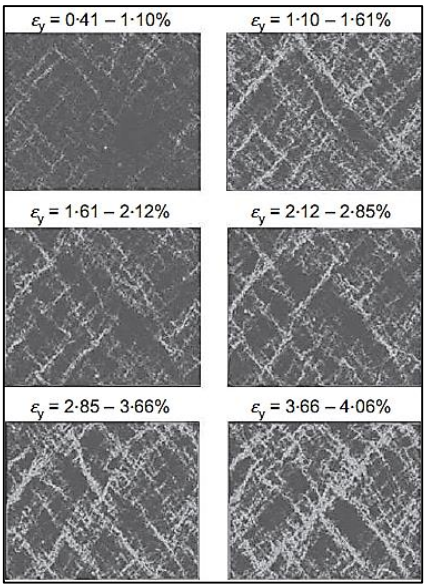

Figure 2-9 Shear band formation in simple shear test apparatus (Muir Wood, 2012)

A 2D plane-strain photoelastic experiment was conducted by Hall et al. (2009) to determine the orientation and thickness of shear bands. Results obtained from their experiment is shown in Figure 2-10, indicating the actual volumetric strains present in the soil, representing shear bands, along with a sketch of the shear bands extracted from the photograph.

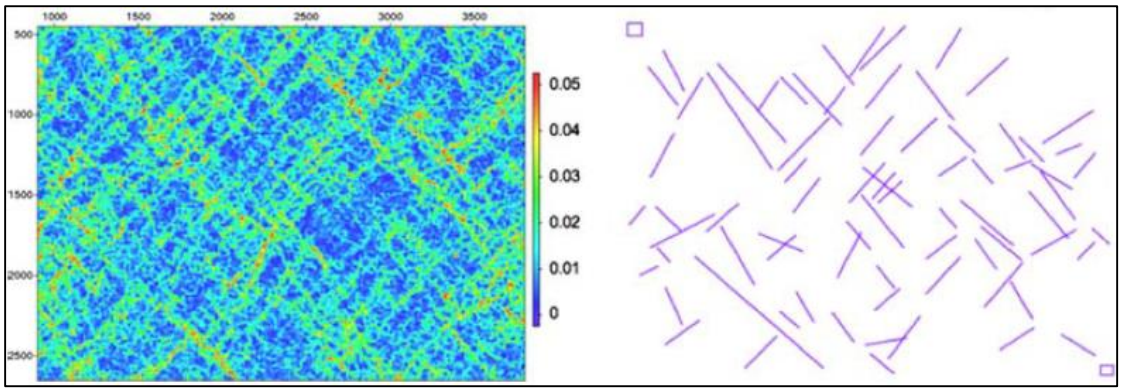

Figure 2-10 Photoelastic experiments with shear band locations extracted (Hall et al., 2009)

© University of Pretoria

Hall et al. (2009) observed a shear band thickness of approximately 10 – 20 D_{50}, with the distance between the bands in the order of 30 D_{50}. Hall et al. (2009) postulated that there are two possible directions in which the shear bands can be localized, namely the Roscoe and Coulomb shear band angles. For the Roscoe method, the orientation of the shear bands are at an angle of $\pi/4 - \psi/2$ (ψ is the angle of dilation) on each side of the principal strain increment direction. For the Coulomb angle, the shear band orientation is at an angle of $\pi/4 - \varphi/2$ (φ is the mobilized friction angle). They concluded that many questions still surround the pattern and spacing of the shear bands, which require extensive research.

Muir Wood (2012) and Hall et al. (2009) observed shear band geometrical features during their experimental analysis. Desrues and Viggiani (2004) also analysed a variety of drained plane-strain tests conducted over 20 years, and concluded that the location and orientation of shear bands are dependent on the following factors:

- Initial state of the material (void ratio and mean effective stress).
- Soil grading (size and uniformity).
- Geometry and slenderness of the specimen.

Throughout this section, progressive failure of a granular material as well as the occurrence of shear bands within a soil mass, which has an influence on the behaviour and bearing capacity of a foundation system have been discussed. Other factors such as the scale effects also contribute to variations in the bearing capacity of foundation systems. Therefore, the influence of the scale effect will be discussed in the next section.

2.3.1.3 Scale Effect

Scale effect is the phenomenon where the bearing capacity of a foundation decreases as the width of the footing increases, although the granular materials properties did not alter. It is well understood that the bearing capacity factor N_γ causes uncertainty within the bearing capacity equation proposed by Terzaghi. To compensate for the uncertainty in the bearing capacity factor N_γ, larger safety factors have been proposed (Ueno et al., 1998). Although Terzaghi's bearing capacity formula has simplified the design of foundations considerably, the inability to compensate for scale effects has led to the overdesign of footings and increased construction cost (Ueno et al., 1998).

Throughout the testing of the bearing capacity of soils it has been noted that the bearing capacity factor N_γ decreases with an increase in the size of the footing (White et al., 2008). Therefore, the bearing capacity of granular soils showed that the increase in bearing capacity was not linear with an increase

© University of Pretoria

in the footing width as predicted by Equation 2-1. Various authors have postulated the reason for the occurrence of the scale effect, with a few explanations described in the following section.

White et al. (2008) stated that the scale effect is due to two possible reasons. Because the stress present during the formation of the failure mechanism is directly related to the size of the footing, and the friction angle and angle of dilation is directly related to the stress applied to the soil (as explained by Bolton (1986)), the value for N_γ reduces as the size of the footing increases. White et al. (2008) named this the 'stress level' effect. He also postulated that the scale effect can occur due to the progressive failure mechanism (Section 2.3.1.2) of granular materials which initially mobilises a peak friction angle, after which the friction angle reduces/changes due to the softening response of the material with an increase in the load applied. Muhs (1963) and De Beer (1967) also stated that the progressive failure mechanism is the reason for the occurrence of the scale effect.

Yamaguchi et al. (1976) and Perkins and Madson (2000) stated that the decrease in the bearing capacity factor N_γ for wider footings can be explained by looking at the curvature of the Mohr-Coulomb envelope of dense soils. With an increase in the footing width, the mean normal stress became larger along the slip lines present in the sand, whilst the maximum friction angle of the soil (φ'_{max}) had to reduce. Hettler and Gudehus (1988) also believed the reduction in bearing capacity factor N_γ is attributed to the stress dependence of the mobilised friction angle, and not due to progressive failure mechanisms. Yamaguchi et al. (1976) conducted centrifuge experiments to determine the bearing capacity of granular soils. With their experimental work they found that the bearing capacity formula proposed by Terzaghi underestimated the value of the bearing capacity for small-scale models and overestimated the value for full-scale models when considering the maximum friction angle obtained with triaxial testing.

A very important consequence of the scale effect is that laboratory tests are not conservative when the data is extrapolated to a full-scale test method, due to the variable friction angle as a result of the lower stresses applied to the soil, as stated before. It is also difficult to accurately model the exact material response of a full-scale test in the field within a laboratory, as it is nearly impossible to collect a perfectly undisturbed soil sample for triaxial or other testing within a laboratory (Perkins and Madson, 2000).

It is clear that the stress-levels below a scale model of the footing is not equal to the stress-levels below a full scale test under 1 G gravitational load. The lower stress-level causes a larger friction angle of the granular material than for higher stress-levels. Therefore, the load-displacement behaviour of a small footing will be different than a large footing when placed on the same granular material under 1 G gravitational conditions (Aiban and Znidarčic, 1995).

© University of Pretoria

To compensate for the discrepancy between the results obtained for small scale testing and full scale testing, a geotechnical centrifuge is used to simulate realistic stresses within the soil mass. Mikasa and Takada (1984) found that the use of a geotechnical centrifuge to model a footing delivers similar stress and strains compared to a full scale test. They also observed the scale effect as many authors have done after them. Yamaguchi et al. (1976) and Kimura et al. (1985) observed larger shear strains at peak load for large footings in the centrifuge compared to smaller footings and attributed the difference to the scale effect. It is therefore clear that the use of a geotechnical centrifuge simulates the stresses in the soil accurately (Aiban and Znidarčic, 1995). The use of a geotechnical centrifuge will be discussed further in Section 2.6.

An understanding of the scale effect can lead to greater accuracy in translating small scale tests to full scale tests with confidence (Ueno et al., 1998). In order to reduce the scale effect in laboratory tests, various authors have proposed mitigating measures for test preparation. There is still no consensus on the mitigating measures, of which a few are listed in the following section.

To limit the scale effect in a geotechnical centrifuge, Muir Wood (2012) suggested a minimum footing to grains size ratio of 35 to avoid any grain size effect in the bearing capacity measured in a model test. Ovesen (1979) also stated a footing diameter to grains size ration of 30 for centrifuge tests, where after the scale effect will become small enough to ignore. Djikstra et al. (2013) stated that the footing to grain size ration should exceed a value of 100 to reduce the scale effect present within a geotechnical centrifuge. It is clear that to reduce the scale effects within a geotechnical centrifuge, the size of the footing needs to be larger than the grains of the soil by a specific factor, although there is still no consensus on the precise value for that factor. It is important to note that the grain size effect is a second distinct effect compared to the stress level effect.

2.3.1.4 Other Factors Affecting Bearing Capacity

Aiban and Znidarčic (1995) conducted plane-strain centrifuge modelling of three aluminium footings and proved experimentally that ignoring the initial deflection of the footing up until the peak load can lead to an overestimation of the bearing capacity factor N_q and N_γ by as much as 22%. This is mainly due to the assumption that the granular material is rigid plastic and the settlement of the soil due to the peak load is ignored (Aiban and Znidarčic, 1995).

Spasojevic and Cabarkapa (2012) analytically examined the best method to model the stress field below a footing by considering their own work as well as work done by other authors and concluded that the value of the bearing capacity factor N_γ is approximately two times larger for footings with rough surfaces compared to footings with smooth surfaces for a similar angle of dilation ($\Delta\varphi$ in the figure), as

© University of Pretoria

can be seen in Figure 2-11. In the figure, the roughness of the footing was set to be equal to the mobilised friction angle of the soil for the top line and zero for the smooth footing at the bottom. Michalowski and You (1998) stated that the effect of the roughness of the footing can be due to the fact that for analytical analysis, the smooth footing/soil interface problems have no friction or adhesion and no internal work needs to be overcome if a section of the footing is separated from the soil surface. Apart from observing the same trend for rough and smooth footings, Banimahd and Woodward (2006) also concluded analytically through FEM that the bearing capacity factor N_γ is larger for strip footings compared to circular foundations.

White et al. (2008) investigated the bearing capacity difference between a flat and conical footing, noting that there is a difference in the value of the bearing capacity factor N_γ due to the roughness and shape of the footing, although the theoretical difference is small (approximately 10%). It is clear that other factors that have an influence on the bearing capacity of the foundation system includes the settlement of the soil up to peak loading, the surface roughness of the footing, the type of footing as well as the shape of the contact surface of the footing.

As the bearing capacity of a foundation system and the factors that can contribute to differences in the bearing capacity have been discussed, the next section focusses on what happens when the bearing capacity is exceeded and failure of the foundation system occurs.

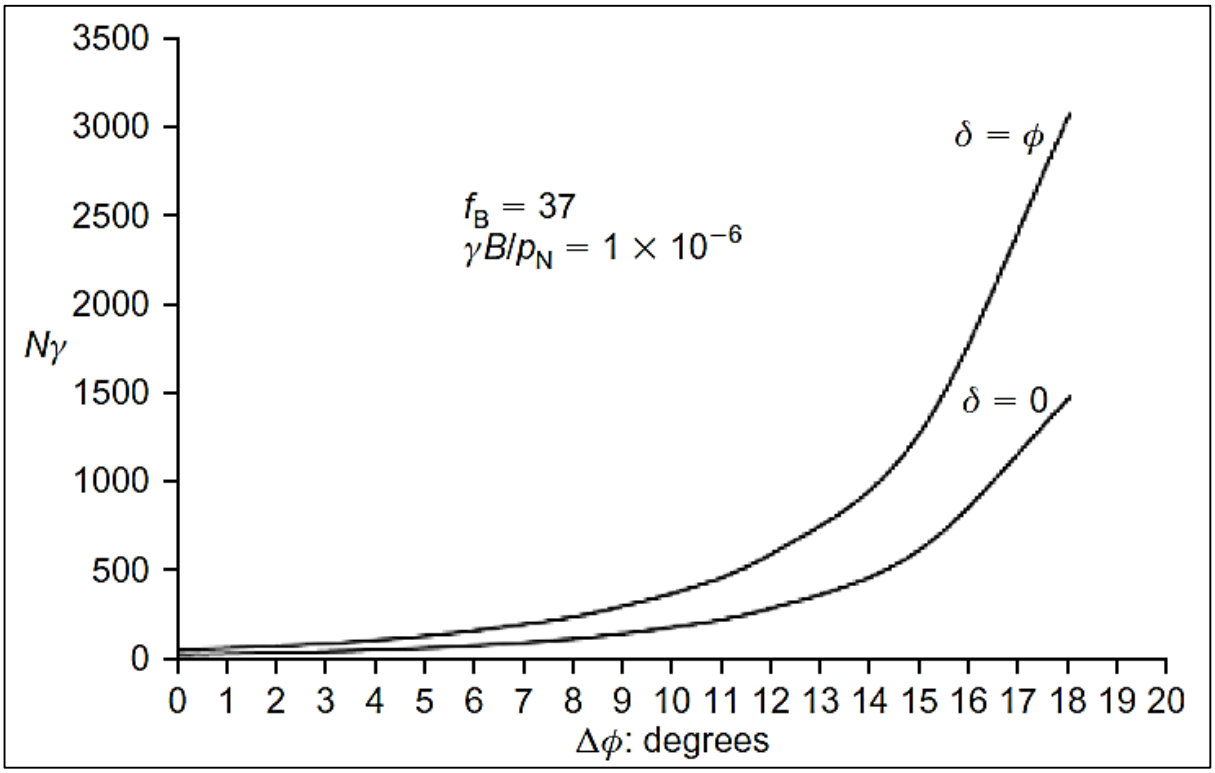

Figure 2-11 Effect of footing roughness on bearing capacity factor Nγ (Spasojevic and Cabarkapa, 2012)

© University of Pretoria

2.3.2 Bearing Capacity Failure of Foundation Systems

Failure of a foundation system can either be due to the failure of the footing, settlement failure or bearing capacity failure. When bearing capacity failure of a foundation system occurs, the soil beneath the footing usually fails in shear (Craig, 2004). Bearing capacity failure can occur in one of three ways: general shear failure (a), local shear failure (b) and punching shear failure (c) as indicated in Figure 2-12. Craig (2004) outlined the three failure types with discussions on the occurrence of each:

- For general shear failure (a), a failure surface develops at the soil-structure interface at the edge of the footing. As the applied pressure increases, plastic conditions are reached at the edge of the footing, expanding downwards and outwards. Plastic equilibrium eventually occurs throughout the soil above the slip surface. Heaving of the soil occurs on both sides of the footing until the final slip movement occurs, accompanied by tilting of the footing. This generally occurs in soils of low compressibility such as dense sand.
- For local shear failure (b), the soil beneath the footing experiences significant compression, along with the partial development of plastic conditions. The slip surface does not develop to the ground surface and only partial heaving occurs, with no tilting of the footing expected. This mechanism is accompanied by excessive settlement of the footing and occurs in soils of high compressibility such as loose sand.
- Punching shear failure (c) occurs due to high compression of the soil under the foundation, accompanied by vertical shearing of the soil at the footing edges. No heaving of the soil surface or tilting of the footing is expected. This generally occurs with highly compressible soils such as loose sand located at depth.

Banimahd and Woodward (2006) determined through finite element analysis that the depth of the failure zone within a granular mass is dependent on two factors. Firstly, it is proportional to the footing size and secondly, rougher footings cause deeper failure mechanisms compared to smooth footings.

© University of Pretoria

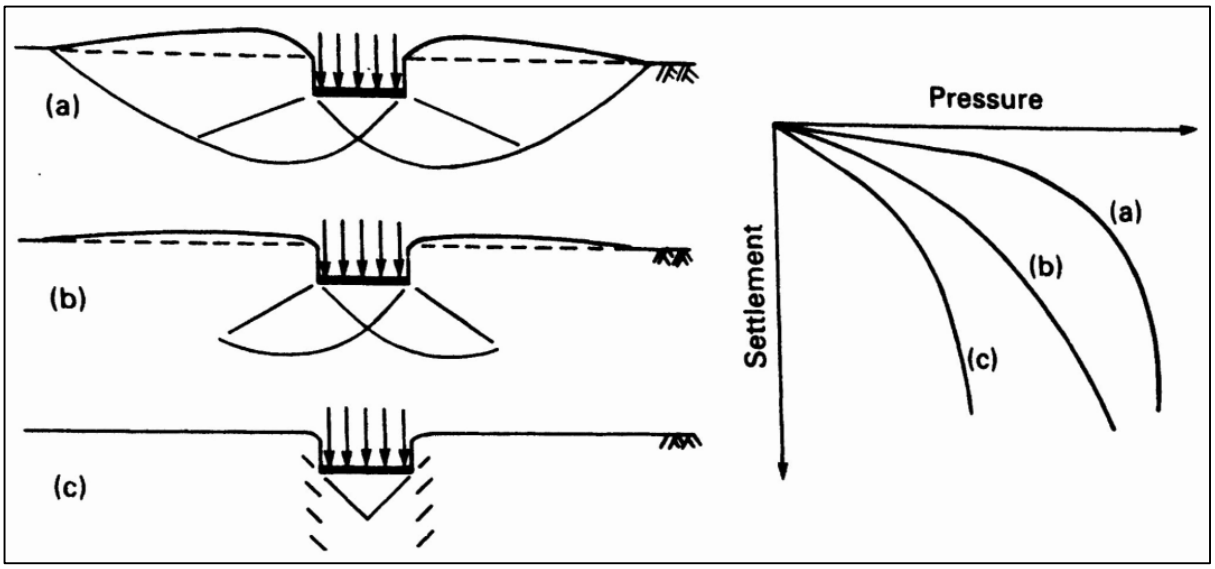

Figure 2-12 Failure mechanism of foundations (Craig, 2004)

The most common type of bearing capacity failure is the general shear failure mechanism. Various authors have proposed methods to determine the exact properties of the slip surfaces which develop beneath the footing. The three most popular methods are proposed by Hill, Prandtl and Terzaghi and can be seen in Figure 2-13. The methods are described in short by Manoharan and Dasgupta (1995) as:

- The Hill mechanism consists of two symmetrical sections, clearly evident in Figure 2-13. The plastic flow of the soil is confined within the slip surface ODEF. The slip surface is then divided into three distinct sections, firstly a rigid triangular wedge OCD with the size of the corner angles indicated in the figure, then a log-spiral section DCE with a central angle of $\pi/2$ and then finally a passive Rankine's triangular wedge ECF. For the Hill mechanism, the base of the footing is considered to be smooth.
- The Prandtl mechanism is similar to the Hill mechanism, only with the central wedges overlapping due to the fact that horizontal movement is not allowed (the footing is considered to be rough).
- The Terzaghi method is a modification of the Prandtl mechanism, with a different proposed angle for the rigid triangular wedge equal to only the mobilised friction angle of the soil (footing is also considered to be rough).

© University of Pretoria

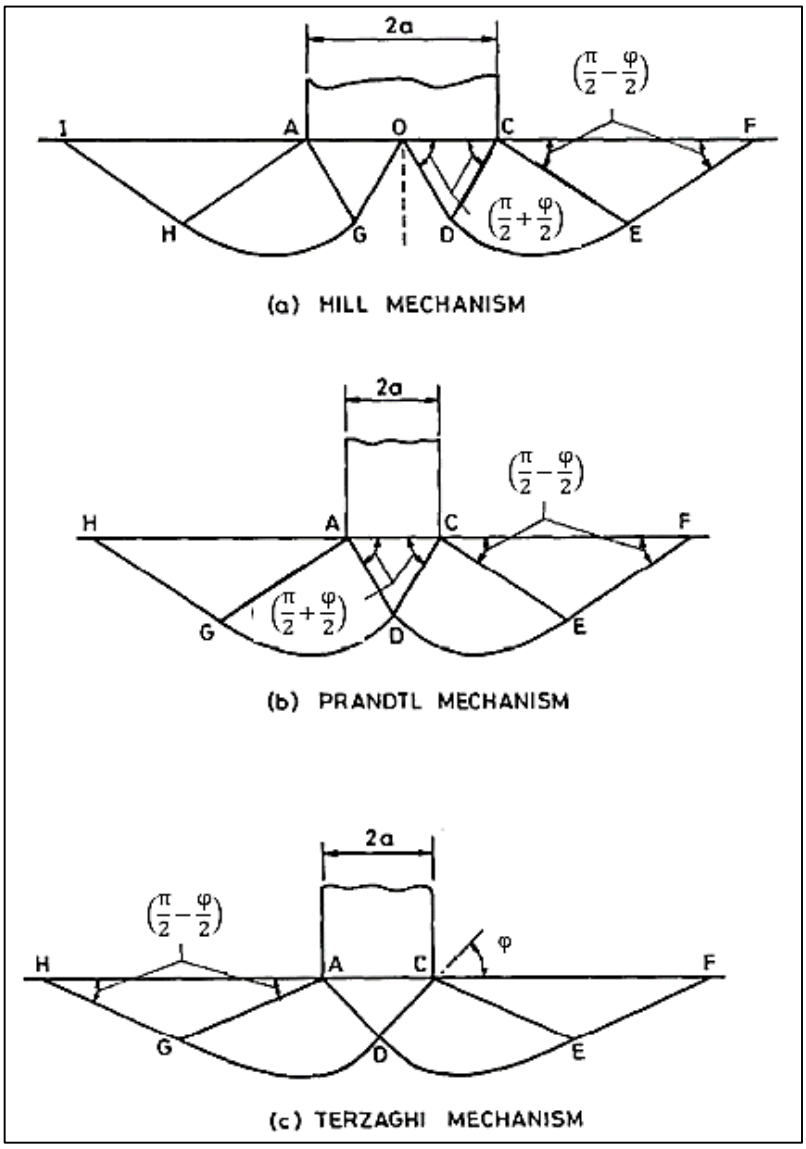

Figure 2-13 Slip line mechanisms (Manoharan and Dasgupta, 1995)

As stated earlier, Conte et al. (2013) analytically determined the bearing capacity of a granular soil through the use of FEM. During their analysis with the method developed by Conte et al. (2013), they also found details of the final loading stage and subsequent bearing capacity failure mechanism of the foundation system. The displacement vectors of the soil particles can be seen in Figure 2-14 below, indicated in red. The footing is located in the top left of the figure and a wedge shaped zone develops below the footing, along with radial shear zones from the edge of the footing. Both the wedge-shaped zone and the radial zone are defined with shear bands (Conte et al., 2013). Their results closely correlates with either the Terzaghi or Prandtl mechanism discussed previously.

© University of Pretoria

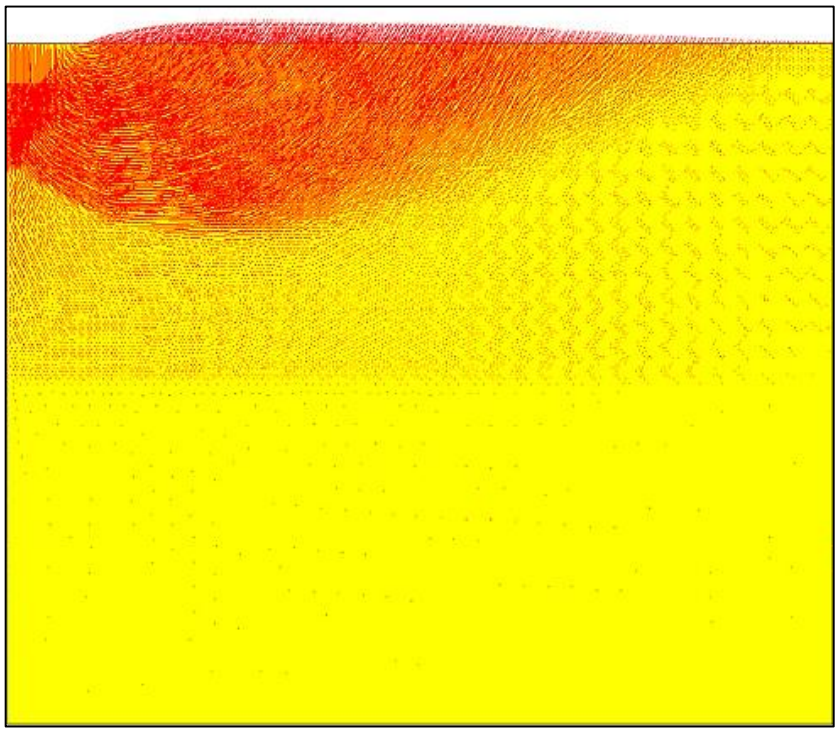

Figure 2-14 Displacement vectors of soil during final loading stage of foundation (Conte et al., 2013)

As bearing capacity failure is only one of the methods with which the foundation system can fail, the next section will discuss settlement failure of the foundation system.

2.3.3 Settlement Failure of Foundations

Generally a structure is considered to have failed due to excessive settlement well before ultimate bearing capacity becomes a problem. Excessive forces are transferred to the superstructure due to large settlements, which can lead to failure of structural elements. Settlement problems can be divided into three categories: architectural, functional and structural (Knappett and Craig, 2012). In order to limit the effect of settlement problems, certain guidelines were proposed by Skempton and MacDonald (1956) as well as Bjerrum (1963) which still serves as a good guideline for design today.

Skempton and MacDonald (1956) imposed limits on angular distortion (differential settlement to length ratio) to compensate for the size of the structure, as well as the allowable deflection. The concept of angular distortion was taken further by Bjerrum (1963) which proposed limits as seen in Table 2-2. All of the guidelines are however empirical and cannot be considered as definitive for all structures.

© University of Pretoria

Table 2-2 Deflection limits on angular distortion (Bjerrum, 1963)

Angular Distortion	Limit
1/150	Structural damage to building
1/250	Tilting of rigid building become visible
1/300	Cracking of panel walls and difficulty with overhead cranes
1/500	Limit if cracking of the structure is not allowable
1/600	Overstressing of frames with diagonals
1/750	Difficulties with machinery sensitive to settlement

Due to the fact that no settlement limits were placed on the experimental work conducted for this paper, the concept of settlement failure will not be discussed any further. Section 2.3 discussed the failure of the soil beneath the foundation, either through bearing capacity failure or settlement failure. When a foundation system fails, it can be attributed to either soil failure or failure of the footing, therefore the next section will discuss failure of footings.

2.4 Failure of Concrete Footings

The exact failure mechanism of a reinforced concrete footing on soil is still up for debate, as various researchers reported different results. Lin et al. (2003) highlighted that the amount of research regarding foundation systems are limited and there is virtually no research conducted on the pre- and post-cracking behaviour of a reinforced concrete footing. The precise failure mode of a reinforced concrete footing is difficult to quantify due to the vast amount of different mechanisms that has an influence on the behaviour of the foundation system, such as the composite reinforced concrete footing's behaviour during cracking, as well as the soil mechanisms that have been discussed in the previous sections.

One of the most challenging aspects regarding reinforced concrete is the fact that it is a composite material, where the behaviour of each individual material, as well as the composite, needs to be understood to accurately model the material. Concrete is a brittle material, whereas steel is a ductile material, complicating the behaviour of the composite. Determining the behaviour of the brittle material in the composite is important due to the danger of a brittle failure. A large amount of literature is available on the study of concrete fracture tests. However, consensus regarding the method which should be used to model fracture has not been reached. This causes a number of models to survive together, prohibiting the use of fracture concepts in concrete design codes (Hoover et al., 2013).

© University of Pretoria

A factor contributing to the lack of consensus regarding the modelling of fracture in concrete is the fact that the tests conducted only consider a limited range of influencing parameters. These tests have also been conducted using different concrete mixes, different batches of the same concrete, at different ages and environmental conditions, as well as using different test procedures with different specimen types and sample sizes (Hoover et al., 2013).

While the exact failure mechanism of reinforced concrete footings is still not fully understood, the material properties of reinforced concrete have been studied extensively. For any reinforced concrete structure, the two most important failure mechanisms to consider are shear and flexural failure of the structure. The governing mechanism is determined through the design of the structure. In almost all the cases, a structure is designed to fail in flexure rather than shear, due to the fact that a flexure failure is not as sudden and without warning as a shear failure. Menétrey (2002) tested footings that were designed to fail in punching shear and flexure respectively. The test results can be seen in Figure 2-15, indicating the loading compared to centre point deflection. It is illustrated that a sudden drop in the load carrying capability for shear failure is evident, supporting the notion of sudden failure. For the footings designed to fail in flexure, a reduction in the load carrying capacity of the structure can also be seen. The reduction is however more gradual than that of the punching shear failure.

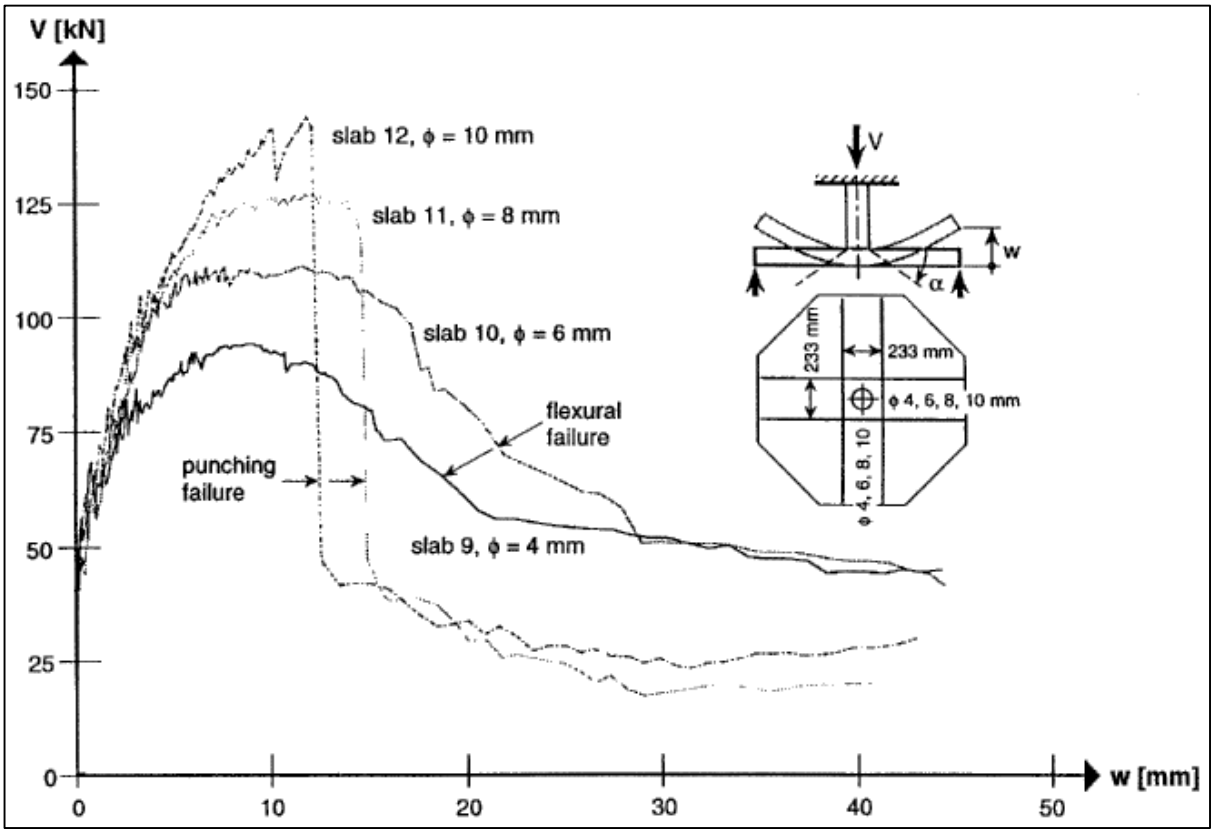

Figure 2-15 Footings designed to fail in shear and flexure respectively (Menétrey, 2002)

© University of Pretoria

Through decades of laboratory and field testing, the mechanism of flexural failure of reinforced structures is well understood and has been incorporated into design codes. The failure mechanism associated with shear forces as well as flexural forces present is not as well defined yet (Kim and Jeong, 2010). Because the mechanism is not fully understood, the design provisions of these reinforced concrete structures are essentially empirical. Guidelines have been imposed to ensure that the initial empirical assumptions are valid. Recently a shift has been made to develop equations based on experimental evidence with fundamental science behind them (Kim and Jeong, 2010; Wei et al., 2011; Shehata, 1990).

2.4.1 Flexural Failure of Footings

Flexural failure of a footing occurs when failure is as a result of the tensile yielding of the reinforcement within the reinforced concrete footing. Flexural failure of slabs is quite well understood and the mechanism can be applied to column footings, taking into account the distributed loading on the cantilever section of the footing (Gibson, 1974). The deflected shape of the footing is very dependent on the stiffness of the soil with depth. The counter pressure of the soil causes the footing to change its deflected shape to match the deflected shape of the soil surface (Gibson, 1974).

Lin et al. (2003) conducted full scale laboratory tests to determine the pre- and post-cracking behaviour of a reinforced concrete footing. In their experiments they also determined the effect of edge-restraints on the deflection of reinforced concrete footings. A schematic of their experimental setup can be seen in Figure 2-16, with the only variation between consecutive tests being the restraints at the edges of the footings.

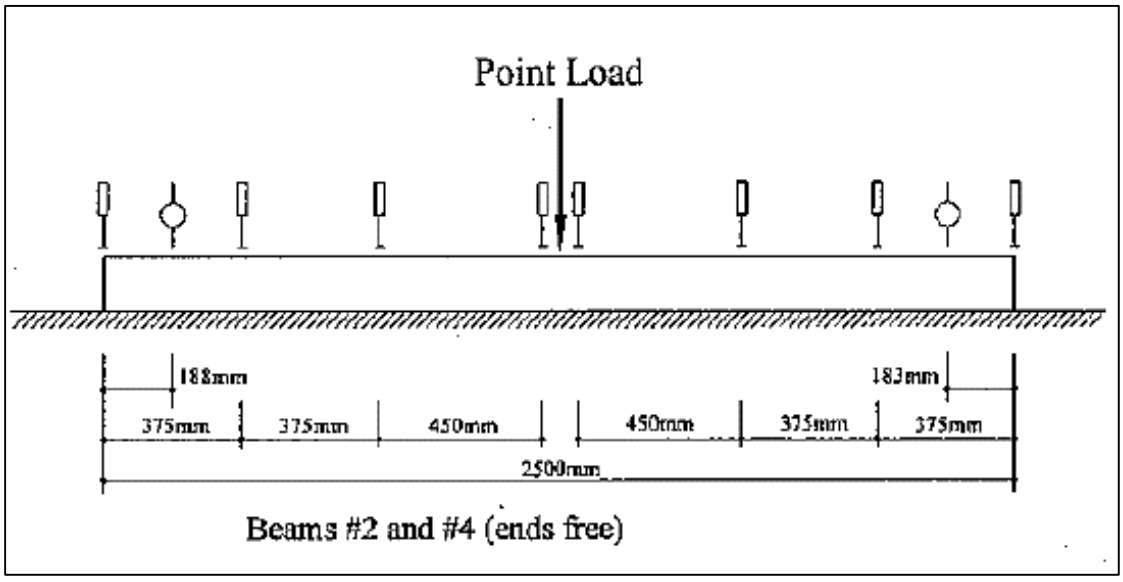

Figure 2-16 Experimental setup to test footings on soil (Lin et al., 2003)

© University of Pretoria

The deflection of the footings were measured at midspan below the point load with the use of LVDTs. As can be seen in Figure 2-17, the load/deflection of both experimental procedures are the same up to first cracking, as both experimental footings were cast from the same concrete batch. However, after the first crack, the two experiments have very different post-cracking behaviour (Lin et al., 2003). It is clear from their results that the stiffness (indicated by the slope of the load/deflection curve) changes for concrete when it starts to crack and the steel contributes towards the tensile resistance of the footing.

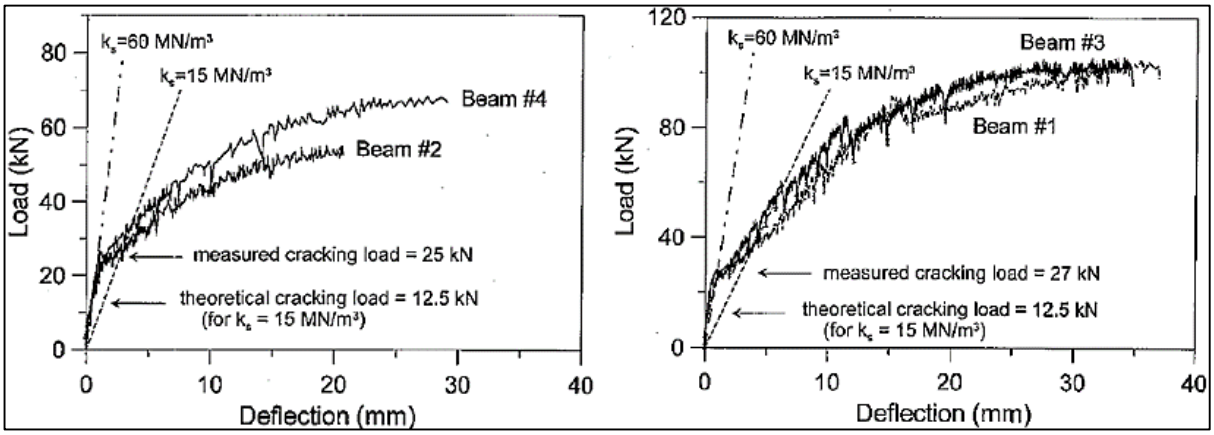

Figure 2-17 Footing test results with edges free (left) and edges fixed (right) (Lin et al., 2003)

From their experimental results Lin et al. (2003) determined that in both tests a crack had formed in the middle of the beams below the load application area. In the test where the edges were fixed, they observed further cracking of the beam, whereas the beams with the edges free only developed one crack that propagated from the bottom of the beam to the top at failure. The deflected shapes for both experiments are shown in Figure 2-18 below. It is clear that no additional cracking occurred after the first crack if the edges of the footings are free to move (Lin et al., 2003).

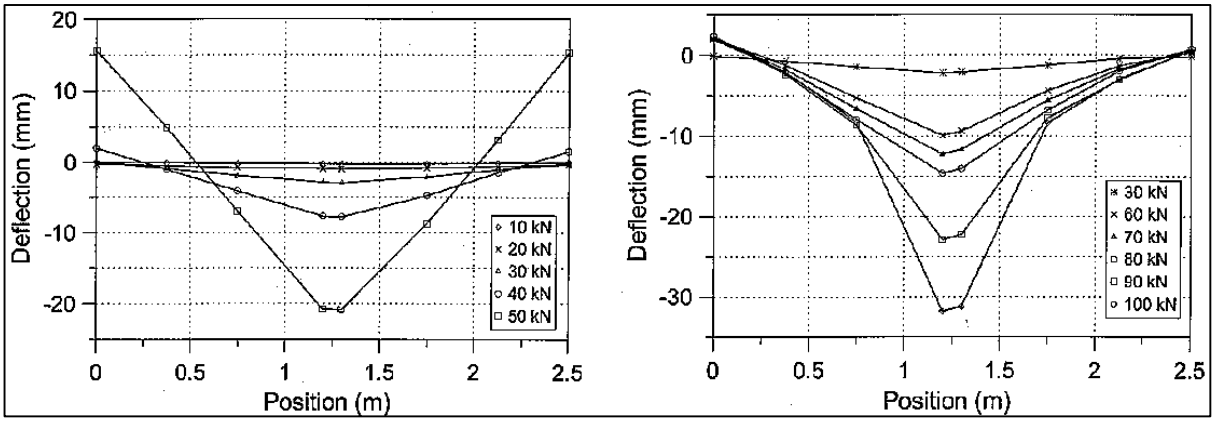

Figure 2-18 Deflected shape of experimental footings, with edges free on the left and edges fixed on the right (Lin et al., 2003)

© University of Pretoria

Reinforced concrete structures are mostly designed to fail in flexure, due to the ductile nature of the failure. However, apart from flexural failure, a reinforced concrete structure can also fail in shear as discussed in the next section.

2.4.2 Shear Failure of Footings

Shear failure of a reinforced concrete footing occurs when sections of the concrete slides against itself until two sections are completely separated from one another. As much as the method of flexural failure is understood, the exact mechanism of shear failure within a reinforced concrete footing is still a subject of debate (Carmona and Ruiz, 2014). Various methods are proposed and experimental observations have been made, but there is still no consensus as to how the mechanism can best be designed for. Shear failure in a footing can be split up into two parts, either shear failure of the footing or punching shear of the slab around the column (Carmona and Ruiz, 2014).

Shear failure of reinforced structures are due to both shear and flexural action (Russo et al., 2004). With the presence of shear stresses within a reinforced concrete structure, the flexural strength of the structure can reduce greatly from the pure flexural strength, which might lead to a sudden failure without warning (Russo et al., 2004).

The design and analysis of punching shear found in design methods and code formulas are based on experimental evidence from the testing of concrete slabs with a relatively high slenderness ratio (shear-span to depth ratio) of more than three to four. They are then used for footing design, with concrete footings usually having a low slenderness ratio. The behaviour of footings when loaded to shear failure is therefore not as clear compared to shear failure in slabs (Hallgren and Bjerke, 2002).

Carmona and Ruiz (2014) proposed a mechanism to predict the shear resistance of a beam and validated the model through experimental work. The aim of their model was to determine the shear strength of reinforced concrete beams without any stirrups, similar to that of a footing. One important aspect of their work was the study of crack propagation through the beam. A schematic of the testing procedure used to determine the shear strength of beams is shown in Figure 2-19.

© University of Pretoria

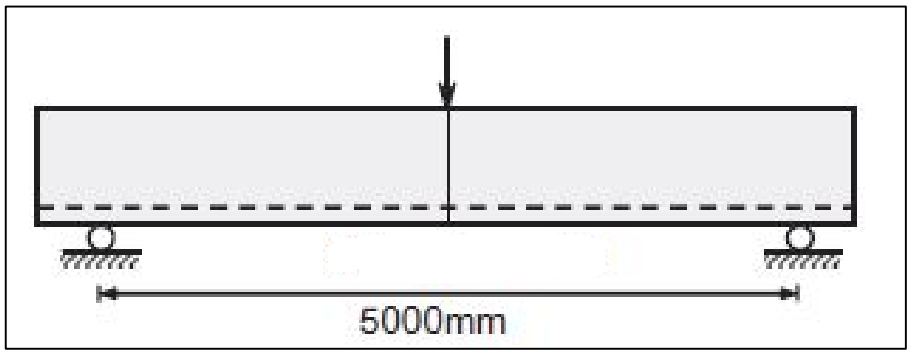

Figure 2-19 Experimental setup to determine shear resistance of a beam (Carmona and Ruiz, 2014)

In Figure 2-20 the variables that are used to determine the strength of a concrete cross-section after cracking has occurred are shown for both a cross-section with and without reinforcing (Carmona and Ruiz, 2014). Crack propagation in a reinforced structure takes place in a stable manner up to a certain depth, known as the critical depth (ξ_{crit}), where after the crack becomes unstable. When the crack is unstable, the crack length can increase beyond the critical depth without the need for external energy, but through solely using the energy stored in the structure (Carmona and Ruiz, 2014). The critical depth of a structure is dependent on the type of loading, boundary conditions and the geometry of the structure.

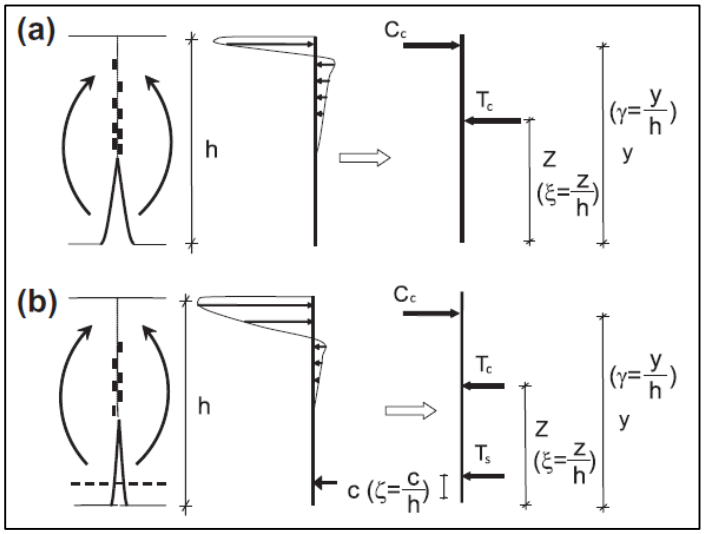

Figure 2-20 Variables used to calculate strength of concrete after cracking (without reinforcement shown in (a) and with reinforcement shown in (b)) (Carmona and Ruiz, 2014)

Carmona and Ruiz (2014) proposed that the critical depth of a crack is proportionate to the bending moments present in the structure. They illustrated with a simple beam, as shown in Figure 2-21, that if the loading was changed on the structure, a different bending moment will develop throughout, which would lead to a different critical depth for crack propagation. Through this analogy it is also assumed that the critical depth is not constant throughout the length of the structure, but rather dependent on the bending moment at a certain point (Carmona and Ruiz, 2014).

© University of Pretoria

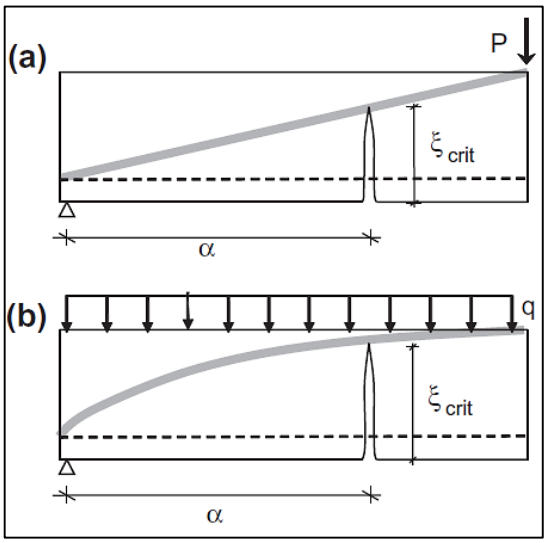

Figure 2-21 Difference in critical crack length due to bending moments in the beam (Carmona and Ruiz, 2014)

Carmona and Ruiz (2014) illustrated the concept of a stable and unstable crack, shown in Figure 2-22. In the figure, the stable crack propagates upwards until it reaches the critical depth, where after the unstable crack branch follows the direction of the bending moment within the beam, when drawn on the compression side of the beam.

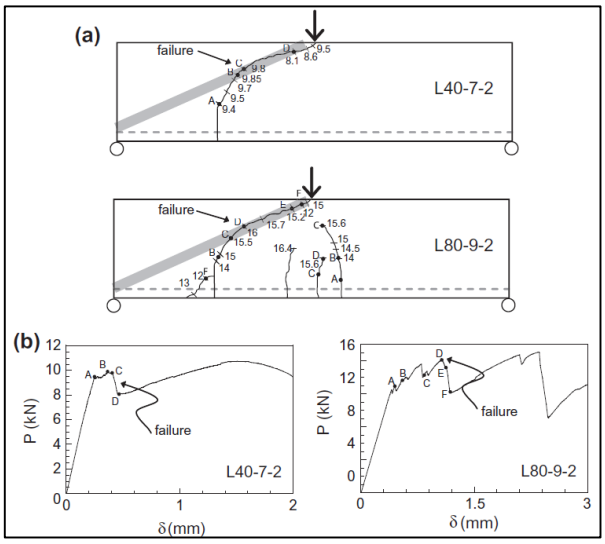

Figure 2-22 Crack propagation in reinforced concrete beam (Carmona and Ruiz, 2014)

The transition between shear failure and flexural failure is dependent on the amount and strength of the reinforcement. If the reinforcement within the structure is increased, the critical section moves away from the load application point to areas where the steel does not yield. This phenomenon is therefore also dependent on the bond strength which mobilises the steel. If the bond strength increases considerably, shear failure can no longer occur as the steel will yield before the crack can reach a critical

© University of Pretoria

depth (Carmona and Ruiz, 2014). They also concluded that with the presence of shear stirrups, unstable crack growth was reduced and subsequently the collapse mode changed from shear to bending. Therefore, the relationship between crack propagation and the collapse of the structure is key to understanding the shear strength. Crack propagation factors need to be considered in order to fully understand and evaluate the failure load (Carmona and Ruiz, 2014).

Russo et al. (2004) stated that the shear strength of a beam/footing without any shear stirrups is due to both the beam and arch action within the structure. The beam mechanism is due to the transfer of forces between the steel and the concrete as a result of the bond between the two components and the arch mechanism is due to the variation in the lever-arm of the cross-section. An example of the mechanism within a crack is shown in Figure 2-23 (Russo et al., 2004), with the beam mechanism represented as V_d and the arch mechanism represented as V_a.

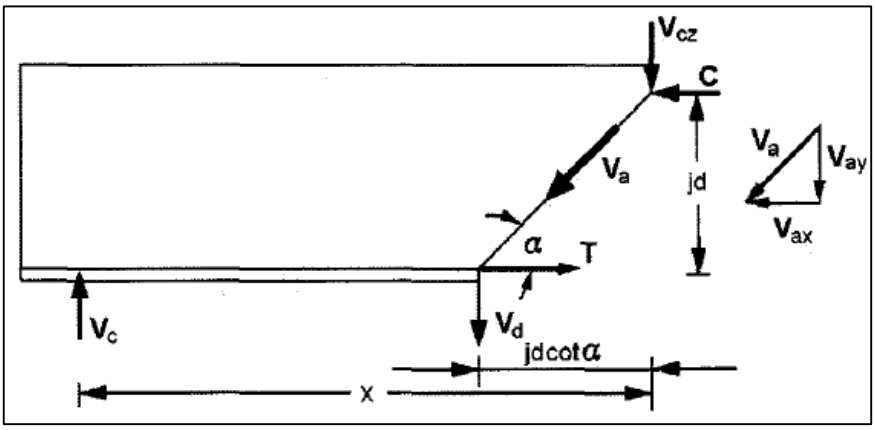

Figure 2-23 Shear failure mechanism in a beam components (Russo et al., 2004)

An example of the arch mechanism within a beam can be seen in Figure 2-24 (Russo et al., 2004).

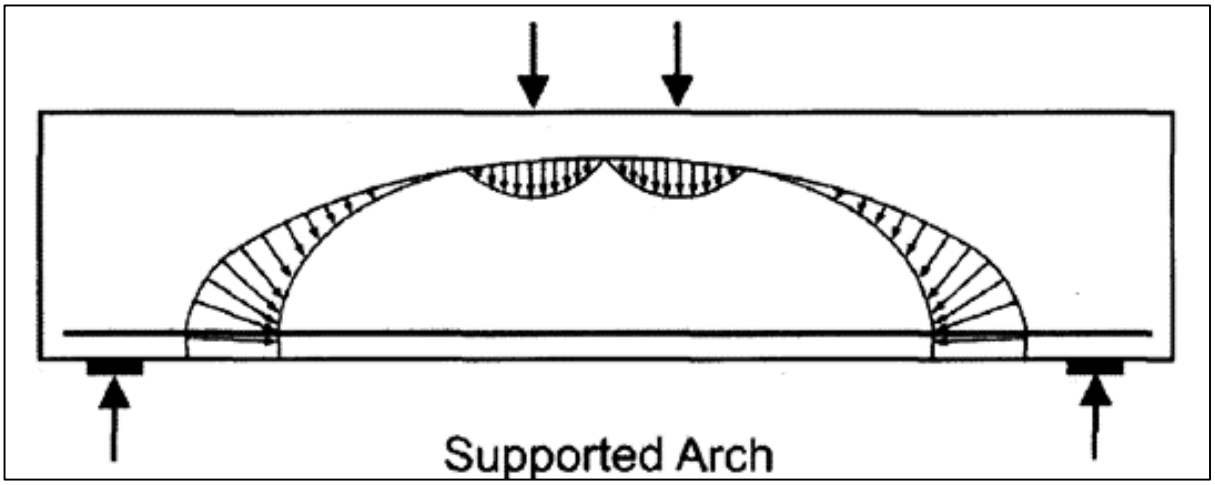

Figure 2-24 Arch mechanism of shear failure example (Russo et al., 2004)

© University of Pretoria

Shear failure in a reinforced concrete footing can also occur through punching shear failure. Punching shear failure of a reinforced concrete footing occurs when a conical plug of concrete suddenly perforates the slab below the column (Menétrey, 2002). Due to the fact that the failure is brittle, a number of construction methods were developed to avoid the occurrence of punching shear. The most common method for reinforced concrete footings is to increase the depth of the footing and in effect increase the shear resistance of the concrete within the cross-section (Menétrey, 2002).

Through FEM, Hallgren and Bjerke (2002) found that the resistance of concrete footings is highly dependent on the strength of the concrete used for the footing. They also found that the angle of punching shear cracks in slender slabs were between 30-40°, whereas the angle for footings were between 50-60°, indicating that the mechanism of punching shear for slender slabs and footings are not the same.

Due to the large depths of the reinforced concrete footing considered in this study, the occurrence of punching shear is unlikely and will not be discussed any further, as it is not relevant to this study. After considering the materials individually for the majority of this chapter, the next section will focus on the behaviour of the foundation system as a whole.

2.5 Relative Stiffness of the Foundation System

The structural behaviour of a footing can largely be attributed to the stiffness thereof. It is important to consider the stiffness of the entire foundation system, and not just the stiffness of the footing (Arnold et al., 2010). Whether or not a footing behaves in a flexible or rigid fashion can be assessed with a formula that uses the Winkler spring models combined with a framework that includes the stiffness of the footing to determine an equivalent system stiffness (Canadian Foundation Engineering Manual, 2006). The parameter K_s indicates whether the system is a stiff or flexible system. For the calculation of K_s, a linear elastic soil spring model is assumed. The formula used to calculate K_s can be seen in Equation 2-11 (Arnold et al., 2010). The values obtained with the equation gives an indication of the stiffness of the system as described in Table 2-3.

© University of Pretoria

$$K_s = \left(\frac{1}{12}\right)\left(\frac{E_b}{E_s}\right)\left(\frac{d}{l}\right)^3 \qquad \text{(Equation 2-11)}$$

Where:

K_s = System stiffness
E_b = Young's modulus of the raft foundation
E_s = Secant stiffness modulus of the soil
d = Thickness of the raft foundation
l = Length of the raft foundation

Table 2-3 Limitations for the stiffness of a system (Arnold et al., 2010)

K_s Range	System stiffness
0	Absolutely flexible
0 – 0.01	Semi-flexible
0.01 – 0.1	Semi-Stiff
0.1 – Infinity	Stiff

Arnold et al. (2010) conducted a series of centrifuge experiments to determine the effect of the system stiffness on the stress distribution below the footing. From their analysis they found that the stress distribution below the footing is dependent on the stiffness of the footing, as well as the footing settlement for similar soil conditions. To determine the secant modulus of elasticity for the granular soil, they determined the settlement of the footing as a result of the load fitting a regression line through the data. The procedure is illustrated in Figure 2-25 (Arnold et al., 2010).

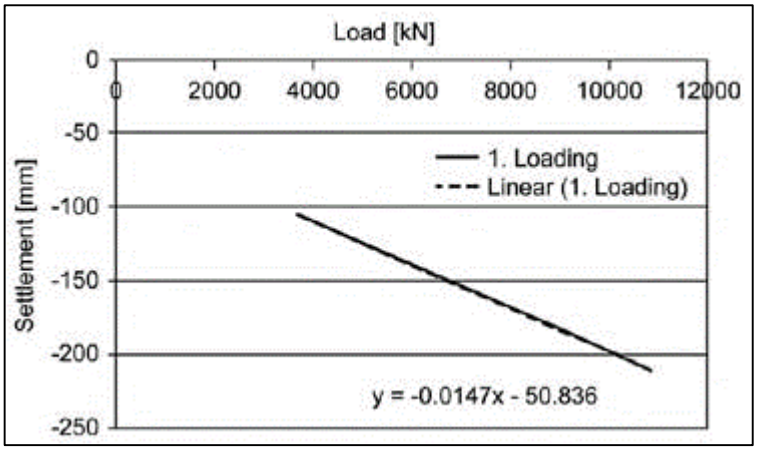

Figure 2-25 Determining the modulus of elasticity of soil through the load settlement curve (Arnold et al., 2010)

Arnold et al. (2010) concluded that the stress distribution on sand is dependent on the magnitude of the load applied to the footing. Initially the behaviour of the footing was equivalent to a stiff system, then later changed to a flexible system with an increase in the applied load. The use of a single system stiffness parameter is therefore not adequate as it does not take loading into account (Arnold et al. 2010). The constant stiffness assumed for reinforced concrete structures is also not valid, as the stiffness of

© University of Pretoria

reinforced concrete footings are significantly influenced by the non-linearity of the concrete material properties (due to cracking), therefore changes in the stiffness of the footing occurs when the concrete starts to cracks (Skorpen and Dekker, 2014).

To test the effect of the footing stiffness of large foundations on the behaviour thereof and correlate with the work found in the literature, the use of full scale testing methods was not an option. Due to the size of the footings and cost involved to cast a number of the large footings, an alternative experimental method was considered. The next section will therefore discuss the use of a geotechnical centrifuge, as it was the experimental method used for this study.

2.6 Geotechnical Centrifuge Modelling

Due to the large size of the footings analysed in this study, a small scale model had to be considered. However, in order for the small scale test to produce reliable results, the model must respond in a similar way than the full scale test. For this to be true, the kinematic, geometric and dynamic relationships of the model need to hold true compared to the prototype (Laefer et al., 2011). The difficulty with testing small scale models under 1 G gravitational loading is the fact that the stresses within the soil mass are not representative of the stresses obtained with full scale testing and therefore the behaviour of the small scale model will alter from that of the full scale model (Jacobsz, 2013). Geotechnical centrifuges have the ability to recreate stress conditions that are similar to real world conditions. The use of a geotechnical centrifuge offers an effective way to model the behaviour of the interaction between soil and a footing (Haigh et al., 2010).

2.6.1 Centrifuge Concept

Laefer et al. (2011) proposed a formula (Equation 2-12) to ensure that the soil interaction problem in a scale model is equivalent to the response of a full scale test. The left hand part of the equation refers to the stresses and modulus of elasticity of the prototype/full scale test and the right hand part refers to the model. This is a similitude relationship for modelling elastic settlement within a scaled model. Using a centrifuge therefore automatically satisfies this as stresses are replicated 1:1 as is stiffness.

$$\left(\frac{\sigma}{E}\right)_p = \left(\frac{\sigma}{E}\right)_m \qquad \text{(Equation 2-12)}$$

Where:

σ = Normal stress of the material
E = Modulus of elasticity of the material

© University of Pretoria

A centrifuge uses centripetal acceleration to increase the forces and stresses within a material model (Schofield, 1980). After selecting the desired gravitational acceleration required for the testing procedure, the radial acceleration can be determine with Equation 2-13. After determining the radial acceleration of the centrifuge arm, the radial velocity of the centrifuge arm can be calculated with Equation 2-14. The centrifuge uses these basic principles to determine the speed required to obtain a certain gravitational acceleration imposed on the material model (Schofield, 1980).

$$r \times \omega^2 = g \qquad \text{(Equation 2-13)}$$

$$r \times \omega = v \qquad \text{(Equation 2-14)}$$

Where:

r = Radius of centrifuge arm
ω = Radial velocity (radians/s)
v = Velocity (m/s)
g = Gravitational acceleration of centrifuge (m/s^2)

In a centrifuge model, the materials are placed within a sample box to confine the material during testing, known as a strongbox. The materials within the strongbox do not experience the same acceleration at each point, as the radial distance from the centrifuge axis to the material changes with the depth in the strongbox (Schofield, 1980). The surface of the material is unstressed, accompanied by an increase in pressure within the material body. Schofield (1980) proposed expressions to determine the error present in a model due to the variation in gravitational acceleration with depth. However, as he determined that the error is mostly less than 2% for accelerations up to a 100 G, the errors are deemed insignificant.

Yamaguchi et al. (1976) concluded that during analysis of their centrifuge problem, the effect of a varying acceleration along the depth of the centrifuge model causes a variation from the true behaviour of the soil of less than 5% and concluded that the use of a geotechnical centrifuge can be used to model real world problems with reasonable reliability. Slight variation in the bearing capacity and slip lines obtained between full scale testing and centrifuge testing in Yamaguchi et al. (1976) experiment can be seen in Figure 2-26.

© University of Pretoria

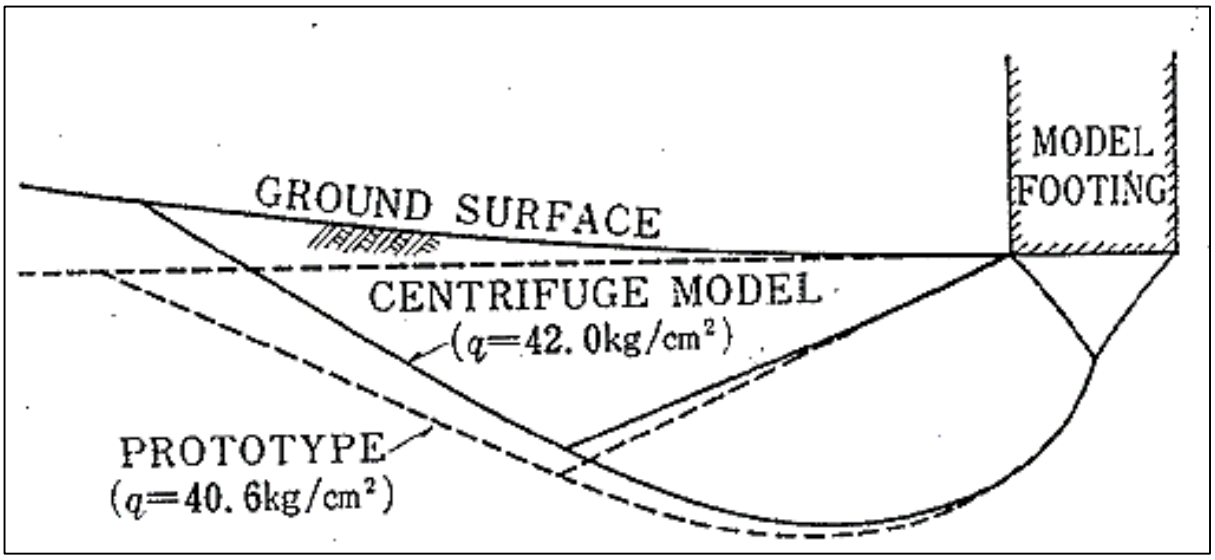

Figure 2-26 Difference between centrifuge test and full scale test (Yamaguchi et al., 1976)

2.6.2 Advantages and Disadvantages of a Geotechnical Centrifuge

Apart from the fact that the geotechnical centrifuge can be used to model realistic stresses within a small scale soil mass, the use of the centrifuge also has a number of other benefits. Some of the other advantages of the use of a geotechnical centrifuge includes (Herbert et al., 2011; Jacobsz, 2013; Laefer et al., 2011):

- Research can be conducted more economically than full scale testing.
- Research can be done at a rapid pace and with a large number of samples, allowing repeatability.
- Testing is generally safer than full scale testing of large footings.
- During failure, instrumentation is less likely to be damaged by the model.
- Time-related problems such as consolidation can be tested in a fraction of the time.

There are clearly many advantages to using a geotechnical centrifuge for laboratory testing, however the side effects also have to be considered.

Although centrifuge testing have a lot of advantages compared to full scale testing, the occurrence of an error during testing or construction of the model is amplified considerably when performing test under high gravitational accelerations (Haigh et al., 2010). Aiban and Znidarčic (1995) outline considerations that need to be taken into account when conducting centrifuge modelling:

- Variations of the gravitational forces with depth.
- The scaling of the soil grains.
- Boundary conditions present during testing.

© University of Pretoria

Due to the difficulty and cost associated with full scale testing, very few full scale tests are available to verify the solutions obtained in laboratory tests. Another difficulty with full scale testing is the non-homogeneity and uniformity of the soil in natural occurring materials. Therefore, the test conducted in a centrifuge are generally not perfectly representative of full scale conditions (Aiban and Znidarčic, 1995). As a geotechnical centrifuge is used to test scale models, it is important to fully understand the exact scale factors of each property required from a geotechnical centrifuge test.

2.6.3 Scaling Laws

The use of a geotechnical centrifuge allows for the testing of material properties at small scales. However, the effect of increasing the gravitational acceleration on a model is not constant for all variables. If a certain property of the material is required, the appropriate scaling law needs to be applied to the results to extrapolate to full scale testing. Table 2-4 contains general scaling laws used in a geotechnical centrifuge from prototype to model as presented by Jacobsz (2013), where n is equal to the gravitational acceleration of the centrifuge during testing.

Table 2-4 Scaling laws for centrifuge testing (Jacobsz, 2013)

Property	Scale Factor
Model Scale	n
Accelerations	n
Linear Dimensions	1/n
Stress	1
Strain	1
Density	1
Mass	$1/n^3$
Force	$1/n^2$
Bending Moment	$1/n^3$
Moment of Area	$1/n^4$
Time (Consolidation)	$1/n^2$
Time (Dynamic)	1/n
Time (Creep)	1/n
Pore Fluid Velocity	n

2.6.4 Scaling of Reinforced Concrete for Geotechnical Centrifuge Modelling

It is becoming more desirable to simulate model stiffness and strength in geotechnical centrifuge models. Knappett et al. (2010) investigated whether it is possible to use scaled models of steel and concrete in a geotechnical centrifuge. In order to test this, they made singly-reinforced concrete beam-columns that are 12.5 mm square and subjected these columns to laboratory testing to determine the mechanical behaviour of the beam-columns.

© University of Pretoria

When considering the use of a geotechnical centrifuge to model a reinforced concrete section, the scale effect of the materials needs to be considered. Conventional structural tests conducted on reinforced concrete scaled down by a factor between 4 and 15 indicate that there is a significant size effect present in the concrete (Knappett et al., 2010). This causes the scaled model to be considerably over-strength compared to a full scale test, with the effect increasing with an increase of the scaling factor (Knappett et al., 2011). To reduce the scale effect of models, researchers have used alternative materials to model concrete, such as polymeric materials or aluminium (Knappett et al., 2010).

The use of small sections of a metal is dependent on the properties of the metal at gravitational load, and does not vary when the material is placed in a geotechnical centrifuge. Therefore, standard tensile tests can be used to determine the stress-strain properties of the metal and used for the analysis of the reinforced concrete (Knappett et al, 2010). In order to obtain a better mechanical bond between the metal and the concrete, sand particles can be glued onto the metal to simulate a rough surface for better bonding (Knappett et al, 2010).

Knappett et al. (2010) tested beam elements under four point bending to determine the transverse shear capacity of the scaled model. Their results can be seen in Figure 2-27, where the scaled results are compared to the results presented by Bažant and Yu (2005) based on empirical relationships validated against a database of test data. The shear capacity is plotted against the percentage steel present in the model. It is clear that the scale models can deliver accurately comparable results to full scale testing.

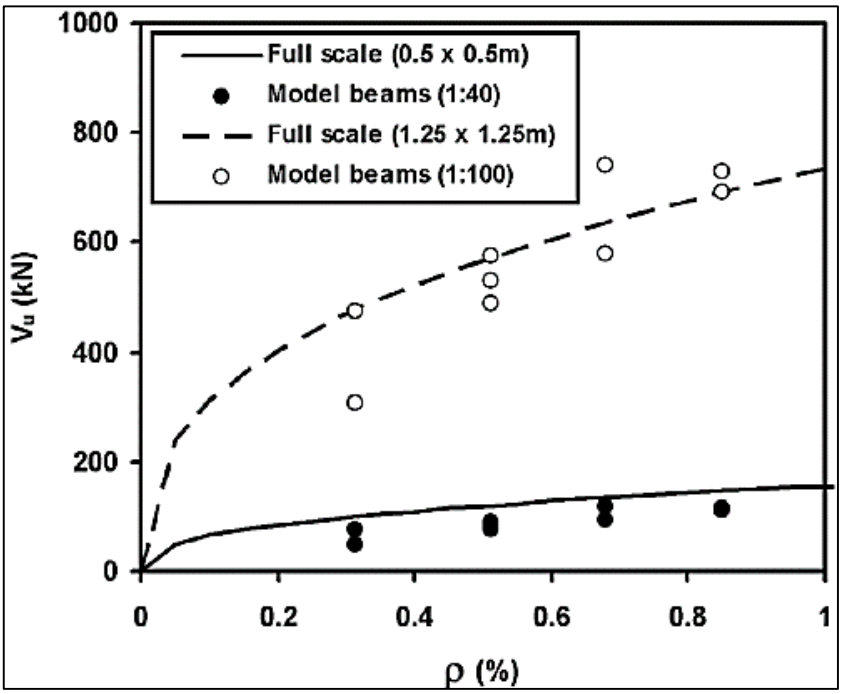

Figure 2-27 Comparing modulus of rupture for scaled model test and full scale test (Knappett et al., 2010)

© University of Pretoria

Along with the modulus of rupture, Knappett et al. (2010) determined the flexural capacity of their scale models, as well as the stiffness of the models during testing. The results can be seen in Figure 2-28, where the flexural capacity is shown on the left and the stiffness of the model is shown on the right compared to the full scale tests. From the stiffness, Knappett et al. (2010) found that the scale models correlated better with the full scale models at low reinforcement percentages. They believed that it was due to the scale model having a lower Young's modulus or that the bond between the reinforcement and concrete can reduce if the spacing between the reinforcement reduces (poor filling of the spaces).

Knappett et al. (2010) concluded that reinforced concrete sections can be scaled down for use in a geotechnical centrifuge. The metal used in the reinforced concrete exhibits identical behaviour to normal gravitational conditions. However, special consideration needs to be made for the concrete mix. If the concrete mix is designed with the effects of scaling of the material in mind, reinforced concrete scale models can accurately represent the material properties of full scale tests.

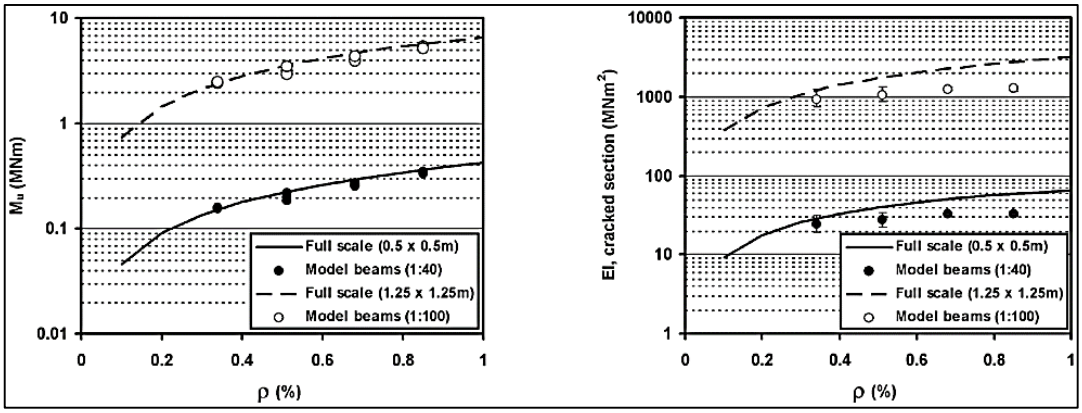

Figure 2-28 Flexural capacity and stiffness of scaled model and full scale test (Knappett et al., 2010)

During the experimental work conducted in this study, different measurement instrumentation was used to determine the behaviour of the footings. An important measuring technique used in this study was particle image velocimetry. Therefore, a short discussion on the method follows in the next section.

2.7 Particle Image Velocimetry

Particle image velocimetry (PIV) or digital image correlation (DIC) is a displacement measuring procedure, originally developed for the use in fluid mechanics and later adopted for the analysis of the displacement of soil in geotechnical engineering problems (Lesniewska and Muir Wood, 2009). PIV is a process where the deformation of a target patch is tracked from one image to the other in order to determine the displacement of the patch (White et al., 2003). DIC or PIV has become a widely used tool in the field of geotechnical engineering. This is mainly due to the high quality images that can be

© University of Pretoria

captured with modern digital cameras, providing enough detail of the material fabric through the glass sides of a sample box for image analysis software to be able to trace the field of displacement of a patch of material and the accompanying strains of the material (Lesniewska and Muir Wood, 2009).

2.7.1 Previous Displacement Measurement Techniques

Previously, the use of photoelasticity was limited to large strain problems such as penetration tests and shear devices. Methods used for image-based measurement techniques includes X-ray and stereo-photogrammetric methods. Due to the advancement in computer based image processing techniques, a method of automatic target tracking could be developed for these techniques (White et al., 2003). However, these techniques rely on the presence of targets (lead shots or coloured beads) placed within the deforming soil mass to provide a reference for the software to track. The use of the targets during the experiment has a few drawbacks (White et al., 2003):

- A dense grid of them can influence the behaviour of the soil mass.
- Widely spaced markers lead to sparse data.
- Markers can be become obscure by soil grains during testing.

An example of the X-ray technique used to determine the slip surfaces beneath a footing by Yamaguchi et al. (1976) can be seen in Figure 2-29. The markers used to track the soil movement are clearly evident within the figure. Due to the limitations of the measurement techniques discussed, the accuracy thereof was considerably less than the measuring techniques available today. With modern digital cameras and image analysis software, accurate analysis of small strain problems can be performed (Lesniewska and Muir Wood, 2009).

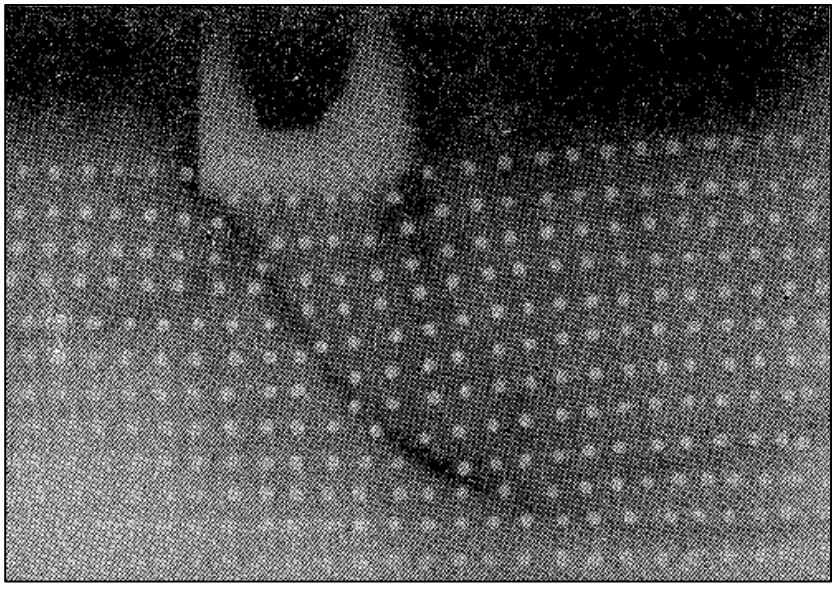

Figure 2-29 Example of X-ray DIC to determine slip lines (Yamaguchi et al., 1976)

© University of Pretoria

2.7.2 PIV Procedure

The use of PIV makes it possible to accurately track soil particles throughout an experiment. In order to be able to conduct a PIV analysis, the following testing conditions are required (Lesniewska and Muir Wood, 2009):

- A transparent medium through which digital images of the test sample can be taken.
- The material being observed needs to have enough texture for the image analysis software to be able to identify particles from one photo to the other.

Due to the fact that granular soils contain different coloured grains, natural texture is present within the soil mass, eliminating the need to add additional colour material to the soil mass (White et al., 2003). As PIV tracks the deformation of the material between images, a minimum of two images is required. The first image is subdivided into a number of patches with a size of L × L pixels. The patches are shown in Figure 2-30 (White et al., 2003), with patch A highlighted to illustrate the PIV process. To determine the displacement (s) from one image to the other, a search zone is defined on the second image for the software to track the patch. The search zone has the same centre pixel coordinates as the patch on image 1, but is a distance s_{max} larger than the test patch (White et al., 2003). The search zone can be seen in Figure 2-30.

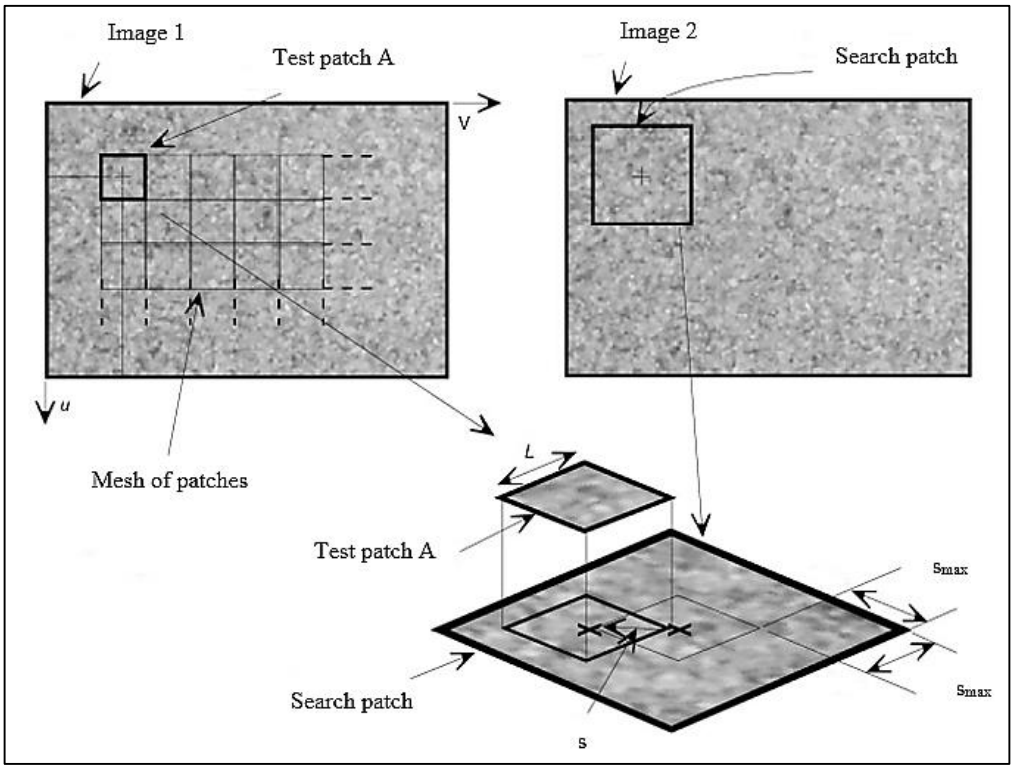

Figure 2-30 Test mesh generated for the use of PIV (White et al., 2003)

© University of Pretoria

White et al. (2003) defined a normalised correlation plane which indicates the extent to which the new patch found in image 2 correlates with the patch in image 1. An example of the normalised correlation plane is indicated in Figure 2-31 for an individual patch, with the peak value obtained indicated in Figure 2-31 (a), whilst a magnification of the peak value obtained is shown in Figure 2-31 (b). The magnified zone close to the maximum value is then fitted through bicubic interpolation (interpolation over an area with the use of a cubic function) to determine the maximum value on a sub-pixel level, thereby increasing the accuracy of the method (White et al., 2003). The highest value obtained with the normalised correlation plane is used as the new position of the test patch, and the displacement between the centres of the two patches can be calculated in terms of sub-pixels (White et al., 2003).

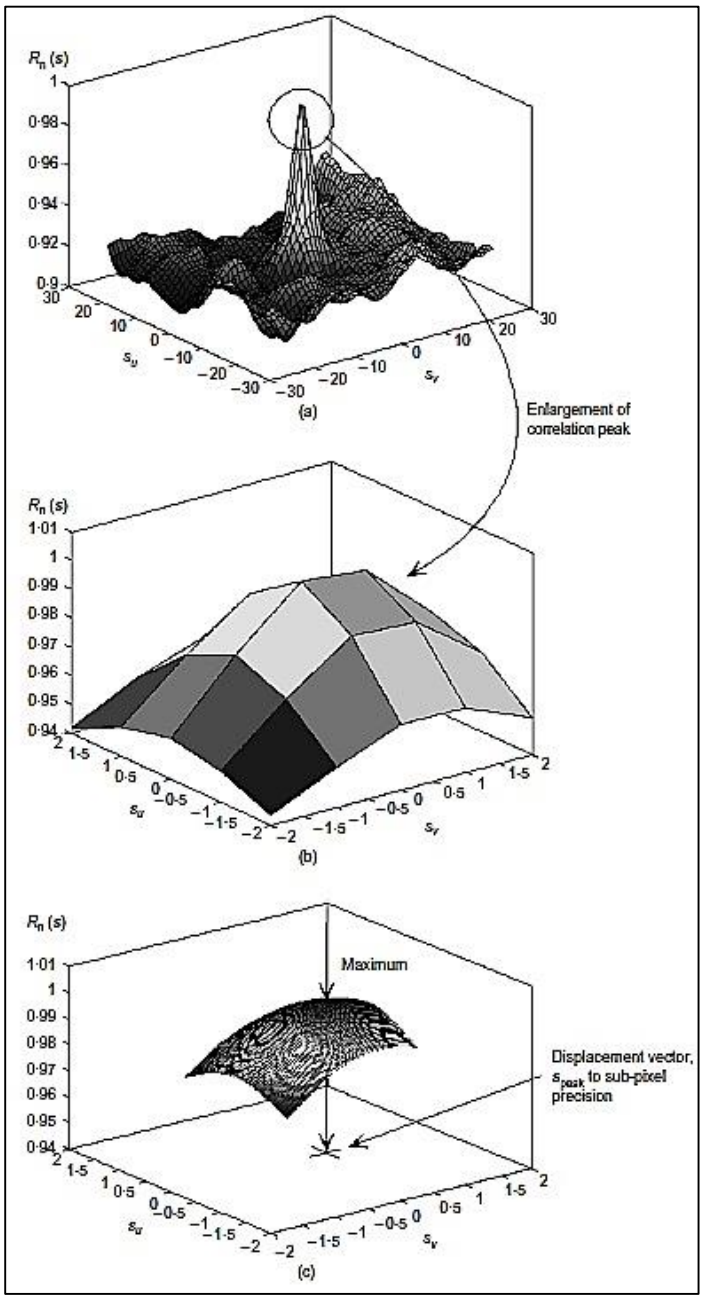

Figure 2-31 Tracking of test mesh with PIV (White et al., 2003)

© University of Pretoria

After obtaining the deformation in terms of pixels (image space coordinates) with the use of PIV, the pixel deformation needs to be converted to millimetres (object-space coordinates), as indicated in Figure 2-32. When converting the data to millimetres, factors contributing to the loss of accuracy (specifically for digital cameras) when capturing the data can lead to inaccurate results. These factors include (White et al., 2003):

- Non-coplanarity between the camera and the object space.
- Both tangential and radial lens distortion.
- Refraction caused by the viewing window.
- Non-squareness of the camera pixels.

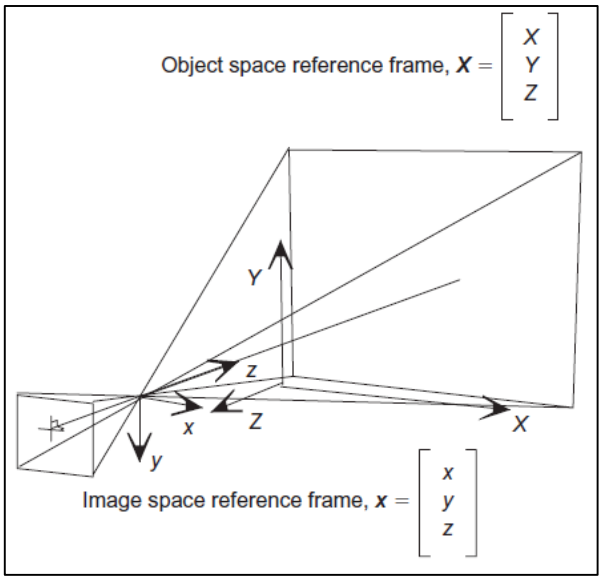

Figure 2-32 Converting image space to object space with PIV (White et al., 2003)

According to White et al. (2003), the factors affecting accuracy of the results can be accounted for by considering 14 different parameters, which falls beyond the scope of this study but can be found in the paper by White et al. (2003). In order to compensate for these 14 parameters that cause inaccuracies in the measured data on an image by image basis, target markers are used of which the exact coordinates are known before testing commences. A black round dot on a white background is the preferred choice for most experiments. The locations of the markers are tracked in all the images that are analysed, compensating for any movement of the experiment or camera. By using the known location of the target markers, the software can create a calibration surface to interpolate between the markers and determine the location of a specific target mesh in each image (White et al., 2003).

The centroids of the target markers are determined by calculating the colour intensity of the markers on a scale of 1 to 255, which is plotted on a graph as shown in Figure 2-33. Sections are taken through the graph at different height intervals to determine the centroid of the specific interval. To find the precise

© University of Pretoria

centroid of the marker, the average of the calculated centroids is determined (Heron, 2013). An illustration of two of these sections are shown in Figure 2-33, with the colour intensity graph shown on the left along with the level where a cross-section is taken, followed by the image of the cross-section in the centre and the location of the centroid of that section on top of the marker image on the right (Heron, 2013).

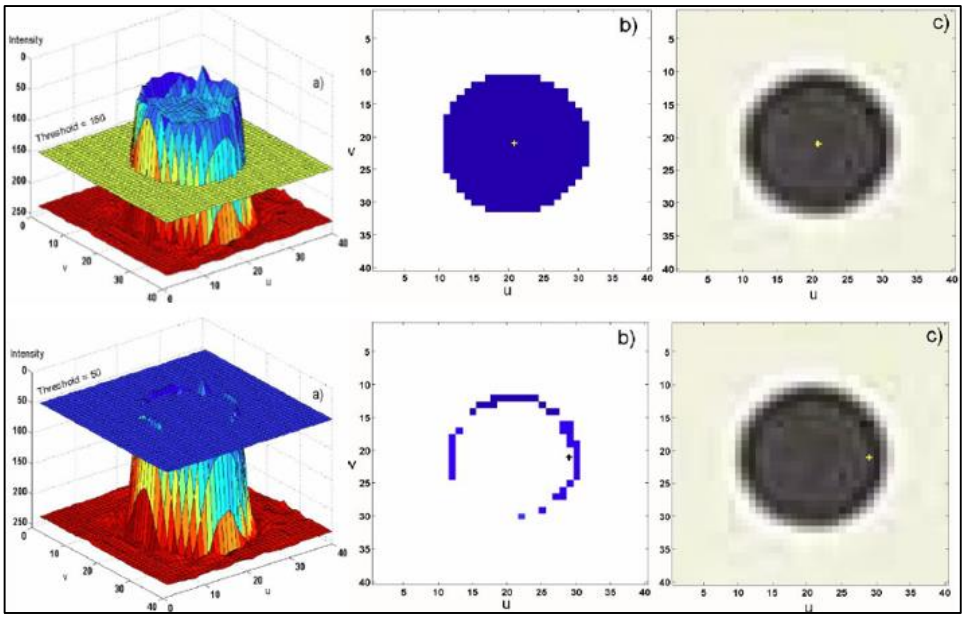

Figure 2-33 Determining tracking marker centre point for PIV (Heron, 2013)

These markers improve the accuracy of the PIV system dramatically, by creating an image specific calibration surface to track image meshes (White et al., 2003). The overall accuracy of the PIV system is highly dependent on the quality of digital camera used during the experiment, but an accuracy of approximately 1-10 µm is achieved with the use of the software, giving more accurate readings during experiments than what was previously achievable with other testing methods (White et al., 2003).

2.7.3 Performance of the Measuring Technique

The performance of any measurement technique is based on the precision, accuracy and resolution of the method (White et al., 2003). The precision of a measuring technique refers to the variation between two measurements of the same quantity. Accuracy of a measuring technique is the difference between the measured and actual quantity of a measurement. Resolution of a measuring techniques is the smallest interval with which the technique can measure (White et al., 2003).

© University of Pretoria

For an image-based measurement technique, the precision of tracking the target markers within the soil mass is dependent on the method used to identify the markers present in the digital image. The accuracy is dependent on the process used to convert the measured locations from pixels to millimetres. The resolution is highly dependent on the camera used for the test. White et al. (2003) expressed the accuracy and precision of the measuring technique as a non-dimensional fraction of the width of field of view (FOV). The accuracy and precision of the various displacement measurement techniques as well as certain limiting factors for each technique, are summarised in Table 2-5 (Heron, 2013), clearly demonstrating the superior performance of the PIV measurement technique.

Table 2-5 Accuracy of PIV compared to alternatives (Heron, 2013)

Type	Dimensions Measure	Precision (FOV)	Comments
LVDT	1	1/200 000	Required physical contact
Laser	1	1/50 000	Required clear view
X-ray	2	1/15 000	Requires addition of particles and bulky equipment
PIV	2	<1/200 000 (dependent on resolution)	Non-intrusive but requires view of object

White et al. (2003) proposed an empirical formula to determine the accuracy as well as an upper bound on the PIV precision error (ρ_{pixel}) as a function of the patch size. The accuracy is therefore a function of the patch size, as can be seen in Equation 2-15.

$$\rho_{pixel} = \frac{0.6}{L} + \frac{150000}{L^8} \qquad \text{(Equation 2-15)}$$

Where:

ρ_{pixel} = PIV precision error
L = Length of the PIV patch

PIV software has the capability to accurately measure displacement if the software is used correctly. The most important considerations to obtain accurate results with PIV software are discussed in the next section.

2.7.4 Factors Affecting Accuracy of PIV

From a practical point of view, the accuracy of the PIV method is dependent on two factors namely the size of the patches and the spacing of the patches. For patches that are chosen too small, the information within the patch might not be adequate for the software to be able to detect the patch with confidence from one image to the other, which might lead to inaccurate displacement values or ‘wild vectors’ (Lesniewska and Muir Wood, 2009). In order to calculate the strains present in the model,

© University of Pretoria

differentiation of the deflection data is required, which can lead to erratic values if the spacing of the patches is too close to one another. Therefore a trial and error method needs to be used to determine the optimal size and spacing of the PIV patches, with a larger patch leading to accurate values of displacement data, but smaller patches leading to a larger number of data available to differentiate and obtain accurate strain values. The best compromise possible is to use large patches which overlap, leading to accurate results and many data points available (Lesniewska and Muir Wood, 2009).

Lesniewska and Muir Wood (2011) compared the use of a fine mesh for PIV analysis with a coarse mesh, as shown in Figure 2-34. It can clearly be seen that the coarse mesh on the left shows a lot less detail compared to a fine mesh on the right. They concluded, however, that if a finer mesh is used, the computation time required to solve the displacement of the patches drastically increases. Therefore, a compromise needs to be made between accuracy and time, depending on the need of the required analysis.

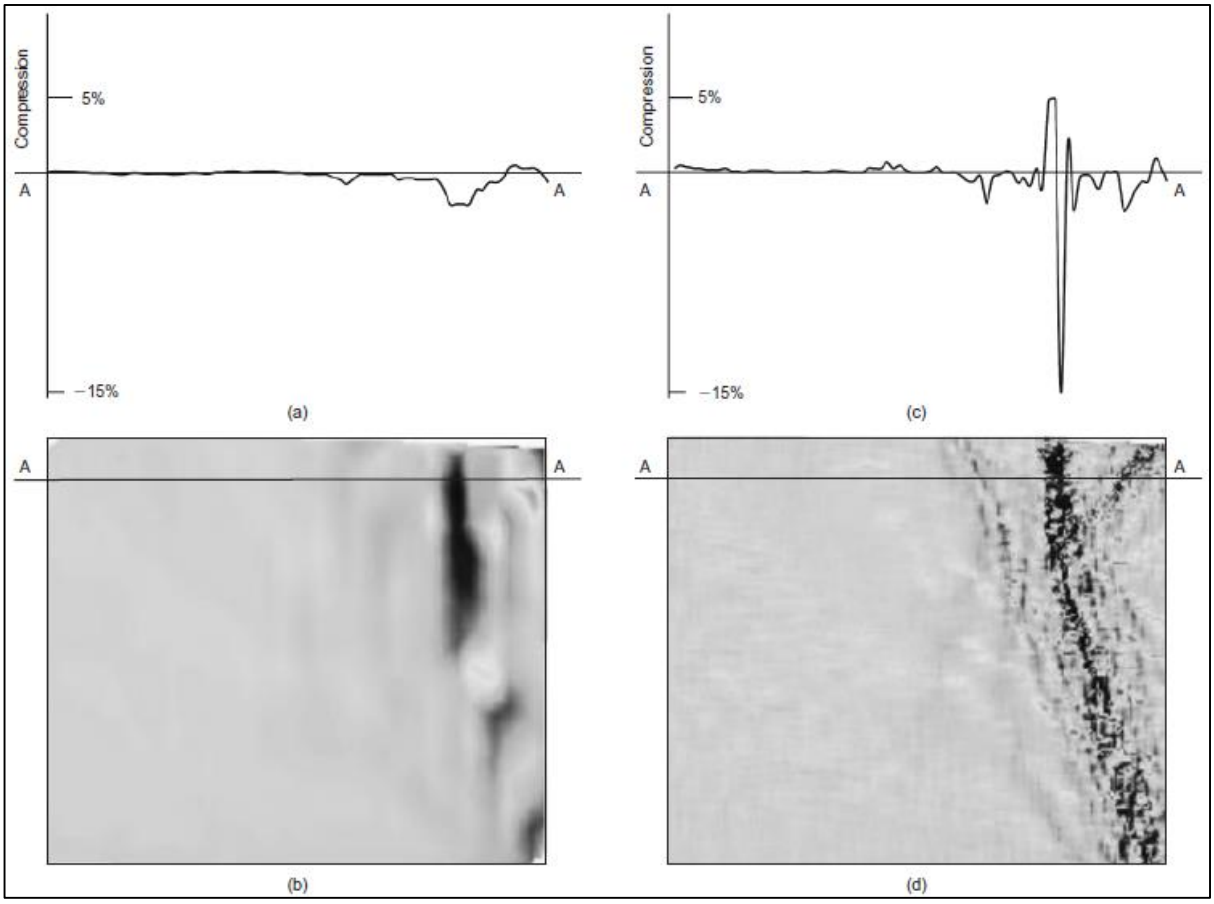

Figure 2-34 Influence of mesh size on the accuracy of PIV (Lesniewska and Muir Wood, 2011)

© University of Pretoria

White et al. (2003) did a series of experiments to determine the influence of the patch size on the accuracy of the PIV results. They found that the patch size correlates with the accuracy of the measurements, as illustrated in Figure 2-35. The inaccuracy or error of the PIV software reduce with an increase in the size of the patches used during the analysis.

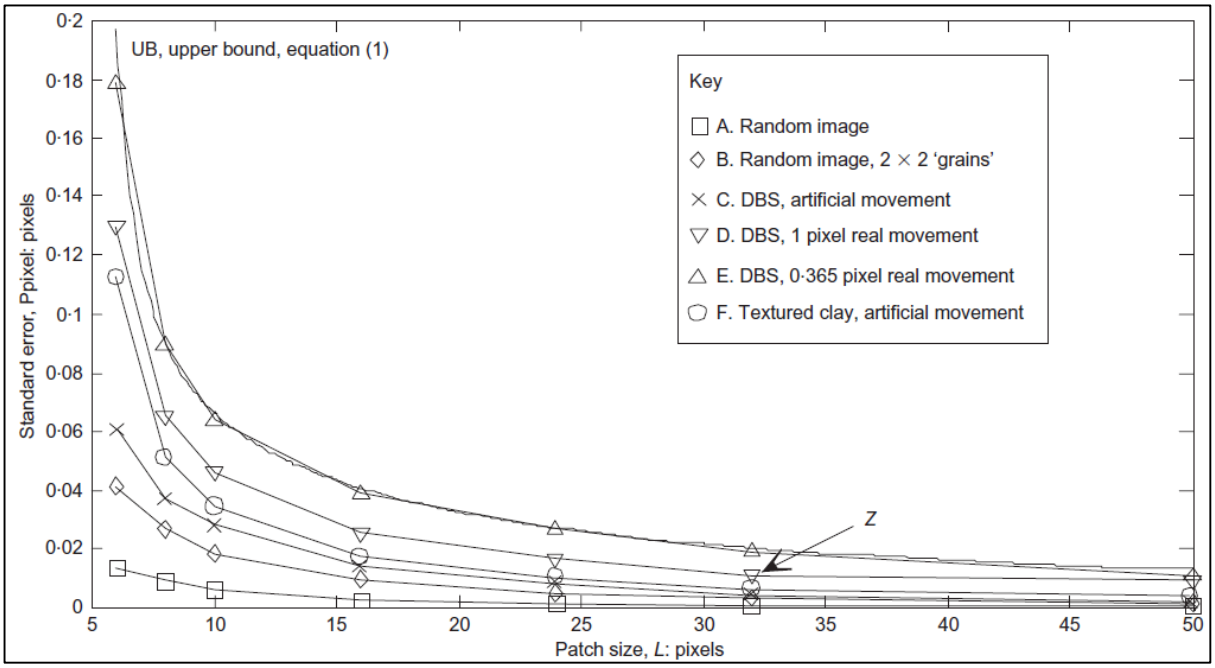

Figure 2-35 Effect of patch size on PIV accuracy (White et al., 2003)

The above illustrates that PIV is a powerful, accurate, non-intrusive and versatile technique for the observation of geotechnical models.

2.8 Summary

In this chapter, a review of the literature relevant to this study was presented. The most important aspects considered in the chapter include the design of surface footings, the contact stress distribution at the soil-structure interface, as well as the failure of the foundation system as a result of either soil or footing failure. Information regarding the use of a geotechnical centrifuge for model testing, as well as particle image velocimetry used as measuring equipment during the experimental work were also discussed.

Although the design and analysis of a foundation system is a complex procedure, structural engineers have simplified the design considerably by assuming a spring model for the soil behaviour. This method can provide accurate representation of the soil behaviour at low strains, but the method cannot be used to accurately model the ultimate failure of a foundation system.

© University of Pretoria

Failure of a foundation system can either occur due to excessive settlement or through failure of either the footing or the soil. The most common method used to predict the bearing capacity failure of the foundation system is the Terzaghi (1943) superposition method. Although this method is used extensively in structural design, it is clear from the literature that there are a number of factors which can change the strength of the foundation system from that proposed with the Terzaghi method. The majority of these factors are related to the properties of the soil, such as progressive failure and shear banding. Various methods have been proposed to quantify the behaviour of the foundation system when failure occurs.

From the literature it is clear that the design of a foundation system is often approached as a segregated problem, with the soil and the footing modelled as two separate systems. As a foundation system is an interaction problem, methods have been proposed to model the stiffness of the entire system as a whole. These methods lead to a better understanding of the behaviour of a foundation system as a large number of strength parameters for both the footing and soil is incorporated in the analysis.

Based on the literature reviewed the following hypothesis will be investigated:

"The settlement and deflection of a footing, as well as the contact stress distribution at the soil-structure interface of a footing on dry cohesionless sand can be predicted based on the stiffness's of the footing and sand."

For the purpose of this project, the work discussed in the literature review was critically evaluated and a series of experiments conducted in a geotechnical centrifuge. The results obtained from the experimental work were combined with that of the literature to evaluate the hypothesis. Throughout the next chapters, the experimental work and results are discussed before a final conclusion is presented at the end of the report.

© University of Pretoria

3 Research Methodology

The effect of footing stiffness on the soil-structure interaction between the footing and the underlying soil was investigated experimentally using physical models. The experiment was designed to examine the soil-structure interaction of a footing on dry, cohesionless sand in a geotechnical centrifuge. A total of eight experiments were conducted in the geotechnical centrifuge under plane-strain conditions, limiting the study to two dimensional movement.

This chapter provides descriptions of the geotechnical centrifuge used in the experiment, the experimental model, the loading equipment used, measurement instrumentation and the data acquisition system. The chapter concludes with an explanation of the experimental preparation and the testing procedure adopted.

3.1 Geotechnical Centrifuge

The 150 G-ton geotechnical centrifuge at the University of Pretoria was used for this study, the details of which are given by Jacobsz et al. (2014). The centrifuge is an Actidyn C67-4, with a 0.8 m × 1.0 m × 1.3 m model platform. The radius of the centrifuge arm is 3 m measured from the rotational axis to the model platform (Jacobsz et al., 2014). The centrifuge is rated to carry a payload of 1 500 kg up to an acceleration of 100 G or 950 kg to 130 G. A photograph of the Actidyn C67-4 in the laboratory is shown in Figure 3-1 (University of Pretoria, 2014).

Figure 3-1 Geotechnical centrifuge at the University of Pretoria (University of Pretoria, 2014)

© University of Pretoria

3.2 Properties of Silica Sand

A clean fine silica sand, referred to as Cullinan sand was used in the laboratory testing. The particle size distribution was determined through sieve analysis, as well as a Malvern Mastersizer 2000 apparatus. The particle size distribution is indicated in Figure 3-2 (Archer, 2014). Archer (2014) determined that the soil can be classified as a poorly graded, slightly silty sand according to the Unified Soil Classification System (USCS) (ASTM Standard D2487, 2011).

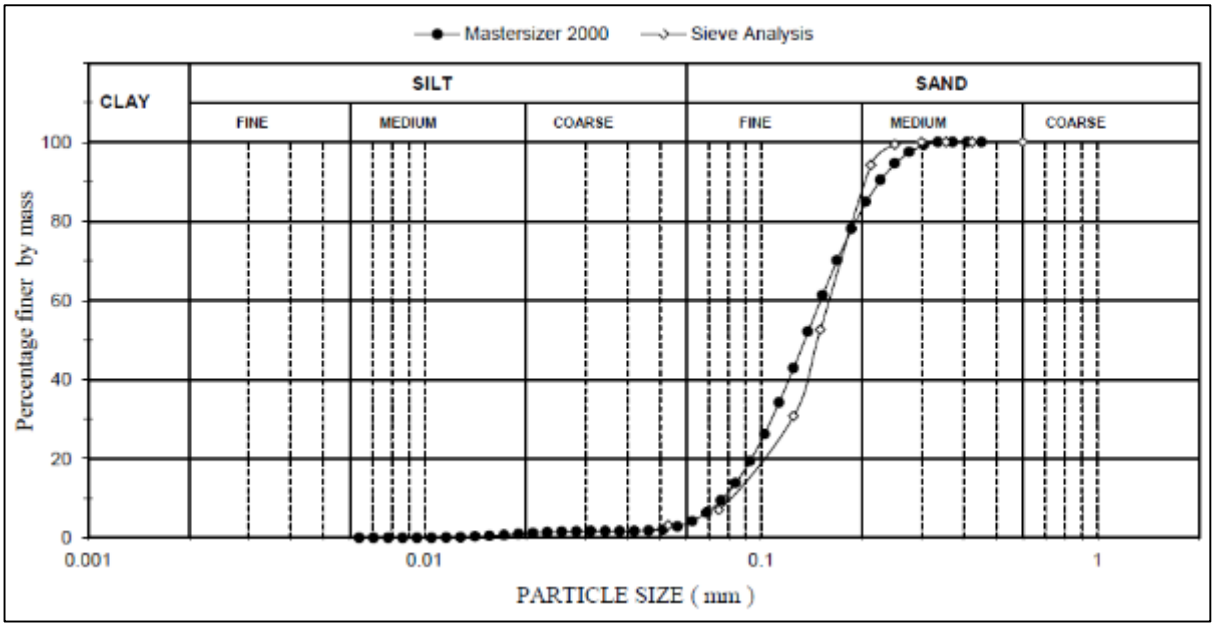

Figure 3-2 Particle size distribution of Cullinan sand (Archer, 2014)

Archer (2014) conducted a variety of tests on the sand to determine the physical properties thereof at specified relative densities. The properties of the sand at 50% relative density and 80% relative density are applicable to this study and are summarised in Table 3-1 (Archer, 2014).

The friction angle for this experiment was determined through interpolation of the data from Archer (2014). The friction angle is plotted as a function of the relative density of the sand as seen in Figure 3-3. By determining the relative density of the sand, the friction angle was estimated with the use of the equation shown in Figure 3-3. The average relative density of the sand as placed in the models was 1 584 kg/m^3, equalling a relative density of approximately 70%. Therefore, a friction angle of 37° was used for the experimental setup calculations (refer to Figure 3-3).

© University of Pretoria

Table 3-1 Properties of Cullinan sand (Archer, 2014)

Property/Parameter	50% RD	80% RD
D_{10} (mm)	0.077	
D_{30} (mm)	0.108	
D_{50} (mm)	0.135	
D_{60} (mm)	0.150	
Uniformity Coefficient, C_u	1.95	
Max dry density (kg/m^3)	1 669	
Min dry density (kg/m^3)	1 392	
e_{max}	0.92	
e_{min}	0.6	
Specific Gravity	2.67	
Particle Shape[a]	Angular to sub-rounded	
USCS Classification	SP	
Angle of friction, φ (°)	34	39
Cohesion, c' (kPa)	0	0
Dry Density	1 531	1 614
e_{RD}[b]	0.74	0.65
Permeability (m/s)	1.9 x 10^{-5}	1.8 x 10^{-5}
Preconsolidation pressure, σ'_p (MPa)	8.94	9.91

[a]Based on visual interpretation of the scanning electron microscope image

[b]Void ratio at relative density value

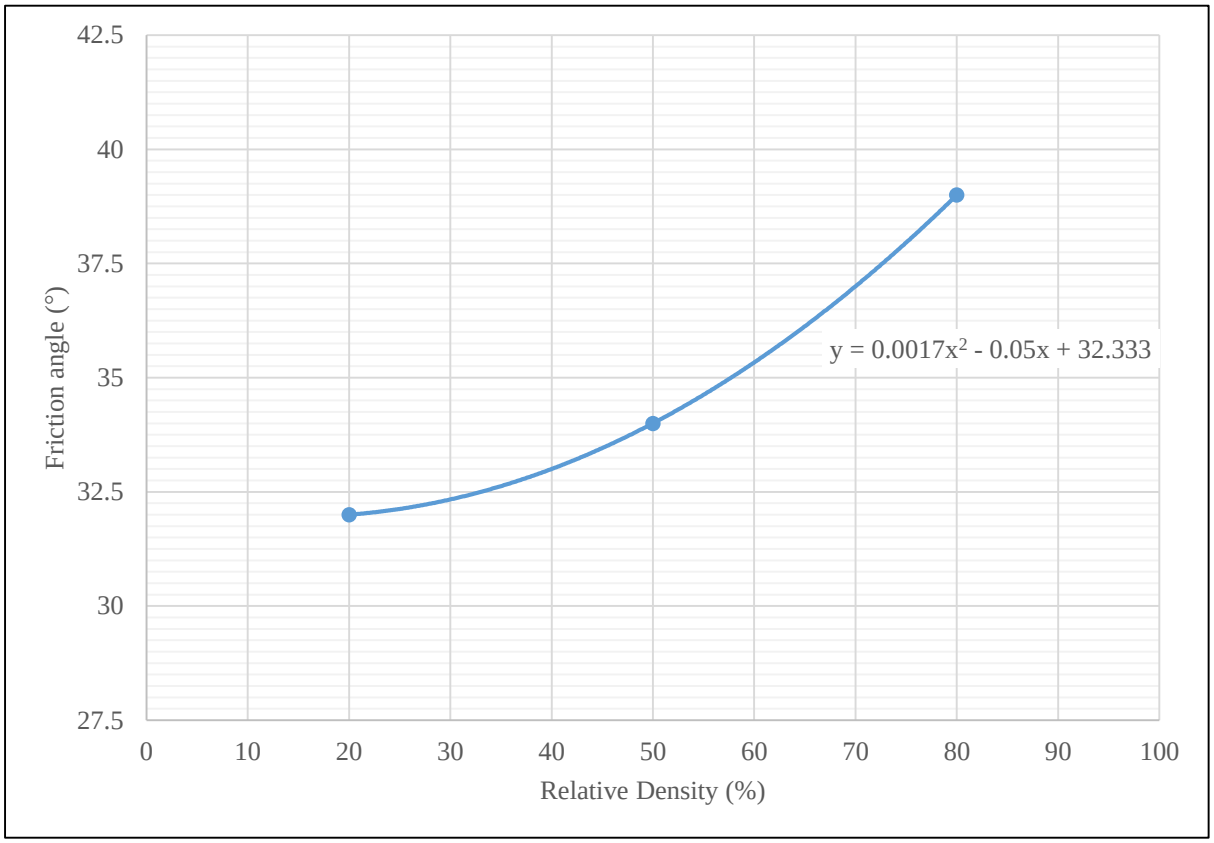

Figure 3-3 Friction angle of Cullinan sand determined from triaxial testing as a function of the relative density (Archer, 2014)

© University of Pretoria

3.3 Experimental Model

The components of the physical model used for this study are described in this section. The experiments were conducted with seven aluminium footings and one reinforced concrete footing. As the focus of this study was large footings, a prototype footing width of 4.5 m was chosen. The scale of the model was selected at 1:30 as the author decided that this would strike a good balance between the model footing sizes and the geometrical confinement of the strongbox. The experiments were therefore conducted at 30 G.

3.3.1 Properties of Footings

For each test the stiffness of the footings (EI) was altered. The footings were made from aluminium and reinforced concrete, with identical plan dimensions. Therefore, the only aspect that varied from one test to the other was the footing thickness. A range of footings were chosen to be tested, from thin to thick. The yield strength of the aluminium was assumed as 200 MPa with a modulus of elasticity of 70 GPa (Domone and Illston, 2010). For design purposes, the modulus of elasticity of concrete was estimated as 24 GPa. The measured properties of the aluminium can be seen in Section 3.3.2.

The thickness of the footings were chosen to ensure a variation in the relative stiffness of the foundation system. The dimensions of all the footings, as well as the designed EI based on the above mentioned material properties used to determine the foundation stiffness can be seen in Table 3-2. Figure 3-4 illustrates a photograph of a 25 mm thick aluminium footing.

Table 3-2 List of different footings used in the experiment

Footing Number	Material	Length (mm)	Width (mm)	Thickness (mm)	Design EI ($N.m^2$)
1	Aluminium	150	150	3	23.6
2	Aluminium	150	150	6.7	263.2
3	Aluminium	150	150	10	875.0
4	Aluminium	150	150	16	3584.0
5	Aluminium	150	150	25	13671.9
6	Aluminium	150	150	35	37515.6
7	Aluminium	150	150	50	109375.0
8	Reinforced Concrete	150	150	30	8100.0

© University of Pretoria

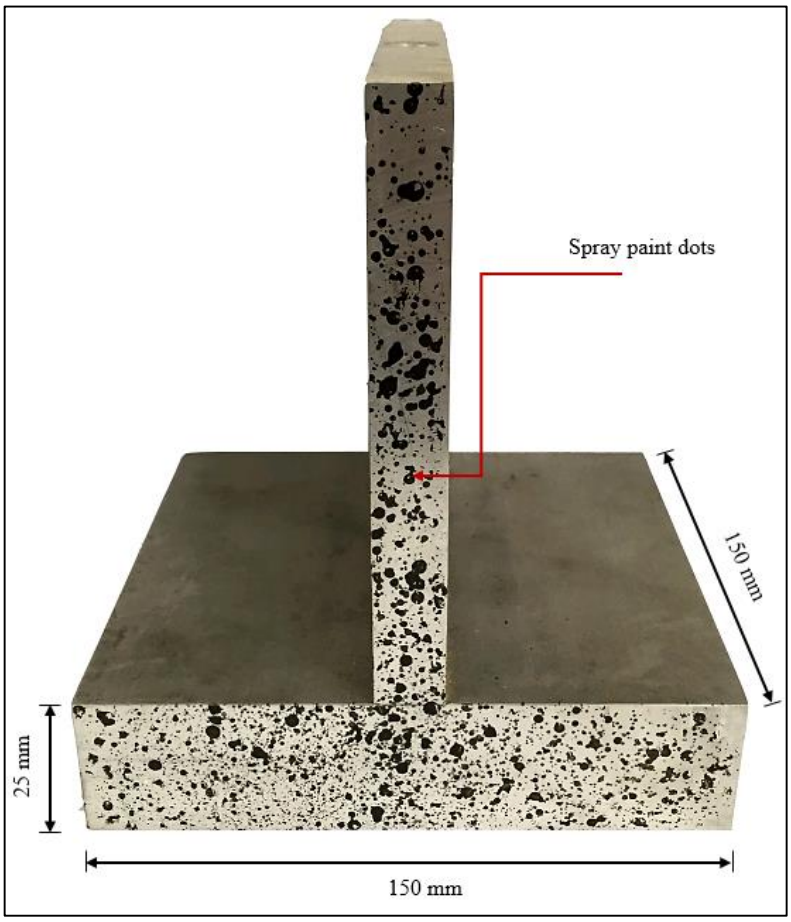

Figure 3-4 The 25mm thick aluminium footing used in model study

A limitation of this study was the fact that the footings had a smooth surface at the soil-structure interface. The roughness of the footing has been shown to have an influence on the properties of the soil-structure interaction as discussed in Section 2.3.1.4 (Spasojevic and Cabarkapa, 2012). However, for this study only smooth footings were considered.

A Tekscan™ pressure mat (discussed in Section 3.5.4) was placed between the footing and the soil surface to determine the contact stress distribution beneath the footing, thus it was decided not to model a rough footing as this could potentially damage the pressure mat. The experiment was conducted to model plane-strain conditions. The same column dimensions were used for all footings.

Where the actuator pressed on the column, a steel ball bearing was used to transfer the load from the actuator to the footing. The ball bearing rested in a machined recess in the middle of the column as can be seen in Figure 3-4, and pressure was applied to the bearing via a specially machined spacer. The spacer and ball can be seen in Figure 3-5. The indent was placed in the centre of the column to ensure repeatable loading of the footing. A schematic of the footings used in the experiment can be seen in Figure 3-6, with the variable H indicating the different footing thicknesses as indicated in Table 3-2.

© University of Pretoria

Figure 3-5 Spacer and ball used to apply loads to footing

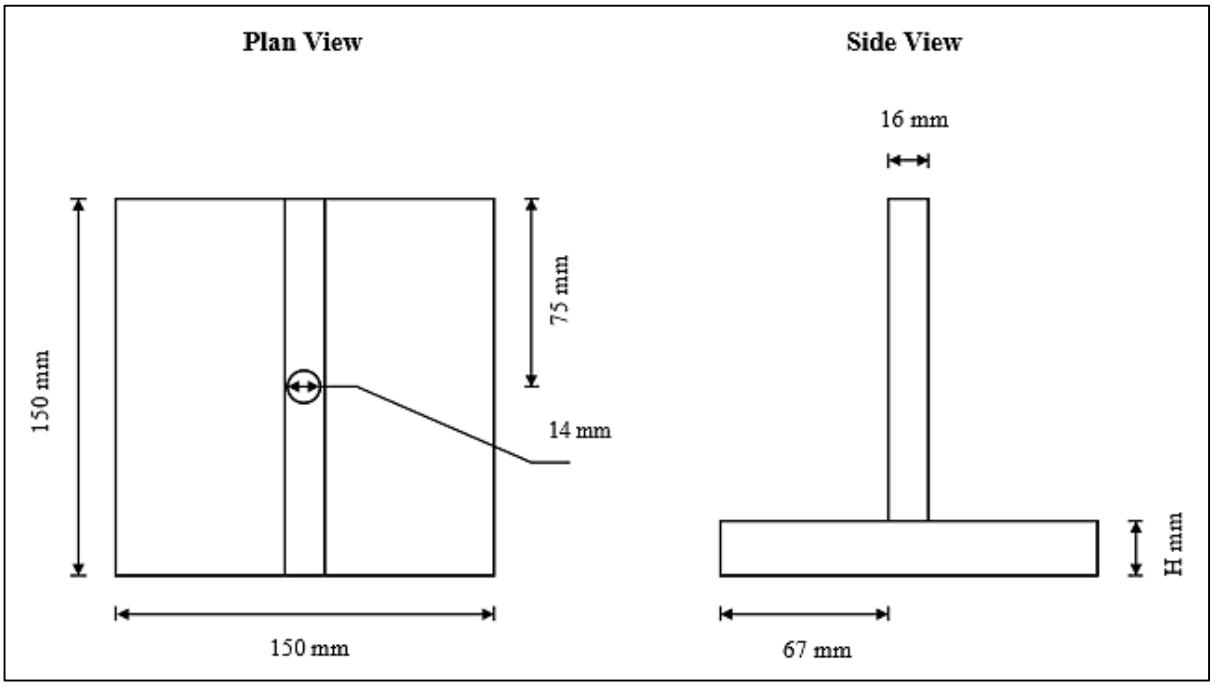

Figure 3-6 Schematic of footings used in the experiment

The reinforced concrete footing had the same width and length as all the other footings, with the thickness of the footing indicated in Table 3-2. The dimensions of the components in the concrete mix design had to be reduced for use in the model (Knappett et al., 2011). One limitation of the concrete mix design is the fact that the size of the cement particles cannot be scaled down. Due to this, the ratio of the cement particle size to the other mix constituents are larger for model tests compared to prototype tests by a factor equal to the scale factor of the model. The use of very small sand particles reduces the workability of the mix considerably, therefore superplasticizer needed to be added to the concrete mix to increase the workability. Chryso Premia 100, a high-range water reducer (Chryso, 2014) was used in the mix design.

© University of Pretoria

The mix design can be seen in Table 3-3, as well as the different constituents used in the mix design. A water/cement ratio of 0.8 was used for the mix design and the target compressive strength of the concrete was 30 MPa.

Table 3-3 Model footing concrete mix design

Constituent	Type	Density (kg/m^3)	Mix Proportions (kg/m^3)
Cement	PPC 52.5N	3 140*	350
Sand	Crusher Dolomite Sand	2 850*	1 723
Water	Water	1 000	280
Admixture	Premia 100	1 200	5

*Particle density

Knappett et al. (2010) suggested that only geometrical scaling of metal for the use in a geotechnical centrifuge is required. Steel wires with a diameter of 0.71 mm were cast into the concrete to increase the tensile strength of the concrete after cracking has occurred (reinforced concrete). The properties of the steel wires were assumed during the experimental setup, with a yield strength of 450 MPa and a modulus of elasticity of 200 GPa. The measured properties of the steel and concrete are further discussed in Section 3.3.3.

The reinforcement wires were predominantly placed in the transverse direction at the bottom of the footing. The location and size of the steel wires are shown in Figure 3-7. Four steel wires were placed above the transverse reinforcement in the longitudinal direction to hold the load carrying reinforcement wires in place. Concrete cover on all the sides, as well as to the bottom was set to 2.5 mm.

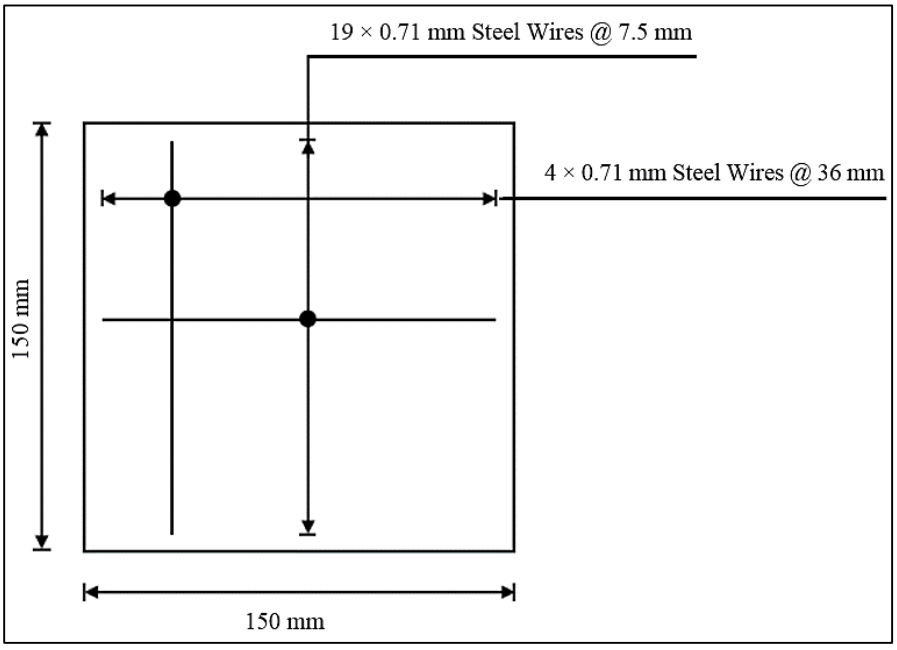

Figure 3-7 Reinforcement design for concrete footing

© University of Pretoria

To ensure that local failure of the concrete did not occur at the load application point on top of the column, a steel strip was cast onto the top of the concrete column where it made contact with the ball bearing applying the load. The steel strip had a width of 16 mm and spanned the entire length of the column. The thickness of the steel strip was 14 mm and the total height of the concrete column plus the steel strip was 111 mm. The same size indent in which the steel ball rested was machined in the steel strip compared to the aluminium footings. The reinforced concrete footing and steel strip can be seen in Figure 3-8.

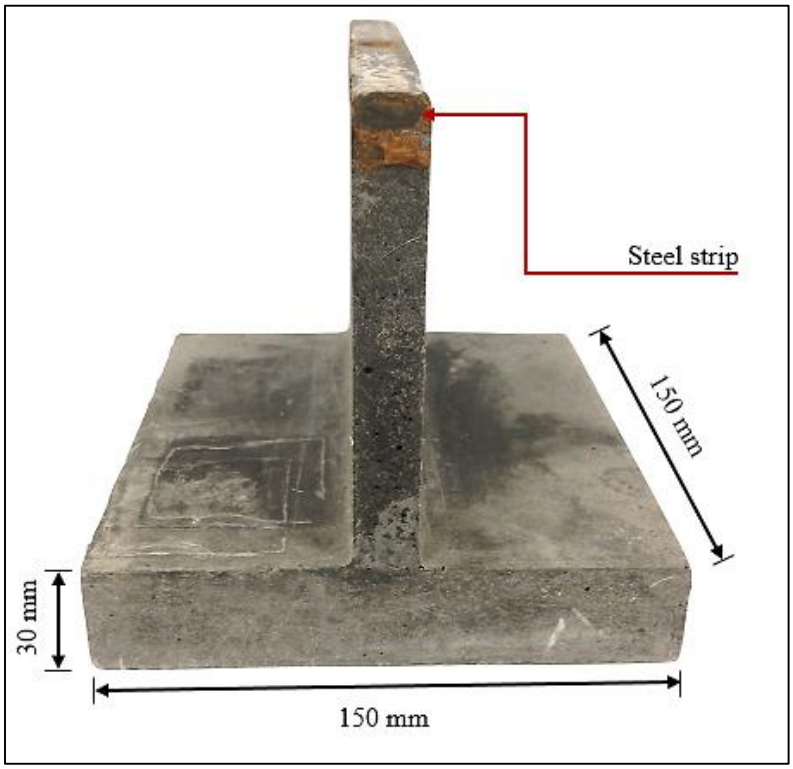

Figure 3-8 Reinforced concrete footing used in experiments

3.3.2 Aluminium Properties

With the design of the footings, an appropriate material had to be chosen, as the material properties play an important role in the behaviour of the footing. Although the majority of structural footings comprise of reinforced concrete, the variation in the pre- and post-cracking behaviour of reinforced concrete complicates modelling. In certain instances aluminium can be used as a substitute for modelling reinforced concrete due to the fact that the densities of the two materials are similar, making aluminium ideal for use in models in a geotechnical centrifuge (Knappett et al., 2010). The tensile and compression properties of the aluminium were determined through standard tensile and compression tests of metals at the University of Pretoria laboratory. The properties of the aluminium can be seen in Table 3-4, while the tensile stress-strain graph of the aluminium can be seen in Figure 3-9.

© University of Pretoria

Table 3-4 Properties of aluminium used in footings

Property	Value	
Tensile Modulus of Elasticity	70.8	GPa
Tensile Yield Stress	300	MPa
Compressive Modulus of Elasticity	69.5	GPa
Compressive Yield Stress	440	MPa

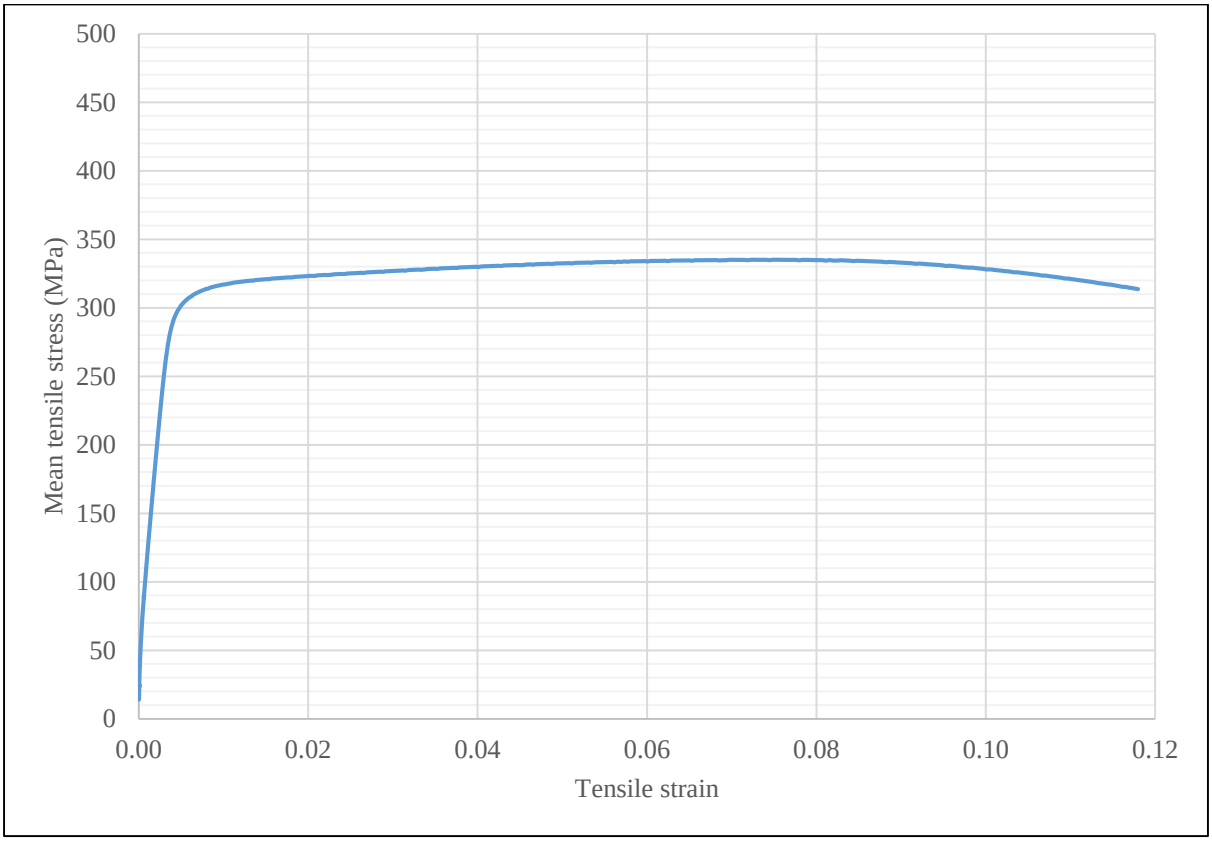

Figure 3-9 Stress strain graph of aluminium used for footings

3.3.3 Reinforced Concrete Properties

The steel used in the reinforced concrete had to be scaled down in order to be use in a geotechnical centrifuge model. Nineteen steel wires with a diameter of 0.71 mm were used to span the length of the footing and four of the same steel wires were used to span the width. The steel wires had a rough surface to allow better bond between the concrete and the wires, as discussed by Knappett et al. (2010). Tensile tests were conducted on two samples of the material in order to obtain their physical properties. The properties of the steel wires used in the reinforced concrete footing are shown in Table 3-5 . The stress-strain graph of one of the steel wires is shown in Figure 3-10.

© University of Pretoria

Table 3-5 Properties of steel wires used in experiment

Property	Value	
Modulus of Elasticity	165	GPa
Tensile Yield Stress	400	MPa

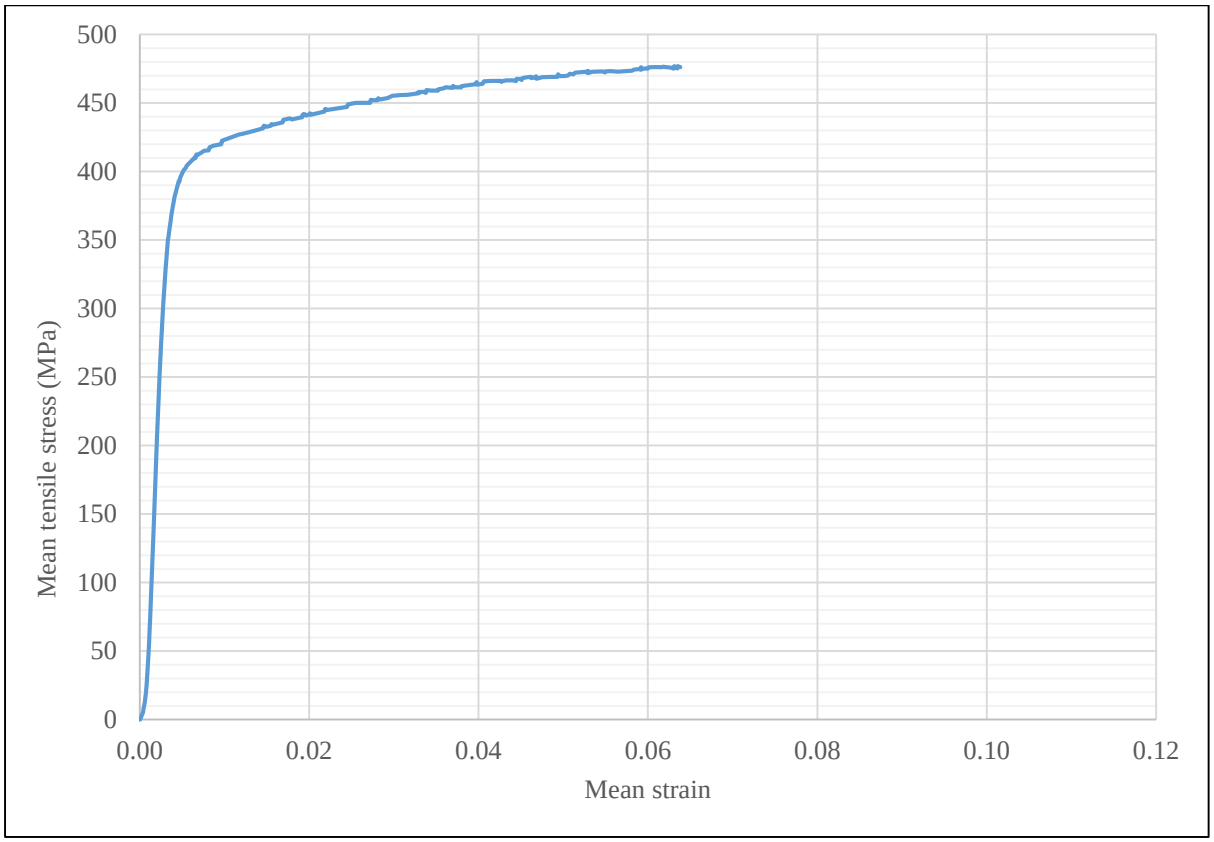

Figure 3-10 Stress strain graph for steel wires used in experiment

The properties of the concrete were determined through four point bending tests of 40 mm × 40 mm × 160 mm bars and crushing of concrete cubes. The reinforced concrete footing was tested 21 days after casting. The compressive strength of the concrete was 30 MPa, with a modulus of elasticity of 25 GPa. The flexural strength of the bars varied between 4 MPa and 5 MPa.

The material properties of both the aluminium and reinforced concrete were fairly close to the designed properties discussed in Section 3.3.1.

© University of Pretoria

3.3.4 Model Composition

In order to test soil in a geotechnical centrifuge, the material should be placed in a strongbox to confine it. A schematic of the strongbox is shown in Figure 3-11, with a view of the top of the box, as well as a section through the box to indicate the dimensions. The strongbox was constructed from aluminium panels with a thickness of 50 mm on three of the four sides, as well as the floor of the strongbox. The front was thicker at 80 mm, as the front portion contains a thick glass window that makes it possible to observe the model from the side. A steel collar with a thickness of 30 mm, as can be seen in Figure 3-12 was machined and bolted to the top of the aluminium box.

The experiment was conducted under plane-strain conditions, therefore it was not necessary to use the entire width of the strongbox. An aluminium partition plate was placed within the strongbox to narrow the model width to 151 mm. With the partition in place, the entire strongbox was filled with sand, but only the front 151 mm of the strongbox was considered in the experiment. The back section ensured that there was pressure on the aluminium partition plate from the back to minimise the deflection of the partition during loading. The width of the front compartment of the strongbox was slightly larger than the footings to make sure that there was no contact friction between the footings and the aluminium spacer or glass window.

The strongbox was filled with sand to a height of 300 mm, which allowed the entire footing to be seen through the glass, regardless of the thickness of the footing. A constant sand volume and mass was used in all the tests. An image of the assembled model can be seen in Figure 3-12, showing the location of the inductive displacement transducers (IDTs) on both sides of the footing, as well as one placed to measure the settlement of the sand adjacent to the footing.

© University of Pretoria

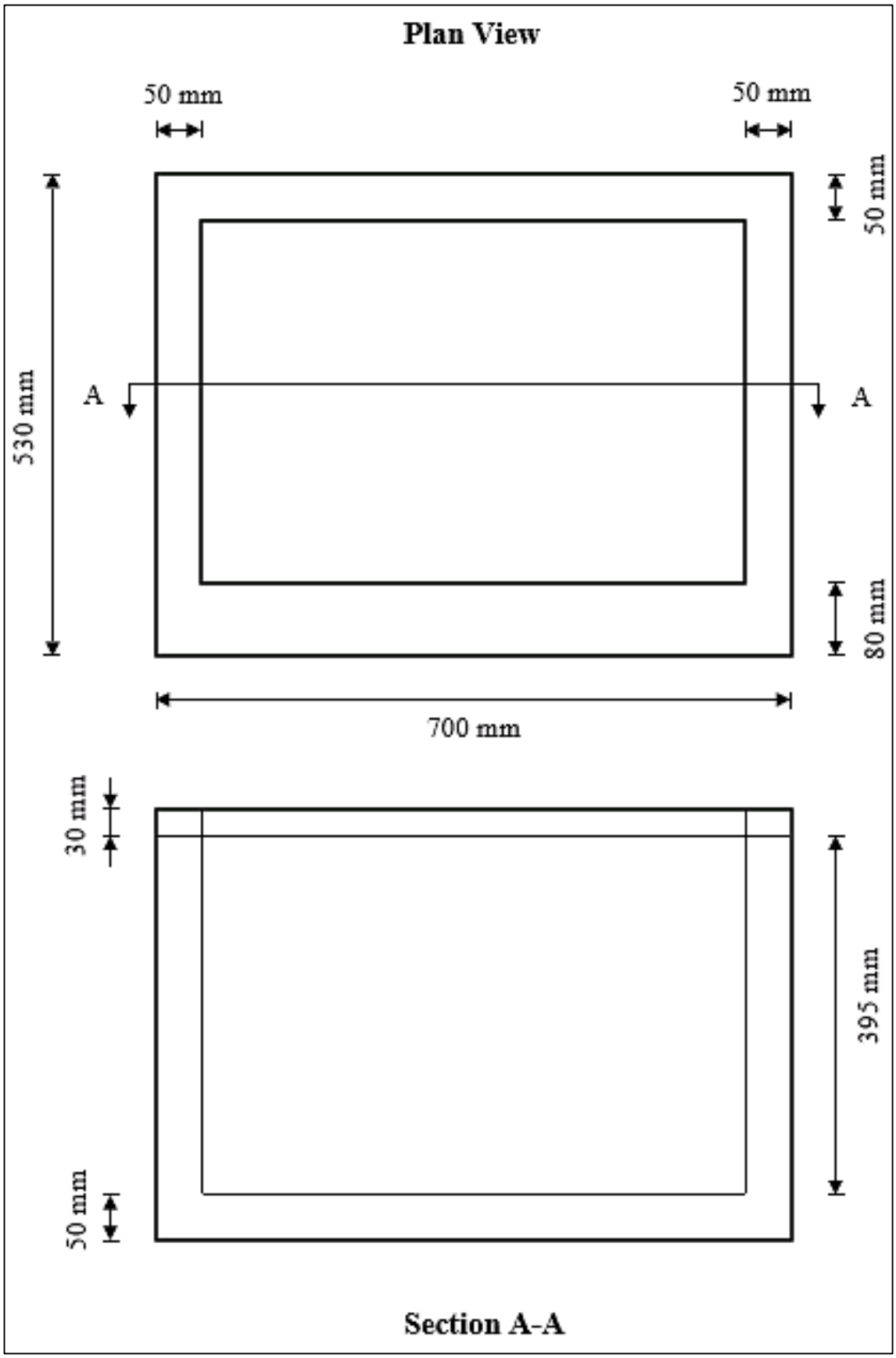

Figure 3-11 Schematic of centrifuge strongbox

© University of Pretoria

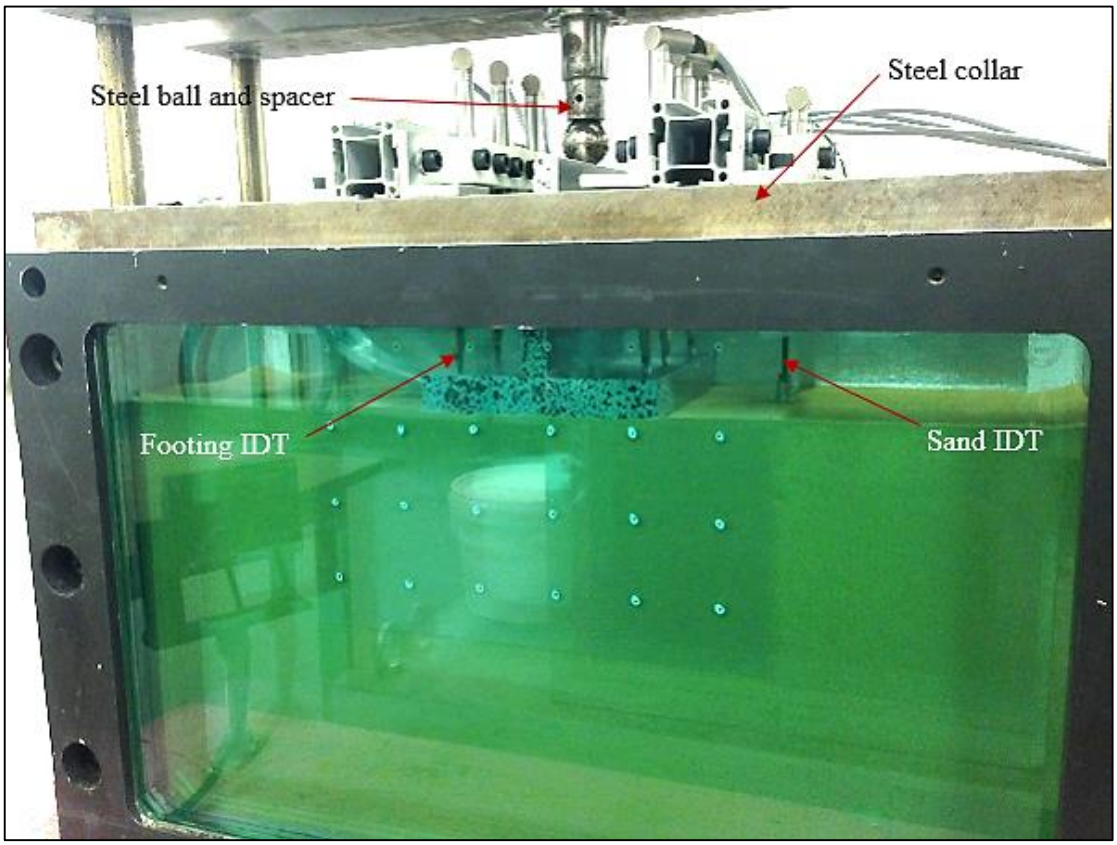

Figure 3-12 Image of assembled strongbox indicating the gap where footing is placed

3.4 Loading Actuator

To design a footing, structural engineers normally obtain the permissible bearing capacity from geotechnical engineers for a particular soil and size of footing. In this project the intension was to apply loads well in excess of what would be considered allowable bearing stresses. A maximum load of 30 kN was chosen, representing a uniform contact stress of 1 333 kPa for each footing. This stress far exceeds the typical permissible bearing capacity assumed for any sand (Robberts and Marshall, 2010).

The load was applied with a mechanical ball screw jack from Pfaff-Silberblau (2013). Specifications of the loading jack can be seen in Table 3-6, with an image of the ball screw jack shown in Figure 3-13. The jack was controlled remotely with a Kollmorgen P70530 (DC) micro-stepping drive (Kollmorgen, 2014), indicated in Figure 3-14. The specifications of the micro-stepping drive can be seen in Table 3-7. The stepper motor allowed the operators to control the movement rate of the jack from the centrifuge control room. The screw was set to press at a rate of 0.01 mm/s, the slowest possible speed for this specific screw jack (required to ensure small displacements between individual . The loading jack and frame can be seen in Figure 3-14, with the force transducer at the bottom of the screw also visible.

© University of Pretoria

Figure 3-13 Pfaff-Silberblau SHE 3.1 ball screw jack (Pfaff-Silberblau, 2013)

Table 3-6 Specifications of the SHE 3.1 mechanical ball screw jack used in the experiments (Pfaff-Silberblau, 2013)

Specifications	Value
Make and model	Pfaff-Silberblau SHE 3.1
Maximum static lifting capacity (kN)*	49.9
Maximum dynamic lifting capacity (kN)	24.1
Ku Ball Screw (diameter × pitch)	25 × 5
Stroke (mm)	150
Gear Ratio	24:1
Lift per revolution (mm/per rev.)	0.25
Efficiency (%)	90

* The jack was mounted upside down on the load frame implying a downward acting load capacity of 49.9 kN.

Table 3-7 Specifications of the P70530 stepper motor used in the experiments (Kollmorgen, 2014)

Specification	Value
Make and model	Kollmorgen P70530
Input voltage range (V)	20-75 VDC
Continuous current (A)	5
Size (W × B × H) (mm)	29 × 111 × 107
Ambient temperature (°C)	0 - 40
Max chassis temperature (°C)	70
Step resolution (steps/rev)	200 - 50 000
Speed range (revs/second)	0-50

© University of Pretoria

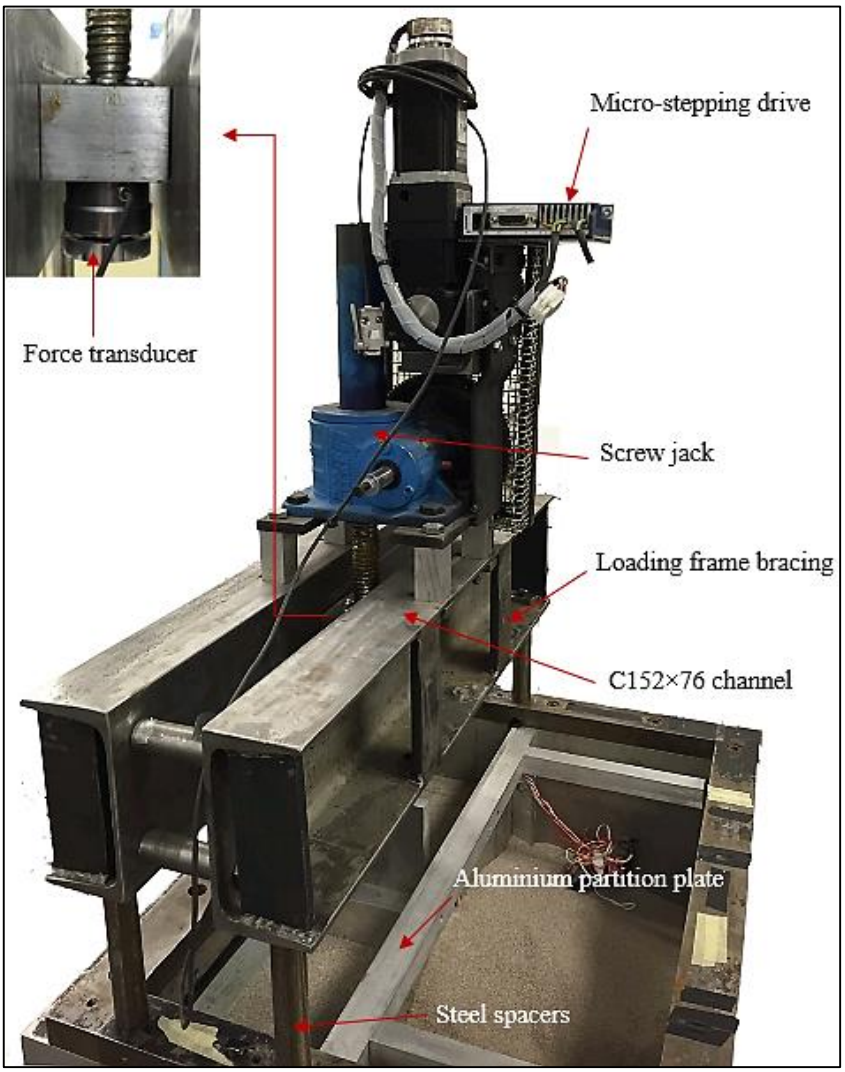

Figure 3-14 Screw jack used in experiments

When the centrifuge model was accelerated to the required G-level, the self-weight of all the elements on the centrifuge model platform increased with a factor equal to the G-level. To limit the amount of movement due to self-weight, a rigid loading frame was constructed from two C152 × 76 steel channels, as can be seen in Figure 3-14. Movement of the loading frame during the experiment was caused by the jack that pulled on the loading frame, as well as the increased self-weight of the jack and loading frame.

To further strengthen the loading frame, bracing was placed at third points along the channel lengths and at the ends. The loading frame was also placed on four 130 mm × 25 mm diameter cylindrical steel spacers to support the loading frame at an elevation thus accommodating the footings and the measurement equipment beneath it. The steel spacers are also indicated in Figure 3-14. The aluminium partition plate is also indicated in Figure 3-14. The deflection of the loading frame was tested under maximum load application and the results indicated that the movement was negligible.

© University of Pretoria

3.5 Instrumentation

The essential data from the experiment was the settlement data of the footings, the stress distribution below the footings at the soil-structure interface and the load applied to the footing. The settlement of the footing was determined through the use of inductive displacement transducers (IDT) as well as PIV. The stress distribution underneath the footing was determined with the use of the Tekscan™ system, whilst the load applied to the footing was measured with a force transducer.

3.5.1 Force Transducer

The force transducer used during the test was a U93 load cell developed by HBM, with a capacity of 50 kN (HBM, 2014). The force transducer was placed at the bottom of the ram of the loading actuator where the load was being applied, as indicated in Figure 3-14. An example of the force transducer can be seen in Figure 3-15. The characteristics of the force transducer are shown in Table 3-8. The calibration data of the force transducer is presented in Appendix A.

Table 3-8 Properties of U93 force transducer (HBM, 2014)

Property	Value
Nominal rated force (kN)	50
Nominal rated sensitivity (mV/V)	1
Operating temperature range (°C)	-30…+85
Excitation voltage (V)	5
Maximum operating force (%)	180 of nominal force
Breaking force (%)	> 300 of nominal force
Mass (g)	600
Diameter (mm)	54

Figure 3-15 Force transducer used in experiment (HBM, 2014)

© University of Pretoria

3.5.2 Inductive Displacement Transducers

Eight inductive displacement transducers (IDT) were used during the experiment to determine the deflection of individual elements as described in the following section. The IDTs measured the settlement of the footings, the sand adjacent to the footings and the deflection of the aluminium partition plate during loading.

3.5.2.1 Footing Displacement

Although PIV software was used to track the deflection of the footing, IDTs were used to confirm the measurements. The experiment was analysed assuming plane-strain conditions and measurements were taken throughout the length of the footing by means of IDTs to ensure this assumption remained valid for all the tests. The location of the IDTs on the footing can be seen in Figure 3-16, indicated with black dots on the footing.

Six spring loaded IDTs (HBM model WA/20-T) (HBM, 2014) were used to record the settlement of the footings during the experiment. Properties of the IDTs can be seen in Table 3-9. The IDTs were fastened onto aluminium support beams that were bolted onto the strongbox and used for all the tests. The position of the IDTs remained constant for all the tests. Data from the IDTs were captured in the control room using HBM software, further discussed in Section 3.6. The calibration data of each IDT is presented in Appendix B.

Table 3-9 Properties of IDTs on footings (HBM, 2014)

Property	Value
Make and model	HBM WA/20-T
Type of displacement transducer	Inductive displacement probe
Nominal displacement range (mm)	20
Nominal sensitivity (mV/V)	80
Deviation of sensitivity from nominal sensitivity (%)	±1
Nominal temperature range (°C)	-20…+80
Nominal excitation value (V_{rms})	2.5
Weight (g)	64
Body diameter (mm)	12

© University of Pretoria

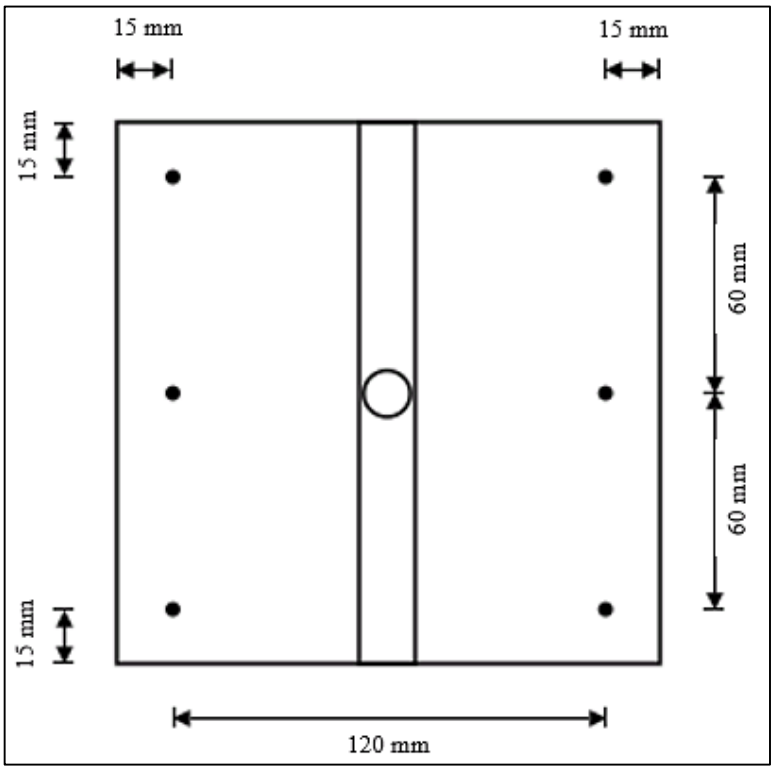

Figure 3-16 Position of IDTs on the footings during the experiments

3.5.2.2 Sand Displacement

To measure the deflection of the sand near the footings, another HBM IDT was placed on the sand as can be seen in Figure 3-12. If the core was spring loaded it would push into the sand at 1 G and low accelerations, therefore a loose core was used. The IDT used was a HBM WA/50-L (HBM, 2014). Properties of this IDT is identical to the others used on the footing, with the only difference being the nominal displacement of 50 mm and the weight of 77 g. Calibration data of the IDT can be seen in Appendix B. An image of both types of IDTs can be seen in Figure 3-17 (the displacement probe is spring loaded and the plunger is a loose core).

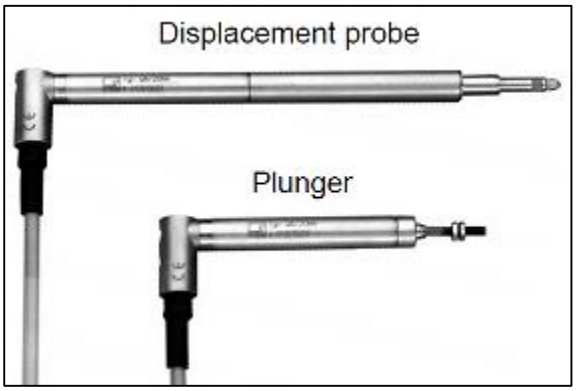

Figure 3-17 IDTs used during the experiment (HBM, 2014)

© University of Pretoria

3.5.2.3 Partition Plate Deflection

Only the front section of the strongbox was used in this experiment. An aluminium partition plate was used to divide the strongbox into two compartments. To minimise deflection of the partition plate, the back compartment behind the partition was also filled with sand. The load was only applied in the front compartment of the sand, which induced larger stresses on the front of the partition. The sand behind the partition helped to limit the deflection of the back plate.

The deflection of the back plate was measured to ensure that it did not deflect excessively thereby affecting model behaviour. If the deflection of the back plate was excessive, the plane-strain assumption would not be valid because out-of-plane deflections are not allowed under plane-strain conditions. This would also result in the stress distribution of the model being incorrect. The deflection at the centre of the back plate was measured using an IDT and a hinge mechanism as shown in Figure 3-18 and Figure 3-19. A small box was constructed with two holes drilled into the centre of the top and the side of the box. Large needles were glued onto the holes, with a small needle placed inside the bigger needle to create a mini-extensometer. Within the box, a bent steel plate could rotate around a fixed rod. The steel plate was positioned so that approximately 5 mm movement of the small needle would be allowed. The inner needle was placed against the side of the aluminium partition. When the partition deflected backward, it pushed the needle inwards, rotating the steel hinge plate in the small box which in turn pushes the top needle upwards. On the top of the needle a flat piece of metal was placed on which an IDT measured the resulting displacement. The upward movement of the needle pushed the IDT core in, measuring the deflection of the aluminium partition. A maximum of ± 5 mm movement was allowed by the steel rotating plate, which was considerably more than the expected movement of the partition. The IDT used was a HBM WA/10-T (HBM, 2014). The weight of the IDT was 62 g and its nominal displacement range was 10 mm.

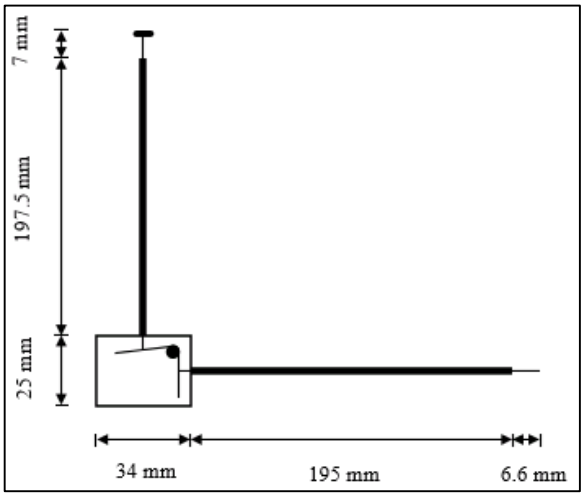

Figure 3-18 Schematic of hinge mechanism used to determine deflection of the back plate

© University of Pretoria

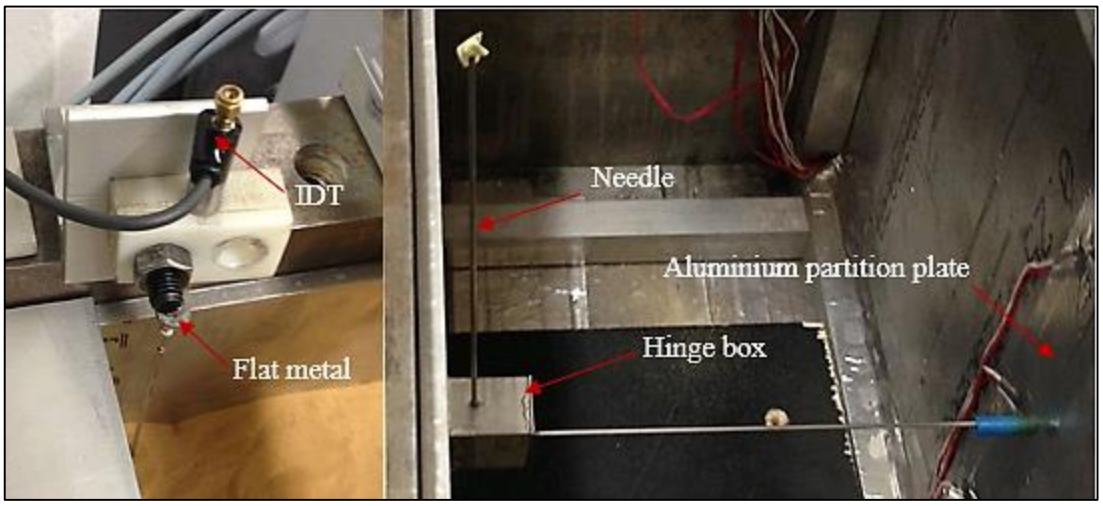

Figure 3-19 Images of hinge mechanism in the strongbox

The data obtained from the partition plate IDT has no effect on the footing stiffness and it is therefore not included in this report. The average horizontal movement of the centre point of the partition plate was 1.5 mm when a load of 30 kN was applied and this was considered acceptable for this study.

3.5.3 PIV Analysis Equipment

Along with the settlement data, it was equally important to determine the deflected shapes of the footings. As explained in the literature, PIV can be used to determine displacements and strains in soils. However, if enough texture is present on the surface of the footings, PIV can be used to determine the deflected shape of the footing. To ensure that enough texture was present for PIV analysis, all the footings were textured by applying black spray paint dots. An example of the texture thus achieved can be seen on the aluminium footing shown in Figure 3-4.

A Canon EOS D100 digital camera with a Canon EF 40mm f/2.8 STM Macro lens (Canon, 2014) was used to capture the photographs used for the experimental analysis. The camera has an 18 MP image sensor. The images captured measured 3 456 × 2 304 pixels, which is more than adequate for the PIV software to track displacements in the model. The camera was controlled with software from the control room of the geotechnical centrifuge.

The centre of the camera lens was placed at a height of 257 mm above the base of the centrifuge strongbox, a distance of 584 mm away from the front of the strongbox. Figure 3-20 displays a side view of the experimental setup, including all the relative elevations and distances between individual components. The camera was placed in the front nose cone of the centrifuge arm. The white nose cone can be seen in Figure 3-1 and Figure 3-21.

© University of Pretoria

Although the camera was focused on the footing for each experiment, any variation was compensated for by the PIV software, eliminating the influence of the camera angle. To ensure constant lighting 10 W LED spot lights were placed on each side of the strongbox. The location of the lights was beyond the ends of the strongbox. The lights were rotated inwards to ensure that there was limited glare captured by the camera. The position of the two LED spot lights attached on the frame, as well as a close-up image of the light is shown in Figure 3-21.

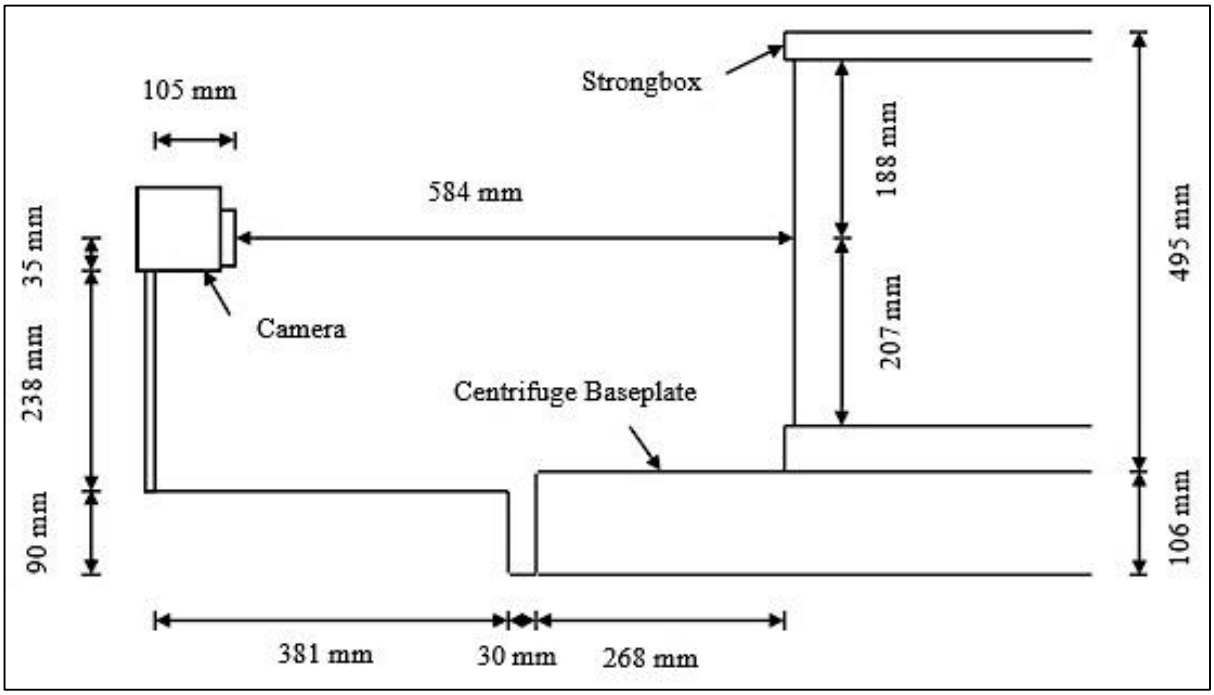

Figure 3-20 Schematic of experimental setup from side

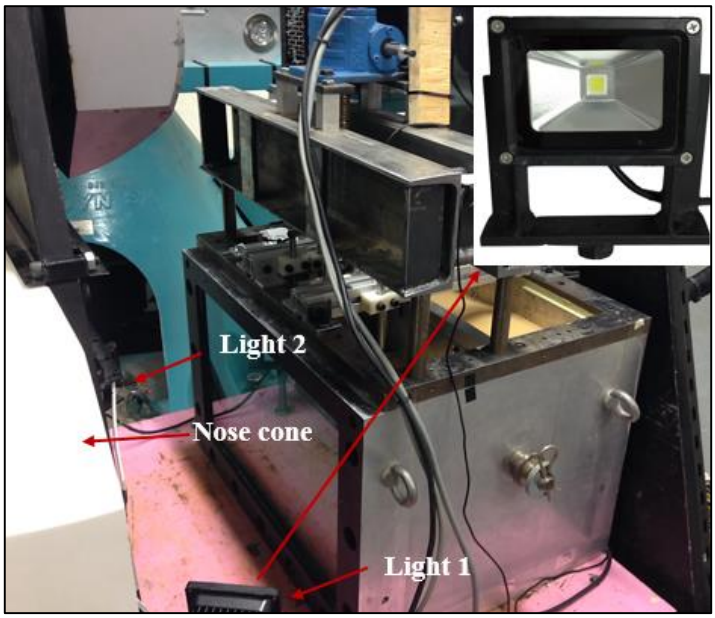

Figure 3-21 Lights used for PIV analysis

© University of Pretoria

3.5.4 Tekscan™ Pressure Sensor

A Tekscan™ pressure mat was used to determine the contact stress distribution at the soil-structure interface. The drawing and technical specifications of the specific pressure sensor used in the experiment can be seen in Figure 3-22 and Table 3-10 respectively. The edge of the sensor matrix was placed at the edge of the footing furthest away from the sensor handle, as the pressure mat was not large enough to have a sensor matrix below the entire footing. Due to the fact that the test would be conducted under plane-strain condition and that the geometry of the footings were symmetrical around the centre of the column, the contact stress distribution on each side of the column was assumed to be symmetrical. Therefore, only the contact stress on the one side of the footing had to be measured.

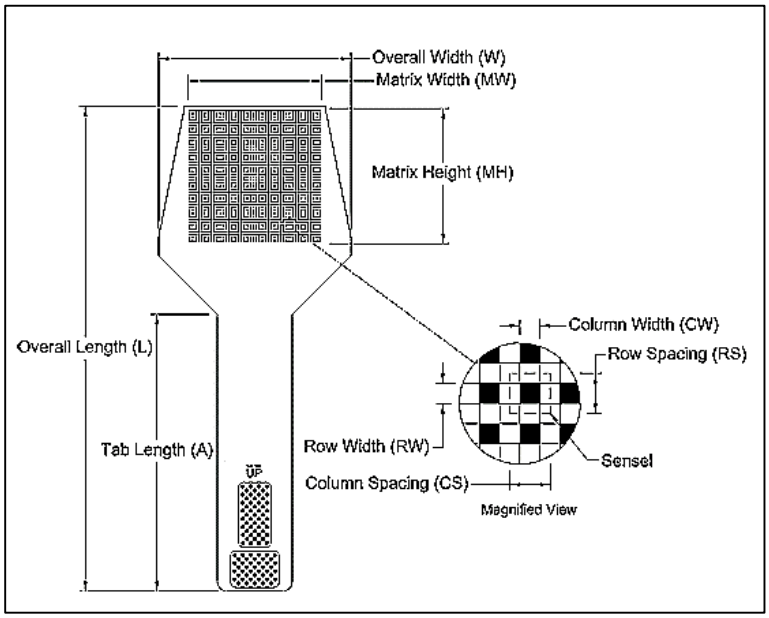

Figure 3-22 Schematic of Tekscan™ pressure sensor 5 101 used in all experiments (Tekscan™, 2014)

Table 3-10 Properties of Tekscan™ 5101 sensor (Tekscan™, 2014)

Property	Value
Overall Length (L) (mm)	340.1
Overall Width (W) (mm)	148.8
Tab Length (A) (mm)	167.4
Matrix Width (MW) (mm)	111.8
Matrix Height (MH) (mm)	111.8
Column Width (CW) (mm)	1.3
Column Spacing (CS) (mm)	2.5
Column Quantity	44
Row Width (RW) (mm)	1.3
Row Spacing (RS) (mm)	2.5
Row Quantity	44
Total Number of Sensels	1 936
Resolution sensel density (sensel per cm^2)	15.5

© University of Pretoria

An image of the sensor used is shown in Figure 3-23 on the left, along with two examples of the location of the sensor below the footings on the right. Placing the sensor between the footing and the soil could potentially have affected the soil-structure interaction somewhat, but the variation from the ideal behaviour would be constant for all tests and the test results could therefore be compared with one another.

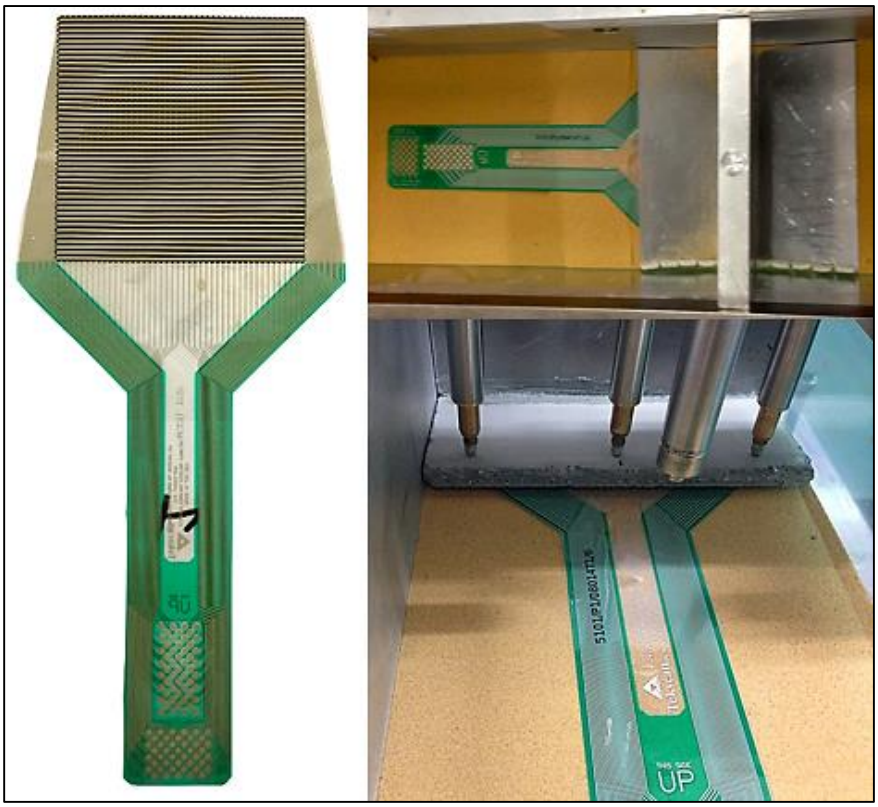

Figure 3-23 Tekscan™ pressure sensor used in experiments

3.6 Data Acquisition System

The centrifuge at the University of Pretoria is equipped with a 24 channel Digidaq system, as well as a 24 channel HBM Quantum X system (Jacobsz et al., 2014). In addition to the above, the Tekscan™ system was also installed on the centrifuge for this specific test. All the data was transferred from the centrifuge to the control room via a 1 Gigabit fibre optic cable (Jacobsz et al., 2014). The Digidaq system was used to determine the initial settlement of the soil mass when the model was accelerated to 50 G. A MX840 HBM module was used to record the experimental data at a sampling rate of 5 Hz. The force transducer, sand IDT and footing IDTs were recorded with the use of Catman AP Measurement Software developed by HMB (2014). The Tekscan™ data was recorded with I-Scan software developed by Tekscan™ (2014). The sampling rate for the pressure sensor data was also set at 5 Hz to correlate with the HBM data.

© University of Pretoria

3.7 Experimental Procedure

With all the components used in the experimental setup discussed, the complete experimental procedure is discussed in the following section. The steps described below were followed carefully for each experiment to ensure that there was minimal variation between the tests.

The soil was rained through a sand hopper with a 2 mm gap at a rate of ± 2.02 kg/min. For all the tests the drop height was 800 mm below the hopper opening, kept constant by continuously lowering the strongbox beneath the hopper. An image of the hopper with the strongbox can be seen in Figure 3-24, with an insert of the sand raining through the hopper also shown in the figure.

The strongbox was then mounted on the centrifuge model platform. During the initial acceleration phase, the model was subjected to an acceleration of 50 G so that the soil was lightly overconsolidated by a factor of 1.67 compared to the nominal working acceleration of 30 G, somewhat increasing the lateral earth pressure coefficient and in effect increasing the density of the soil slightly.

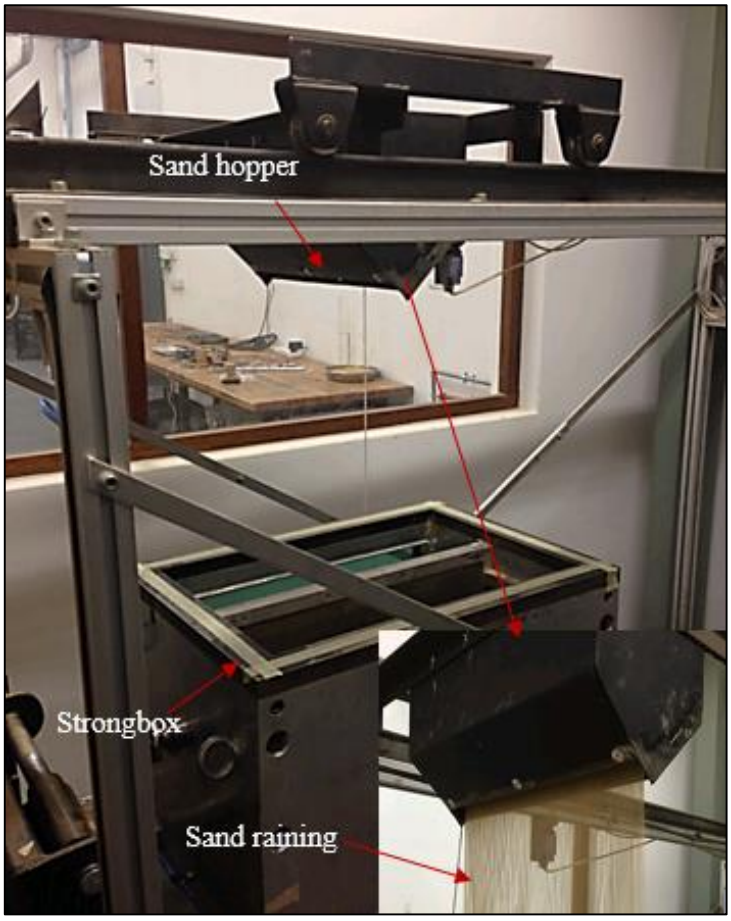

Figure 3-24 Sand hopper and strongbox

© University of Pretoria

Five IDTs were placed inside the box to determine when the soil stopped settling at 50 G acceleration, where after the centrifuge could be stopped. Data from these IDTs have no relevance to the experimental results and will not be shown in this report, except to mention that the settlement recorded during the overconsolidation phase typically amounted to 1.4 mm. The five IDTs can be seen in Figure 3-25, also showing the sand fill behind the aluminium partition.

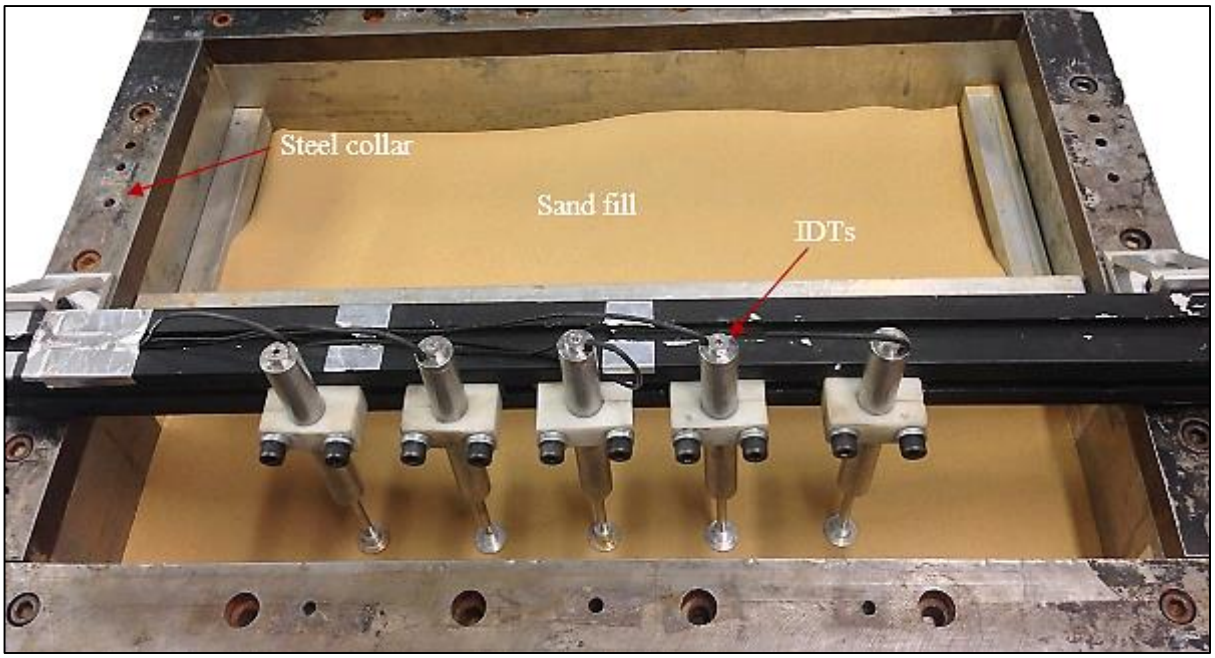

Figure 3-25 IDTs used for centrifuge acceleration at 50 G

After compaction, the top sand layer was levelled to create a smooth surface to place the footings and ensure as little as possible stress variations present under the footing at the beginning of the test. The Tekscan™ sensor was placed first, using reference markers to ensure installation at the same position for all the tests. The footing was placed on top of the sensor, with the edge of the footing placed on the edge of the sensor matrix. The IDTs were placed on top of the footing and the sand by bolting the beams down, thus ensuring that the readings would always be taken at the same locations. The loading frame and screw jack were bolted to the steel collar before the strongbox was placed on the centrifuge platform.

The strongbox was accelerated to 30 G. The angular velocity of the centrifuge was calculated to be 30 G at a radius measured to 250 mm above the centrifuge platform. Only the data obtained when the sample was at 30 G was used, as the self-weight of the equipment would then remain constant and any settlement recorded was only due to the load increase caused by the loading jack.

© University of Pretoria

The camera was set up to take images every 10 seconds. The time stamp of each photo was correlated with the data of the force transducer to determine the exact load at each image. The Tekscan™ data was recorded at 5 Hz and also calibrated with the corresponding load with the use of the time stamp on each reading. Finally, the IDTs and force transducer data were recorded with the same software, therefore the load at each reading was easily correlated. The test was conducted at 30 G, with the loading jack moving at a rate of 0.01 mm/s until 30 kN was reached. An image of the fully assembled strongbox can be seen in Figure 3-26, with the important elements discussed throughout this chapter highlighted in the figure.

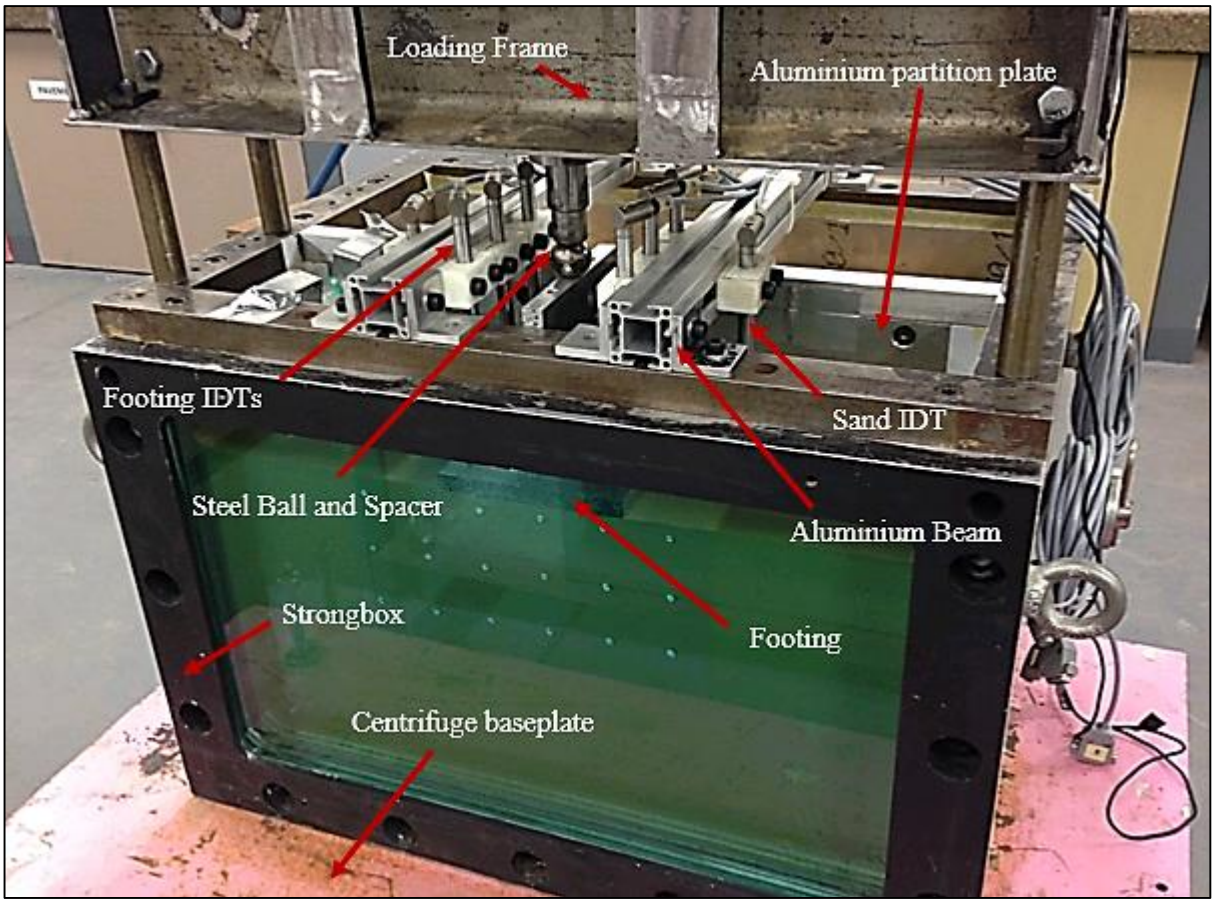

Figure 3-26 Complete experimental setup from the front

© University of Pretoria

4 Results and Discussions

4.1 Introduction

This chapter presents the results obtained from the experimental modelling discussed in Chapter 3. As indicated earlier, a total of eight centrifuge tests were conducted, seven with aluminium footings and one with a reinforced concrete footing.

The chapter starts by discussing the settlement and deflected shapes of all the aluminium footings. The settlement of the footings refers to the amount that the footing was pressed into the sand, whereas the deflection and deflected shape refers to the curvature of the footing during load application. This is followed by the contact stress distribution beneath the aluminium footings. For both of these sections, the footings will be discussed individually, followed by a combined analysis of the results.

After the behaviour of the aluminium footings have been analysed, the reinforced concrete footing is discussed to determine whether there is a correlation between the behaviour of it and the aluminium footings. The chapter concludes by discussing the displacement of the sand beneath the footings at the maximum applied load.

4.2 Foundation System Properties

As discussed in Section 3.2, the materials used in the experiment were silica sand, aluminium, steel and concrete. All the calculations in Chapter 3 were made with the use of theoretical material properties. In this section, the actual material properties that were determined are discussed, along with alterations made to the theoretical calculations in Chapter 3.

4.2.1 Silica Sand Properties

The structural behaviour of the footing is highly dependent on the properties of the soil on which it is constructed. Some of the properties of the sand applicable to each test were back calculated after the experiment was conducted, as the stress level and the sand packing density changed somewhat during the experiment. The sand properties required for the analysis of the footings were the density, a representative Young's modulus and mobilised friction angle.

© University of Pretoria

An average secant Young's modulus was determined for the model soil profile by considering one dimensional settlement of the footing along the footing's centreline. Due to the deflection of the flexible footings, it was difficult to calculate a representative soil strain because the settlement varied along the width of the footing. However, the secant Young's moduli were determined from the settlement data of the stiff footings as they did not deflect noticeably during load application (based on PIV measurements discussed in later text) and the settlement along the width of the footing remained constant. The secant Young's modulus was determined with the use of Equation 4-1 (Mac Donald, 2011). The equation below presents the relationship between vertical stress increment, horizontal and vertical strain and the Young's modulus and Poisson ratio for plane strain conditions.

$$\sigma_y = \frac{E_s}{(1+\nu)(1-2\nu)}\left[\varepsilon_x \nu + \varepsilon_y(1-\nu)\right] \qquad \text{(Equation 4-1)}$$

Where:

σ_y = Average vertical stress increase in sand
E_s = Secant stiffness modulus of the soil
ν = Poisson's ratio of soil
ε_x = Horizontal strain of sand
ε_y = Vertical strain of sand

A secant Young's modulus of the sand along the footing centreline was calculated by dividing the material below the footing into a number of layers. For each layer the average vertical stress increase due to the contact stress exerted by the footing was calculated using Boussinesq's equations (Knappett and Craig, 2012). By considering a depth of 2B (300 mm, depth of the sand layer), the mean stress with depth in the sand layer was 58.4% of the applied contact stress.

The vertical displacement contours from the PIV analyses indicated relatively constant strain with depth along the footing centreline. The mean strain below the footing was therefore calculated by simply taking the footing settlement and dividing it by the depth of the sand (justified in Section 4.3.1). The Young's modulus for each layer was calculated from this equation along the footing centreline. Due to symmetry, zero horizontal strain was assumed. A Poisson's ratio of 0.2 was assumed. The final Young's modulus was taken as a weighted average of the individual layer stiffness.

The secant Young's modulus of the sand determined as explained above for the stiff footing tests were plotted as a function of the density of the sand during the experiment, indicated in Figure 4-1. The secant Young's modulus of the sand beneath the flexible footings could not be determined with the simplified method described for the rigid footings because of the variation in the settlement along the width of the footing. However, in cases of flexible footings, an appropriate modulus was determined from the density of the sand beneath the flexible footings and determining the corresponding secant Young's modulus with Figure 4-1.

© University of Pretoria

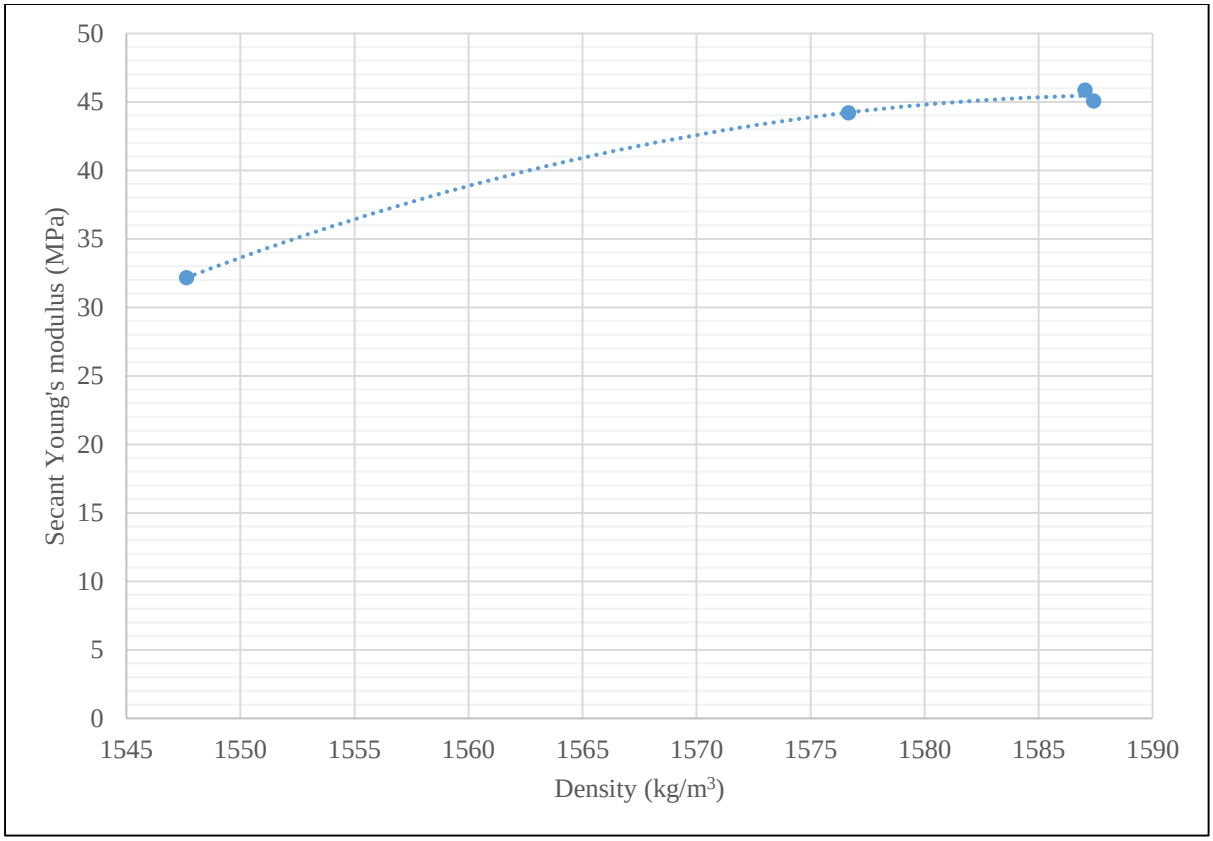

Figure 4-1 Average secant Young's modulus for model soil profile as a function of sand density

The friction angle of the sand was determined as a function of the relative density of the sand (measured post-test) from Figure 3-3 (Archer, 2014) shown in Section 3.2. With the use of these properties the bearing capacity of the foundation system was determined from Equation 2-1 (Terzaghi, 1943) indicated in Section 2.3.1. Equation 2-1 was proposed for 2D strip foundations (Knappett and Craig, 2012) discussed in Section 2.3.1, similar to the footings considered in this study. Since the footing was not embedded into the soil and the sand had no cohesion, only the bearing capacity factor N_γ had to be determined. The factor N_γ could be determined from either Equation 2-4 (Meyerhof, 1963) or Equation 2-5 (Hansen, 1968). However, the equation which produced the lowest bearing capacity factor was used for the calculation of the bearing capacity of the system. Equation 2-5 (Hansen, 1968) produced the smallest value for N_γ in all the experiments. The width of the prototype footing (4.5 m) was used in the calculations. The results for each experiment are shown in Table 4-1.

The calculated bearing capacity for all the aluminium foundations exceeded the maximum applied stress of 1 333 kPa (30 kN over a 150 mm × 150 mm area), assuming a uniform contact stress distribution. If a uniform contact stress distribution is also assumed for the reinforced concrete footing, then the bearing capacity of the foundation system could be exceeded at 30 kN, as the bearing capacity of the system was only 1 222 kPa. This is discussed further in Section 4.5.

© University of Pretoria

Table 4-1 Properties of sand used in the experiments and associated bearing capacities

Material	Footing Thickness (mm)	Density (kg/m^3)	Relative Density (%)	Secant Young's Modulus (MPa)	Friction Angle (°)	N_γ	q_f (kPa)
Aluminium	3	1 578	67	44.4	36.5	48.4	1 686
Aluminium	6.7	1 587	70	45.4	37.1	54.3	1 901
Aluminium	10	1 560	61	39.0	35.5	40.3	1 387
Aluminium	16	1 587	70	45.3	37.1	53.8	1 883
Aluminium	25	1 587	70	45.9	37.1	54.0	1 892
Aluminium	35	1 577	67	44.2	36.4	47.8	1 664
Aluminium	50	1 587	71	45.1	37.1	54.3	1 901
Reinforced Concrete	30	1 548	56	32.2	34.8	35.8	1 222

N_γ = Bearing capacity factor

q_f = Bearing capacity of foundation system

4.2.2 Relative Foundation Stiffness

The secant Young's modulus of the sand for each test was used to determine whether the foundation systems were considered as flexible or rigid with Equation 2-11 (Arnold et al., 2010), shown in Section 2.5. The measured properties of the aluminium and concrete discussed in Sections 3.3.2 and Section 3.3.3 were used for the calculations, along with the secant Young's modulus of the sand indicated in Table 4-1. The results are shown in Table 4-2, along with a description of the flexibility of the footings. As indicated in the table, a wide range of foundation stiffnesses were considered in this study, ranging from semi-flexible to stiff, as required for this study.

Table 4-2 Rigidity of footings using actual material properties

Material	Footing Thickness (mm)	K_s	Description
Aluminium	3	0.0011	Semi-flexible
Aluminium	6.7	0.0116	Semi-stiff
Aluminium	10	0.0448	Semi-stiff
Aluminium	16	0.1581	Stiff
Aluminium	25	0.5955	Stiff
Aluminium	35	1.6956	Stiff
Aluminium	50	4.8504	Stiff
Reinforced Concrete	30	0.5181	Stiff

*Based on uncracked stiffness of reinforced concrete footing

© University of Pretoria

4.3 Footing Settlement and Deflection

The settlement and deflection of footings are affected by factors including the material properties of the footing and soil, the load applied to the footing, as well as the geometry of the footing. In this section, the settlement of the footings, as well as their respective deflected shapes at model scale are analysed. The settlement data and deflected shapes were determined with the use of PIV software. The settlement data was calculated at four locations on the footings: at the edge of the column, 25 mm from the centre of the column, 50 mm from the centre of the column as well as the edge of the footing, represented as numbers 1 to 4 in Figure 4-2 respectively. The plane-strain assumption, as well as the symmetrical shape and deflection of the footing allowed the author to only consider one side of the footing for analysis. These locations were analysed due to the fact that the edge of the column is the location where structural engineers consider the maximum design moment to occur, while the other intervals were chosen to represent a third of the width of one side of the footing.

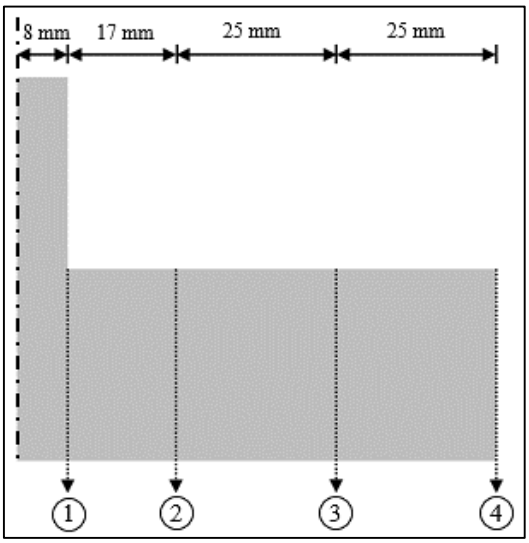

Figure 4-2 Locations of points considered on footing for analysis

The settlement data is presented in 1 kN intervals and the deflected shapes are presented in intervals of 5 kN. Normalised settlement (the actual settlement divided by the footing width) of the footing is used in the analysis of the settlement data, while the actual settlement is shown in the deflected shape graphs. The larger intervals for the deflected shapes allow a much clearer representation of the change in the footing shapes. However, any significant behavioural change at intervals not shown is discussed where applicable. The initial load of the footings was not taken as 0 kN, but rather at the weight of the footing at 30 G acceleration. Therefore, the starting point of each graph in this section differs slightly.

© University of Pretoria

During the experiment, both images for PIV analysis and IDT data were recorded to determine the settlement of the footing and in effect the curvature of the footing. PIV analysis was the preferred method of analysis as it enables the entire footing width to be analysed without the need for a large amount of equipment. PIV was also chosen due to the high accuracy achievable (White et al., 2003). However, the IDTs were placed on the footings to correlate the settlement data obtained with the PIV analysis and also validate the plane-strain assumption. The data from all six IDTs, as well as the PIV analysis at the same location as the IDT placement for the 50 mm aluminium footing are shown in Figure 4-3, demonstrating that the results obtained through PIV analysis are similar to that obtained with the use of IDTs. The figure illustrates that realistic results are obtained with PIV analysis, therefore this section only discusses the data obtained with PIV analysis. The IDT settlement data for each experiment can be found in Appendix C.

The settlement and deflection behaviour of the aluminium footings are discussed in sequence from the thickest to the thinnest footing. The aluminium footings are discussed individually first, where after the settlement and deflection results of all the aluminium footings are compared to determine the influence of the footing stiffness on the settlement and deflection behaviour.

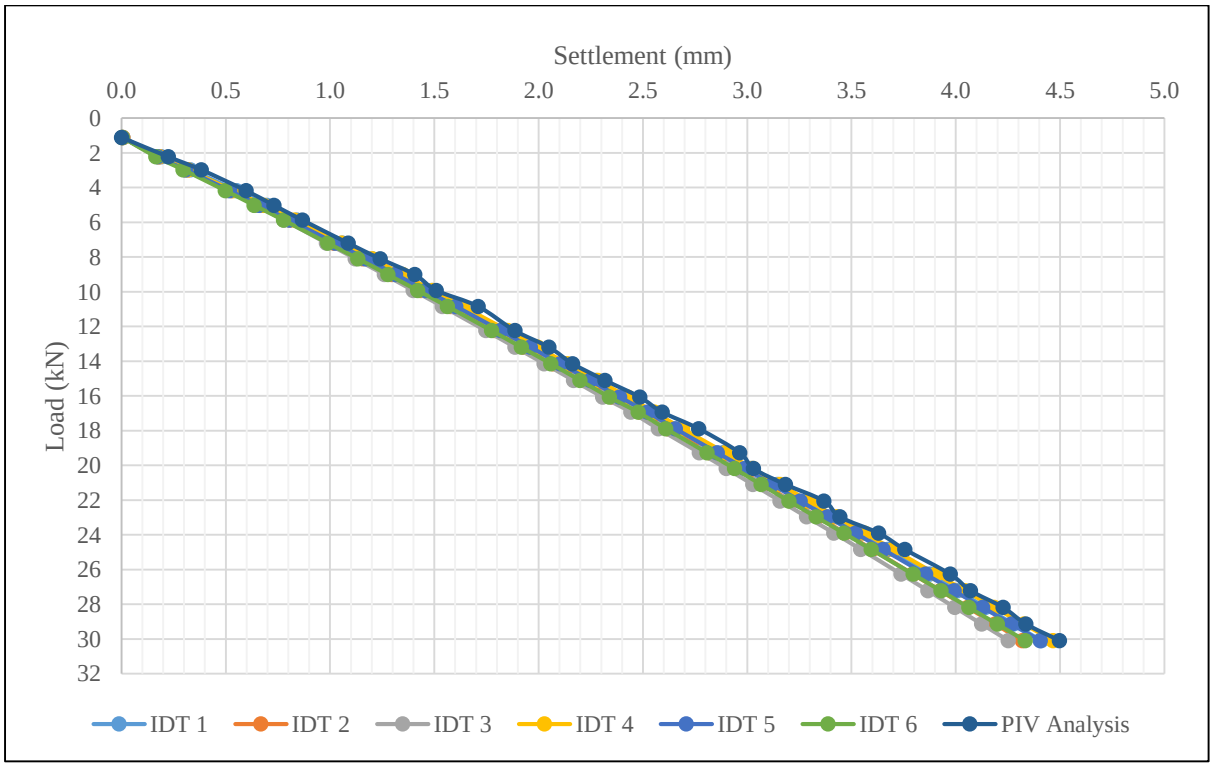

Figure 4-3 PIV settlement data compared to IDT settlement data of 50 mm aluminium footing

© University of Pretoria

4.3.1 Stiff Aluminium Footings

The 16 mm, 25 mm, 35 mm and 50 mm aluminium footings are classified as stiff based on Equation 2-11 (Arnold et al., 2010) and indicated in Table 4-2. The behaviour of the stiff footings were similar (apart from the 16 mm footing) and are therefore discussed as a collective and not individually. However, the 16 mm footing is discussed individually in Section 4.3.2. Only a single graph of the settlement and deflected shapes are shown as representative of all the stiff footings. The other settlement and deflected shape graphs omitted can be found in Appendix D and Appendix E respectively.

The normalised settlement graph for the 25 mm footing is indicated in Figure 4-4, along with the deflected shapes of the 50 mm footing in Figure 4-5. It is clear that there is no noticeable difference in the settlement of the various points along the width of the footing. This confirms that the footing is indeed stiff and no curvature occurred when a 30 kN load was applied. The settlement of the different points on the footing appears to increase linearly with an increase in the load applied, although slight non-linearity can be seen between certain load increments. This can be due to the PIV analysis or slight non-linearity in the settlement behaviour. Slight non-linearity of the settlement behaviour does support the notion of progressive failure of sand (Section 2.3.1.2). However, the maximum applied contact stress of 1 333 kPa is still far from the calculated bearing capacity of 1 892 kPa for the system and accurate analysis of failure cannot be made as failure of the sand did not occur.

© University of Pretoria

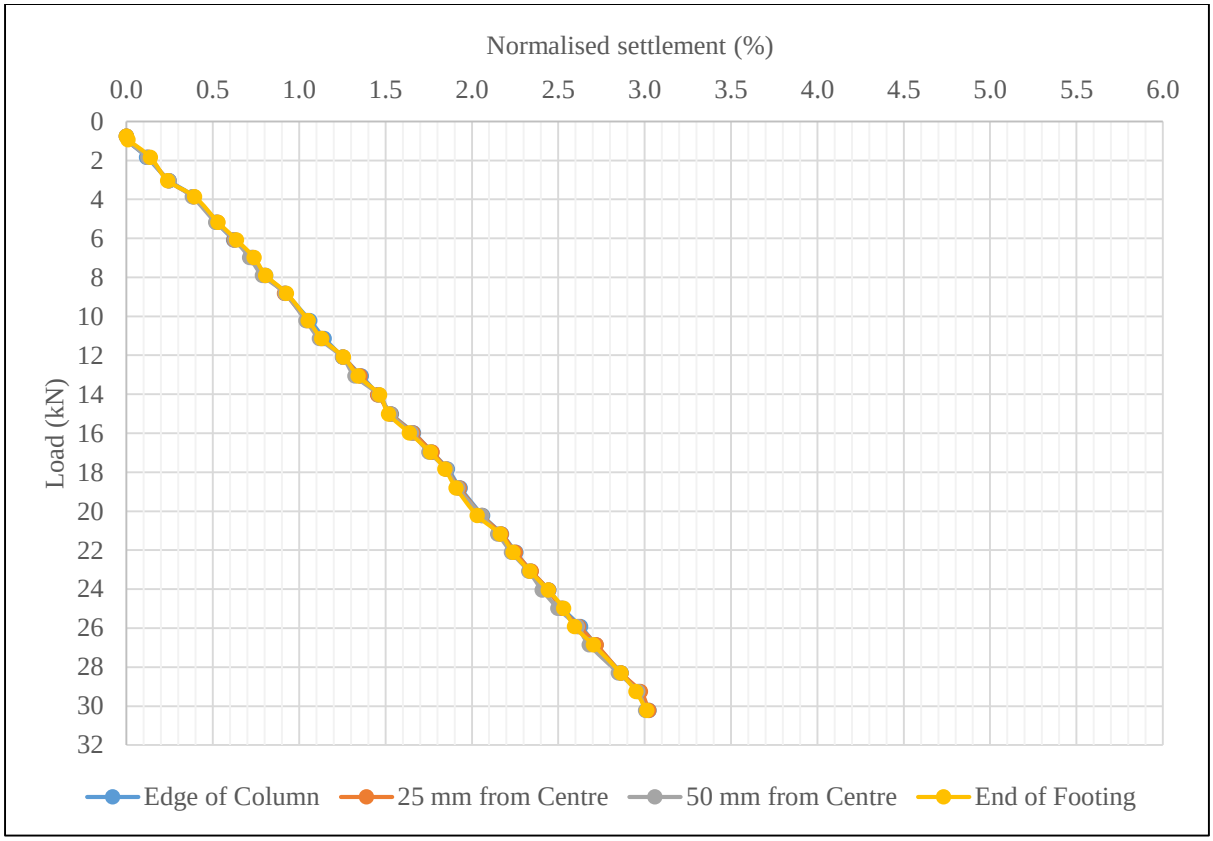

Figure 4-4 Settlement of 25 mm aluminium footing at various points on the footing

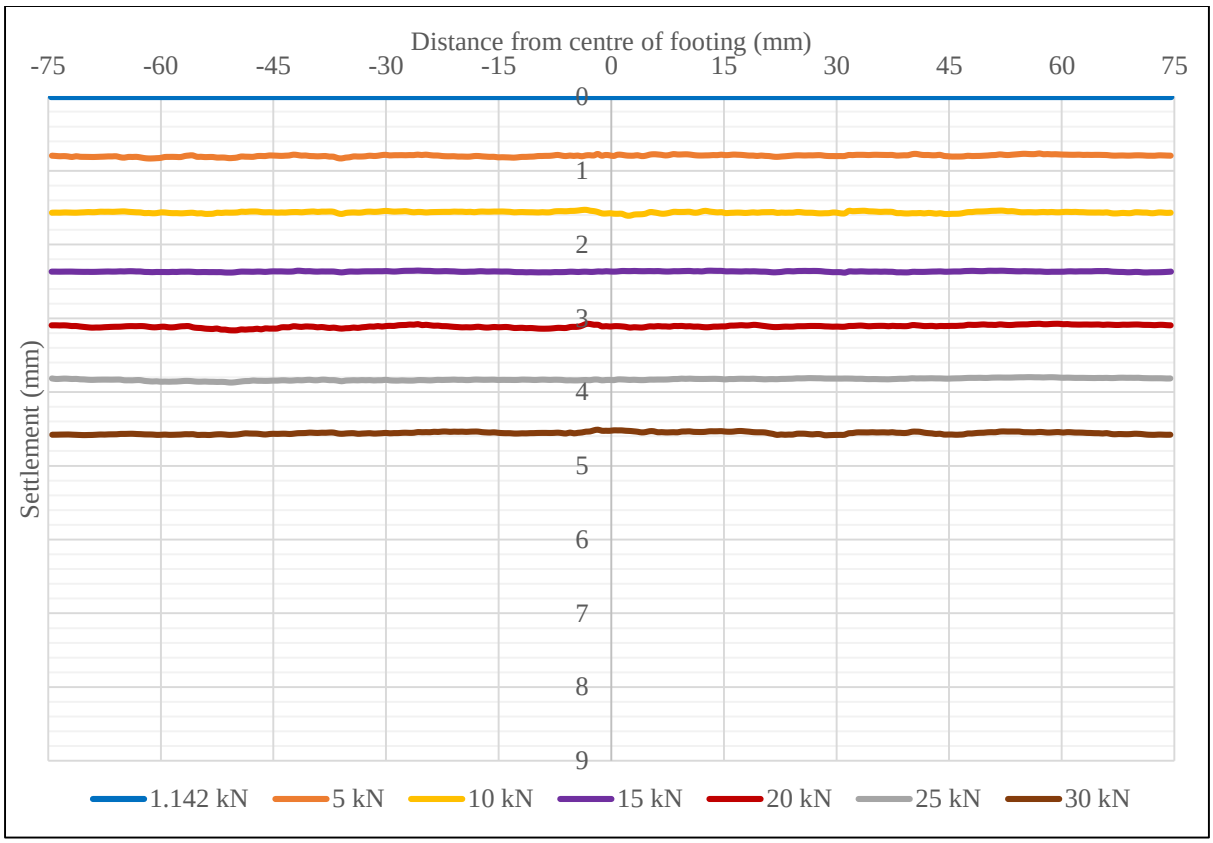

Figure 4-5 Deflected shapes of 50 mm aluminium footing at 5 kN load intervals

© University of Pretoria

The deflected shapes of the 50 mm aluminium footing are presented in Figure 4-5 as an example of the deflected shapes for all the stiff footings. Slight variations from perfectly straight shapes can be due to the analysis of the PIV, but the general trend is clearly visible. From the deflected shapes it is clear that no noticeable curvature occurred for the stiff footings. The amount of settlement of the footing is dependent on the strength of the sand if curvature of the footing does not occur, due to the fact that the contact area of the footing remains constant throughout load application.

As discussed earlier, the stiff footings were combined due to the fact that they all had similar settlement and deflection behaviour based on the stiffness of the sand. However, the behaviour of the 16 mm footing differed from the other stiff footings. As indicated in Table 4-2, the remaining footings are classified as either semi-stiff (10 mm and 6.7 mm) or semi-flexible (3 mm). Their behaviour is expected to differ from one another and will therefore be discussed individually.

4.3.2 16 mm Aluminium Footing

Although this footing was also classified as a stiff footing with a K_s value of 0.1581 (Table 4-2), the behaviour thereof differed from that of the other stiff footings. Therefore, this footing will be discussed individually from the other stiff footings. The normalised settlement of the 16 mm aluminium footing is shown in Figure 4-6. The magnitude of the normalised settlement of the footing is very similar to that of the stiff footings. However, there is a slight difference in the normalised settlement of the various points along the footing width. Up until a load of 4 kN (uniform contact stress of 177.8 kPa), the slope of the load-settlement curve remains constant for all the points along the footing width, where after the slopes of the various points starts to change. The changed slopes of the load-settlement curves of the different points on the footing remain close to one another, indicating minimal curvature along the width of the footing.

The deflected shapes of the 16 mm aluminium footing confirm the curvature thereof as shown in Figure 4-7. The difference in normalised settlement of the edge of the footing and edge of the column at 30 kN is equal to 0.15%. The actual settlement difference between the two points is equal to 0.225 mm or 1.41% of the footing thickness. As slight curvature is present when a large load is applied to the footing, the classification of stiff is not entirely appropriate, as the stiff footings did not exhibit any curvature during load application. This may suggest that a slight adjustment of the threshold value indicating a stiff foundation may be appropriate, proposed as $K_s > 0.2$.

© University of Pretoria

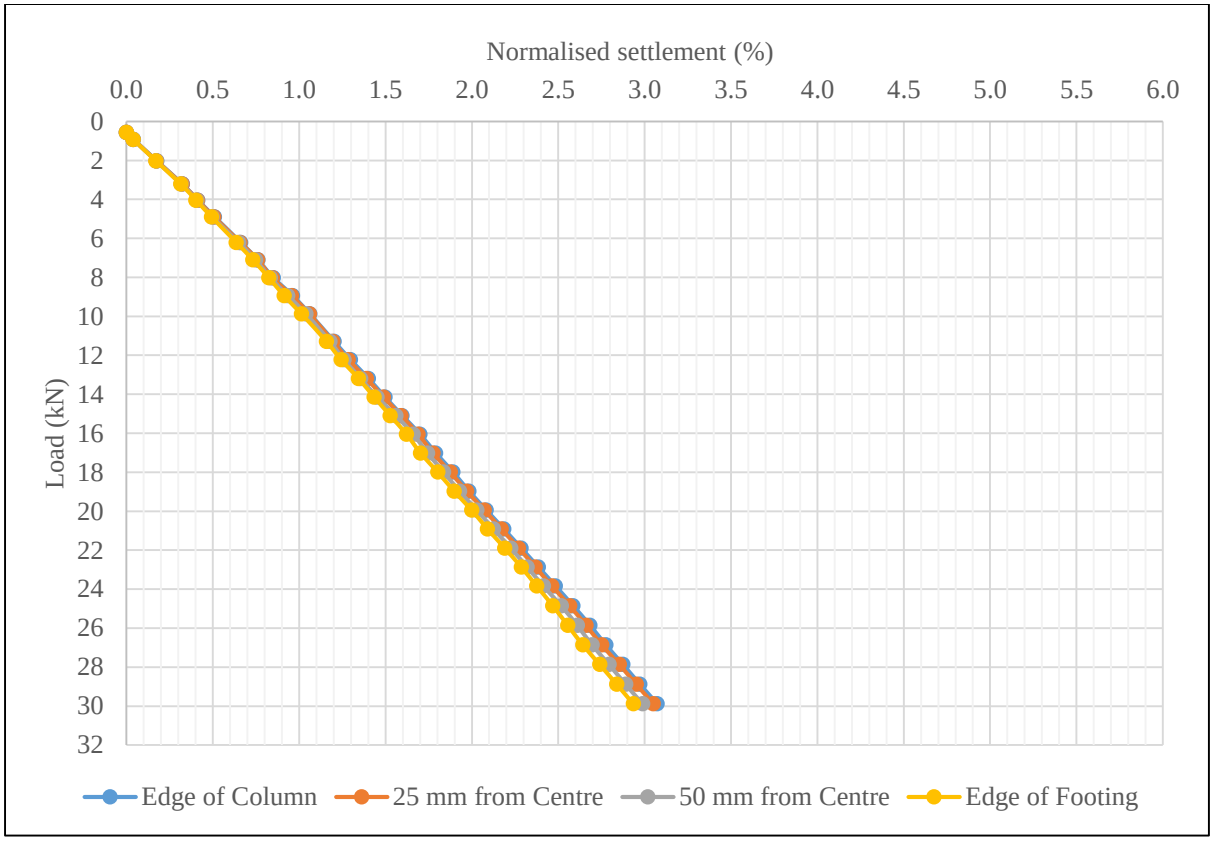

Figure 4-6 Settlement of 16 mm aluminium footing during experiment

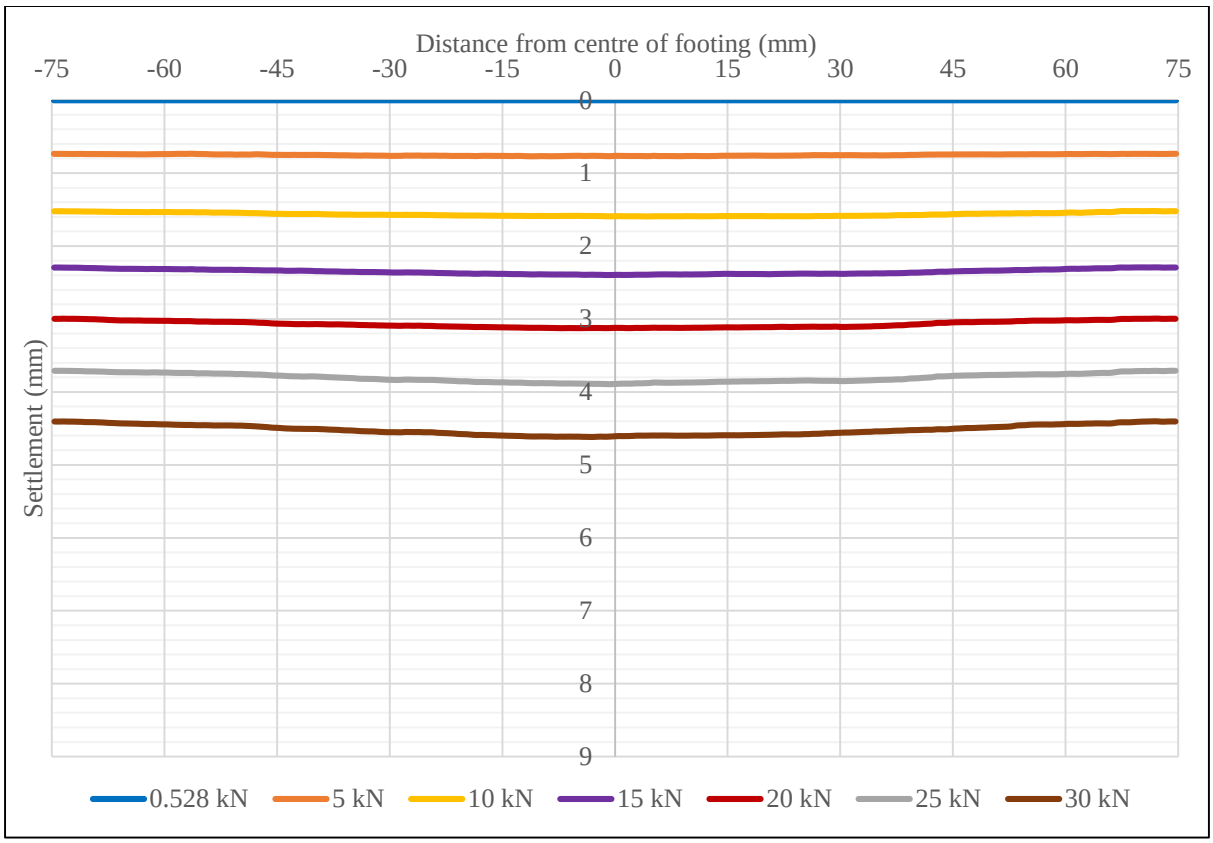

Figure 4-7 Deflected shapes of 16 mm aluminium footing at 5 kN intervals

© University of Pretoria

4.3.3 10 mm Aluminium Footing

This footing is considered as semi-stiff (K_s value of 0.0448), according Arnold et al. (2010). The footing does not fall in the same category as the previous aluminium footings, therefore different settlement and deflection behaviour compared to the stiff footings is expected.

The normalised settlement of the 10 mm aluminium footing is indicated in Figure 4-8. There is a large initial settlement between 0.42 kN (self-weight at 30 G) and 1 kN, due to the low relative density of the sand (61%) compared to the previous footings discussed, which caused a larger initial compression of the sand layer during load application. The different points along the footing width start to exhibit a different rate of normalised settlement increase at a load of 2 kN, with the variation between the different points larger than that of the 16 mm aluminium footing.

The deflected shapes for the 10 mm aluminium footing are shown in Figure 4-9. The curvature of the footing is clearly visible in the figure. The maximum difference between the normalised settlement of the footing at the edge of the column and edge of the footing is equal to 0.50%, or the actual settlement is equal to 0.74 mm, representing 7.44% of the base thickness. The increased curvature of the footing with an increased load applied changes the contact area of the soil-structure interface from the initial state of no curvature. The effects of this are discussed in Section 4.4.3.

It is clear from the data that the settlement and deflection behaviour of the semi-stiff footings differs significantly from the stiff footings. The behaviour of the 16 mm aluminium footing was close to that of the 10 mm aluminium footing, experiencing curvature during load application, whereas the other stiff footings did not (discussed in Section 4.3.2). Therefore, the 16 mm aluminium footing behaves in a similar manner to the semi-stiff footings, as opposed to the stiff footings. Although the 10 mm experiences a larger amount of deflection compared to the 16 mm aluminium footing, the behaviour of the two footings are similar.

© University of Pretoria

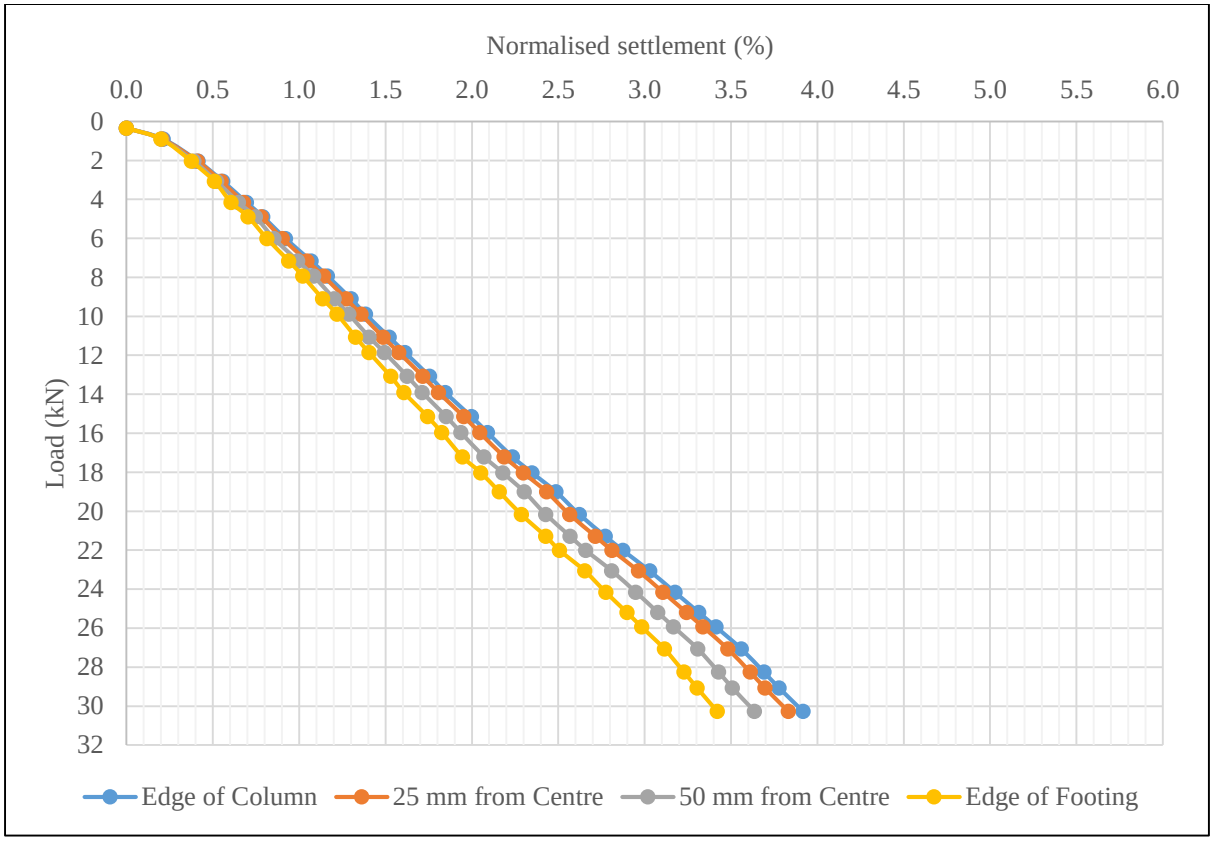

Figure 4-8 Settlement of 10 mm aluminium footing during experiment

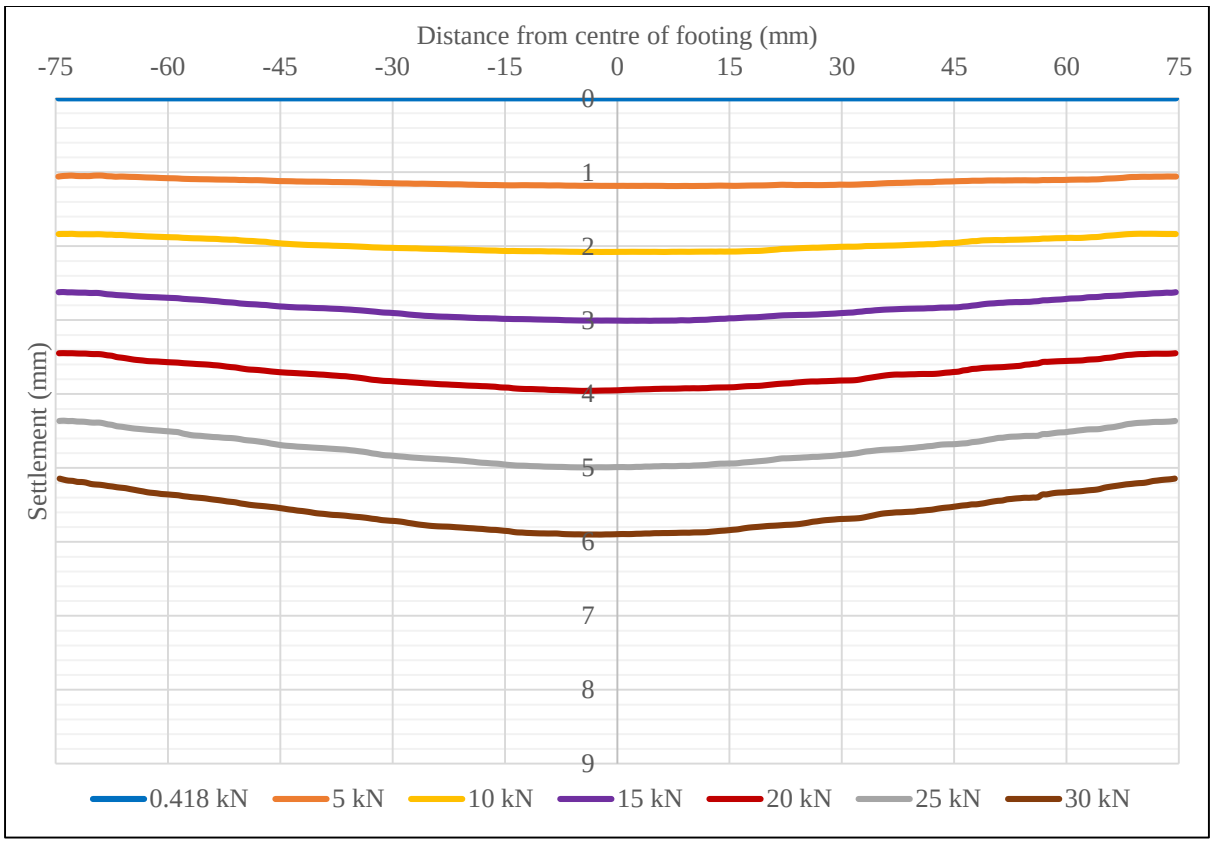

Figure 4-9 Deflected shapes of 10mm aluminium footing at 5 kN intervals

© University of Pretoria

4.3.4 6.7 mm Aluminium Footing

The 6.7 mm aluminium footing is also considered as semi-stiff according to Arnold et al. (2010), with a K_s value of 0.0116 (K_s 0.01-0.1 is considered as semi-stiff). The footing is classified as semi-stiff, however it is very close to being considered as semi-flexible and the behaviour thereof is expected to differ significantly from the stiff footings.

The normalised settlement of the 6.7 mm aluminium footing is shown in Figure 4-10. From the start of load application, the different points along the width of the footing starts to settle at different rates, as evident in the figure. The normalised settlement at the edge of the column and 25 mm from the centre of the column is much larger than that of the other points along the footing width. This might be due to the fact that as the contact area of the soil-structure interface changes due to the curvature of the footing, the contact stress distribution alters beneath the footing.

The normalised settlement of the edge of the column is almost 1% larger than that of the stiff footings (10 mm footing had larger settlements due to low relative density of the sand). When considering the behaviour of a semi-stiff footing, relatively close to the boundary of semi-flexible, the normalised settlement and deflection of different points along the footing must be an important consideration. The normalised settlement is the largest at the edge of the column and reduces for each point to the edge of the footing. The curvature of the footing is evident from the onset of load application.

The curvature of the footing is clearly visible through the deflected shapes of the footing shown in Figure 4-11. The deflection in the centre was considerably more than the deflection at the edge of the footing. The symmetry in the deflected shape of the footing is also clearly visible. The maximum difference in the normalised settlement between the edge of the column and edge of the footing is 1.54%. The actual settlement difference is 2.31 mm which represents 34.4% of the total thickness of the footing base. The deflected shapes indicate the significant difference in the curvature behaviour of this footing compared to the other footings analysed. Although the amount of settlement of the 10 mm aluminium footing was excessive, the deflected shape of the 6.7 mm aluminium footing follows on from the 10 mm aluminium footing.

© University of Pretoria

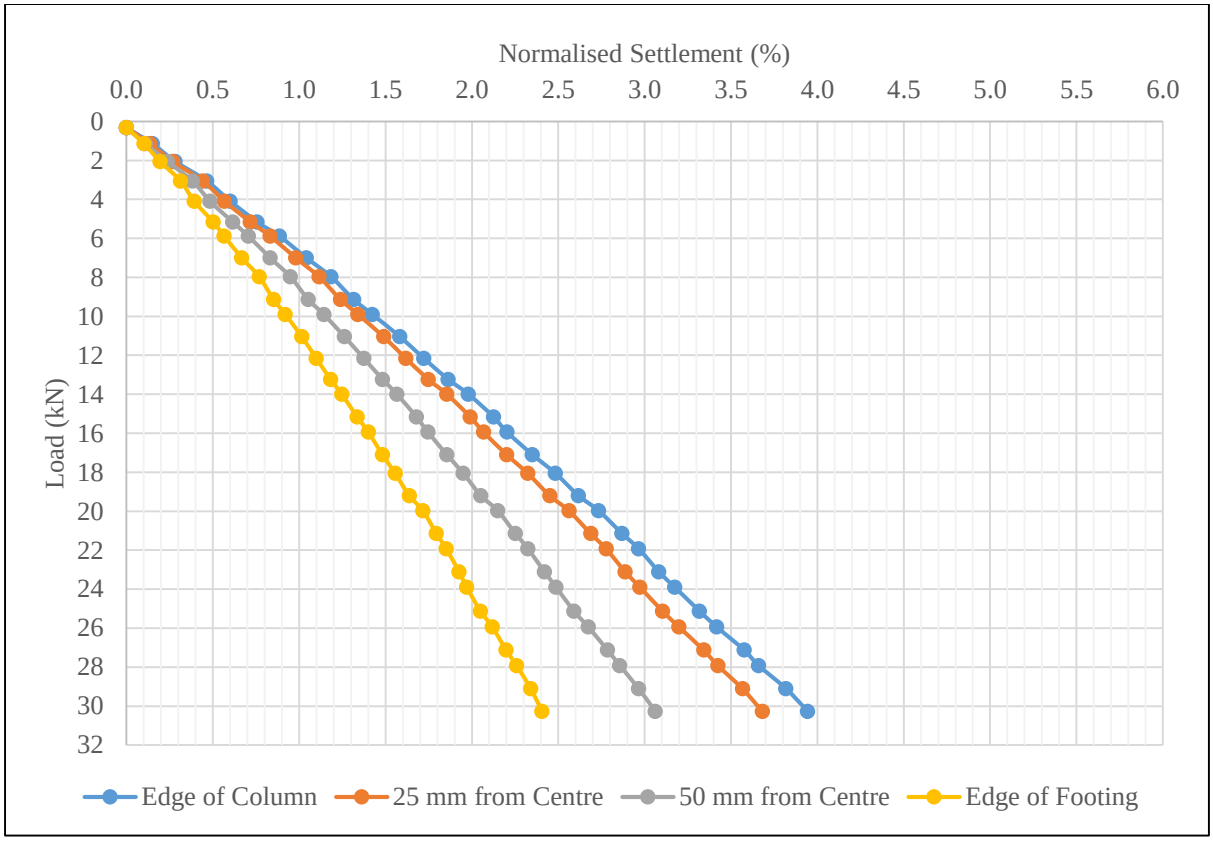

Figure 4-10 Normalised settlement of 6.7 mm aluminium footing during experiment

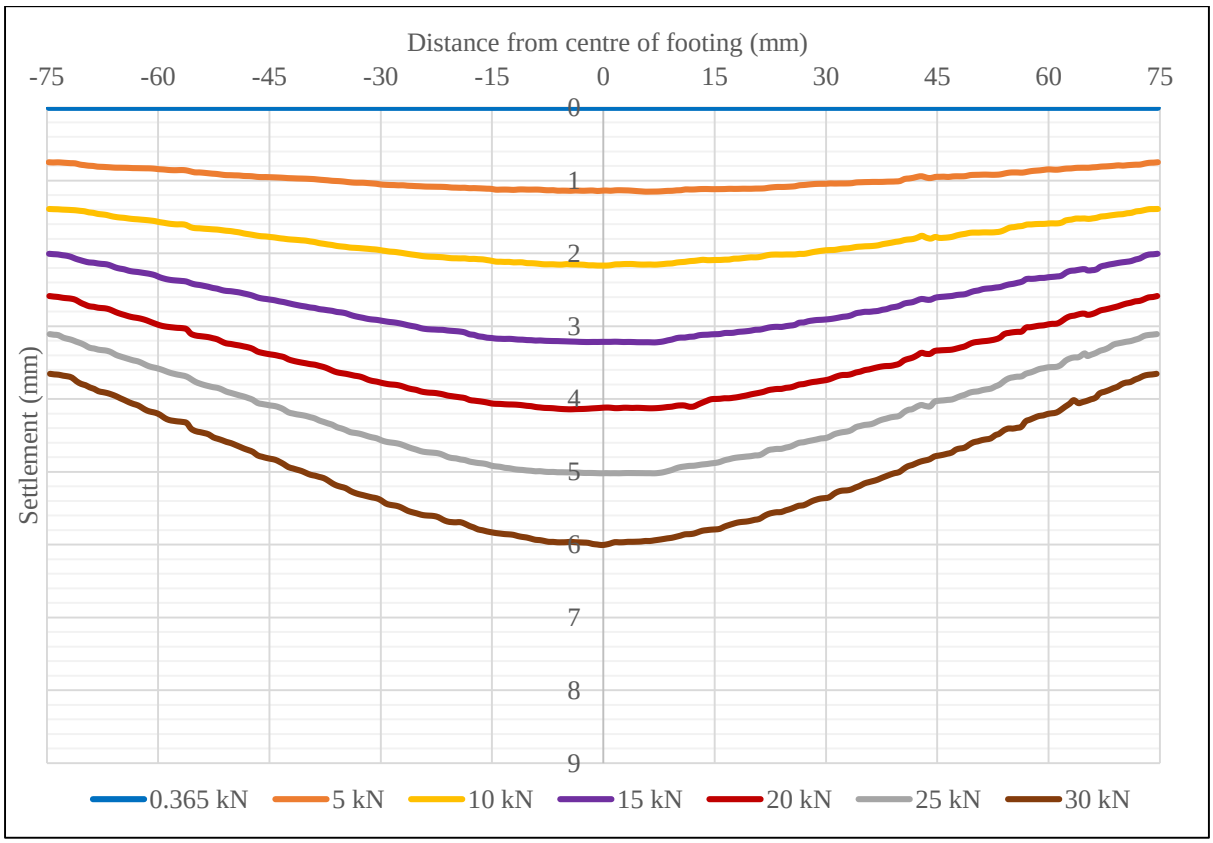

Figure 4-11 Deflected shapes of 6.7mm aluminium footing at 5 kN intervals

© University of Pretoria

4.3.5 3 mm Aluminium Footing

The 3 mm aluminium footing was the thinnest one considered in this experiment and the only one considered as semi-flexible. The footing had a K_s value of 0.0011, which is very far from the boundary of being considered semi-stiff (Arnold et al., 2010). The very small thickness of the footing created a problem in using PIV software. When a force is applied to the footing, it could easily be pressed into the sand mass, resulting in loss of visibility of the footing. The thickness of the footing also made it difficult to add enough texture for accurate PIV analysis. To compensate for this, small pieces of rubber were glued to the base top on which texture was sprayed. The rubber provided no strength to the footing and was spaced far enough apart to avoid them pushing against each other and altering the results. An image of the footing with the rubber after the test was conducted is shown in Figure 4-12.

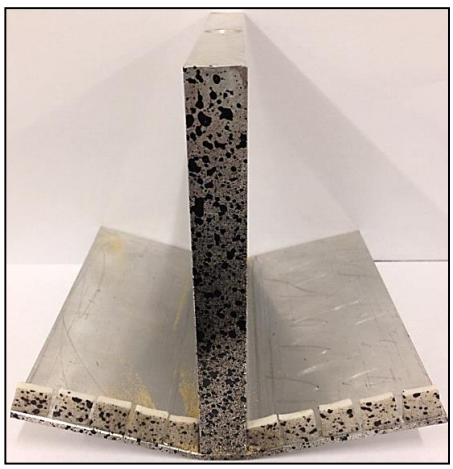

Figure 4-12 Permanently deformed 3 mm aluminium footing after experiment

As shown in the graphical presentation of the normalised settlement data in Figure 4-13, the footing started to curve from the onset of load application. Due to the high flexibility of the footing, a certain point was reached where the edges of the footing experienced negative settlement (uplift) as a result of the load applied on the footing. The entire footing was pushed down into the sand up until a load of 8 kN (increase in normalised settlement across the entire footing), where after the edge of the footing started to lift up. At this point, the aluminium base at the edge of the footing started to curve upwards at a faster rate than what the centre was being pushed down by the applied load. At a load of 14 kN, a slope change developed at the column edge due to yielding of the aluminium. The negative relative deflection shown in the figure indicates that the edge of the footing was higher than when the load application commenced. The load could not be increased beyond 15 kN for this experiment due to failure of the footing. The deflected shapes of the 3 mm aluminium footing are shown in Figure 4-14 and gives a good indication of the extent of footing deformation. Due to yielding of the aluminium, the footing never recovered to its initial position as is indicated in Figure 4-12.

© University of Pretoria

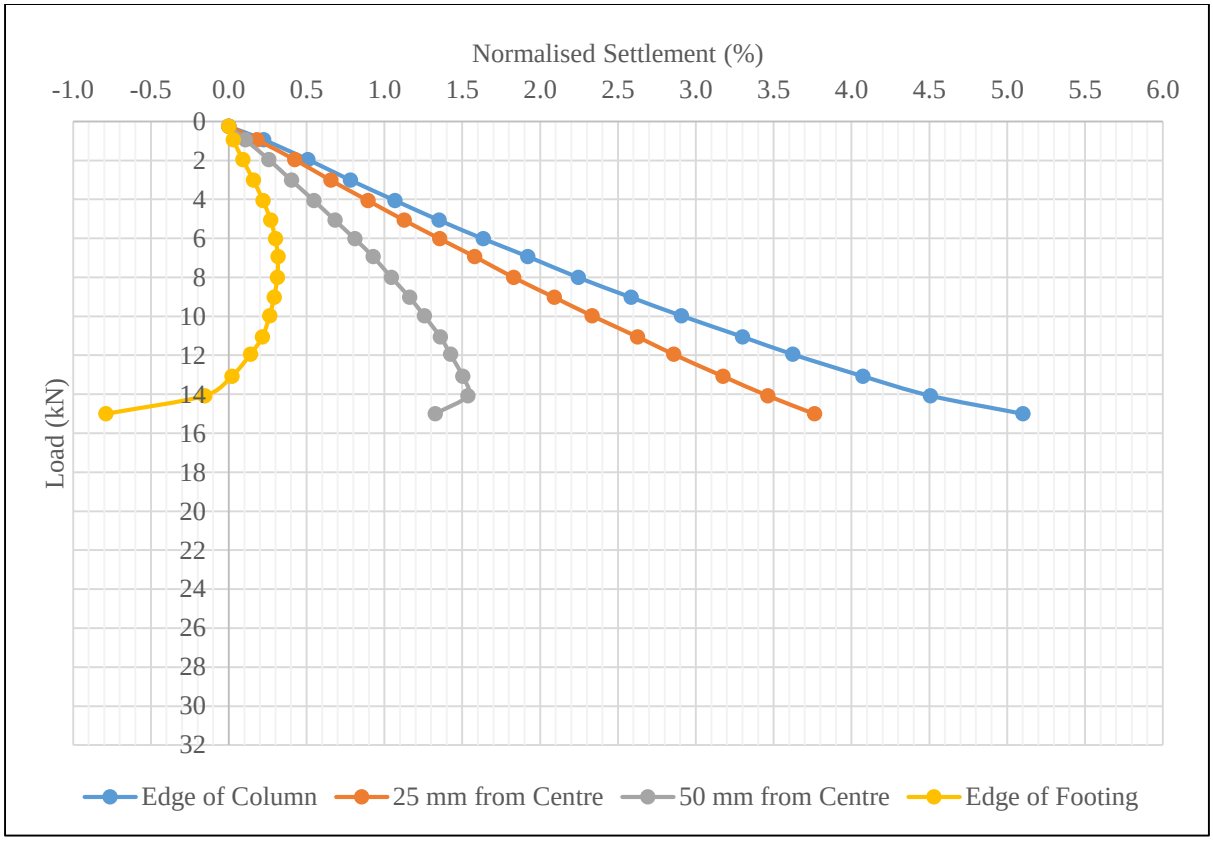

Figure 4-13 Settlement of 3 mm aluminium footing during experiment

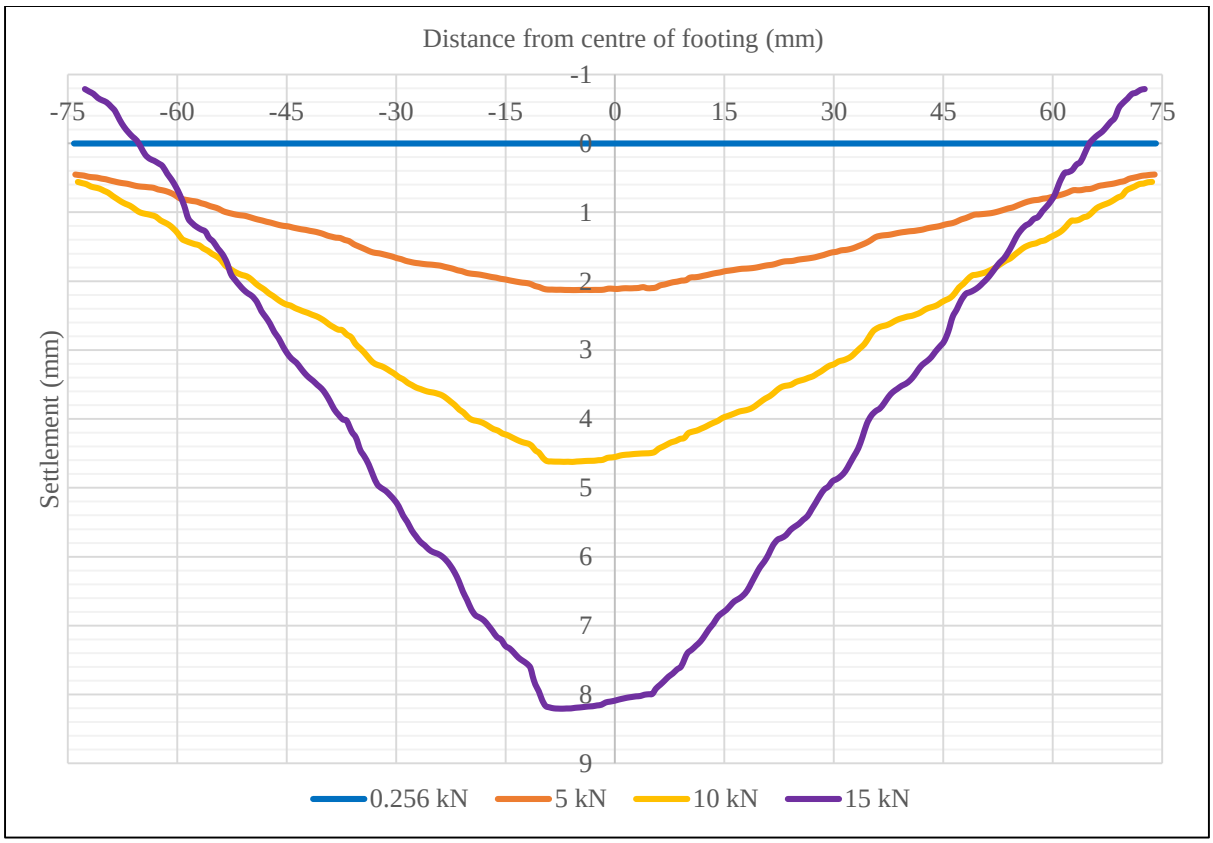

Figure 4-14 Deflected shapes of 3mm aluminium footing at 5 kN intervals

© University of Pretoria

To determine whether the footing experienced yielding during load application, Equation 4-2 (Hibbeler, 2008) was used to calculate the moment required to cause the footing to yield.

$$\sigma = \frac{My}{I} \qquad \text{(Equation 4-2)}$$

Where:

σ = Normal stress
y = Distance to neutral axis of footing
I = Inertia around neutral axis through width of footing

By determining the inertia and the neutral axis of the footing, and using the tensile yield stress of aluminium indicated in Table 3-4, it was determined that the footing would yield at a moment of 62 500 N.mm. By assuming a uniform pressure distribution beneath the entire footing, the distributed load from the sand was determined as 100 N/mm when 15 kN was applied to the footing (15 kN over a length of 150 mm), which causes a moment of 224 450 N.mm at the edge of the column. If the pressure distribution was uniform beneath the footing, the footing would yield at an applied load of 4.18 kN, therefore the footing yielded under the applied load of 15 kN. With the same procedure it was found that the 6.7 mm aluminium footing would yield at an applied moment of 336 675 N.mm. This is further discussed in Section 4.4.4. The thickness of the other aluminium footings ensured that failure did not occur.

The maximum difference in normalised settlement between the edge of the column and the edge of the footing is 5.91%. It is clear that the behaviour of this footing does not represent the behaviour of a reinforced concrete footing, as the ductility of the aluminium allowed excessive deflections. It is also evident that an increase in the flexibility does not always deliver better load-bearing capacity of the system, as proposed by Leshchinsky and Marcozzi (1990), because the footing might fail early, preventing the full bearing capacity of the foundation system to be utilised had it been stiffer. However, the other footings which also exhibited flexural behaviour were not all loaded until failure occurred, therefore no conclusive findings could be made regarding the increased bearing capacity of the foundation system with a reduction in the footing stiffness. It is clear from the data that the use of a semi-flexible footing should be done with caution, as the settlement and curvature thereof is excessive.

After discussing the settlement and deflection data of the aluminium footings individually, the information is combined in the next section to determine the effect of footing stiffness on settlement and deflection behaviour.

© University of Pretoria

4.3.6 Settlement and Deflection Behaviour of Aluminium Footings

To determine the effect of footing stiffness on the behaviour of the foundation, similar soil properties were required in every test, thus ensuring that the stiffness of the footings was the only variable. Although this was not achieved for all the tests, due to some variation in the soil density, the results still provide a trend to determine the effect of the footing stiffness on the settlement and deflection behaviour. The normalised settlement of all the aluminium footings, the normalised settlement as a function of the footing stiffness, as well as the combined deflected shapes of the aluminium footings are discussed in this section.

(a) Normalised Settlement of Aluminium Footings

The normalised settlements at the edge of the column and at the edge of the footing for all the aluminium footings are discussed in this section. At the edge of the column, the normalised settlement increased for all the footings with an increase in the load applied, as illustrated in Figure 4-15. In the figure it seems as if there are three clear bands of settlement increase. The data from the 10 mm aluminium footing does not correlate with the trend due to the low relative density of the sand in this experiment, but it can be seen that at a 1 kN load the settlement of the 10 mm footing is greater than all the other footings. If this is taken into account, then the rate of normalised settlement increase (slope of the line) is slightly less for the 10 mm footing compared to the 6.7 mm footing. It is clear in the figure that the normalised settlements of the flexible footings are larger than that of the stiff footings at the edge of the column.

From the figure it appears as if the normalised settlement of the 16 mm footing is equal to that of the stiff footings, but this is only true at the edge of the column due to the fact that the 16 mm footing did experience slight deflection when large loads were applied to it. The normalised settlement of the stiff footings also appear to increase linearly with an increase in applied load, justifying the method used to determine a representative secant Young's modulus of the sand by using the settlement data of the stiff footings. The data presented in the figure illustrates that the settlement performance of an already stiff footing does not improve when its thickness is increased further and that there is a thickness where after the settlement performance of the footing remains constant. This is discussed in more detail in Section 4.3.6 (b).

© University of Pretoria

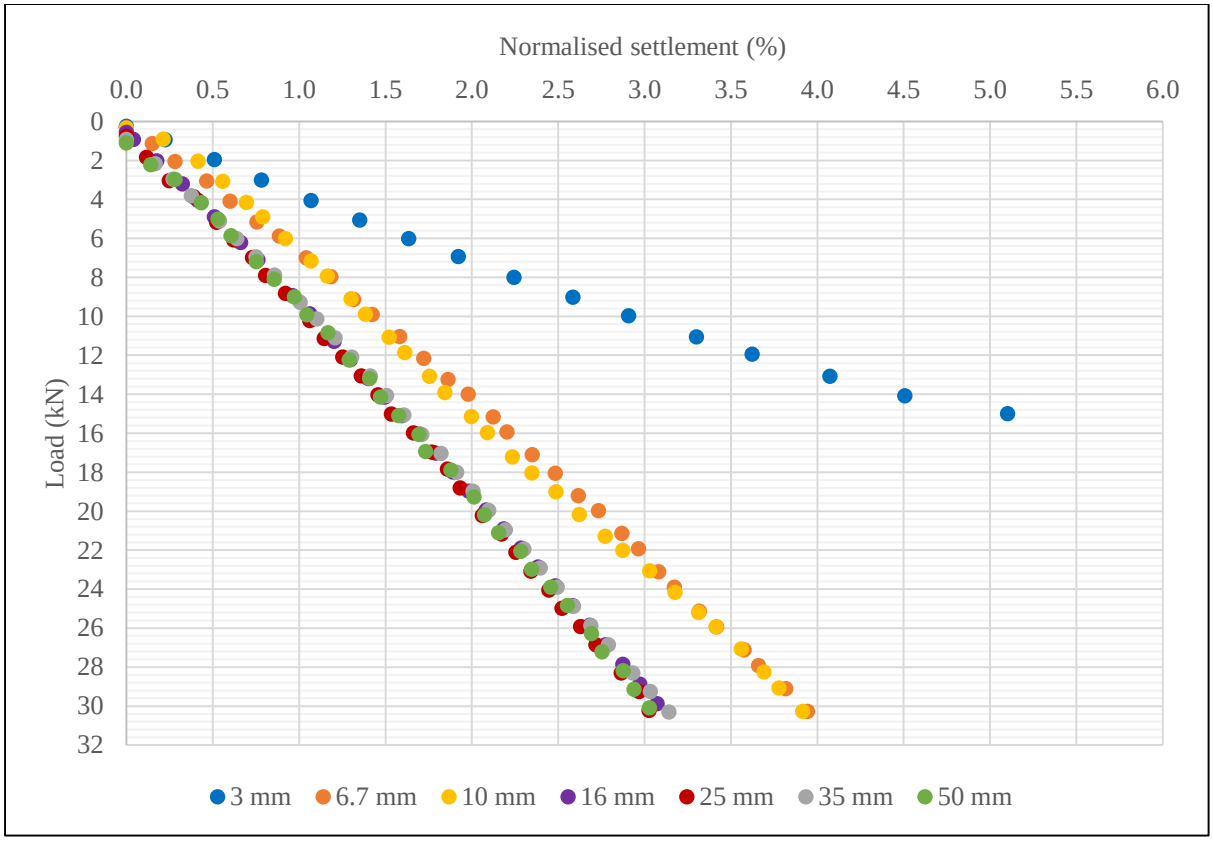

Figure 4-15 Normalised settlement of aluminium footings at edge of the column

When considering the edge of the footing, trends in the normalised settlement data is the reverse of the settlement data from the edge of the column, as indicated in Figure 4-16. At the edge of the footing, the normalised settlement of the stiff footings are the largest and that of the flexible footings are the lowest (the 10 mm footing settles more as discussed earlier). This is due to the flexibility of the thin footings, causing the edges thereof to curve upwards and reduce the normalised settlement at that point.

There is a definite difference in the behaviour of flexible and stiff footings. From the data a trend for the deflection characteristics on approximately the same sand can be seen. The relative deflection as a function of the stiffness (EI) of the footings is discussed in the next section.

© University of Pretoria

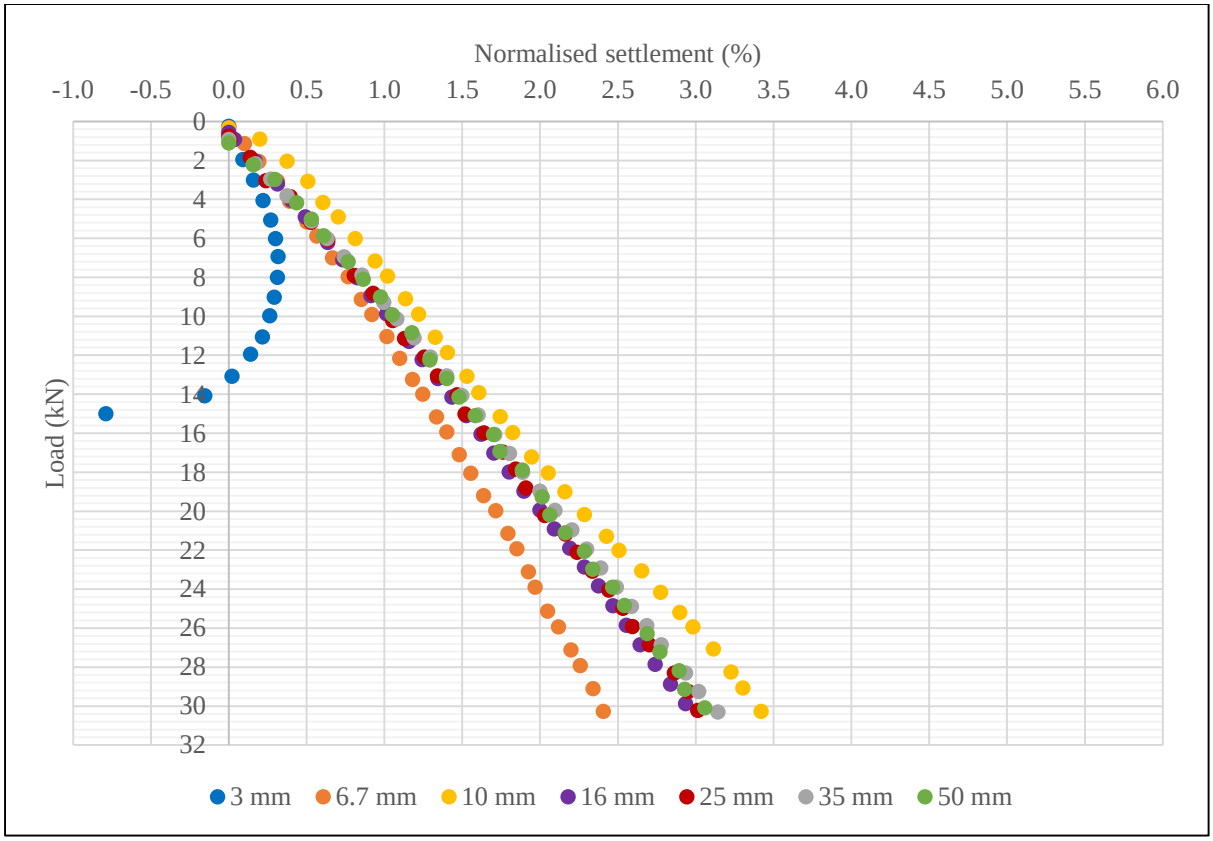

Figure 4-16 Normalised settlement of aluminium footings at edge of footing

(b) Relative Deflection as a Function of Footing Stiffness

The main objective of this study is to determine the effect of the footing stiffness on the settlement, deformation and contact stress distribution beneath a footing. In this section the normalised settlement of the footings are illustrated as a function of footing stiffness (EI). The normalised settlement of the footings as a function of the stiffness of the footings are shown in Figure 4-17 to Figure 4-20. The figures are divided into the points on the footings that were analysed individually, namely the edge of the column (Figure 4-17), 25 mm from the centre of the column (Figure 4-18), 50 mm from the centre of the column (Figure 4-19) and finally the edge of the footing (Figure 4-20). The stiffness's used in the graphs are that of the model footing and not the prototype footing. The stiffness values are presented on a log scale due to the large range of the values.

© University of Pretoria

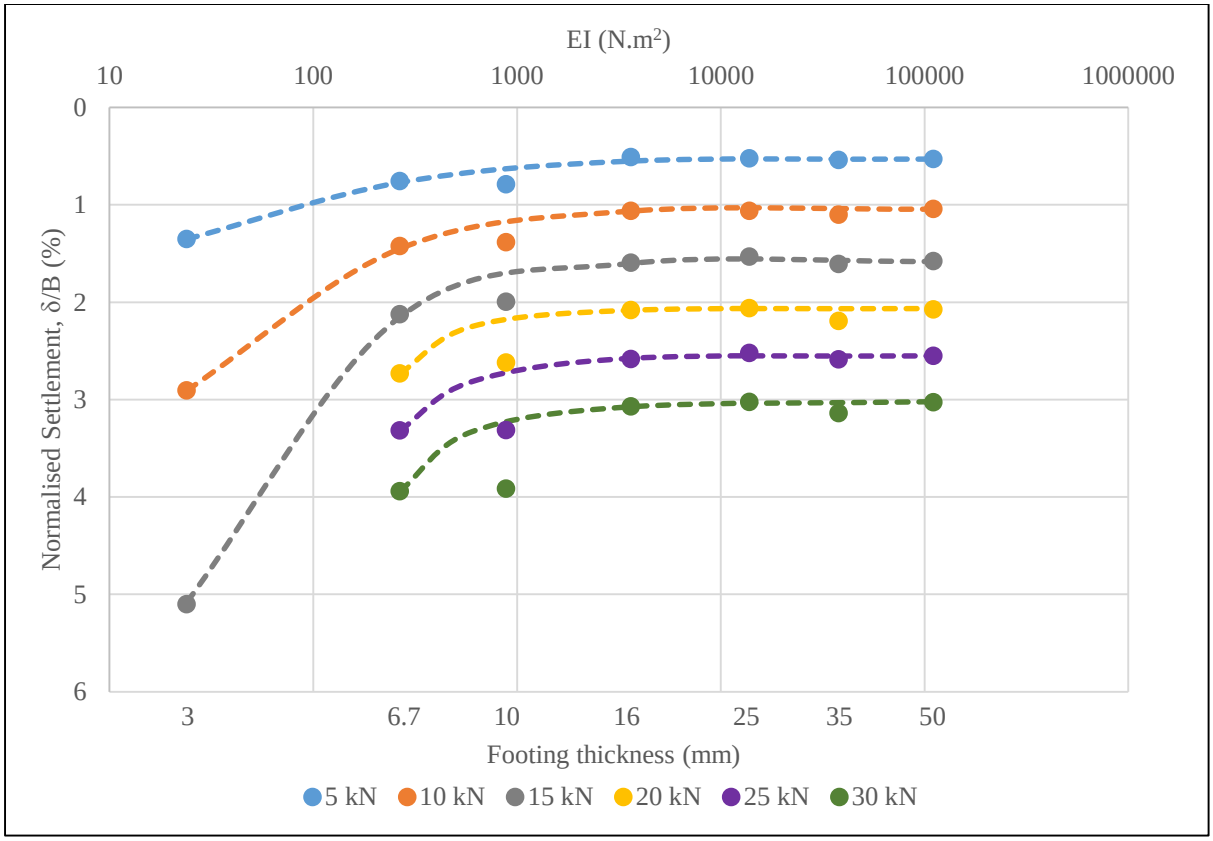

Figure 4-17 Influence of the footing stiffness on the settlement behaviour at the edge of column

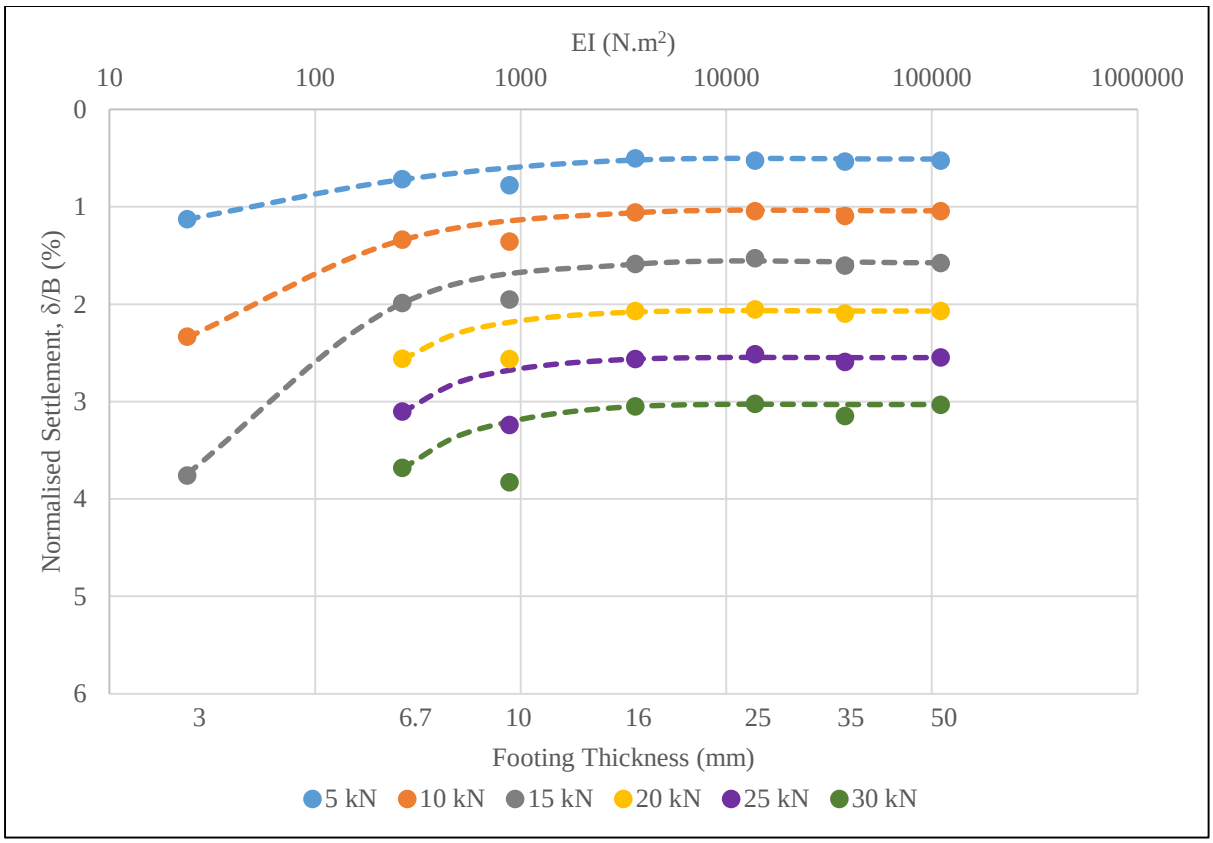

Figure 4-18 Influence of the footing stiffness on the settlement behaviour 25 mm from the centre of the column

© University of Pretoria

The normalised settlements shown in Figure 4-17 are from all the aluminium footings tested. The normalised settlement of the 10 mm aluminium footing is larger than expected due to the lower relative density of the soil. However, the trend of the normalised settlement is still clearly visible in the figure. The data beyond 15 kN does not include the 3 mm footing, as the footing could not be loaded beyond that point.

It is evident from Figure 4-17 that the stiffness of the footing does play a very important role in determining the footing settlement. When the stiffness of a footing is increased beyond a certain critical value, the settlement behaviour becomes almost identical, as is clear for the normalised settlement of the 16 mm footing and thicker in the figure (stiffness of 3 625 N.m^2 at model scale).

Figure 4-18 represents the normalised settlement 25 mm away for the centre of the column. The same trend is followed as the edge of column data, but the difference in normalised settlement between the very thin footings and the very thick footings reduces considerably. This is due to the upward curvature action of the flexible footings, which reduces the normalised settlement considerably compared to the edge of the column settlement. Figure 4-19 represents the deflection data 50 mm away from the centre of the column. The normalised settlement at this section is almost constant regardless of the thickness of the footing. This is discussed further in Section 4.3.6 (c).

Figure 4-20 represents the deflection data at the edge of the footing. The deflection of the 3 mm aluminium footing did not increase when the load was increased from 5 kN to 10 kN, indicating that the footing's upward curvature occurred at the same rate as the settlement of the footing. At a load of 15 kN, the edge of the 3 mm footing was no longer in contact with the sand surface, due to the excessive curvature of the footing. The negative value indicated for the 3 mm aluminium footing is due to the excessive curvature of the footing, causing the edge of the footing ending at a higher position that what the footing initially started on. The occurrence of this in practise is highly unlikely.

© University of Pretoria

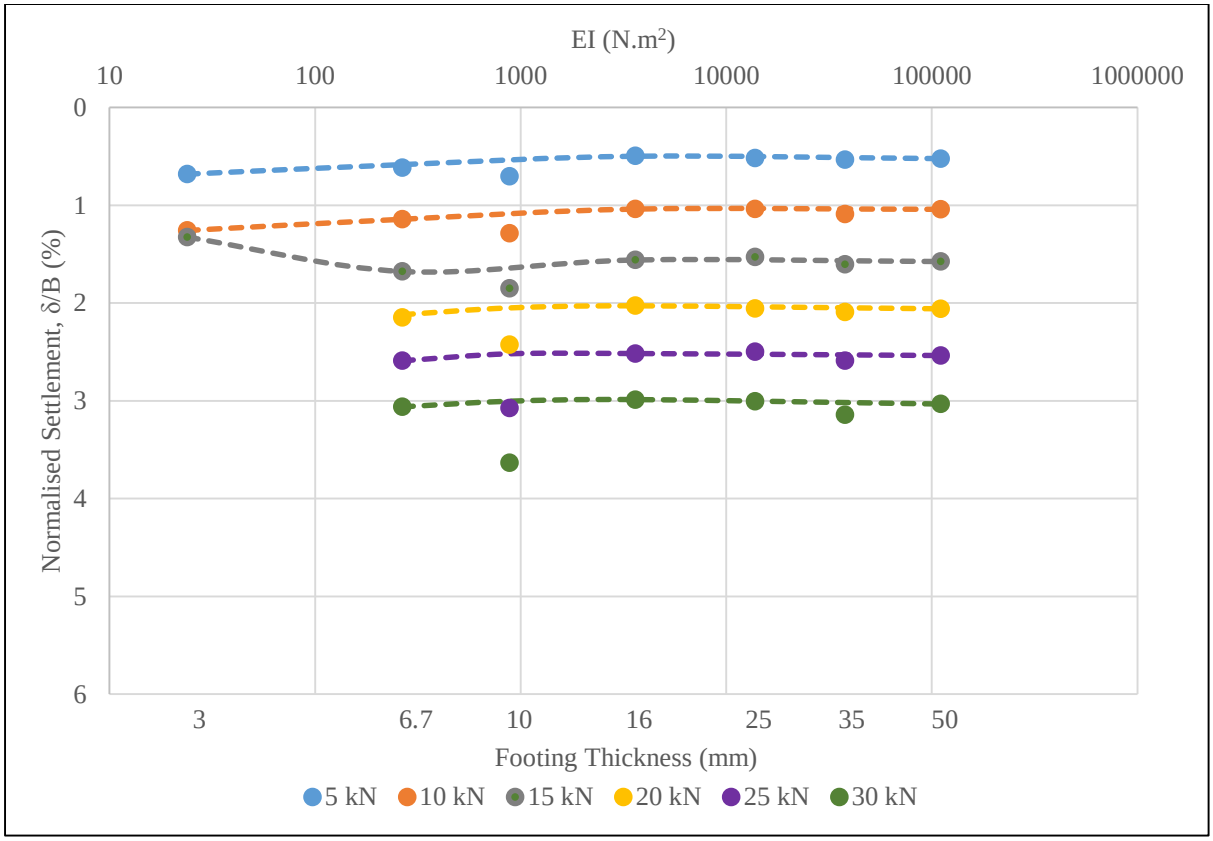

Figure 4-19 Influence of the footing stiffness on the settlement behaviour 50 mm from the centre of the column

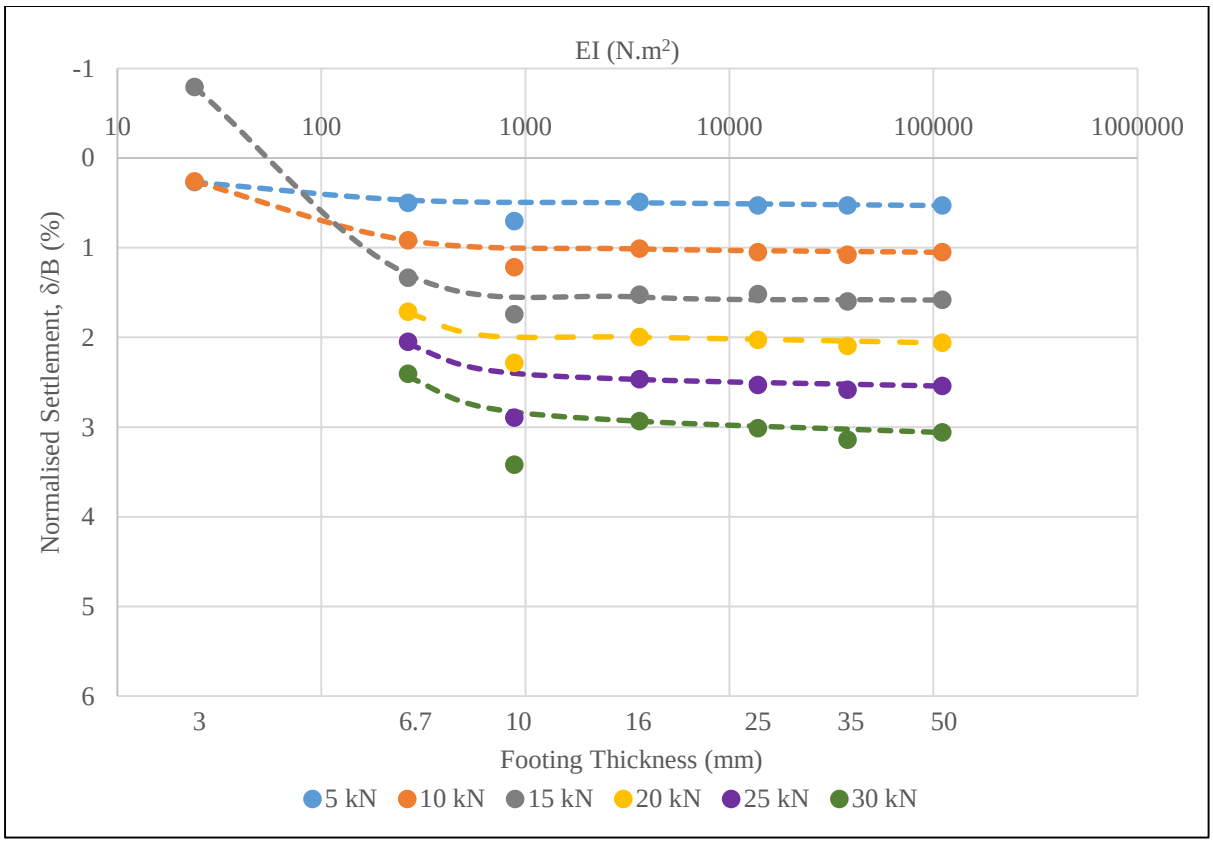

Figure 4-20 Influence of the footing stiffness on the settlement behaviour at the edge of the footing

© University of Pretoria

As soon as the stiffness of the footings reach a certain value (classified as stiff), the behaviour of the footings are more predictable than for a flexible footing. Although the results shown in the figures are only applicable to Cullinan sand at a relative density of approximately 70%, the results discussed in this section indicate that it would be possible to predict the normalised settlement of a footing if the stiffness of the footing and the load applied to the footing is known. Further research needs to be conducted on sand with other relative densities.

(c) Deflected Shape Comparison for Aluminium Footings

In Figure 4-21, the deflected shapes of all the aluminium footings at 10 kN and 25 kN are superimposed. It appears as if there is no change in the settlement of the footings at an offset of approximately 50 mm from the centre of the column regardless of the stiffness of the footing and it is clear that there is a specific distance away from the centre of the footing where the settlements are the same regardless of their deflected shapes. This is evident for all the loads analysed in this study. For this experiment, the common deflection point was at 54 mm from the centre of the footing, but this could be influenced by the variable secant Young's modulus and subsequent settlement of the sand on which the footings were tested. It appears that a common settlement occurs, approximately two-thirds away from the centre of the column, regardless of the stiffness of the footing. Therefore, the settlement of any footing can be calculated at this point, regardless of the stiffness thereof. For a stiff footing, the settlement is constant across the entire width of the footing, whereas the settlement of the centre of the footing would be more than the settlement calculated at this point and less at the edge of the footing for more flexible footings. The extent of the increase and decrease in settlement of a flexible footing is dependent on the stiffness of the footing and the underlying soil. This may be used as a simple method for an initial prediction of the shape of a footing during loading. However, more tests should be conducted to confirm whether this is a general trend for soil of different stiffness's.

© University of Pretoria

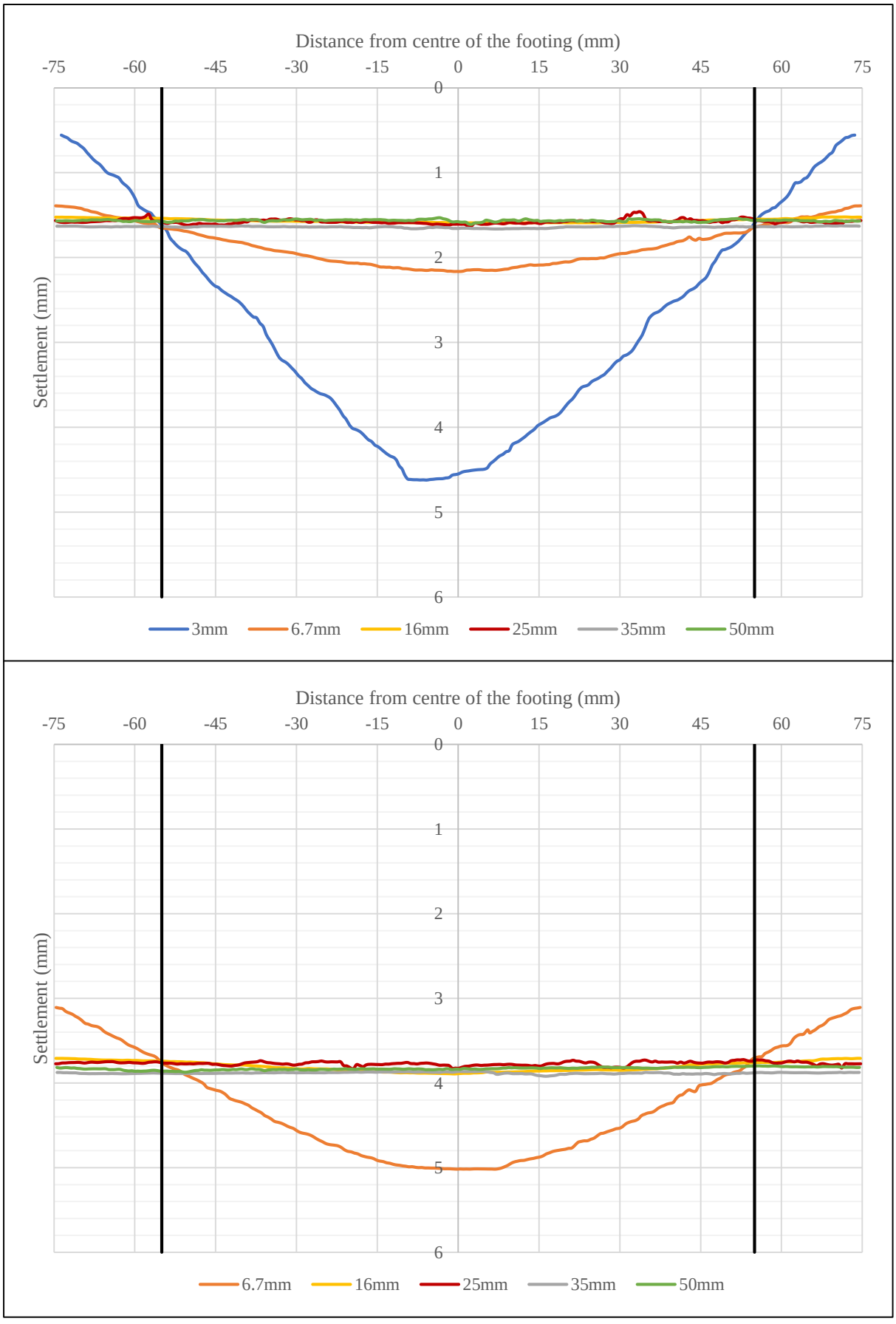

Figure 4-21 Determining common deflection point between deflected shapes (10 kN at the top and 25 kN at the bottom)

© University of Pretoria

4.4 Stress Distribution beneath Aluminium Footings

The contact stress distribution beneath a footing plays an important role in the settlement and deflection behaviour of the footing. The contact stress distribution was measured at the soil-structure interface with the Tekscan™ system, as indicated in Section 3.5.4. A number of Tekscan™ sensors were used during the course of the experiment due to damage to the sensors in certain tests. Each sensor was calibrated against the applied load, which was continuously measured with a load cell. The calibration of each sensor revealed that the calibration coefficient of the sensors varied for each test. An example of the calibration coefficients determined for some of the stiff footings are shown in Figure 4-22. As seen in the figure, the calibration coefficient is neither constant nor a linear function of the applied load. The values are also different for each test and certain calibration factors at high loads (> 25 kN) could not be accurately determined as the sensels (individual sensor of Tekscan™ pressure sensor) exceeded their maximum capacity in certain tests.

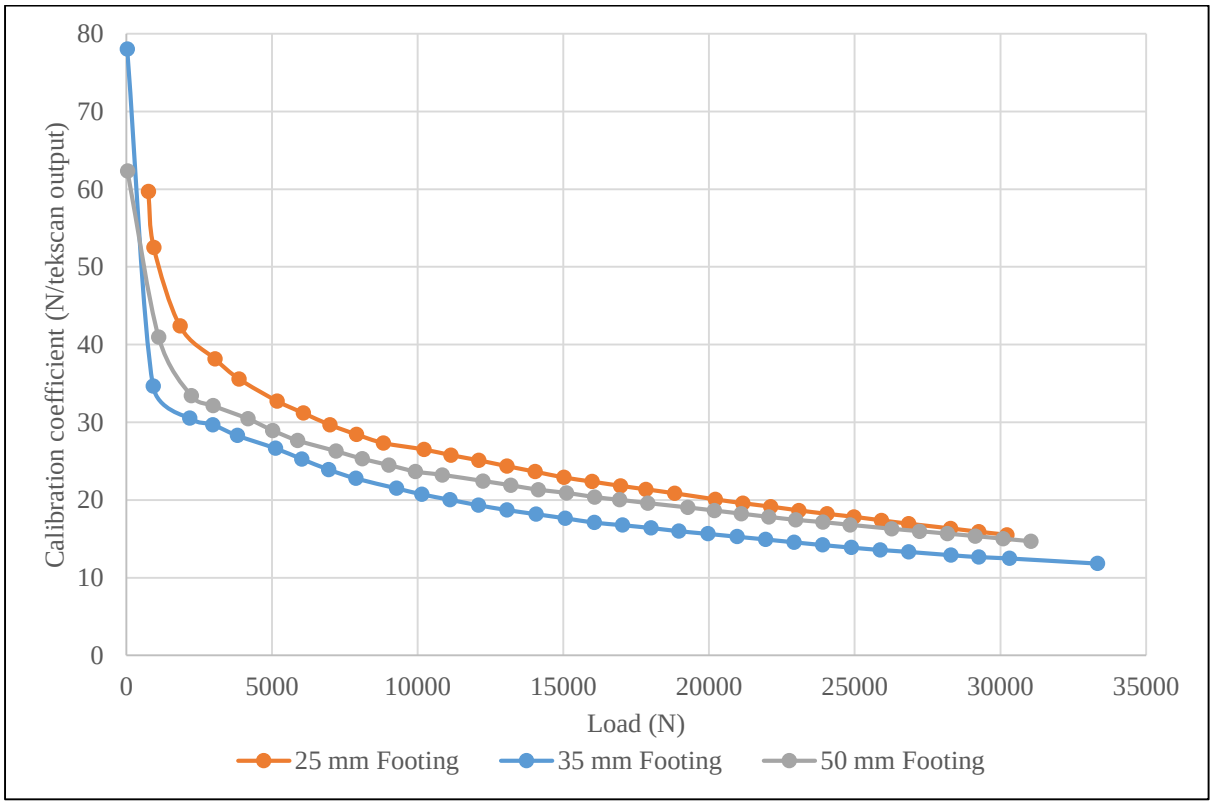

Figure 4-22 Calibration value for Tekscan™ pressure sensor

Due to difficulties in calibrating the pressure mats, it was decided to use the raw output values (ranging from 0 to 255) of the Tekscan™ sensor to determine trends in the pressure distribution beneath the footing, and not to assign actual pressure values to the output data as the accuracy of these values could not be confirmed. Therefore, only qualitative observations are presented in this section.

© University of Pretoria

As mentioned in the experimental setup, pressure data was captured with the Tekscan™ sensor by arranging sensels (the equivalent of pixels) in a matrix of columns and rows. The location of the sensor beneath the footing as well as the orientation of the rows and columns of the sensor is illustrated in Figure 4-23. By arranging the sensels of the sensor in a matrix of rows and columns, a 3D grid of pressure distribution beneath the footing could be measured and used for analysis.

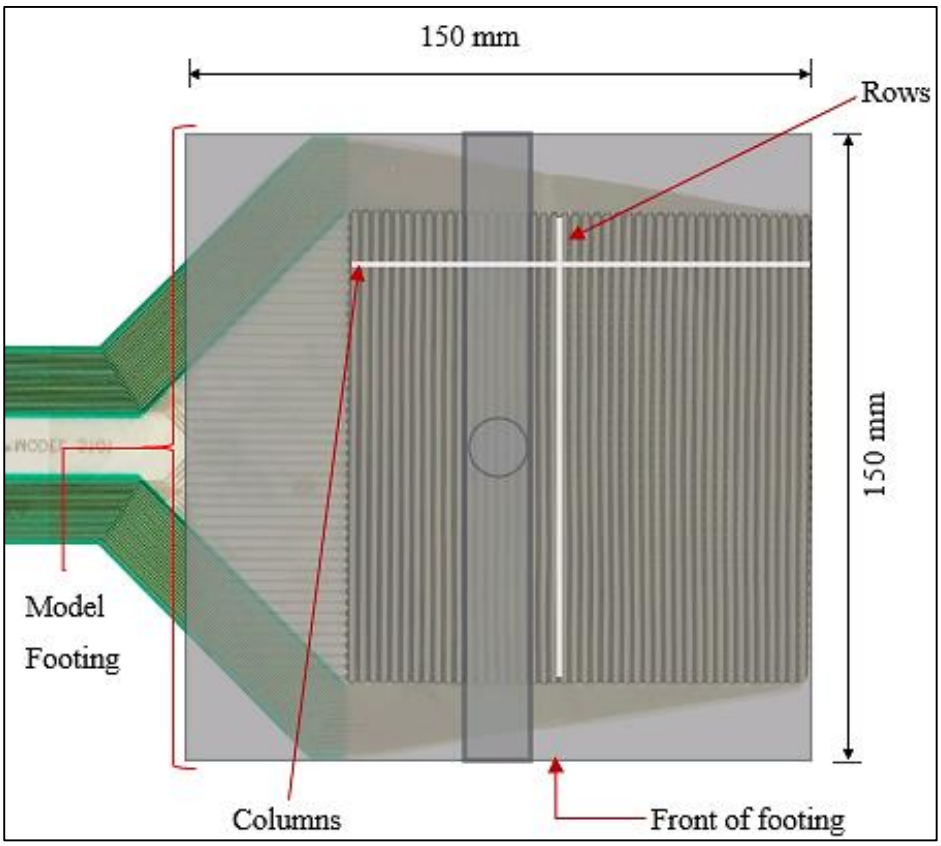

Figure 4-23 Location of rows and columns of Tekscan™ sensor beneath footings

To obtain plane-strain data from the Tekscan™ sensor, the average output of each column and row was calculated. The average row data represented the width of the footing, from the front to the back, while average column data represented the length of the footing, from left to right, as illustrated in Figure 4-23. The sensel spacing is 2.54 mm. Due to slight experimental differences, the pressure sensor was not located at exactly the same location with respect to the footing in each experiment. However, the differences between tests were less than 1% of the width of the footing.

In order for the plane-strain assumption to hold true, the data obtained from the sensel columns of the pressure sensor needed to show qualitatively the same pressure distribution beneath the footing from the front to the back. The contact stress distribution from the front to the back of the footing is not used, as they should be identical.

© University of Pretoria

The data obtained by analysing the sensel rows of the sensor is used to determine the contact stress distribution from left to right of the footing and is discussed in this section. It is clear from Figure 4-23 that the sensor did not cover the entire width of the footing, therefore only one side of the footing is analysed, based on the assumption that the other side experiences the same pressure distribution due to symmetry in the testing conditions.

4.4.1 Stiff Aluminium Footing

The results for the stiff aluminium footings (apart from the 16 mm footing) are combined for this analysis, due to the same reasons discussed for the settlement data. Therefore, the contact stress distribution at the soil-structure interface were similar for all the stiff footings apart from the 16 mm footing (discussed individually in Section 4.4.2). The contact stress distribution beneath one of the stiff footings is illustrated as representative of all the stiff footings. The contact stress distribution of the other stiff footings can be found in Appendix F.

The arrangement of the sensels in a matrix of rows and columns allow the sensor to construct a 3D image of the contact stress distribution beneath the footing. An example of the 3D contact stress distribution is illustrated in Figure 4-24. The orientation with which the 3D contact stress distribution for each footing is illustrated, is demonstrated in the figure.

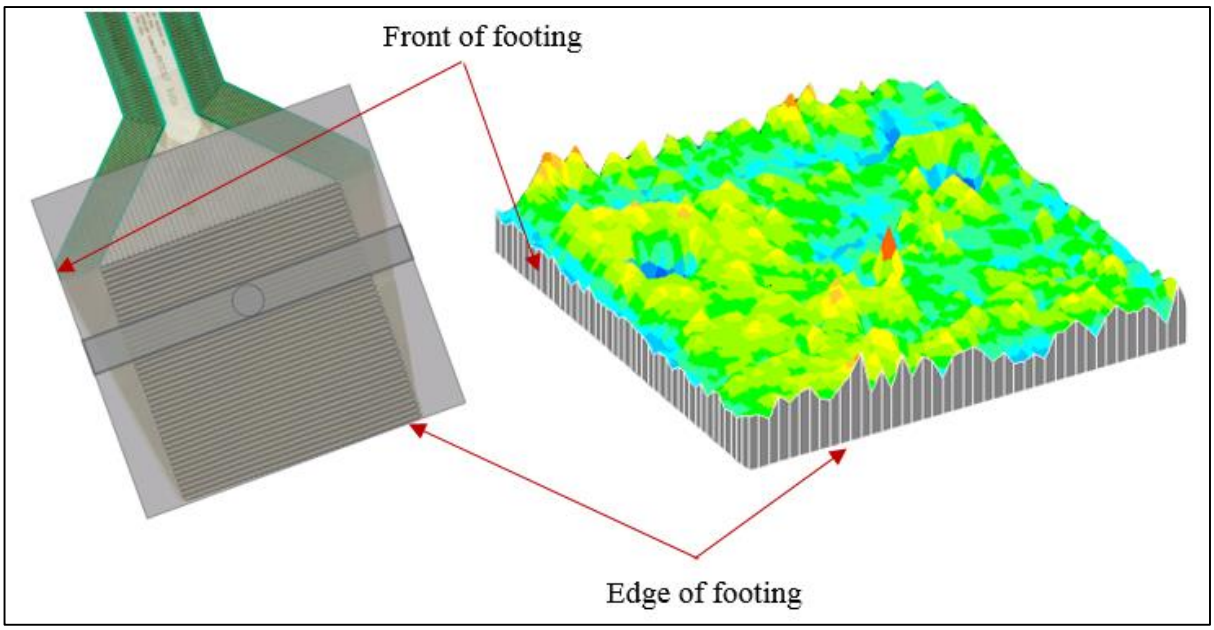

Figure 4-24 Orientation of 3D contact stress distribution data

© University of Pretoria

The 3D contact stress distribution beneath the 25 mm aluminium footing is shown in Figure 4-25. The initial load, approximately one third of the maximum and two thirds of the maximum load applied to each footing is shown in the figure, illustrating the 3D contact stress distribution beneath the footing. The contact stress distribution at maximum load cannot be illustrated for all the footings as the sensor exceeded its capacity at certain sensels when the maximum load was applied.

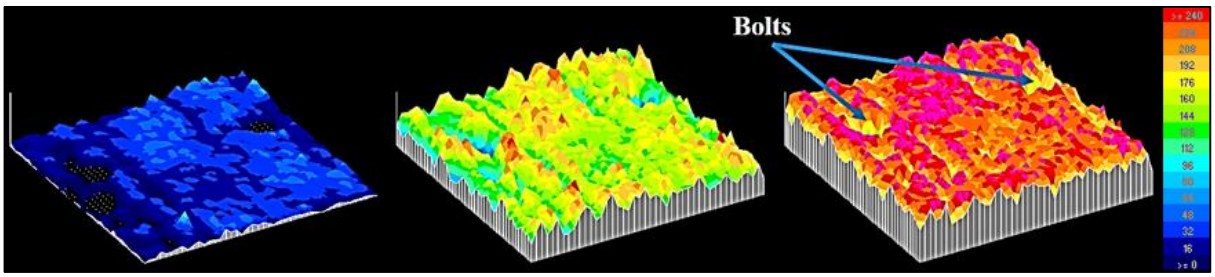

Figure 4-25 Three dimensional representation of stress distribution beneath 25 mm footing (Left: 0.756 kN; Middle: 10 kN; Right: 20 kN)

The Tekscan™ software represents low pressure as black, with an increase in the pressure indicated as blue, then green, then yellow, then red and finally pink when the pressure capacity has been exceeded. A colour scale is shown in Figure 4-25, representing the raw Tekscan™ data (this is shown in each figure regarding the 3D contact stress). It is clear that the distribution was predominantly uniform across the entire footing, with a few stress concentrations visible in each segment shown in the figure. These stress concentrations at individual sensels are the result of the sand particle distribution beneath the footing affecting the contact surface between the footing and the sensor.

With the construction of the aluminium footings, the column had to be bolted onto the footing. Although the bolts were machined to be flush with the footing, contact stress variations are still present in the area of the bolts, indicated for the 20 kN load shown in Figure 4-25. These bolts cause slight variations in the contact stress distribution at their specific location, therefore the data at these locations were not considered in this analysis.

The analysed contact stress distribution from the Tekscan™ data with increasing load for the 25 mm aluminium footing is represented graphically in Figure 4-26 as an example of the contact stress distribution beneath a stiff footing. The results show that the contact stress distribution is essentially uniform beneath the footing, as was the case with all the stiff footings in this section. The slight contact stress drop for the very last sensel could be due to the sensel losing partial contact with the footing at the edge. The drop in the contact stress close to the centre point of the footing is due to the presence of the column bolts, and will not be considered for the analysis.

© University of Pretoria

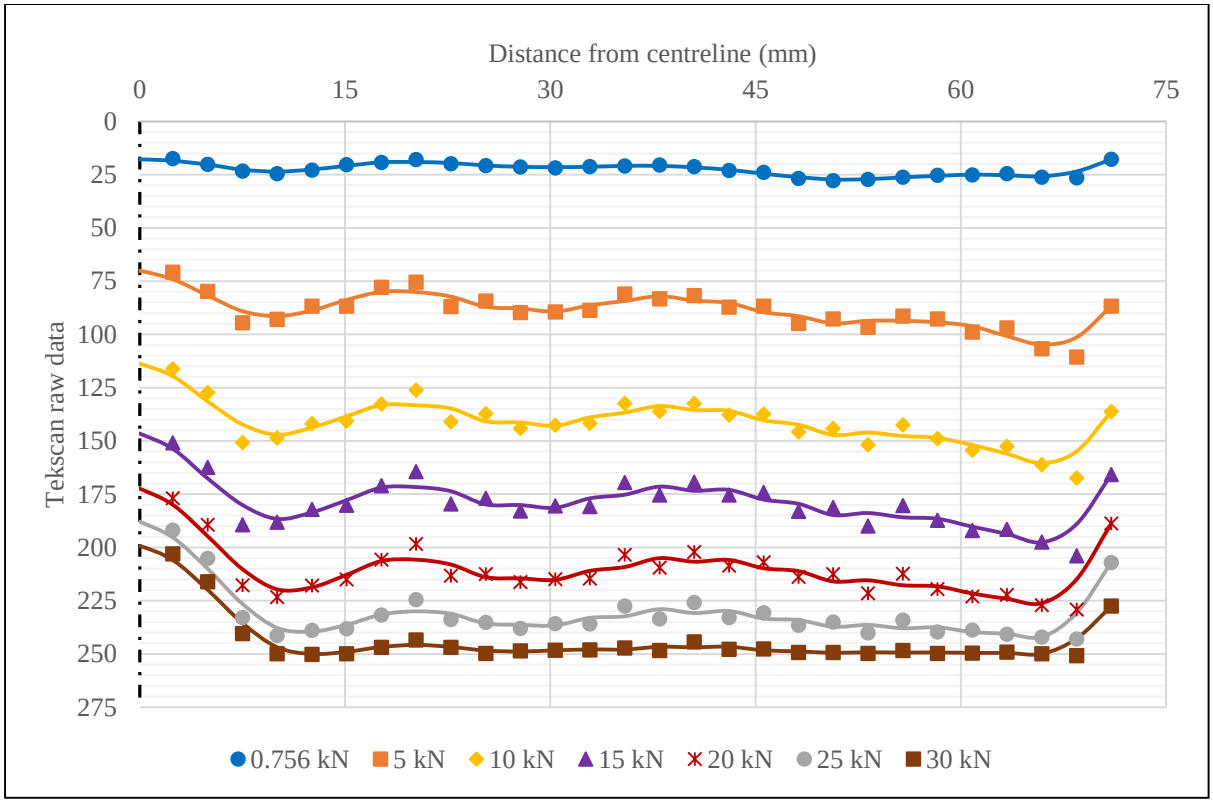

Figure 4-26 Contact stress distribution from Tekscan™ data for 25 mm aluminium footing

4.4.2 16 mm Aluminium Footing

The 16 mm aluminium footing is also considered as stiff (K_s value of 0.1581), and as indicated earlier in Section 4.3.2, the behaviour thereof differed from that of the other stiff footings. The 3D contact stress distribution of the footing is shown in Figure 4-27, indicating a slight tendency of increased contact stress at the column side of the footing when a 10 kN load was applied, illustrated in Figure 4-27. As established in Section 4.3.2, the 16 mm aluminium footing did deflect slightly, which was the cause for the slight contact stress increase over the central part of the footing. The predominantly pink colour visible for the 20 kN load indicates that the applied pressure exceeded the load capacity of the Tekscan™ pressure sensor.

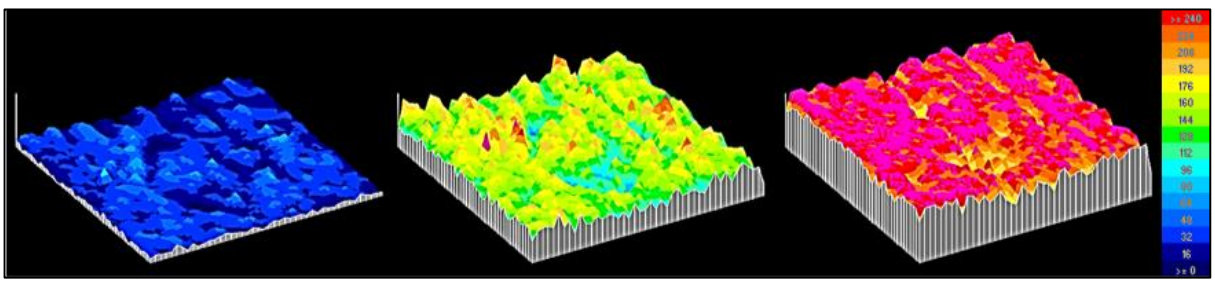

Figure 4-27 Three dimensional representation of stress distribution beneath 16 mm footing (Left: 0.556 kN; Middle: 10 kN; Right: 20 kN)

© University of Pretoria

The analysed contact stress distribution of the footing is shown in Figure 4-28, demonstrating that the contact stress distribution is similar to that of the stiff footings (uniform distribution), although a slight decrease in contact stress at the edge of the footing is visible for larger applied loads. This reduction in contact stress could be due to the curvature of the footing during load application. The slight reduction in contact stress at the edge of the footing indicates that the footing did not exhibit the same behaviour as the other stiff footings. Therefore, the classification of the footing as stiff is not justified and alterations to the classification is required.

The contact stress at 25 kN and 30 kN exceeded the capacity of the sensor and will not be analysed any further, although it can be seen that for 25 kN the contact stress at the edge did not exceed the capacity of the sensor, indicating a lower contact stress compared to the centre of the footing. During load application, the contact stress at the edge of the footing was approximately 85% of the contact stress experienced by the centre of the footing, based on the output readings of the pressure sensor. It appears as if the reduction in the contact stress distribution at the edge of the footing is linked to the deflection of the footing.

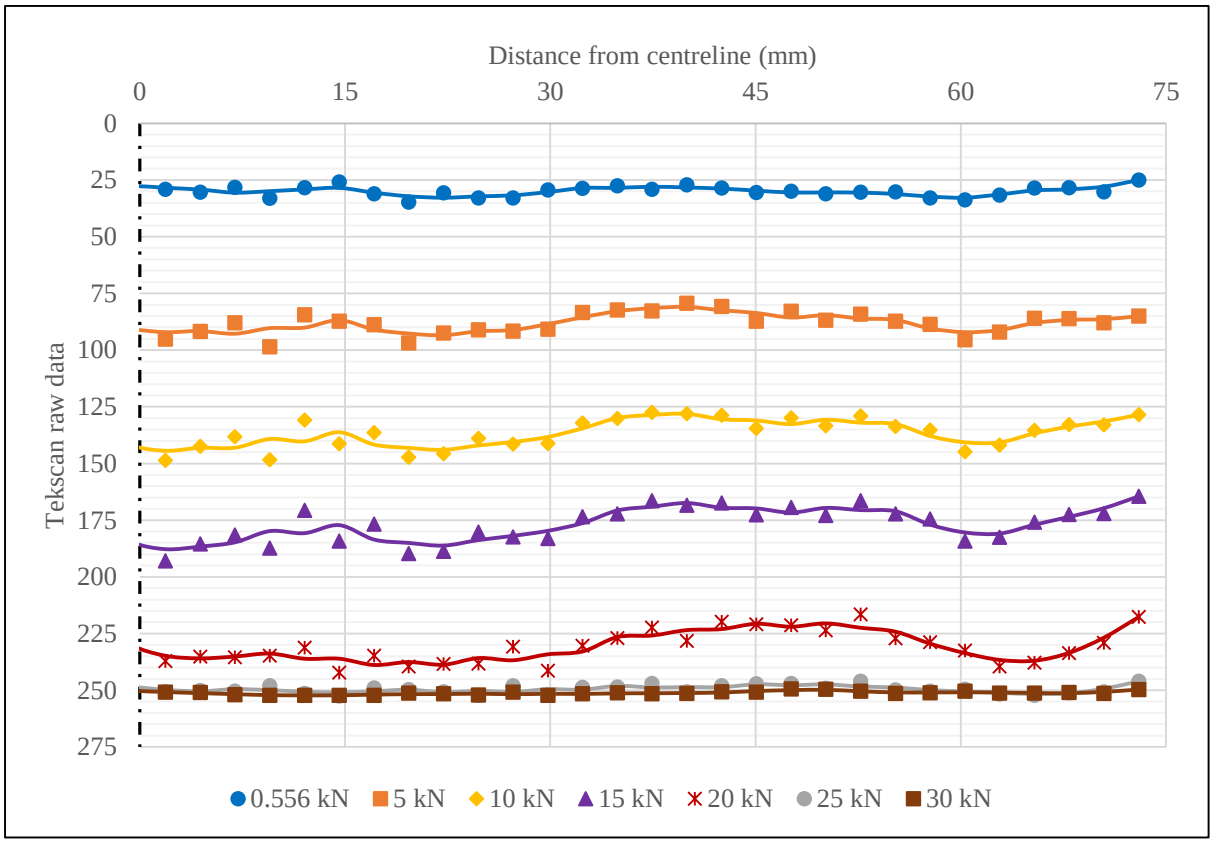

Figure 4-28 Contact stress distribution from Tekscan™ data for 16 mm aluminium footing

© University of Pretoria

4.4.3 10 mm Aluminium Footing

The 10 mm aluminium footing is classified as semi-stiff (K_s value of 0.0448), with the behaviour thereof expected to differ from that of the stiff footings as discussed in Section 4.3.3. The 3D contact stress distribution beneath the footing is shown in Figure 4-29 and it is evident that the contact stress distribution at the edge of the footing is lower at applied loads of 10 kN and 20 kN compared to the central part of the footing.

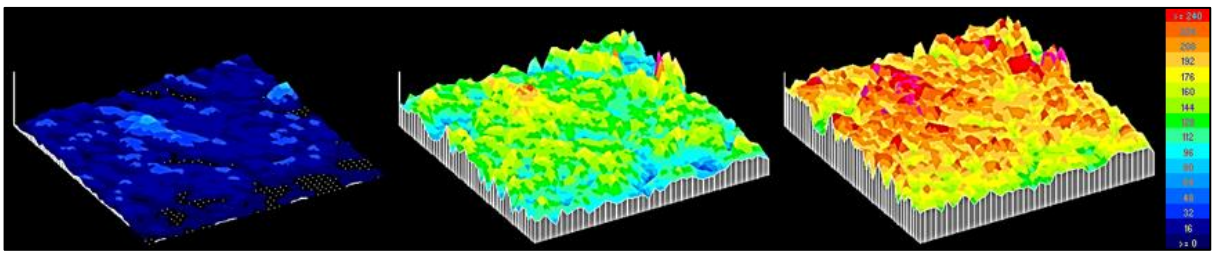

Figure 4-29 Three dimensional representation of stress distribution beneath 10 mm footing (Left: 0.418 kN; Middle: 10 kN; Right: 20 kN)

The analysed contact stress distribution beneath the footing is shown in Figure 4-30, indicating that the contact stress distribution remains relatively constant up to a distance of 50 mm (two thirds the width) away from the centre of the footing. At this point there is a significant drop in the contact stress towards the edge of the footing for larger loads. It is clear in the figure that the contact stress distribution is no longer uniform. The difference in contact stress between the edge of the footing and the central part of the footing increases as the load applied is increased. As it has been established that the curvature of the 10 mm footing increases significantly at larger loads (Section 4.3.3), the drop in contact stress at the edge of the footing could be related to the curvature of the footing. The stress at the edge of the footing as a percentage of the stress over the central part of the footing reduces from 70% at 10 kN, to 66% at 20 kN and 60% at 30 kN applied load.

© University of Pretoria

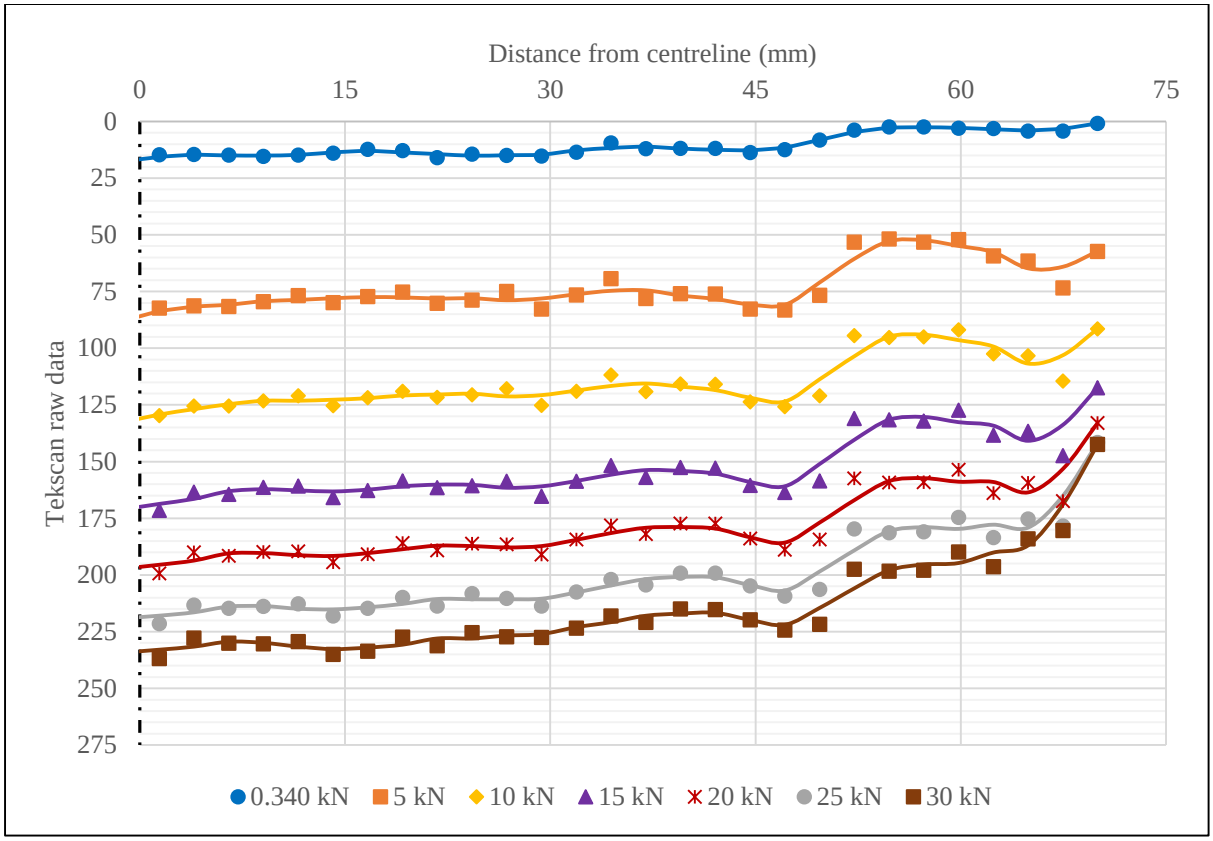

Figure 4-30 Tekscan™ data for 10 mm aluminium footing

4.4.4 6.7 mm Aluminium Footing

The 6.7 mm footing is classified as semi-stiff (K_s value of 0.0116), although very close to the boundary of being considered semi-flexible. Therefore it should exhibit a significantly different contact stress distribution than all the previous footings analysed. The 3D Tekscan data thereof is shown in Figure 4-31. The contact stress distribution has a similar trend to that of the 10 mm footing, however the difference in contact stress between the central part and the edge of the footing is considerably more than the difference observed for the 10 mm footing. In Figure 4-31 it can be seen that at a load of 10 kN, there is still a very low stress at the edge of the footing (indicated as blue), with the same holding true for an applied load of 20 kN.

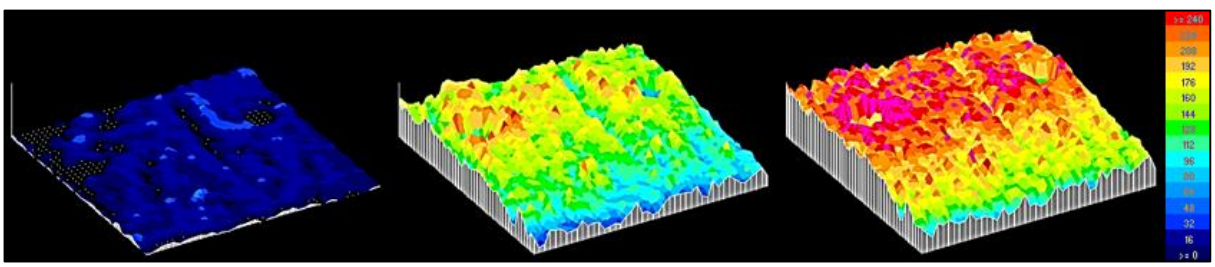

Figure 4-31 Three dimensional representation of stress distribution beneath 6.7 mm footing (Left: 0.365 kN; Middle: 10 kN; Right: 20 kN)

© University of Pretoria

The analysed contact stress distribution is represented graphically in Figure 4-32. Although the lower contact stress due to the bolts is clearly visible close to the centre of the footing in the figure, the maximum contact stress at each load increment is located at the same point along the footing width. The contact stress variation beneath the footing is almost linear from 5 kN to 15 kN, where after the contact stress distribution becomes parabolic at higher loads. The magnitude of the contact stress at the edge of the footing compared to the centre of the footing increases as the load applied is increased (opposite of what is expected). At a load of 10 kN, the contact stress at the edge of the footing is 41% and finally reaches 49% at a load of 30 kN.

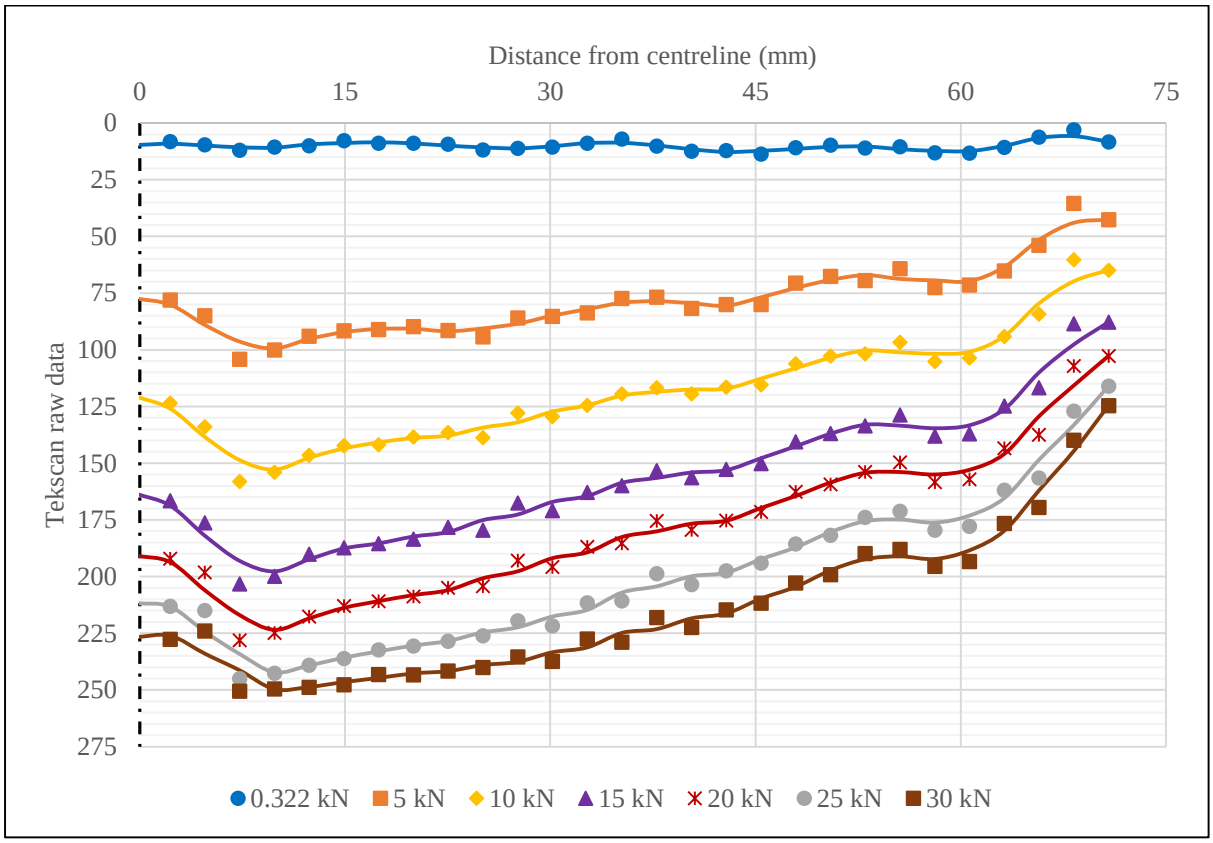

Figure 4-32 Tekscan™ data for 6.7 mm aluminium footing

At a maximum load of 30 kN, the moment at the centre of the footing was equal to 491 400 N.mm. As indicated in Section 4.3.5, the yield moment is less than that. Therefore, the footing had yielded at an applied load of 30 kN.

4.4.5 3 mm Aluminium Footing

The thinnest aluminium footing was the most flexible one tested (K_s value of 0.0011) and would give an indication of the contact stress distribution beneath a very flexible footing. The Tekscan™ data is illustrated as a 3D model in Figure 4-33. The load increments indicated in the figure are smaller than

© University of Pretoria

that of the other footings, due to the fact that the footing could not be tested beyond 15 kN. The figure clearly indicates that the stress distribution is far from uniform beneath the footing, and tends towards a parabolic shape at large loads.

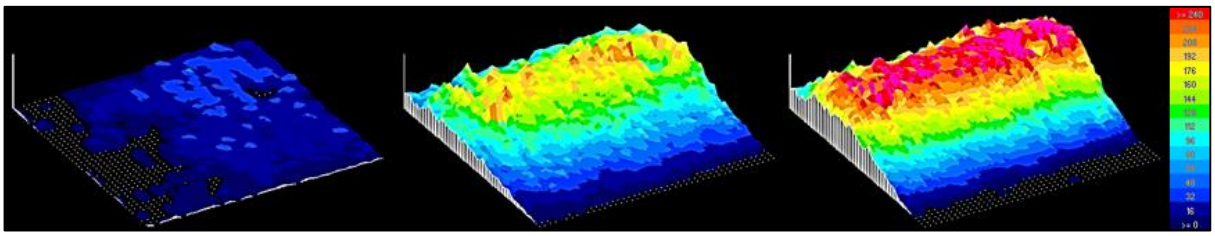

Figure 4-33 Three dimensional representation of stress beneath 3 mm footing (Left: 0.3 kN; Middle: 5 kN; Right: 10 kN)

In Figure 4-34 the data is shown for 5 kN intervals to correlate with the deflected shape data. The stress distribution beneath the footing is uniform across the entire footing under its own weight at 30 G, where after the edges of the footing do not experience further contact stress increase due to bending of the footing.

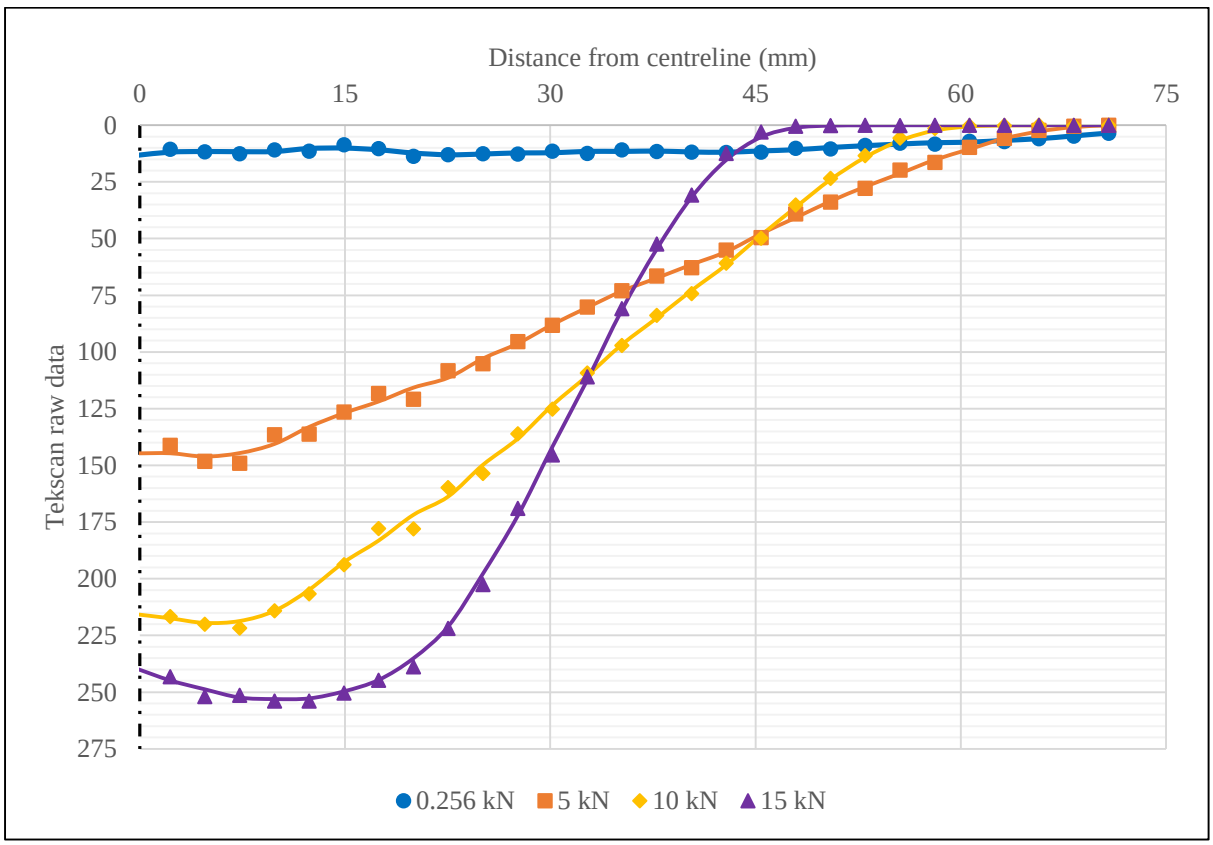

Figure 4-34 Tekscan data for 3 mm aluminium footing

© University of Pretoria

At a load of 10 kN, approximately 15 mm or 20% of the width of one side of the footing does not experience any contact stress, with the distance increasing to 30 mm or 40% of one side of the footing width at a load of 15 kN. The higher peak stress under the reduced loaded area explains why the settlement of the centre of the footing is higher compared to the other footings.

The contact stress beneath the footing was estimated by assuming that the shape of the contact stress distribution was triangular for the 5 kN and 10 kN, and changed to the shape illustrated in Figure 4-34 for the 15 kN load. The contact stress distribution across the width of the footing can be seen in Figure 4-35. Although the footing has a width of 75 mm from the centre of the footing in each direction, the contact stress is not distributed across the entire width of the footing when excessive deflection occurs. The figure indicates the width to one side of the footing where a certain percentage of the contact stress is experienced. The values obtained in the figure are not absolute, but give a good indication of the contact stress distribution beneath the footing. It is clear that from a load as small as 5 kN that 80% of the load is distributed over 53% of the footing. At a load of 15 kN, an equivalent constant stress of approximately 533 kPa acts over a width extending 28 mm from the centre of the column. It is clear that the contact stress below the centre of the footing becomes excessive for a very flexible footing.

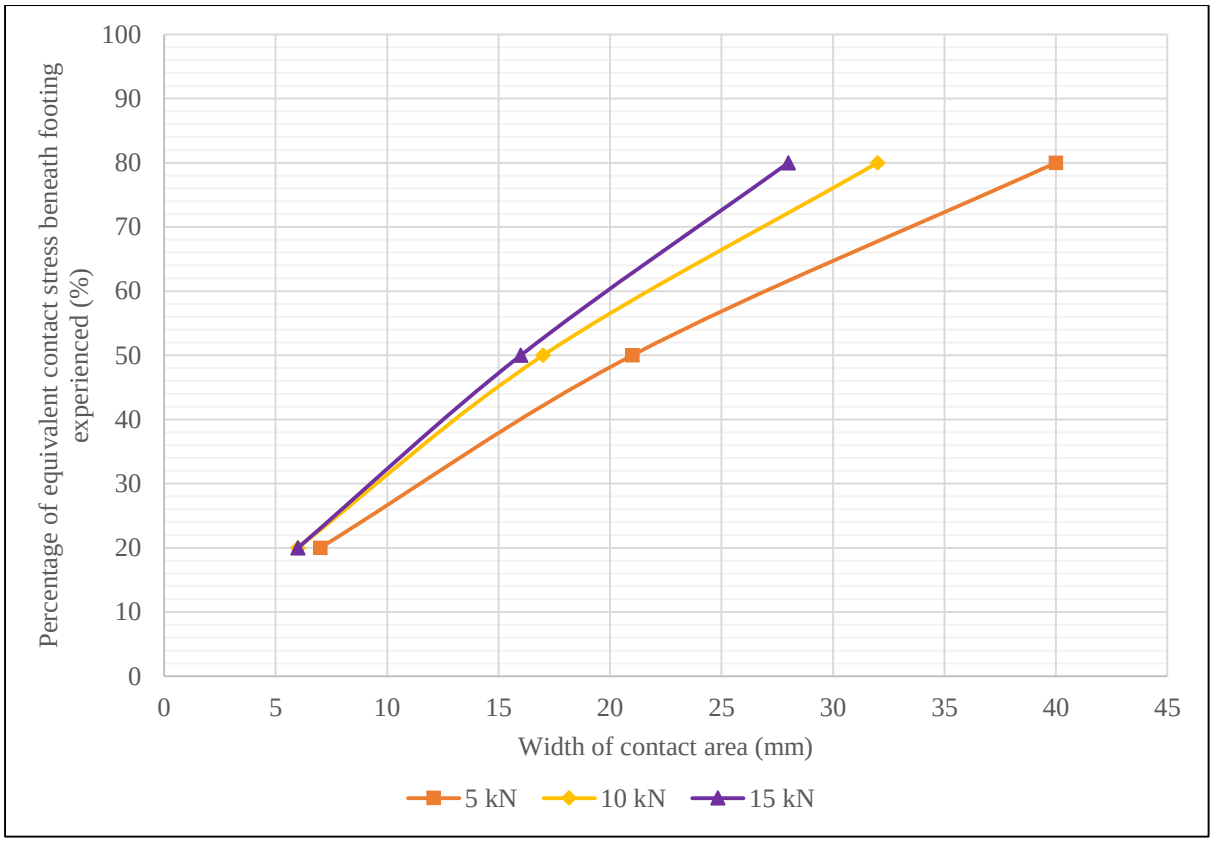

Figure 4-35 Percentage contact stress distribution across the width of the 3 mm footing

© University of Pretoria

Although the distance where 20% and 50% of the equivalent contact stress is experienced does not change significantly with an increase in the load, the distance to 80% changes considerably. This is due to the excessive curvature of the footing when larger loads are applied as the contact area reduces significantly. The assumption of uniform stress distribution beneath a footing by structural engineers is therefore not valid for this footing. For a very flexible footing, the central part of the footing carries the load resulting on localised high stresses beneath the footing. Therefore, the contact stress distribution used to design flexible footings cannot be assumed as uniform as the results obtained from the analysis would not yield realistic results.

Utilising the actual contact stress distribution beneath the footing, the bending moment at the edge of the column could be calculated. Assuming a triangular contact stress distribution to a distance of 48 mm away from the edge of the column at an applied load of 15 kN, the maximum moment experienced at this point is equal to 240 000 N.mm. This far exceeds the maximum moment capacity of the footing of 62 500 N.mm, therefore yielding of the footing did occur at a load applied of 15 kN.

The analysis of the contact stress distributions beneath the footing at the soil-structure interface illustrates that the proposed contact stress distribution shapes presented by Mosley and Bungey (1987), which depend on the stiffness of the aluminium footing could be realistic (Section 2.2.2). The contact stress distribution proposed by Leshchinsky and Marcozzi (1990) (illustrated in Section 2.2.2) differed significantly from the results obtained through the analysis.

4.4.6 Stress Distribution Trends for Aluminium Footings

After analysing the footings individually, the contact stress distribution results were combined to determine the effect of the footing stiffness on the contact stress distribution beneath footings. The contact stress variation beneath footings at different load intervals are compared. For the analysis, the 3 mm footing was not considered as the applied load did not result in any measured contact stress at the edge of the footing. The contact stress at the edge of the footing as a percentage of the contact stress experienced at the centre of the footing at 5 kN intervals are shown in Figure 4-36 as a function of the stiffness of the footing.

It is clear from the figure that the variation in the percentage contact stress between load intervals reduces as the stiffness of the footings increase. The value obtained with the dotted line cannot be considered as absolute, due to the fact that the contact stress percentage varies for each load applied, but the effect of footing stiffness on contact stress distribution can clearly be seen. The assumption of

© University of Pretoria

uniform contact stress distribution and in effect the linear Winkler model is only valid for stiff footings which do not yield, which correlates with the findings of Morfidis and Avramidis (2002).

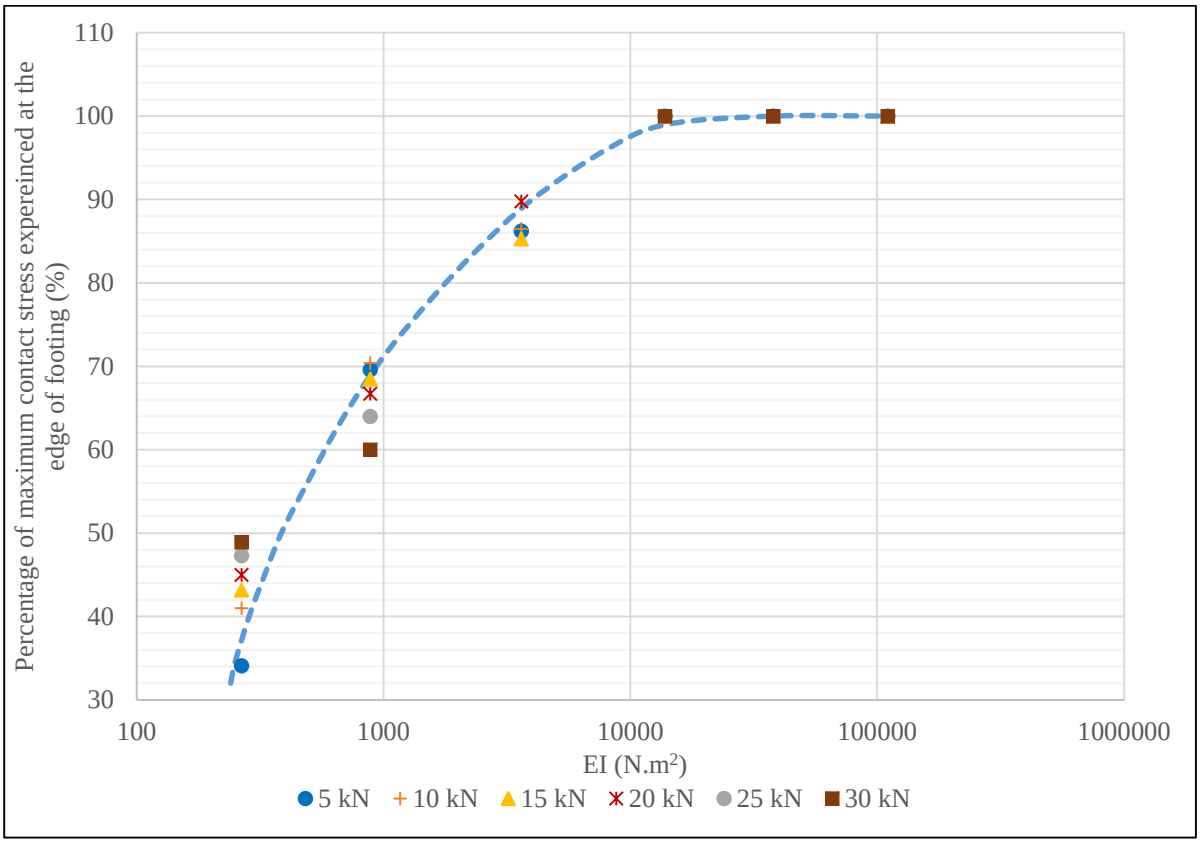

Figure 4-36 Percentage of the contact stress at the centre of the column experienced by the edge of the footing

4.4.7 Effect of Contact Stress Distribution on Deflected Shapes of the Footings

Structural engineers commonly assume a uniform contact stress distribution (Winkler method) to calculate contact stresses beneath and deflections of footings, as discussed in Section 2.2.1. Throughout Section 4.4 it was found that the contact stress distribution can only be considered as uniform for a stiff foundation system (not considering the 16 mm footing). In this section the deflected shapes of the footings were calculated mathematically to determine whether the assumed contact stress distribution could be used to predict the deflected shape of the footing accurately. The maximum applied stresses were considerably higher than the working stresses commonly assumed when a footing is design. Therefore, the measured and calculated deflected shapes were compared at an applied working load of 10 kN.

© University of Pretoria

The contact stress distribution beneath the footings tested in this study changed as the load applied to the footing increased. The initial contact stress distribution beneath the footings was uniform, after which it changed to a linear variable shape (trapezoidal when considering only one half of the footing). Finally, when large loads were applied and excessive strains were experienced by the footing and/or the sand, the shape of the contact stress distribution became parabolic. The contact stress distribution beneath the 3 mm footing was assumed to be triangular at a load of 10 kN, while the contact stress distribution beneath the stiff footings was uniform. A trapezoidal contact stress distribution was assumed for the intermediate footings, including the stiff 16 mm aluminium footing. Examples of the contact stress distributions used to calculate the deflected shapes are illustrated in Figure 4-37. As in previous sections, only one half of the footing was considered.

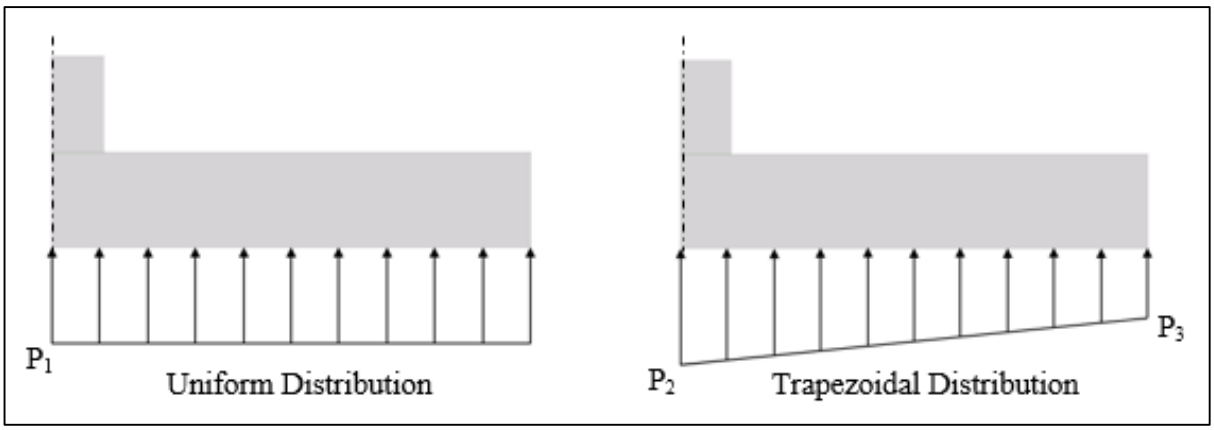

Figure 4-37 Contact stress distributions considered for deflection calculations

The deflected shapes of the footings were calculated with the use of Equation 4-3 (Kassimali, 2011). By integrating the moment equation twice and assuming zero curvature and zero deflection at the centre of the footing, the deflected shapes were established.

$$\frac{d^2z}{dx^2} = \frac{M}{EI} \qquad \text{(Equation 4-3)}$$

Where:

z = Vertical deflection of footing
x = Distance along width of footing
M = Moment present at specific point of footing
E = Modulus of elasticity of material
I = Inertia around neutral axis through width of footing

For a uniform contact stress distribution at a constant applied load of 10 kN, the variation between the deflected shapes of the footings is only as a result of the stiffness (EI) of the footing. Throughout this section the deflected shapes were determined in order from thick to thin footings.

© University of Pretoria

(a) Stiff footings

The contact stress distribution beneath the footing at the soil-structure interface was determined as uniform for all the stiff footings in Section 4.4.1 and the deflection of the footings were considered negligible in Section 4.3.1. Mathematical calculation of the deflected shape of the 25 mm aluminium footing indicated that the deflection at the edge of the footing is 0.019 mm at a load of 10 kN. The values for the 35 mm and 50 mm aluminium footings are even less. Therefore, the calculated value of the deflection is small enough that it would be fair to assume that for all practical purposes, the footing does not experience any deflection. The calculated deflected shapes of the stiff footings correlate well with the measured deflected shapes.

(b) 16 mm Aluminium Footing

The contact stress distribution at the soil-structure interface of the 16 mm aluminium footing did exhibit a slight trapezoidal shape at an applied load of 10 kN, with the contact stress at the edge of the footing approximately 85% of the contact stress over the central part of the footing. The calculated uniformly distributed load beneath the stiff footings (P_1 in Figure 4-37) was 66.7 N/mm. For the trapezoidally shaped stress distribution, P_2 (Figure 4-37) was calculated as 72.07 N/mm and P_3 (Figure 4-37) was calculated as 61.26 N/mm. The measured deflected shape, as well as calculated deflected shapes due to the uniform and trapezoidal load distribution is illustrated in Figure 4-38.

The calculated and actual measured results do not conform. Although the amount of deflection is similar for the calculated and measured deflected shapes, the calculated shapes exhibit a more gradual increase in the vertical deflection, whereas the actual measured deflection exhibited a significant change in the rate of deflection increase at approximately 35 mm from the centre of the column. The presence of bolts beneath the column could have altered the measured deflected shape of the footing, locally altering the stiffness. However, the calculated values give a realistic indication of the footing deflection. The difference in the calculated curvature of the footing between the trapezoidal and the uniform load distribution is negligible.

It is also clear from the figure that the deflection of this footing was approximately 3.5 times larger than that of the 25 mm aluminium footing. Due to the larger deflection and variable contact stress distribution, the behaviour of this footing differs significantly from that of the other stiff footings and should not be considered in the same category as them.

© University of Pretoria

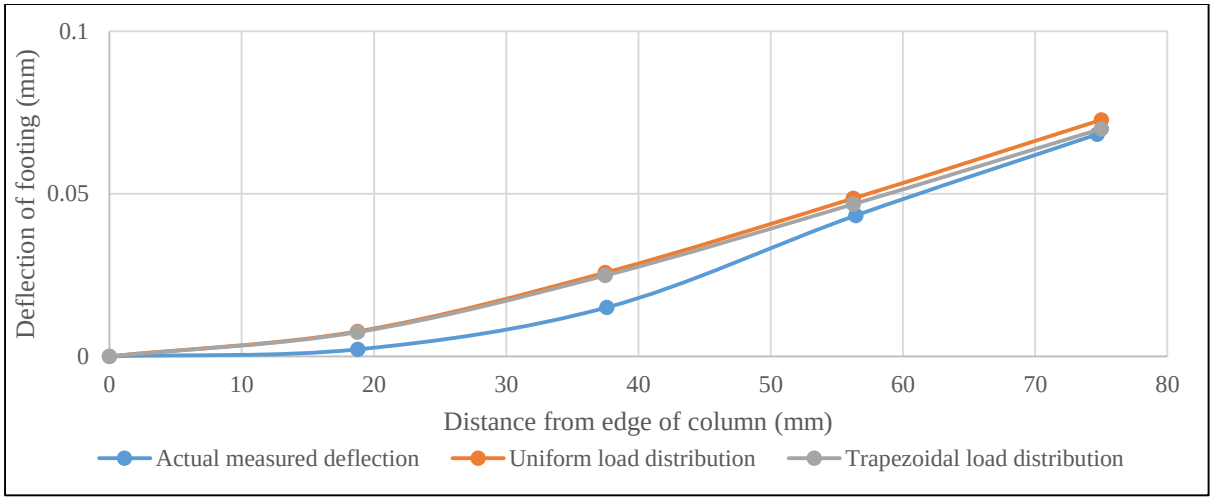

Figure 4-38 Different deflected shapes measured and calculated for 16 mm aluminium footing

(c) 10 mm Aluminium Footing

The trapezoidal load distribution at the soil-structure interface of this footing was considerably larger than that of the 16 mm aluminium footing, with the triangular section accounting for approximately 30% of the load distribution. The uniform load distribution remains constant, while the value of P_2 was calculated as 78.43 N/mm and the value of P_3 was calculated as 54.90 N/mm. The different deflected shapes are illustrated in Figure 4-39.

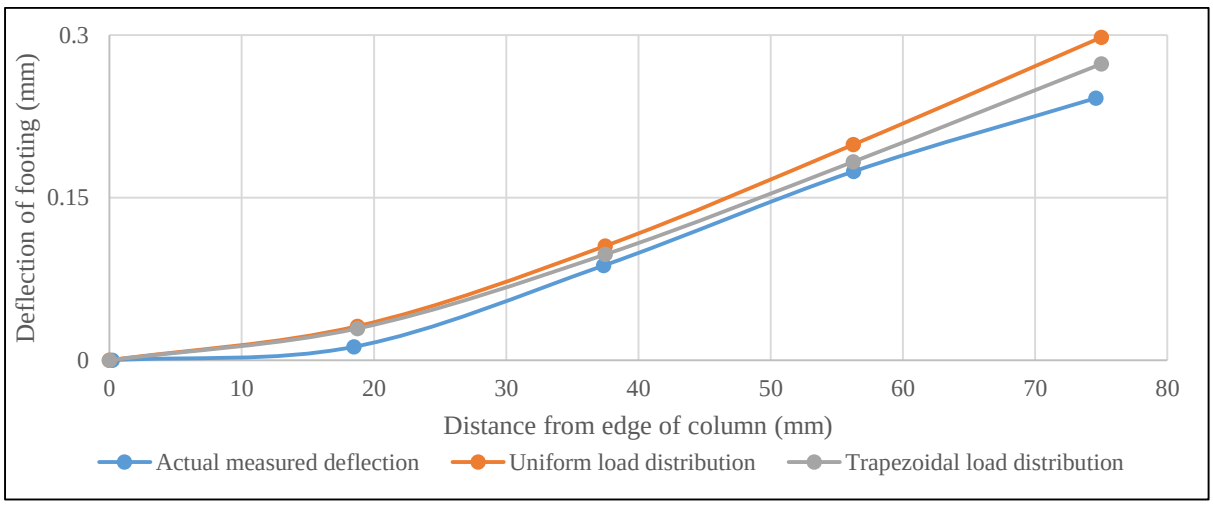

Figure 4-39 Different deflected shapes measured and calculated for 10 mm aluminium footing

It is clear from the figure that when the load distribution changes from uniform to become more trapezoidal in shape, the difference in the calculated results become noticeable. The difference between the calculated values and the actual measured deflection increased as the stiffness of the footings decreased.

© University of Pretoria

The deflection of the footing calculated using the trapezoidal shape predicts the deflection of the footing more accurately than the uniformly distributed contact stress. The location were the measured deflected shape exhibits an increase in the rate of deflection increase occurs closer to the centre of the footing, at approximately 15 mm from the centre of the footing, compared to the 16 mm aluminium footing. The fact that a reduction in footing thickness resulted in a reduced area with lower than expected curvature again indicates that the difference between the calculated and measured curvature in the central part of the footing could be caused by the column. It is clear from the figure that with an increase in the triangular section of the trapezoidal shape, the difference in the calculated results become noticeable. The calculated values do however still predict the deflection of the edge of the footing with an error margin of less than 10%.

(d) 6.7 mm Aluminium Footing

The 6.7 mm aluminium footing was considered as semi-stiff. However, it experienced a large amount of settlement and deflection during load application. The contact stress at the edge of the footing was approximately 45% of the contact stress over the central part of the footing, yielding values of 91.95 N/mm for P_2 and 41.38 N/mm for P_3. The calculated and measured deflected shapes of the footing can be seen in Figure 4-40.

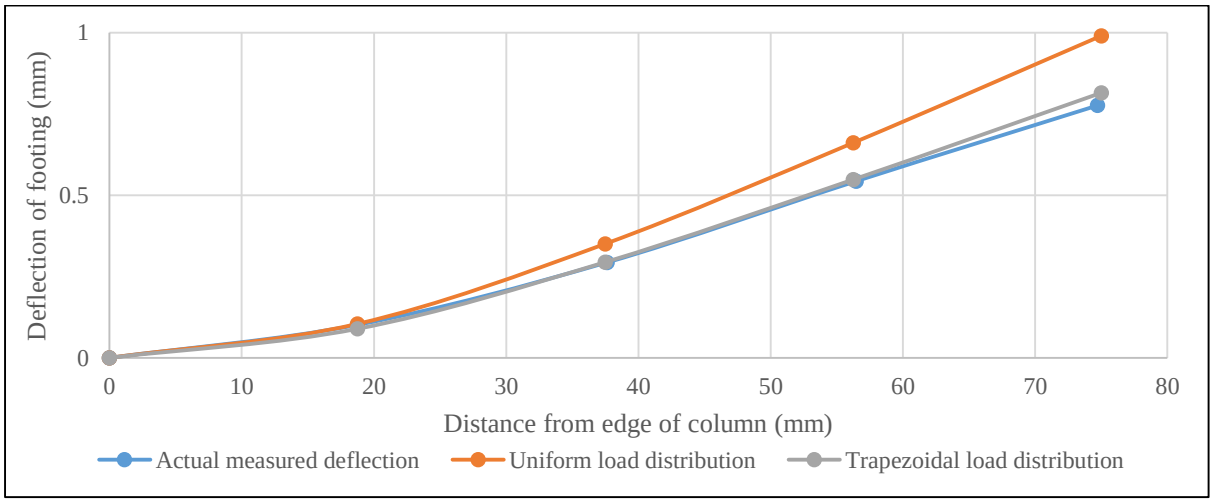

Figure 4-40 Different deflected shapes measured and calculated for 6.7 mm aluminium footing

As illustrated with the 10 mm aluminium footing, the difference between the deflected shapes calculated with the uniform load distribution and trapezoidal load distribution is increasing. Although both mathematical calculations exhibit similar deflections near the centre of the footing, the deflection of the uniform load distribution at the edge of the footing is considerably more than that of the trapezoidal load distribution. The use of the trapezoidal load distribution produces an accurate prediction of the

© University of Pretoria

deflected shape of the footing compared to the actual measured deflection. The results also confirm that the measured contact stress distribution beneath the footing delivers accurate results when determining the deflected shape thereof. Therefore, the reading obtained with the Tekscan™ sensor was realistic. It is clear that as the stiffness of the footing reduces, the use of a uniform load distribution does not deliver accurate results to predict the deflected shape of the footing. The last footing considered in this analysis is the 3 mm aluminium footing.

(e) 3 mm Aluminium Footing

As illustrated in Section 4.4.5, the contact stress distribution beneath the footing varied considerably between load intervals. At a load of 10 kN, a portion of the footing did not experience any contact stress as a result of the excessive deflection of the footing. However, for the analysis of this footing, a perfect triangular load distribution across the entire width of the footing will be used, as well as the smaller triangular pressure distribution over 58 mm of the footing width (width which experienced contact stress at 10 kN). The maximum load experienced at the centre of the triangle is 133.33 N/mm for the triangular distribution over the entire width of the footing, whereas the load experienced was 172.41 N/mm for the smaller triangle. The use of a uniform load distribution clearly does not deliver accurate results to determine the deflected shape of the footing, as illustrated in Figure 4-41. Although the triangular load distribution over the entire footing width predicts a more accurate deflected shape compared to the measured deflected shape, it still does not correlate well with that of the measured results. This is due to the fact that the actual load was not spread across the entire width of the footing, but rather a smaller section thereof as discussed in Section 4.4.5. The deflected shape of the footing determined with the use of the smaller triangular pressure distribution delivers the most accurate results. However, the use thereof for design purposed might be too complicated and the triangular pressure distribution over the entire footing width is recommended.

The difference between the uniform load distribution and triangular load distribution is considerable for this footing. The difference between the measured deflection and the deflection calculated with the use of the uniform load distribution is large and cannot be used with confidence. It is therefore recommended that alternative pressure distribution shapes be utilised when calculating the deflected shapes of footings, dependent on the stiffness of the foundation system. This is further discussed in Section 4.4.7 (f).

© University of Pretoria

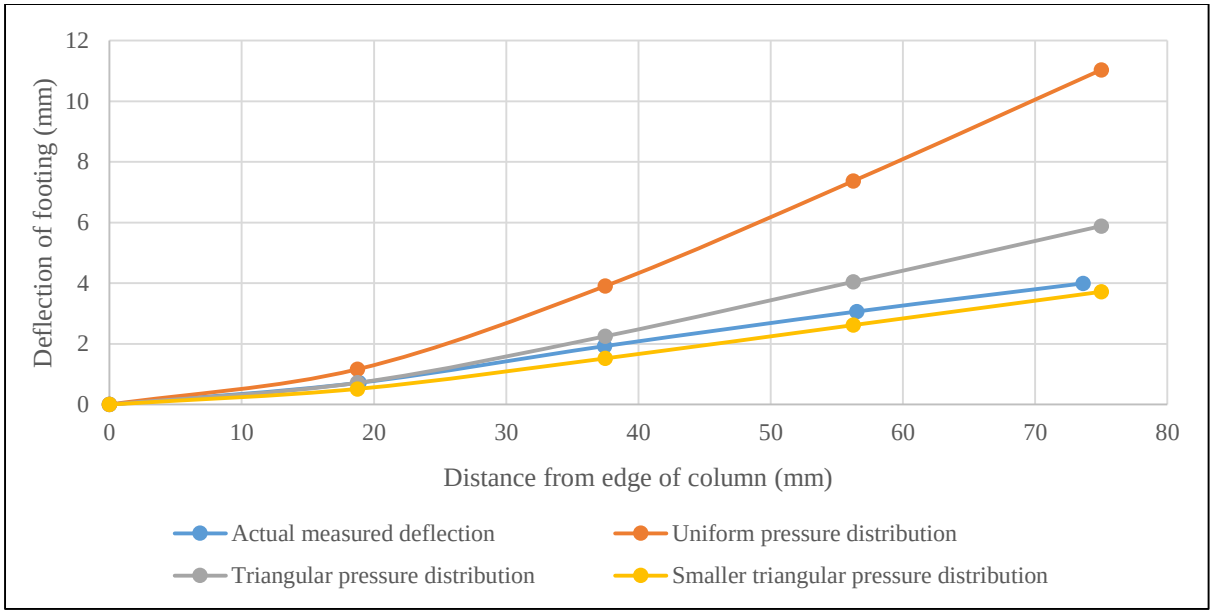

Figure 4-41 Different deflected shapes measured and calculated for 3 mm aluminium footing

(f) Contact Stress Distributions for the Determination of the Deflected Shapes of Aluminium Footings

It is evident in Section 4.4.7 that the use of a uniform contact stress distribution for design purposes does not always yield accurate results. As the stiffness of the footing reduces and in effect the flexibility thereof increase, the contact stress distribution beneath it changes from uniform to linearly varying (trapezoidal when considering symmetry) to parabolic. Table 4-3 indicates proposed contact stress distribution shapes which can be used for analysis of footings to obtain more realistic settlement and deflection data. The data is divided into three distinct contact stress distribution shapes, namely uniform, linearly varying (trapezoidal) and triangular. Although the boundary of stiff footings and semi-stiff footings is a K_s value of 0.1 (Arnold et al., 2010), the 16 mm footing (K_s value of 0.1581) did not exhibit the same behaviour of the stiff footings. Therefore, the proposed boundary to use a uniform pressure distribution is adjusted to a K_s value of 0.2, to ensure that the pressure distribution is uniform.

Table 4-3 Contact stress distribution shapes to determine settlement and deflection of aluminium footings

K_s Range	Contact Stress Distribution Shape
< 0.01	Triangular
0.01 - 0.2	Linearly Varying (Trapezoidal when considering symmetry)*
> 0.2	Uniform

* Extent of variation can be found using Figure 4-36

© University of Pretoria

4.5 Reinforced Concrete Footing

Although aluminium footings are deemed to be a good substitute for reinforced concrete footings in centrifuge modelling, the vast majority of prototype structural footings comprise of reinforced concrete. The difference in the behaviour of the two materials are discussed in this section. The behaviour of a centrifuge model reinforced concrete footing is compared to the behaviour of aluminium footings in this section.

The properties of all the materials used in the experiment are indicated in Table 4-4. As can be seen in the table, the relative density of the sand used in this experiment was considerably lower than in any of the other experiments discussed thus far. The lower sand density resulted in greater settlement of the footing and this must be taken into account when the results are compared with those of the aluminium footings.

Table 4-4 Properties of materials used in reinforced concrete footing experiment

Concrete Properties			**Steel Properties**		**Soil Properties**	
Compressive Strength (MPa)	**Tensile Strength (MPa)**	**Modulus of Elasticity (GPa)**	**Tensile Strength (MPa)**	**Modulus of Elasticity (GPa)**	**Relative Density (%)**	**Secant Young's Modulus (MPa)**
30	5	25	400	165	56	74.7

The thickness of the reinforced concrete footing was chosen to ensure that for an uncracked section, the foundation system was classified as stiff (K_s value of 0.5187). The stiffness of the reinforced concrete footing is similar to that of an aluminium footing with a thickness of 21.34 mm. Therefore, the behaviour of the footing is expected to be similar to that of the stiff aluminium footings up to the moment that the concrete starts cracking, where after the concrete footing stiffness should gradually decrease as the crack grows under increased load.

4.5.1 Settlement and Deflection

The settlement of the reinforced concrete footing was determined at the same points along the width of the footing, indicated in Figure 4-2. The normalised settlement of the reinforced concrete footing is illustrated in Figure 4-42, whilst the deflected shapes of the reinforced concrete footing during load application are illustrated in Figure 4-43. From both figures it is clear that the behaviour of the footing is not similar to any of the aluminium footings tested. There is a clear difference in the behaviour of the footing before and after cracking of the concrete. The maximum load applied to the footing was 18.7 kN, as the footing failed at this point.

© University of Pretoria

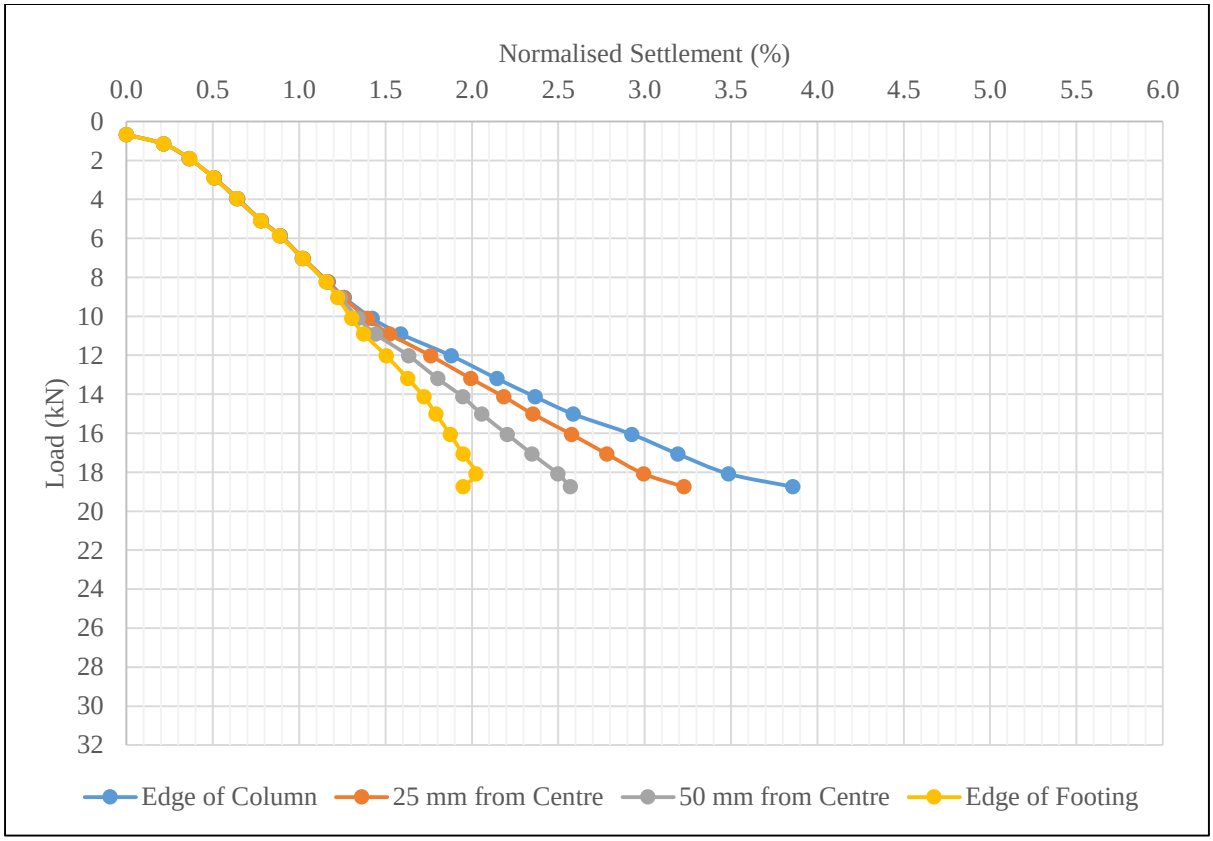

Figure 4-42 Settlement of reinforced concrete footing during experiment

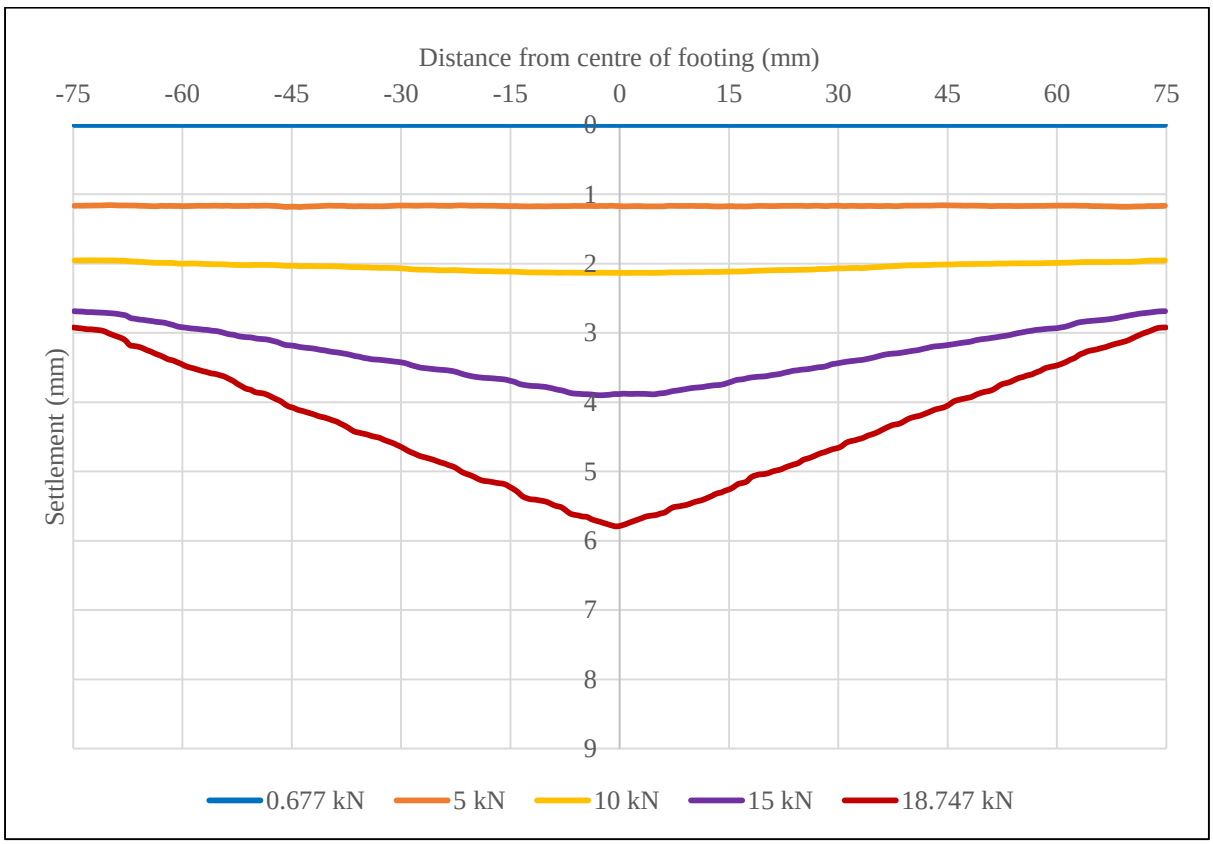

Figure 4-43 Deflected shapes of reinforced concrete footing at 5 kN intervals

© University of Pretoria

As can be seen in Figure 4-42, the normalised settlement of the footing increased at a constant rate for all the points along the footing until a load of 8 kN was applied. At this point, the concrete in the footing started to crack. When an 8 kN load is applied to the footing, the tensile stress in the concrete at the bottom of the footing was equal to 6.5 MPa, which is slightly more than the measured tensile strength of the concrete at 5 MPa, however the result is realistic.

Before cracking of the concrete, the settlement of all four points along the width of the beam were similar, where after the slope of settlement increase varied. At relatively low loads the behaviour of the foundation system was thus similar to that of the stiff footings, as calculated with Equation 2-11 (Arnold et al., 2010) and illustrated in Table 4-2. After the concrete cracked, the behaviour changed as the stiffness of the reinforced concrete footing decreased. When the concrete cracks, the neutral axis of the cross-section of the reinforced concrete footing shifts and the strength of the steel is activated (responsible for the tensile resistance of the footing). It is also clear in Figure 4-43 that no deflection of the footing occurred at 5 kN (remained this way up until 8 kN). After cracking the concrete footing started to deflect. The deflected shapes of the concrete indicates that cracking only occurred along the centreline of the footing and the sides of the footing did not experience any visible curvature, but rather rotated around the centre of the footing.

The concrete crack depth (from the bottom of the concrete footing) was determined visually through the images captured with the PIV camera. Although it is clear from the settlement data in Figure 4-42 that the concrete cracked at approximately 8 kN, the crack could not be detected visually at that load. The crack could be seen for the first time at an applied load of 10 kN. The depth of the concrete crack as a function of the load is illustrated in Figure 4-44, along with the resulting variable stiffness (EI) of the footing due to the crack depth. The figure indicates the crack depth on the primary vertical axis along with the equivalent stiffness of the footing on the secondary vertical axis.

From Figure 4-44 it can be seen that a load increment of 2 kN resulted in a reduction in the stiffness of the system from 8 600 N.m^2 (for the uncracked section) to 4 117 N.m^2. This is a reduction of 47.8% (from the uncracked section), clearly illustrating the effect of cracking on the stiffness of the reinforced concrete footing. The reduction in stiffness of the concrete footing occurs rapidly until the crack had propagated through approximately 50% of the thickness of the footing (15 mm), where after the reduction in the stiffness of the footing occurs at a slower rate. It must be noted that at a crack length of 50% of the footing thickness, the stiffness of the footing had reduced to approximately 18% of the uncracked stiffness.

© University of Pretoria

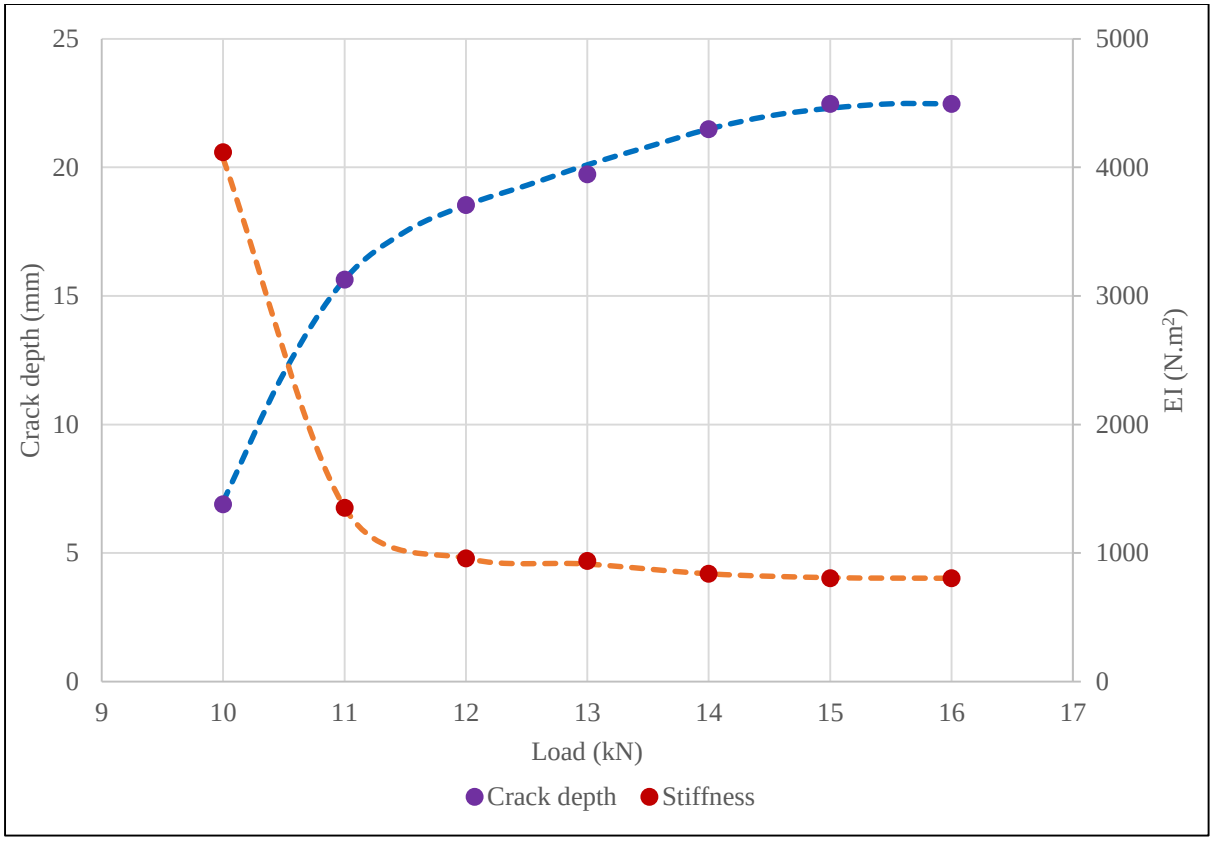

Figure 4-44 Stiffness and crack depth of reinforced concrete at various loads

When substituting reinforced concrete with aluminium, careful consideration of the stiffness of the footing is required, as the stiffness of a reinforced concrete footing decreases drastically when cracking occurs. An example of the reduction in the equivalent aluminium footing thickness for this specific test is indicated in Figure 4-45. By considering both Figure 4-44 and Figure 4-45, it is clear that as soon as crack propagation starts, the required aluminium footing thickness reduces drastically. Between 10 kN and 11 kN, the crack depth increased by 8.74 mm, reducing the equivalent aluminium footing thickness by approximately 5 mm. The rate of decrease in the equivalent aluminium thickness as a function of the load applied to the footing is therefore drastic. When considering the behaviour of either the footing or the soil beneath the footing with the use of an aluminium footing as substitute for a reinforced concrete footing, careful consideration of the applied load is required, as the post-cracking behaviour of a reinforced concrete footing cannot accurately be simulated with the use of an aluminium footing. This is important as the steel in reinforced concrete is designed to work in cracked concrete sections and structural engineers design reinforced concrete structures limiting the crack widths to 0.3 mm (Roberts and Marshall, 2010).

© University of Pretoria

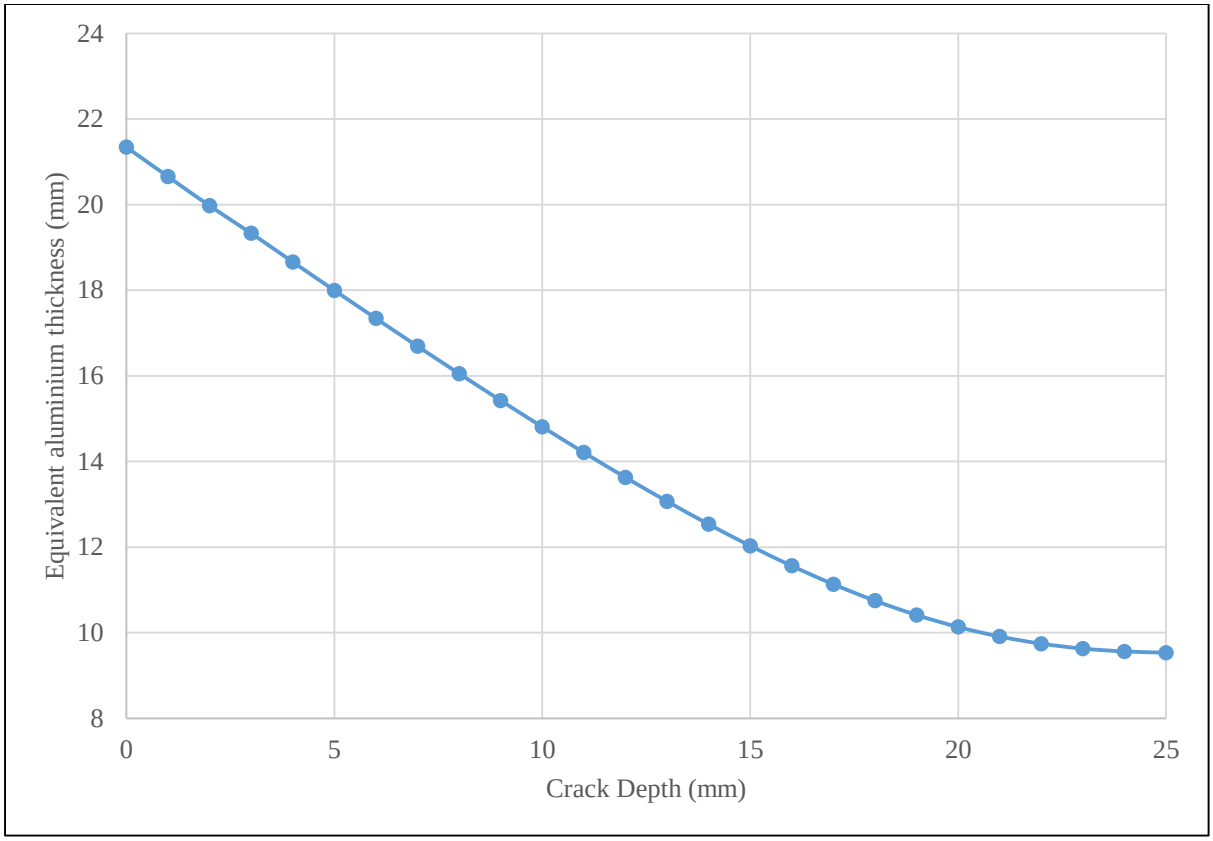

Figure 4-45 Equivalent aluminium footing thickness due to crack depth

The crack pattern and the deflected shapes of the reinforced concrete model footing observed in this experiment was similar to the pattern observed by Lin et al. (2003). As opposed to a large number of cracks forming across the entire width of the footing, a single large crack formed near the centre of the footing around which the sides of the footings rotated without any additional curvature. The single crack through the centre of the footing is visible in Figure 4-46.

As the load applied to the footing was increased whilst cracking of the concrete occurred, the crack propagated upwards until a certain crack depth was reached (critical crack length, ξ_{crit}). This is visible in Figure 4-44, where the crack depth remained constant at 15 kN and 16 kN. By increasing the load beyond 16 kN, the crack no longer propagated upwards, but started growing towards the edges of the column. This behaviour is similar to the behaviour found by Carmona and Ruiz (2014), where the crack propagated in a stable manner until failure of the beam started to occur, where after the cracks propagated in an unstable manner. Due to the occurrence of unstable cracks and subsequent failure of the footing, the load could not be increased beyond 18.7 kN. As a result of the lower load applied, bearing capacity failure of the foundation system did not occur. An example of the stable and unstable cracks are visible in Figure 4-47.

© University of Pretoria

Figure 4-46 Single crack formation beneath reinforced concrete footing

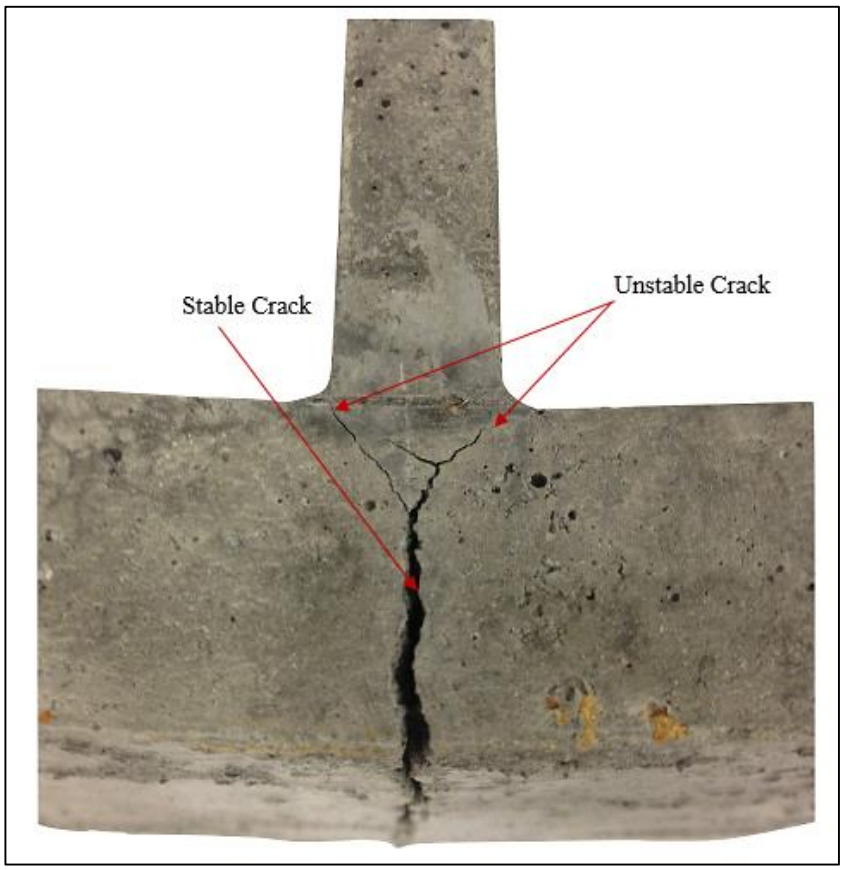

Figure 4-47 Stable and unstable crack propagation

© University of Pretoria

4.5.2 Stress Distribution beneath Reinforced Concrete Footing

The contact stress distribution beneath the reinforced concrete footing is expected to change between pre-cracking and post-cracking behaviour. The 3D contact stress distribution beneath the footing is shown in Figure 4-48. Only a slight increase in the contact stress experienced under the column is visible for the cracked reinforced concrete footing (right side of the figure).

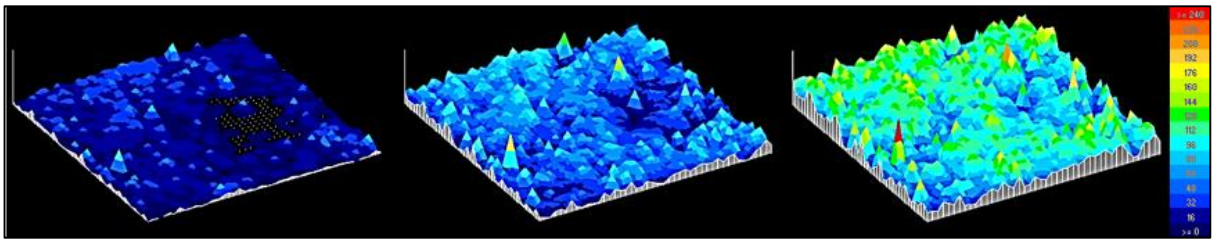

Figure 4-48 Three dimensional representation of stress beneath reinforced concrete footing (Left: 0.677 kN; Middle: 6 kN; Right: 12 kN)

The contact stress distribution beneath the reinforced concrete footing is illustrated in Figure 4-49. The distribution initially remains uniform, with a slight increase experienced at 10 kN in the region of the column. After cracking has occurred, the contact stress distribution started to increase over the central part of the footing. At the maximum applied load, the contact stress distribution became trapezoidal, mimicking the deflected shape of the footing. At the maximum applied load, the contact stress at the edge of the footing is approximately 48% of the contact stress experienced under the column. The large drop in the contact stress at the very edge of the footing for each load increment might be due to partial contact loss of the sensel with the footing surface. The contact stress distribution not only confirms that there is a difference between the pre- and post-cracking behaviour of the reinforced concrete footing, but also illustrates the different behaviour compared to that of the aluminium footings.

© University of Pretoria

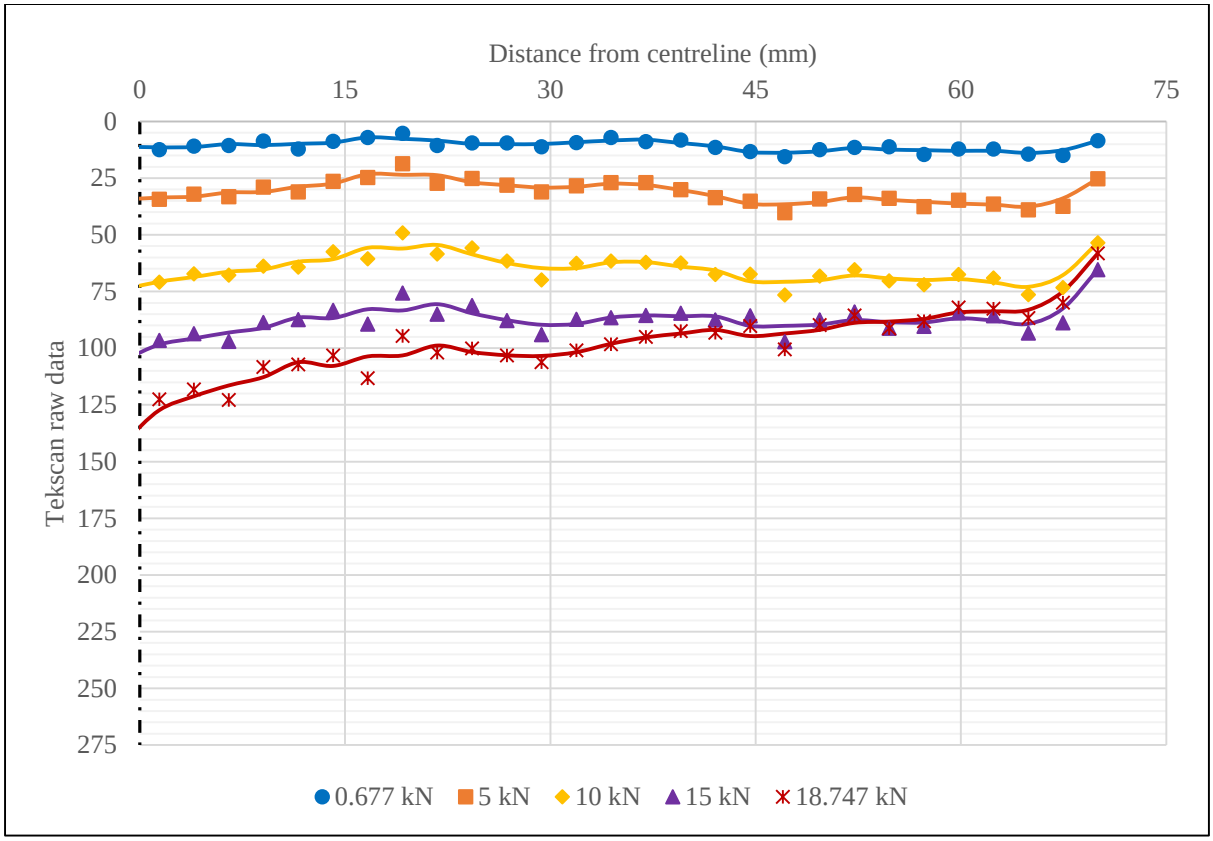

Figure 4-49 Tekscan™ data for reinforced concrete footing

Up to this point the behaviour of the footings have been discussed. The next section briefly presents the effect of the footing behaviour on the sand supporting the footing.

4.6 Sand Displacement beneath Footing

As a load was applied to the footing, the footing started to settle, which in turn caused displacement of the soil beneath the footing. In this section the displacement of the sand layers beneath the footings, from the start of the test up to an applied load of 30 kN is discussed for all the aluminium footings, apart from the 3 mm aluminium footing as the load was only applied up until 15 kN. The displacement of the sand beneath the footing was determined with the use of PIV software (Section 2.7).

Soil displacement is dependent on the contact stress applied to the soil, as well the flexibility of the footings. When the load is increased continuously, the sand is expected to displace until a slip surface eventually starts to form, mobilising a failure mechanism. However, the loads applied to the sand were not large enough to cause the formation of a slip surface in these tests conducted. Therefore, only the horizontal and vertical displacement of the sand beneath the footings are discussed in this section, starting from the thickest to the thinnest footing.

© University of Pretoria

4.6.1 Stiff Footings

The stiff footings are presented together as the sand beneath the stiff footings displaced in a similar manner for all the stiff footings (apart from 16 mm footing). As indicated earlier, the stiff footings did not experience any noticeable deflection and in turn were subjected to a uniform contact stress distribution beneath the footing as indicated in Section 4.4.1. Due to the rigidity of the footing, the sand mass beneath the footing was pushed down by the same amount across the entire width of the footing. The horizontal and vertical displacement of the sand beneath the 35 mm aluminium footing is shown in Figure 4-50, and is representative of all the stiff footings.

For all the figures in this section the vertical displacement is presented first, followed by the horizontal displacement. Each figure extends to a depth of 200 mm and a width of 150 mm on either side of the footing centreline. In the majority of the figures in this section, sand patches that were not tracked accurately caused irregular displacement data resulting in small areas of large displacement. This can be due to the sand particles that rearranged during loading of the sand layer, resulting in incorrect image correlation and subsequent “wild” displacement vectors.

Absolute displacement values are not analysed in this section, but rather the trends that are visible. The plots in the figures are plotted at 0.1 mm contour intervals, therefore the movement of the sand beneath the different footings can be compared by the number of intervals present and the contour shapes.

In Figure 4-50 it is clear that approximately concentric circles trend in vertical displacement occurs beneath the footing. The concentric circles starts at the edges of the footing, extending downward. The horizontal displacement beneath the footing can be divided into two segments, a column beneath the centre of the footing along with two teardrop shaped segments on either side of the column. The start of the teardrop shapes occurs at the edge of the footing, extending downward. Both the horizontal and vertical displacement of the sand beneath the footing exhibits a symmetrical shape around the centre of the footing, supporting the assumptions used earlier in the chapter to only analyse one side of the footing.

The 35 mm aluminium footing is representative of all the stiff footings, as they all exhibited similar behaviour. As with the settlement, deflection and contact stress distribution data before, the behaviour of the flexible footings are expected to differ from the stiff footings.

© University of Pretoria

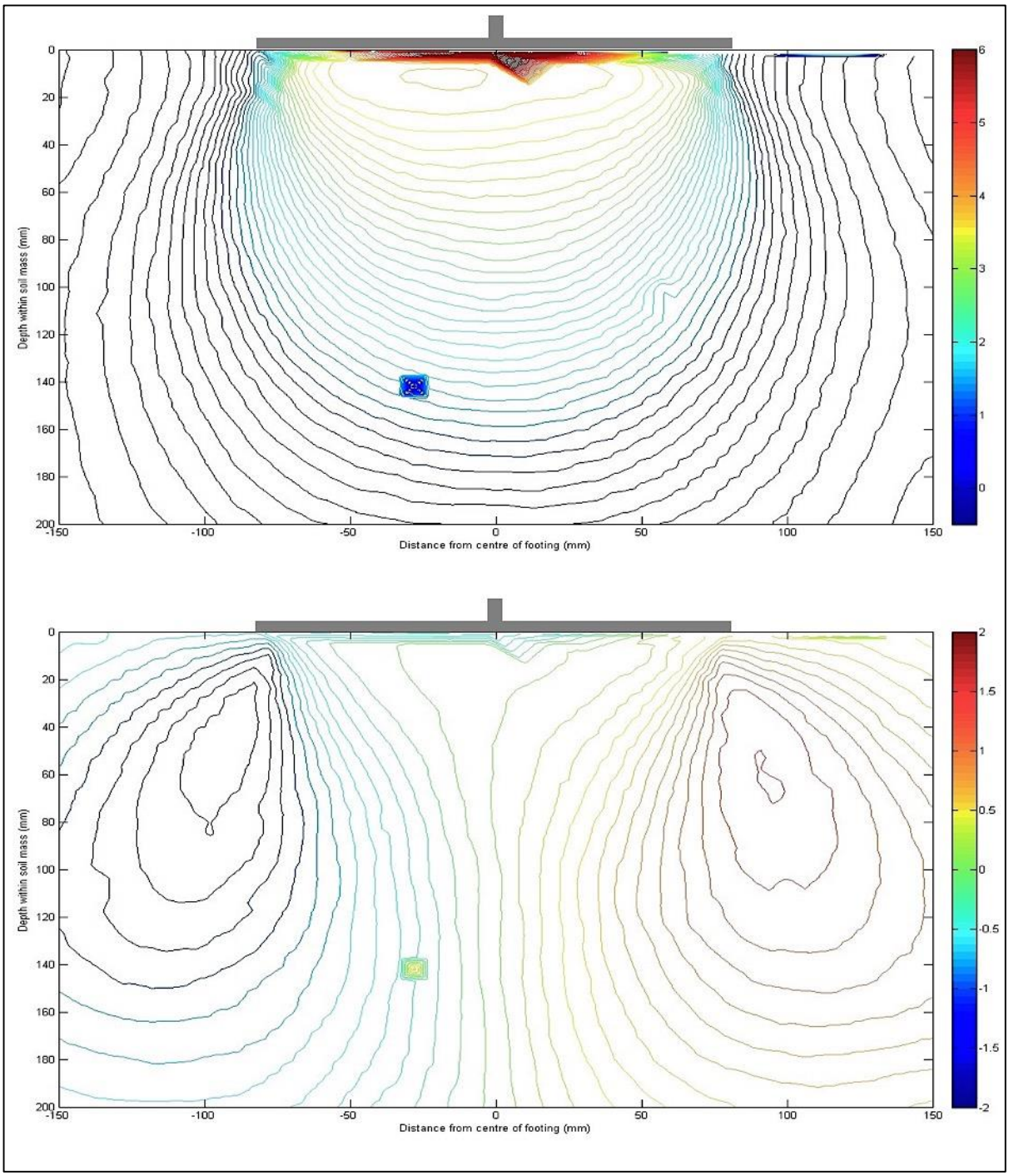

Figure 4-50 Displacement of sand beneath 35 mm aluminium footing (Top: Vertical displacement; Bottom: Horizontal displacement)

4.6.2 16 mm Aluminium Footing

The 16 mm footing did not exhibited the same settlement and deflected shape behaviour as the stiff footings, although it is also classified as a stiff footing (discussed in Section 4.3.2). Therefore, the displacement of the sand beneath the footing, as illustrated in Figure 4-51, is expected to differ from that of the other stiff footings.

© University of Pretoria

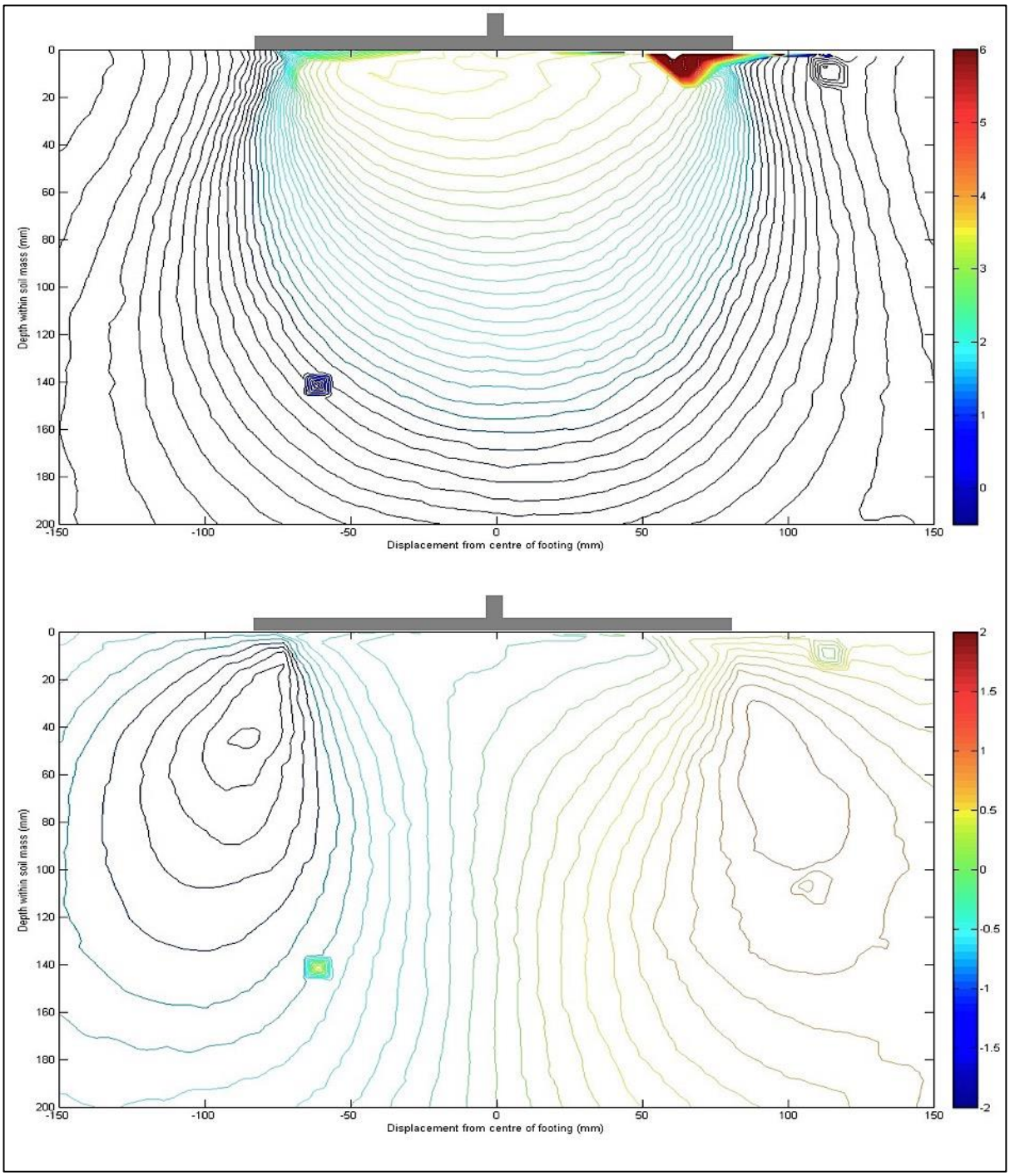

Figure 4-51 Displacement of sand beneath 16 mm aluminium footing (Top: Vertical displacement; Bottom: Horizontal displacement)

The vertical displacement of the sand is similar to that of the stiff footings, although the depth of the concentric circle shaped intervals have increased slightly, particularly close to the surface of the footing. The horizontal displacement alters slightly from the stiff footings, with the size of the teardrop displacement intervals reducing as the amount of intervals present increases, particularly on the left hand side of the figure. The teardrop shapes also tend to rotate further away from the centre of the footing compared to the other stiff footing.

© University of Pretoria

4.6.3 10 mm Aluminium Footing

As was discussed in Section 4.3.3, the 10 mm aluminium footing did exhibit curvature during load application, which is expected to alter the displacement of the soil beneath the footings as illustrated in Figure 4-52.

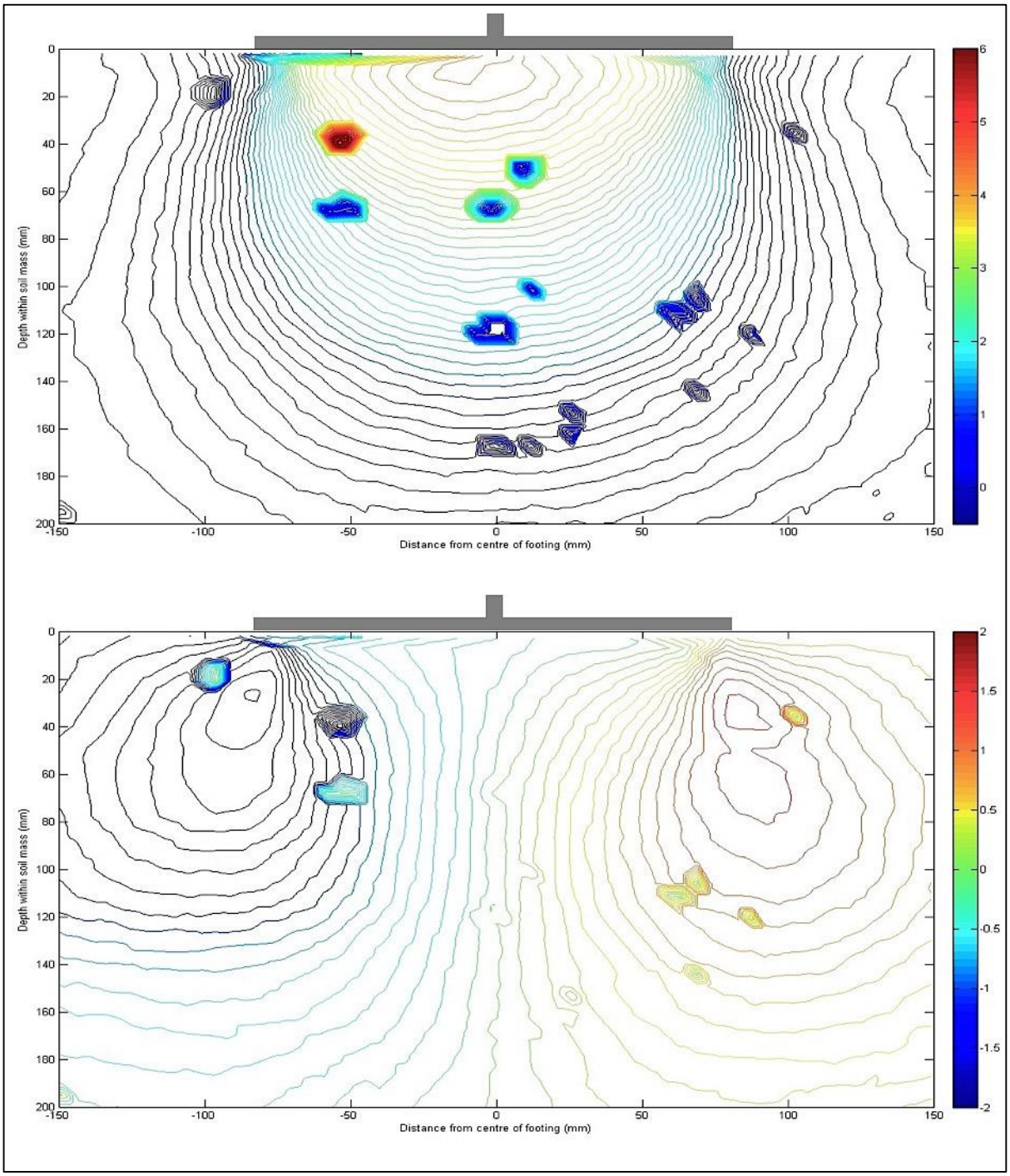

Figure 4-52 Displacement of sand beneath 10 mm aluminium footing (Top: Vertical displacement; Bottom: Horizontal displacement)

© University of Pretoria

The vertical displacement of the soil is similar to that of the previous footings, although a slight increase in the number of intervals is visible as their depths has reduced. This gives an indication that the vertical displacement of the sand beneath the footing increased from the previous tests. However, as was discussed in Section 4.3.3, the settlement of the footing was considerably more than the stiff footings due to the low relative density of the sand during this experiment. Therefore, the reason for the increase in intervals can be attributed to the low relative density of the sand.

The trends of the horizontal displacement of the soil intervals have changed, with the size of the teardrop shapes reducing, whilst the number of intervals increased. As the number of teardrop intervals increased and their width start to increase further away from the sand surface, they reduced the width of the central column of horizontal displacement present beneath the footing.

4.6.4 6.7 mm Aluminium Footing

The behaviour of the 6.7 mm aluminium footing in terms of settlement, deflection and contact stress distribution differed considerably from the other semi-stiff and stiff footings throughout this chapter. This footing is deemed to be semi-stiff, however it exhibited considerable curvature during load application, as discussed in Section 4.3.4. As a result, the behaviour of the sand beneath the footing is also expected to differ. The displacement of the sand beneath the footing can be seen in Figure 4-53.

The vertical displacement of the sand clearly demonstrates a very large number of intervals, indicating the displacement of the particles increased in comparison to the footings analysed before. The concentric circle intervals of displacement exhibits different behaviour at different points along the sand surface. The curves that originate beneath the surface of the footing, exhibits a linear downward trend before the intervals start to rotate. However, the curves that originate beyond the edge of the footing on the sand surface, exhibit a more comprehensive concentric circle curve, with a narrow upper section increasing in width as the depth within the sand mass increases. These curves appear wider than all the curves presented for the other footings.

The horizontal displacement of the sand does not correlate well with the trend exhibited by the other footings analysed. The teardrop shaped curves do not originate from the edge of the footing, whilst the size of the central column beneath the surface of the footing has increased and the number of intervals present reduced.

© University of Pretoria

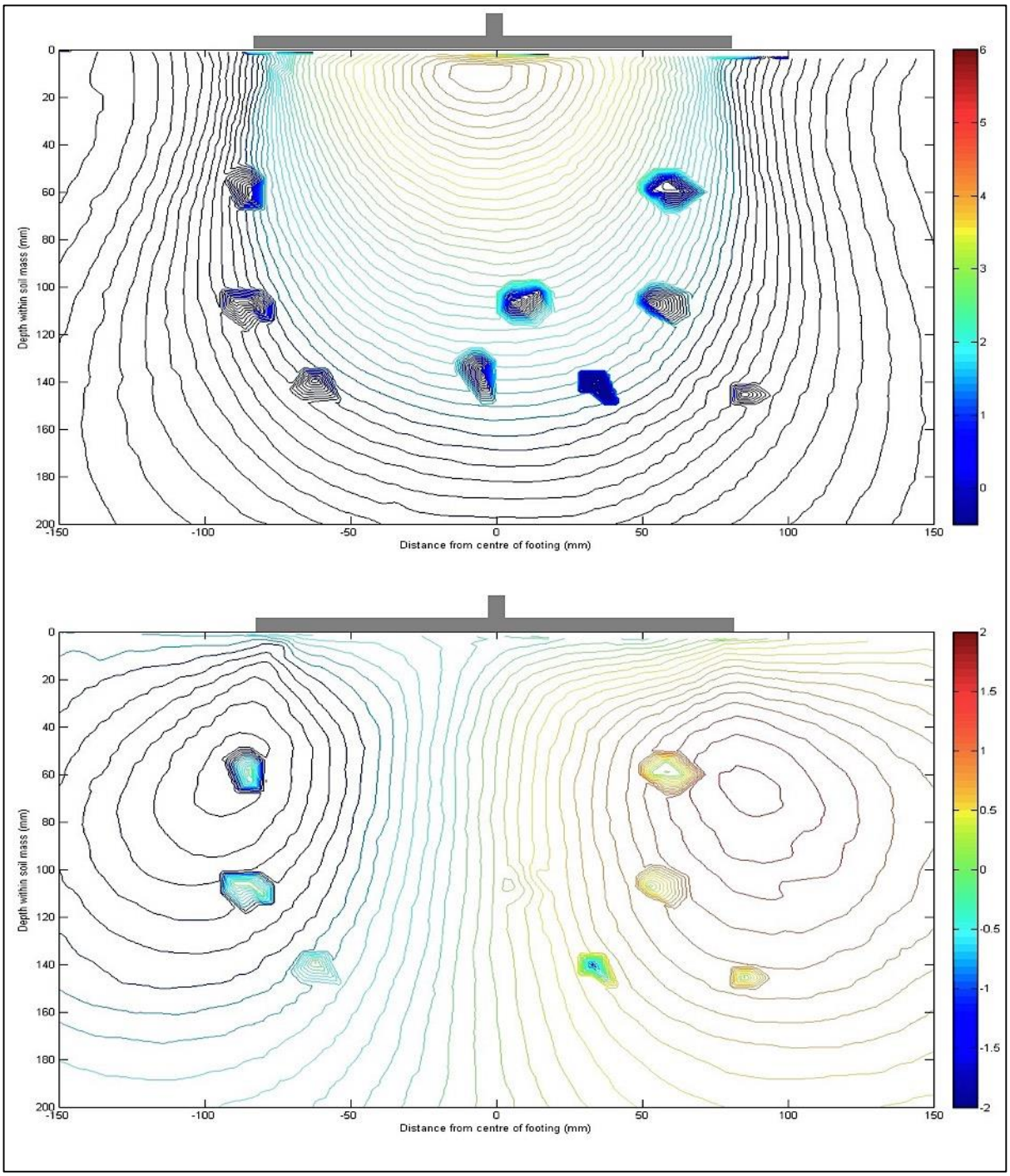

Figure 4-53 Displacement of sand beneath 6.7 mm aluminium footing (Top: Vertical displacement; Bottom: Horizontal displacement)

4.6.5 3 mm Aluminium Footing

Due to the excessive curvature of the footing and the large contact stress beneath the central part of the footing, considerable displacement of the sand beneath the footing is expected. The sand displacement is shown in Figure 4-54.

© University of Pretoria

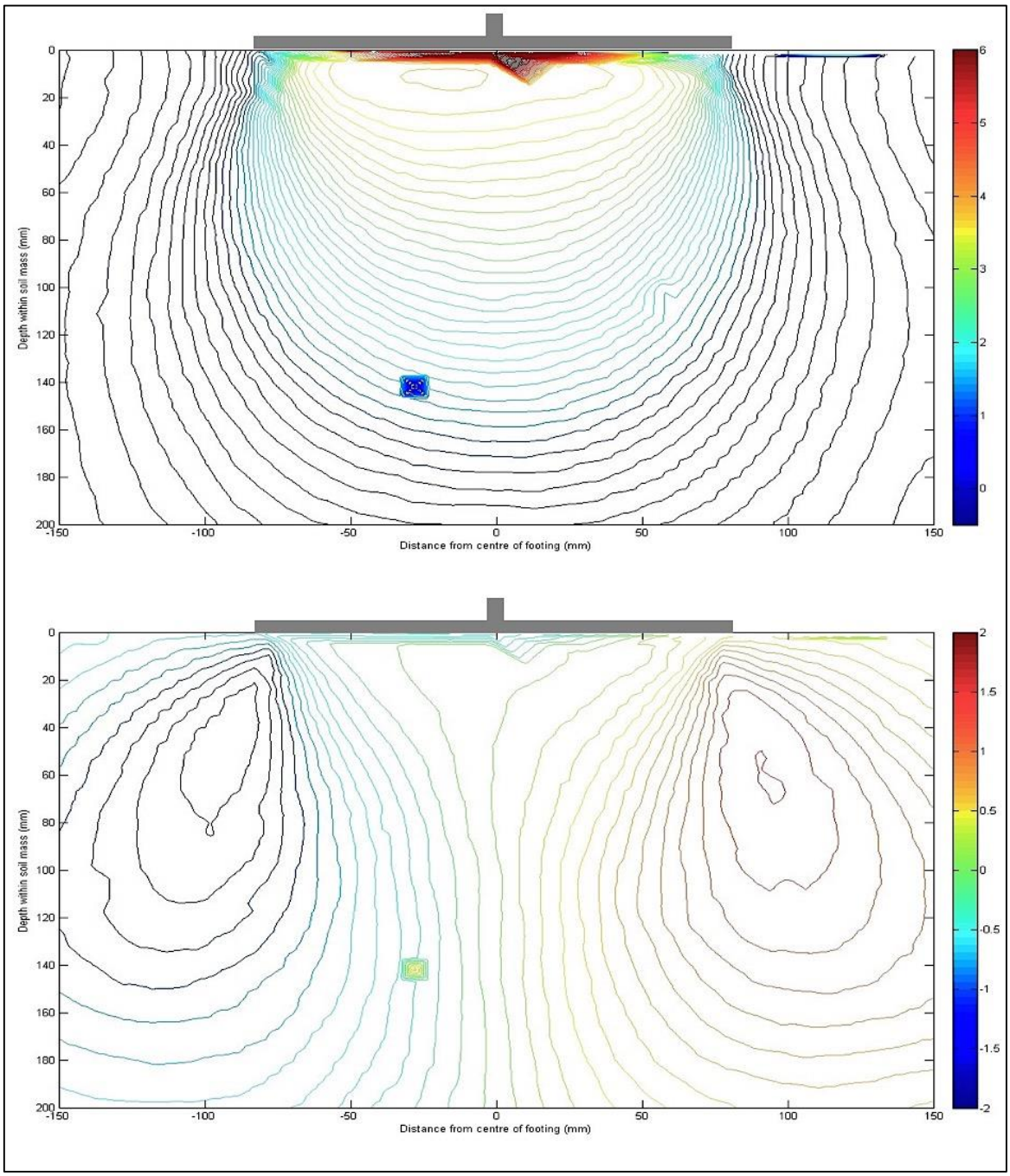

Figure 4-54 Displacement of sand beneath 3 mm aluminium footing (Top: Vertical displacement; Bottom: Horizontal displacement)

As illustrated in the figure, the displacement of the soil beneath the most flexible footing tested differs considerably from that of the other footings. The number of intervals of vertical displacement increased significantly, indicating that the settlement of the footing caused large displacement of the soil. When a load of 15 kN was applied to the footing, the contact surface of the footing changed from flat to a conical shape. This shaped causes the concentric circle curves to increase their width at the bottom compared to all the other footings. As the contact stress distribution was concentrated over the column of the footing (Section 4.4.5), the displacement at this point increased considerably.

© University of Pretoria

The central column of horizontal displacement beneath the footing has become substantially narrower as a result of the increase in the number and spacing of teardrop intervals present. Due to the variation in the shape of the footing during loading, the location of the teardrop intervals moved during the test. At a load of 15 kN, the contact stress beneath the footing ended approximately 48 mm away from the centre of the column (Section 4.4.5). The location of the start of the teardrop intervals is approximately at this point, indicating that they generally start at the end of the contact stress experienced by the footing.

Throughout this section it is clear that the amount of displacement of the sand beneath the footing is directly related to the thickness and in effect stiffness of the footing. As the settlement of the thinner footings was larger than that of the thick footings, the displacement of the sand is directly related to the settlement of the footing. However, the manner in which the displacement of the sand occurs is highly dependent on the stiffness of the footing. The intervals of vertical displacement of the stiffer footings are fewer, while the concentric circle intervals appear less curved compared to the flexible footings. Similar trend in the horizontal displacements intervals are visible in terms of the size, although the width of a central column section reduces with reducing stiffness (related to the deflected shape causing a larger percentage of soil to displace horizontally). It was also found that the teardrop displacement intervals originate at the end of the pressurised area beneath a footing.

4.7 Summary

In this chapter the effect of footing stiffness on the behaviour thereof was analysed. It was found that as the stiffness of the footing reduced, the deflection of the footing increased for a similar applied load compared to the stiff footings. This in turn increased the settlement of the deflected footing over the central part of the footing. Finally, the deflected shapes of the flexible footings changed the stress distribution shape beneath the footings, varying from uniform, to linearly varying (trapezoidal) to parabolic. The behaviour of a reinforced concrete footing was analysed to determine to what extent it correlates with the behaviour of the aluminium footings. It was found that the pre-cracking behaviour is similar to that of the aluminium footings, however as soon as cracking occurred the behaviour changed considerably.

Finally, the displacement of sand beneath the footings while the footing deflected was investigated. As the stiffness of the footings reduces, the horizontal settlement increased and the shape of the displacement intervals changed. A similar pattern was observed for the vertical displacement of the sand.

© University of Pretoria

5 Conclusions and Recommendations

The main conclusions reached from the study are summarised below.

5.1 Conclusions

The stiffness of a footing has a significant effect on the settlement and deflection behaviour, with flexible footings differing from stiff footings. The classification of the stiffness of a foundation system proposed by Arnold et al. (2010) can be utilised if the material properties of both the footing and the underlying soil is known. However, it is clear that an adjustment to the classification system is required with regard to stiff footings. As evident from the behaviour of the 16 mm aluminium footing throughout this study, the behaviour thereof was different than all the other stiff footings. Therefore, adjusting the classification of stiff footings from a K_s value of > 0.1 to a K_s value of > 0.2 would produce a more realistic classification of the stiffness of a foundation system.

The deflection of the footings were clearly defined as a function of the stiffness thereof. The stiff footings (using the new K_s value of 0.2) did not exhibit any noticeable curvature, whereas the 16 mm did exhibit slight curvature during loading. The footings classified as semi-stiff (10 mm and 6.7 mm aluminium footings) did exhibit curvature, with the extent of curvature increasing as the stiffness of the footing reduced. Therefore, the 16 mm aluminium footing should be classified as semi-stiff as opposed to stiff, as the behaviour thereof was consistent with the semi-stiff footings. The curvature of the semi-flexible footing (3 mm aluminium footing) was excessive and caution should be exercised when designing semi-flexible footings.

The stiff footings exhibited significantly less settlement over the central part of the footings, while exhibiting larger settlement at the edge of the footings than the flexible footings. As a result of the significant curvature of the flexible footings, the settlement varied across the width of the footing.

The stress distribution under the footings was largely influenced by the deflection of the footings. It was found that the assumption of uniform contact stress distribution at the soil-structure interface only applies to stiff footings (K_s > 0.2). Although the flexible footings also exhibited a uniform contact stress distribution at small loads, the load distribution changed from uniform to linearly varying as the load increased and finally to parabolic as the maximum applied load was approached. The change in the contact stress distribution is related to the deflection of the footings, with the stiff footings which did not deflect noticeably during loading having a uniformly distributed contact stress throughout the test.

© University of Pretoria

For the flexible footings (K_s < 0.2) the contact stress distribution changed as the shape of the footings changed during loading. The extent to which the contact stress at the edge of the footings differs from that at the centre of the footing can be utilised to predict the deflected shape of the footing with greater confidence.

It was found that the assumption of a linearly varying contact stress distribution under the footing results in a more accurate prediction of the actual deflected shape of the flexible footings. Therefore it is proposed that a uniform pressure distribution is used to analyse stiff footings (K_s > 0.2), a linearly varying pressure distribution for semi-stiff footings (K_s value of 0.01 – 0.2) and a triangular pressure distribution for semi-flexible footings (K_s value of 0 – 0.01). Utilising a uniform pressure distribution would lead to inaccurate prediction of the behaviour of a semi-stiff and semi-flexible footing and can lead to the overdesign of footings.

The behaviour of the reinforced concrete footing differed considerably from that of the aluminium footings as a result of the changing stiffness following the onset of cracking of the concrete footing. The reinforced concrete footing behaviour changed from that of a stiff footing to a flexible footing as the extent of cracking increased. As cracks developed, the settlement, deflection and contact stress distribution under the footing changed with increasing load as the stiffness of the footing changed. It can be concluded that careful consideration of the required properties of reinforced concrete footings are necessary when modelling with aluminium, as the behaviour of the two materials differ considerably with aluminium being a ductile and concrete a brittle material.

The displacement of the sand beneath the footings was influenced by the deflected shapes of the footing. The vertical and horizontal displacement distributions of the sand beneath the footings were determined at constant displacement intervals at an applied load of 30 kN. The vertical displacement contours developed generally as approximately concentric circles originating from the base of the footing and extending downward in the sand with increasing load. The shape narrowed as the stiffness of the footing decreased. The horizontal displacement contours developed as a combination of teardrop shapes originating from the edges of the footing and a central vertical column. As the stiffness of the footings reduced, the central column width reduced, whilst the size of individual teardrop intervals reduced and the number of contour intervals increased (the horizontal displacement increased).

© University of Pretoria

During the analysis of the experimental results the following behavioural trends associated with the footings were observed:

- The settlement of all the aluminium footings was similar at a distance of approximately one-third the width of the footings from the edge of the thereof, regardless of the deflected shapes and applied load. Therefore, for a flexible footing, the centre of the footing will exceed the settlement at the common point, while further away from it, the settlement will be less. A stiff footing will have a constant settlement equal to the one calculated using this point. This can be used as a prediction method when considering different footing stiffness's.
- The crack pattern of the reinforced concrete footing consisted of a single large crack forming in the centre of the footing, without the addition of other cracks along the width of the footing.
- The single crack migrated upwards as the load increased until it finally reached a critical length, where after the crack grew towards the edges of the column.

It can be concluded that the settlement, deflection and contact stress distribution below the footing at the soil-structure interface of a footing on a dry cohesionless sand can be predicted as a function of the stiffness of the footing, both qualitatively and quantitatively.

5.2 Recommendations

The following recommendations for further research are proposed:

- Altering the relative density of the sand used in tests.
- Testing the footings on different sands and soil types such as clay.
- Testing of a wider range of footing thicknesses, particularly of flexible footings.
- Refinement of the classification system to determine whether a footing is stiff or flexible.
- A comprehensive study examining the behaviour of reinforced concrete footings to determine how the behaviour of a brittle concrete footing differs from that of ductile aluminium footings.
- Investigating different footing widths to determine the effect thereof.
- Using suitable numerical models to simulate the foundation system behaviour.

© University of Pretoria

6 Reference List

Aiban, S.A. and Znidarčic, D. (1995). Centrifugal modelling of bearing capacity of shallow foundations on sands. *Journal of Geotechnical Engineering*. 121 (10), 704-712.

Algin, H.M. (2007). Practical formula for dimensioning a rectangular footing. *Engineering Structures*. 29 (1), 1128-1134.

Archer, A. (2014). *Using small-strain stiffness to predict the settlement of shallow foundations in sand.* Masters Dissertation. University of Pretoria.

Arnold, A., Laue, J., Espinosa, T. and Springman, S.M. (2010). Centrifuge modelling of the behaviour of flexible raft foundations on clay and sand. In: Springman, S.M., Laue, J. and Seward, L *Physical Modelling in Geotechnics*. London: Taylor and Francis. 679-684.

ASTM Standard D2487. (2011). *Standard Practice for Classification of Soils for Engineering Purposes (Unified Soil Classification System)*. DOI: 10.1520/D2487-11. West Conshohocken, PA: www.astm.org

Banimahd, M. and Woodward, P.K. (2006). Load-displacement and bearing capacity of foundations on granular soils using a multi-surface kinematic constitutive soil model. *International Journal for Numerical and Analytical Methods in Geomechanics*. 30 (1), 865-886.

Baumann, R.A. and Weisgerber, F.E. (1983). Yield-line analysis of slabs-on-grade. *Structural Engineering Journal*. 109 (11), 1553-1567.

Bažant, Z.P. and Yu, Q. (2005). Designing against size effect on shear strength of reinforced concrete beams without stirrups: II - Verification and calibration. *Journal of Structural Engineering*. 131 (12), 1886-1897

Beckett, D. (1995). Thickness design of concrete industrial ground floors. *Concrete*. 29 (4), 21-23.

Bjerrum, L. (1963). Allowable settlement of structures. *European Conference on Soil Mechanics and Foundation Engineering*, Weisbaden, Germany, Vol. 3, pp. 135-137.

Bolton, M. D. (1986). The strength and dilatancy of sands. *Géotechnique*. 36 (1), 65–78.

© University of Pretoria

Brooker, O. (2006). *How to Design Reinforced Concrete Flat Slabs using Finite Element Analysis*. Surrey: The Concrete Centre. 1-16.

Camp, C.V. and Assadollahi, A. (2013). CO_2 and cost optimization of reinforced concrete footings using a hybrid big bang-big crunch algorithm. *Structural and Multidisciplinary Optimization*. 48 (2), 411-426.

Canadian Foundation Engineering Manual. (2006). *Canadian Geotechnical Society*. 4th ed. Richmond. Canada.

Canon. (2014). *EOS 100D.* Available from: http://www.canon.co.za/For_Home/Product_Finder/Cameras/Digital_SLR/EOS_100D/index.aspx. [Accessed: 1st November 2014]

Carmona, J.R. and Ruiz, G. (2014). Bond and size effects on the shear capacity of RC beams without stirrups. *Engineering Structures*. 66 (1), 45-56.

Chryso. (2014). *CHRYSO Fluid Premia 100.* [Online] Available from: http://chryso.com/upload/t_documents/Fichier_L2/42902/ft_CHRYSO_Fluid_Premia_100_GB.pdf. [Accessed: 28th October 2014].

Conniff, D.E. and Kiousis, P.D. (2007). Elastoplastic medium for foundation settlements and monotonic soil-structure interaction under combined loadings. *International Journal for Numerical and Analytical Methods in Geomechanics*. 31 (1), 789-807.

Conte, E., Donato, A. and Troncone, A. (2013). Progressive failure analysis of shallow foundations on soils with strain-softening behaviour. *Computer and Geotechnics*. 54 (1), 117-124.

Craig, R.F. (2004). Bearing capacity. In: *Craig's Soil Mechanics*. 7th ed. Oxon: Taylor and Francis. 277-289.

De Beer, E.E. (1948). Donnees concernant la resistance au cisaillement deduites des essais de penetration en profondeur. *Géotechnique*. 1 (1), 22-40 (in French).

De Beer, E.E. (1967). Bearing capacity and settlement of shallow foundations on sand. *Proceedings of the Symposium on Bearing Capacity and Settlement of Foundations*. Durham, N.C. 15-43.

© University of Pretoria

Dempsey, J.P. and Li, H. (1989). A flexible rectangular plate on an elastic layer: Large area contact. *Journal of Tribology*. 111 (3), 518-524.

Desrues, J. and Viggiani, G. (2004). Strain localisation in sand: An overview of the experimental results obtained in Grenoble using stereophotogrammetry. *International Journal for Numerical and Analytical Methods in Geomechanics*. 28 (1), 279-321.

Dijkstra, J., Gaudin, C. and White, D.J. (2013). Comparison of failure modes below footings on carbonate and silica sands. *International Journal of Physical Modelling in Geotechnics*. 13 (1), 1-12.

Domone, P. and Illstron, J. (2010). *Construction Materials: Their Nature and Behaviour*. 4th ed. Oxon: Spon Press. 78-86.

Gajo, A., Wood, D.M. and Bigoni, D. (2007). On certain critical material and testing characteristics affecting shear band development in sand. *Géotechnique*. 57 (5), 449-461.

Gibson, R.E. (1974). The analytical method in soil mechanics. *Géotechnique*. 24 (2), 115-140.

Haigh, S.K., Houghton, N.E., Lam, S.Y., Li, Z. and Wallbridge, P.J. (2010). Development of a 2D servo-actuator for novel centrifuge modelling. In: Springman, S.M., Laue, J. and Seward, L *Physical Modelling in Geotechnics*. London: Taylor and Francis. 239-244.

Hall, S.A., Wood, D.M., Ibraim, E. and Viggiani, G. (2009). Localised deformation patterning in 2D granular materials revealed by digital image correlation. *Granular Matter*. 12 (1), 1-14.

Hallak, A. (2012). *Soil-Structure Interaction and Foundation Vibrations.* [Online] Available from: http://www.slideshare.net/ahmadhallak1973/soil-structure-interaction-amec-presentationfinal?qid=eea2ecf3-23b5-442e-84ed-5791caeed555&v=default&b=&from_search=1. [Accessed: 22th November 2014].

Hallgren, M. and Bjerke, M. (2002). Non-linear finite element analyses of punching shear failure of column footings. *Cement and Concrete Composites*. 24 (1), 491-496.

Hansen, J.B. (1968). A revised extended formula for bearing capacity. *Danish Geotechnical Institute Bulletin.* No. 28.

© University of Pretoria

Hasan, A. and Alshibli, K.A. (2010). Experimental assessment of 3D particle-to-particle interaction within sheared sand using synchrotron microtomography. *Géotechnique*. 60 (5), 369-379.

HBM. (2014). *Inductive Standard Displacement Transducers.* [Online] Available from: http://www.hbm.com/fileadmin/mediapool/hbmdoc/technical/b0553.pdf. [Accessed: 29th October 2014].

HBM. (2014). *Force Transducers.* [Online] Available from: http://www.hbm.com/fileadmin/mediapool/hbmdoc/technical/b2083.pdf [Accessed: 29th October 2014].

Herbert, D.M., Gardner, D.R., Harbottle, M., Thomas, J. and Hughes, T.G. (2011). The development of a new method for testing the lateral load capacity of small-scale masonry walls using a centrifuge and digital image correlation. *Construction and Building Materials*. 25 (1), 4465-4476.

Heron, C. (2013). *5r5 2013 Section 2 Particle Image Velocimetry (PIV).* Cambridge University. Cambridge.

Hettler, A. and Gudehus, G. (1988). Influence of the foundation width on the bearing capacity factor. *Soils and Foundations*. 28 (4), 81-92.

Hibbeler, R.C. (2008). *Mechanics of Materials*. 7th ed. Singapore: Pearson Education.

Hoover, C.G., Bažant, Z.P., Vorel, J., Wendner, R. and Hubler, M.H. (2013). Comprehensive concrete fracture tests: Description and results. *Engineering Fracture Mechanics*. 114 (1), 92-103.

Jacobsz, S.W. (2013). Centrifuge modelling of a soil nail retaining wall. *Journal of the South African Institute of Civil Engineering*. 55 (1), 85-93.

Jacobsz, S.W., Kearsley, E.P. and Kock, J.H.L. (2014). The geotechnical centrifuge facility at the University of Pretoria. In: Springman, S.M., Laue, J. and Seward, L *Physical Modelling in Geotechnics*. London: Taylor and Francis. 169-174.

Kassimali, A. (2011). *Structural Analysis*. 4th ed. Stamford: Cengage Learning.

© University of Pretoria

Kim, W. and Jeong, J. (2010). Non-Bernoulli-compatibility truss model for RC members subjected to combined action of flexure and shear - Part I: It's derivation of theoretical concept. *KSCE Journal of Civil Engineering*. 15 (1), 101-108.

Kimura, T., Kusakabe, O. and Saitoh, K. (1985). Geotechnical model tests of bearing capacity problems in a centrifuge. *Géotechnique*. 35 (1), 33-45.

Knappett, J.A. and Craig, R.F. (2012). *Craig's Soil Mechanics*. 8th ed. CRC Press.

Knappett, J.A., O'Reilly, K., Gilhooley, P., Reid, C. and Skeffington, K. (2010). Modelling precast concrete piling for use in the geotechnical centrifuge. In: Springman, S.M., Laue, J. and Seward, L *Physical Modelling in Geotechnics*. London: Taylor and Francis. 141-146.

Knappett, J.A., Reid, C., Kinmond, S. and O'Reilly, K. (2011). Small-scale modelling of reinforced concrete structural elements for use in a geotechnical centrifuge. *Journal of Structural Engineering*. 137 (1), 1263-1271.

Kollmorgen. (2014). *P7000 Series.* [Online] Available from: http://www.kollmorgen.com/en-us/products/drives/stepper/p7000-series/. [Accessed: 30th October 2014].

Kotake, N., Tatsuoka, F., Tanaka, T., Siddiquee, M.S.A. and Haung, C.C. (2004). FEM simulation of the failure of reinforced sand slopes subjected to footing load. *Geosynthetics International*. 11 (1), 1-18.

Laefer, D.F., Hong, L.T., Erkal, A., Long, J.H. and Cording, E.J. (2011). Manufacturing, assembly, and testing of scaled, historic masonry for one-gravity, pseudo-static, soil-structure experiments. *Construction and Building Materials*. 25 (1), 4362-4373.

Leshchinsky, D. (2001). Design dilemma: Use peak or residual strength of soil. *Geotextiles and Geomembranes*. 19 (1), 111-125.

Leshchinsky, D. and Marcozzi, G.F. (1990). Bearing capacity of shallow foundations: Rigid versus flexible models. *Journal of Geotechnical Engineering*. 116 (11), 1750-1756.

Lesniewska, D. and Muir Wood, D.M. (2009). Observations of stresses and strains in a granular material. *Journal of Engineering Mechanics*. 135 (9), 1038-1054.

© University of Pretoria

Lesniewska, D. and Muir Wood, D.M. (2011). Photoelastic and photographic study of a granular material. *Géotechnique*. 61 (7), 605-611.

Lin, S., Bischoff, P.H. and Valsangkar, A.J. (2003). Pre- and post-cracking behaviour of fibre reinforced concrete beams on grade. *International Journal of Physical Modelling in Geotechnics*. 1 (1), 19-29.

Liu, X., Scarpas, A. and Blaauwendraad, J. (2005). Numerical modelling of nonlinear response of soil. Part 2: Strain localisation investigation on sand. *International Journal of Solids and Structures*. 42 (1), 1883-1907.

Mac Donald, B.J. (2011). *Practical Stress Analysis with Finite Elements*. 2nd ed. Dublin: Glasnevin Publishing. 17-46.

Manoharan, N. and Dasgupta, S.P. (1995). Bearing capacity of surface footings by finite elements. *Computers and Structures*. 54 (4), 563-586.

Menétrey, P. (2002). Synthesis of punching failure in reinforced concrete. *Cement and Concrete Composites*. 24 (1), 497-507.

Meyerhof, G.G. (1953). The bearing capacity of foundations under eccentric and inclined loads. *3rd ICSMFE*. (1). Zurich. 440-445.

Meyerhof, G.G. (1963). Some recent research on the bearing capacity of foundations. *Canadian Geotechnical Journal*. Ottawa. 1(1). 16–26.

Michalowski, R.L. and You, L. (1998). Effective width rule in calculations of bearing capacity of shallow footings. *Computer and Geotechnics*. 23 (1), 237-253.

Mikasa, M. and Takada, N. (1984). Selfweight consolidation of very soft clay by centrifuge. *Proceedings: Symposium on Sedimentation/Consolidation Models, American Society of Civil Engineers*. 121-140.

Morfidis, K. and Avramidis, I.E. (2002). Formulation of a generalised beam element on a two-parameter elastic foundation with semi-rigid connections and rigid offsets. *Computers and Structures*. 80 (1), 1919-1934.

© University of Pretoria

Mosley, W.H. and Bungey, J.H. (1987). *Reinforced Concrete Design*. 3rd ed. Houndmills: Macmillan Education LTD. 270-291.

Muhs, E. (1963). UÅN ber die zullaÅN ssige bellastung nichtibindiger BoÅN den. *Mittielungen der Deutschen Forschungsgesellshaft FuÅN r Bodenmechanik (Degebo).* Berlin, Heft. 16. 102–121. (in German).

Muir Wood, D.M. (2012). Heterogeneity and soil element testing. *Géotechnique Letters*. 2 (1), 101-106.

Müller, G. and O'Sullivan, M. (1999). Model scale experiments to determine bending moments of beams resting on sand. *Géotechnique*. 49 (2), 267-272.

Ovesen, N. K. (1979). Panel discussion in session 9: The use of physical models in design. *Proceedings: 7th International Conference of Soil Mechanics and Foundation Engineering*, Mexico City 4, 318–323.

Perkins, S.W. and Madson C.R. (2000). Bearing capacity of shallow foundations on sand: A relative density approach. *Journal of Geotechnical and Geoenvironmental Engineering*. 126 (1), 521-530.

Pfaff-Silberblau. (2013). *Compedium Screw Jacks.* [Online] Available from: http://www.pfaff-silberblau.com/at-brochures/. [Accessed: 28th October 2014]

Pisanty, A. and Gellert, M. (1972). Automatic design of sloped spread footings. *Building Science*. 7 (1), 53-59.

Prandtl, L. (1921). ‘‘U¨ ber die eindrigungsfestigkeit (ha¨rte) plastischer baustoffe und die festigkeit von schneiden.’’ *Zeitschrift fu¨r angewandte Mathematik und Mechanik*, Berlin, 1(1), 15–20 (in German).

Reissner, H. (1924). ‘‘Zum Erddruckproblem.’’ *Proc., 1st Int. Congr. Of Appl. Mech.*, Delft, The Netherlands, 295–311 (in German).

Robberts, J.M. and Marshall, V. (2010). *Analysis and Design of Concrete Structures*. South Africa: Nuclear Structural Engineering. 12.1-12.21.

Rowe, P.W. (1962). The stress-dilatancy relation for static equilibrium on an assembly of particles in contact. *Proceedings A*. 269 (1339), 500-527.

© University of Pretoria

Russo, G., Somma, G. and Angeli, P. (2004). Design shear strength formula for high strength concrete beams. *Materials and Structures*. 37 (1), 680-688.

Schofield, A.N. (1980). Cambridge geotechnical centrifuge operations. *Géotechnique*. 30 (3), 227-268.

Shehata, I.A.E.M. (1990). Simplified model for estimating the punching resistance of reinforced concrete slabs. *Materials and Structures*. 23 (1), 364-371.

Skempton, A.W. and MacDonald, D.H. (1956). Allowable settlement of buildings. *Proceedings ICE*. 5 (3). 727-728.

Skorpen, S. and Dekker, N. (2014). The application and interpretation of linear finite element analysis results in the design and detailing of hogging moment regions in reinforced concrete flat plates. *Journal of the South African Institute of Civil Engineering*. 56 (1), 77-92.

Spasojevic, A. and Cabarkapa, Z. (2012). Extended stress fields analysis of surface strip footing on sand. *Géotechnique*. 62 (8), 733-740.

Tekscan™. (2014). *I-Scan System.* [Online] Available from: http://www.tekscan.com/products/industrial/pressure-distribution-measurement-system. [Accessed: 29th October 2014].

Tekscan™. (2014). *Sensor Model 5105.* [Online] Available from: http://www.tekscan.com/5101-pressure-sensor. [Accessed: 29th October 2014].

Terzaghi, K. (1943). *Theoretical Soil Mechanics*. London: John Wiley and Sons, Inc. 118-143.

Terzaghi, K. (1955). Evaluation of coefficients of subgrade reaction. *Géotechnique*. 4 (1), 279-326.

Ueono, K., Miura, K. and Maeda, Y. (1998). Prediction of ultimate bearing capacity of surface footings with regard to size effects. *Soils and Foundations*. 38 (3), 165-178.

University of Pretoria. (2014). *Geotechnical Centrifuge Laboratory.* [Online] Available from: http://web.up.ac.za/default.asp?ipkCategoryID=18991andsub=1andparentid=2407andsubid=5663andipklookid=7 [Accessed: 28th October 2014].

© University of Pretoria

Wei, W., Gong, J. and Che, Y. (2011). Shear strength prediction for reinforced concrete beams without stirrups. *Magazine of Concrete Research*. 63 (6), 433-440.

Wei, H., Wu, Y. and Yu, Z. (2012). Design parameter optimization of beam foundation on soft soil layer with nonlinear finite element. *Journal of Central South University*. 19 (6), 1753-1763.

Westergaard, H.M. (1925). Stresses in concrete pavements computed by theoretical analysis. *Public Roads*. 7, 25.

Westergaard, H.M. (1937). What is known of stresses. *Engineering news record.* 118 (1). 26-29.

White, D.J, Take, W.A and Bolton, D. (2003). Soil deformation measurement using particle image velocimetry (PIV) and photogrammetry. *Géotechnique*. 53 (7), 619-631.

White, D.J., Teh, K.L., Leung, C.F. and Chow, Y.K. (2008). A comparison of the bearing capacity of flat and conical circular foundations on sand. *Géotechnique*. 58 (10), 781-792.

Yamaguchi, H., Kimura, T. and Fuji-i, N. (1976). On the influence of progressive failure on the bearing capacity of shallow foundations in dense sand. *Soil and Foundations*. 16 (4), 11-22.

Zhang, W., Wang, J. and Jiang, M. (2013). DEM-aided discovery of the relationship between energy dissipation and shear band formation considering the effects of particle rolling resistance. *Journal of Geotechnical and Geoenvironmental Engineering*. 139 (9), 1512-1527.

© University of Pretoria

Appendix A Calibration of Force Transducer

The force transducer was calibrated by Archer (2014).

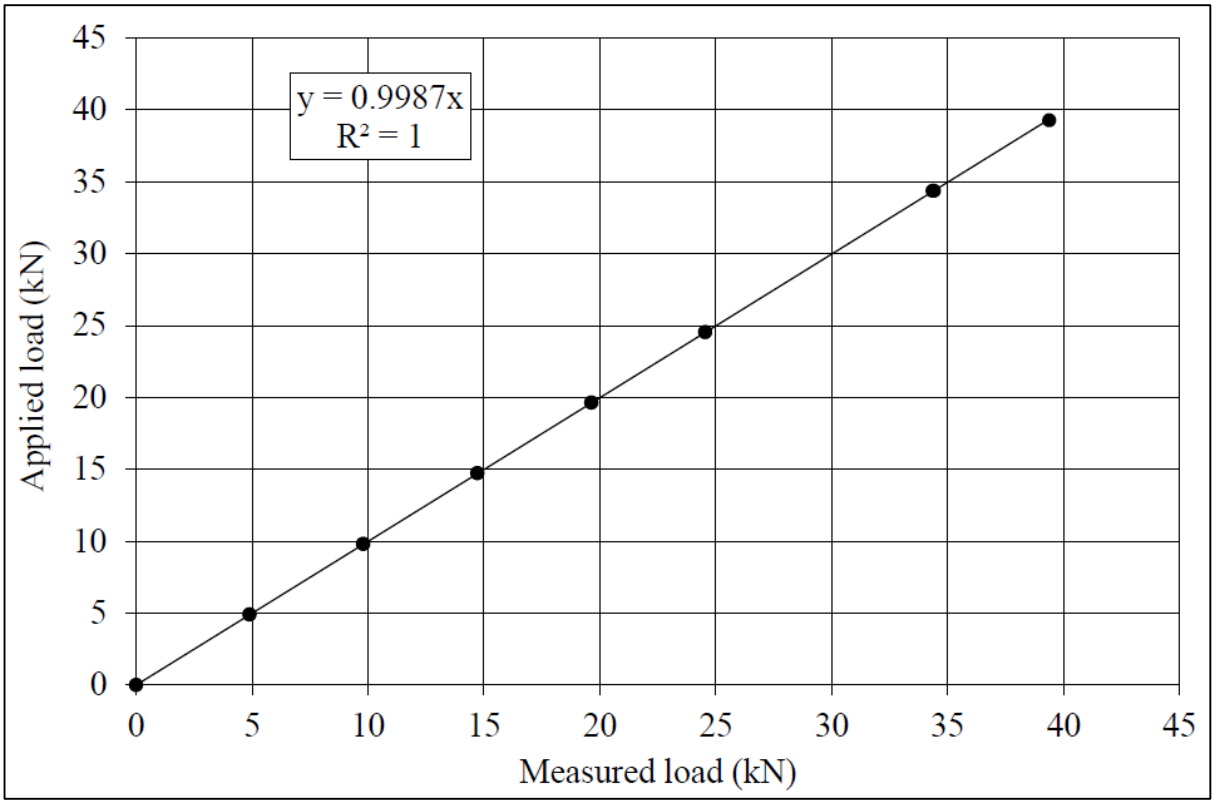

Figure A-1 Calibration of load cell

© University of Pretoria

Appendix B Calibration of Inductive Displacement Transducers

All the inductive displacement transducers were calibrated with the use of a Mitutoya depth gauge in both measuring directions.

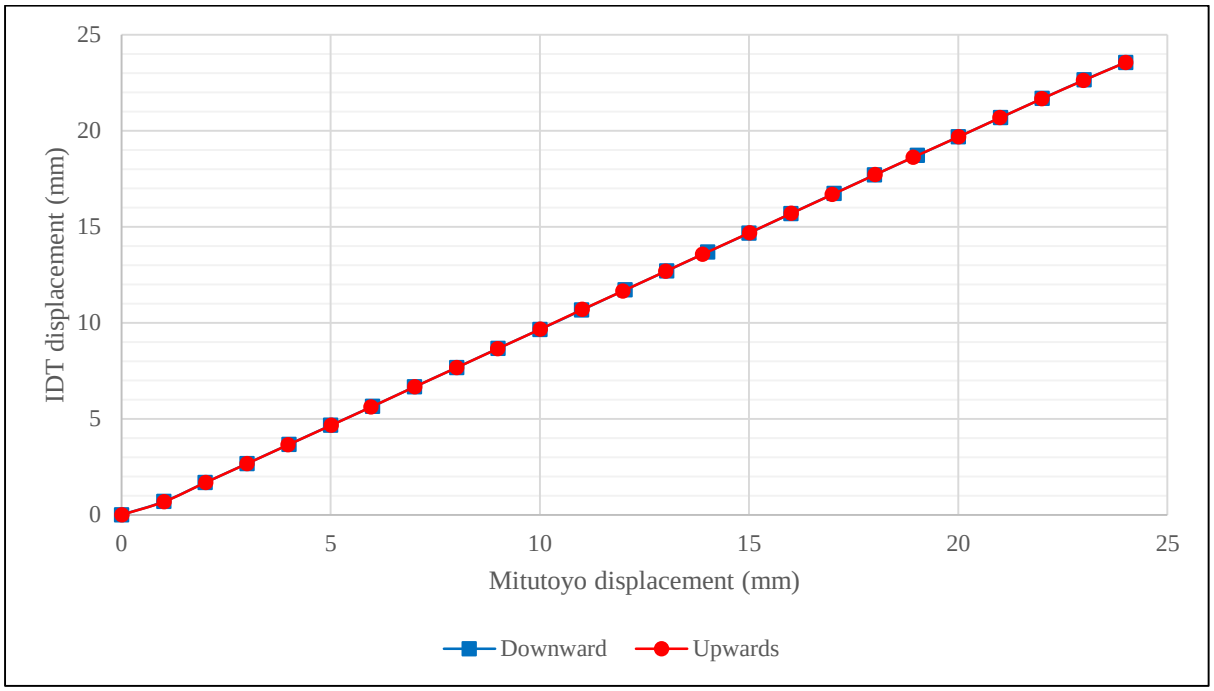

Figure B-1 Calibration of footing IDT 1

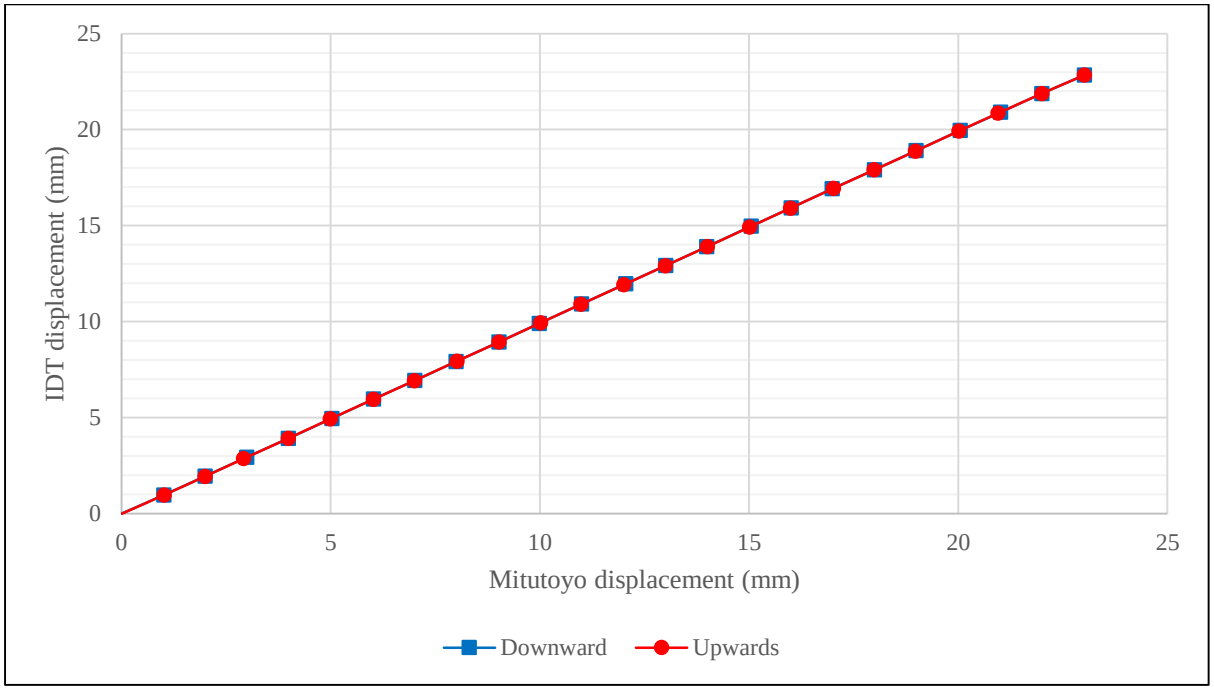

Figure B-2 Calibration of footing IDT 2

© University of Pretoria

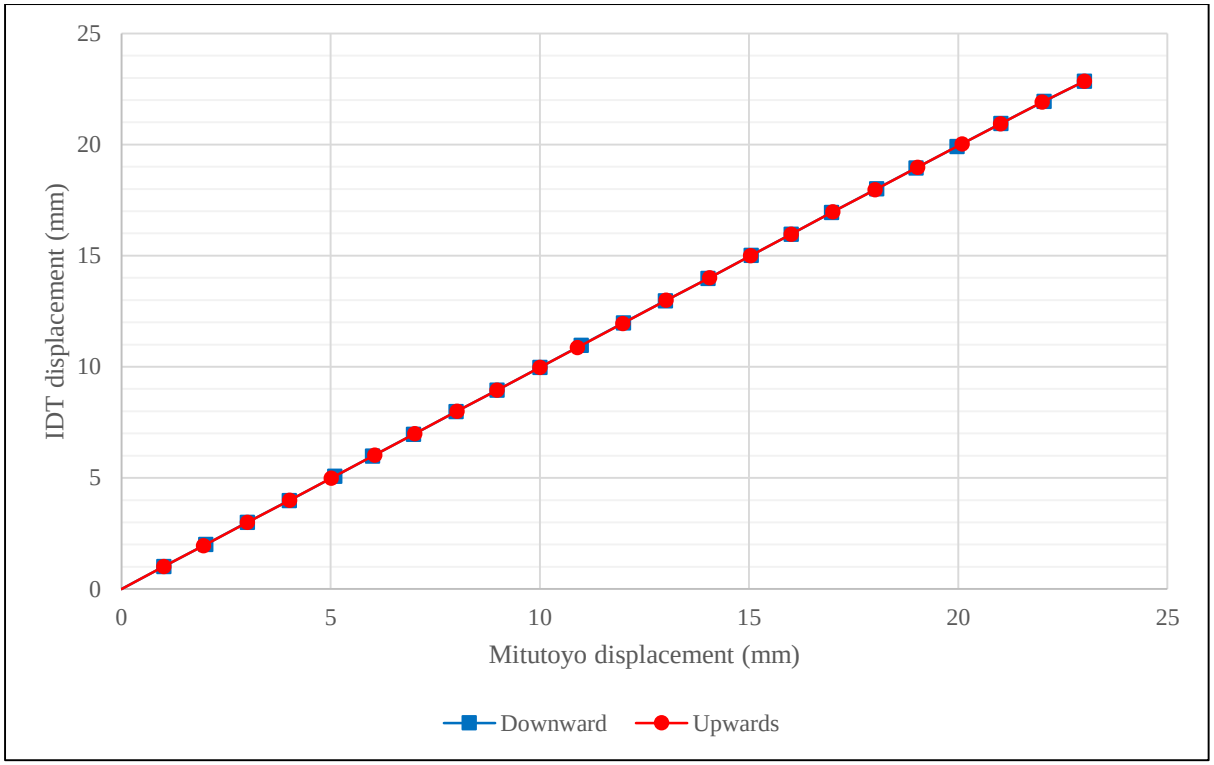

Figure B-3 Calibration of footing IDT 3

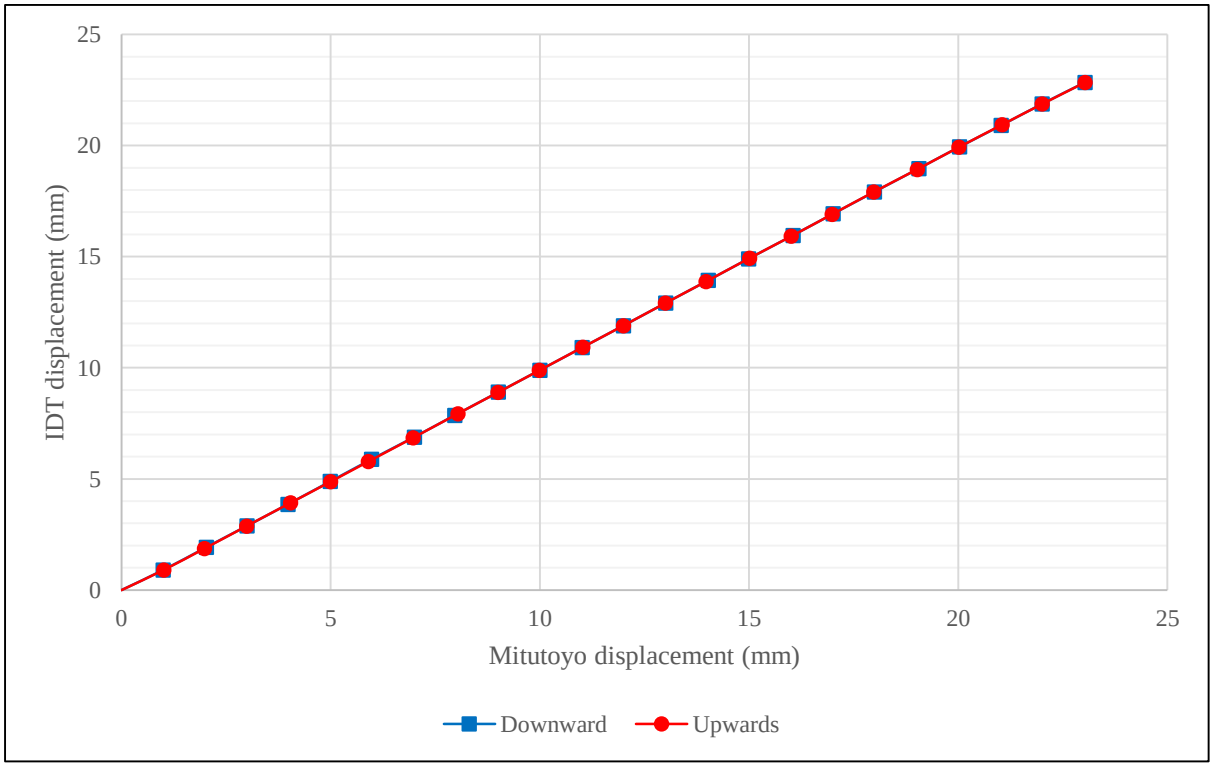

Figure B-4 Calibration of footing IDT 4

© University of Pretoria

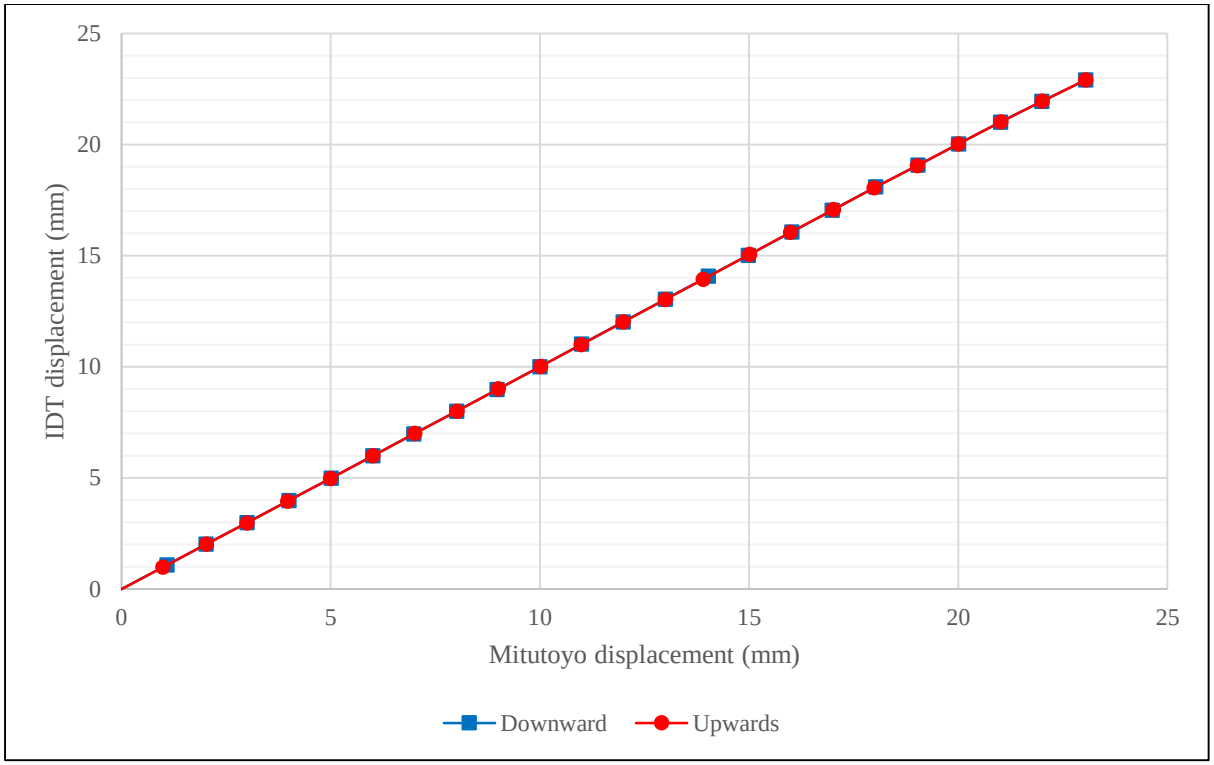

Figure B-5 Calibration of footing IDT 5

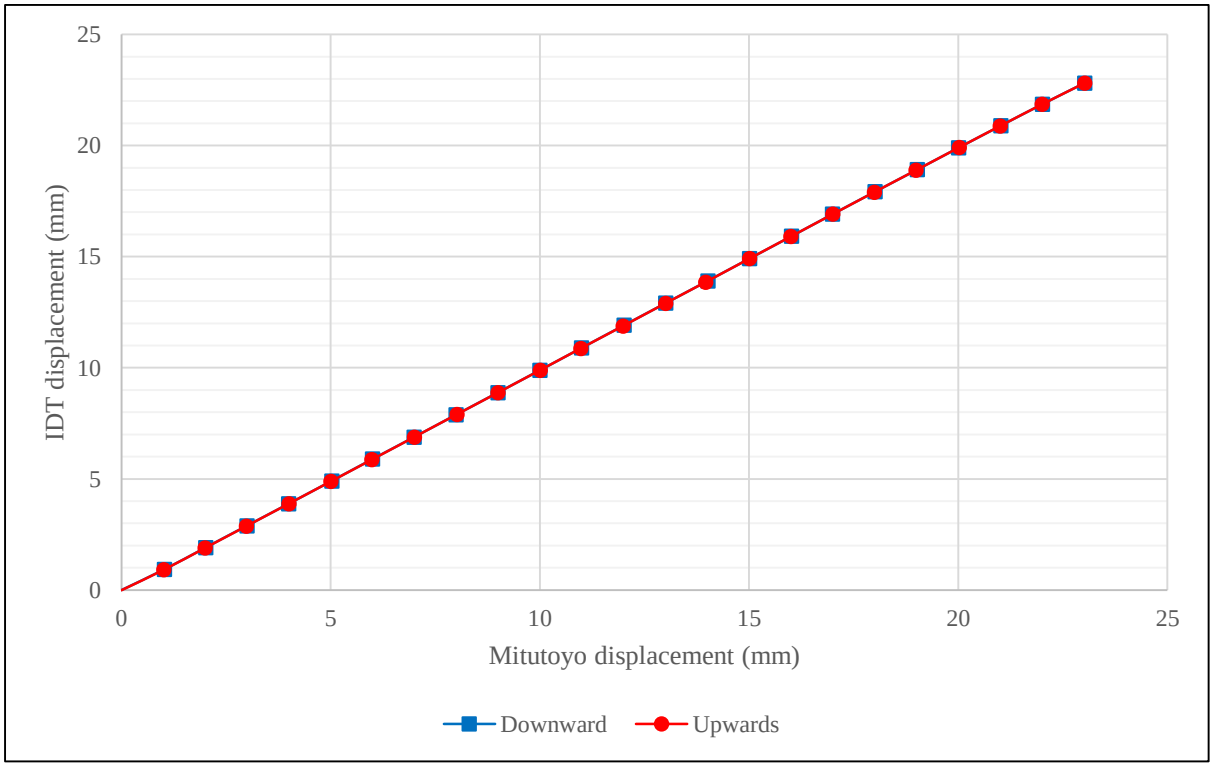

Figure B-6 Calibration of footing IDT 6

© University of Pretoria

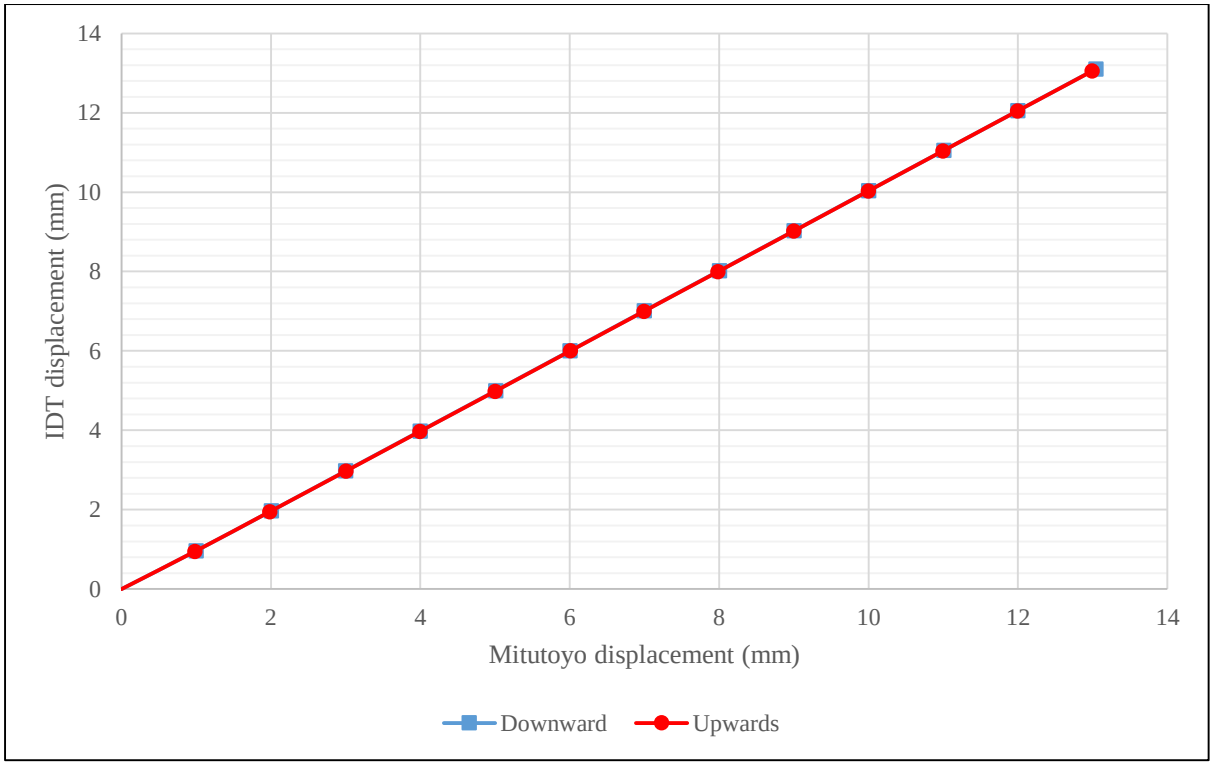

Figure B-7 Calibration of aluminium divider IDT

© University of Pretoria

Appendix C Load Settlement Data from Inductive Displacement Transducers

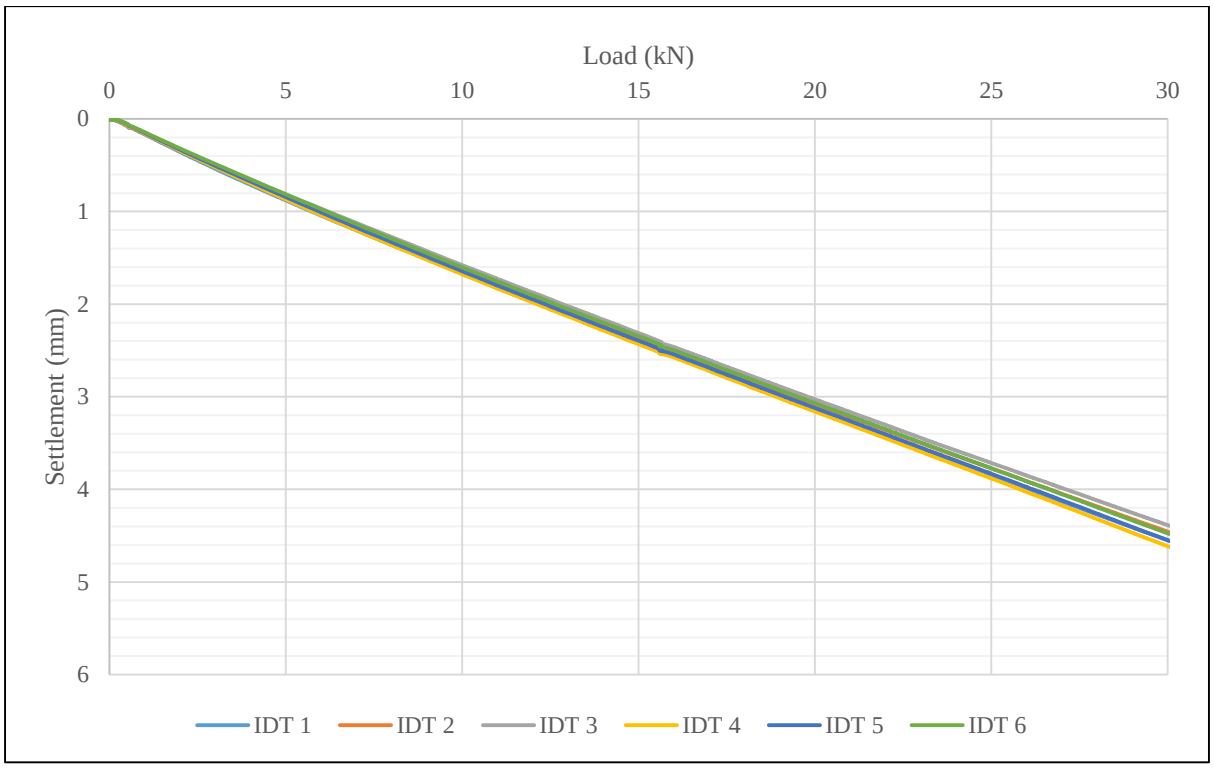

Figure C-1 Settlement data from IDT for 50 mm aluminium footing

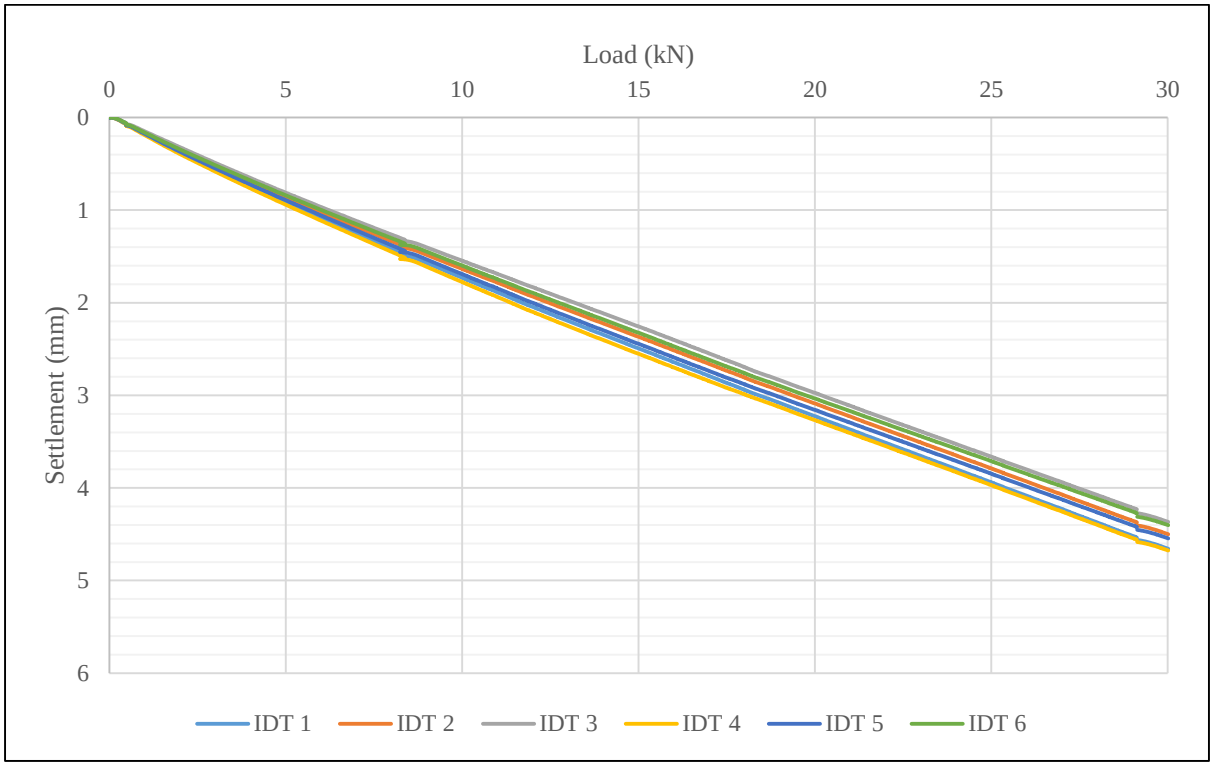

Figure C-2 Settlement data from IDT for 35 mm aluminium footing

© University of Pretoria

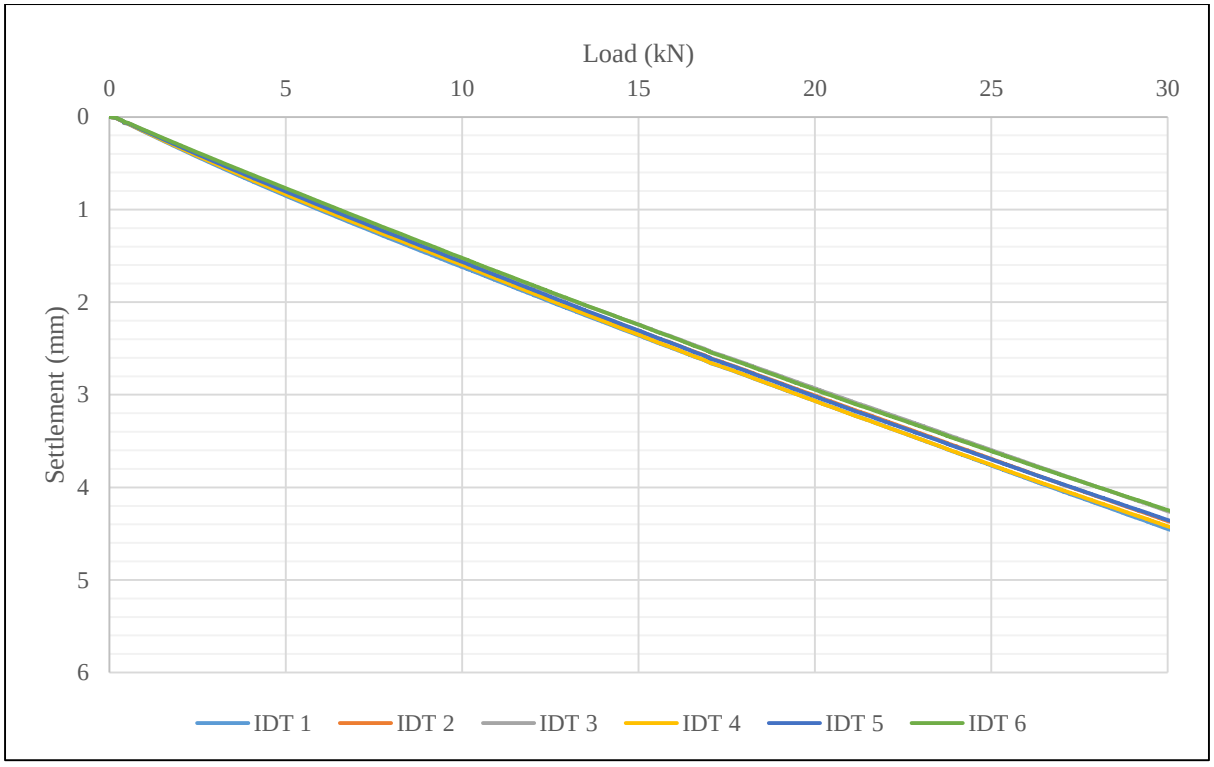

Figure C-3 Settlement data from IDT for 25 mm aluminium footing

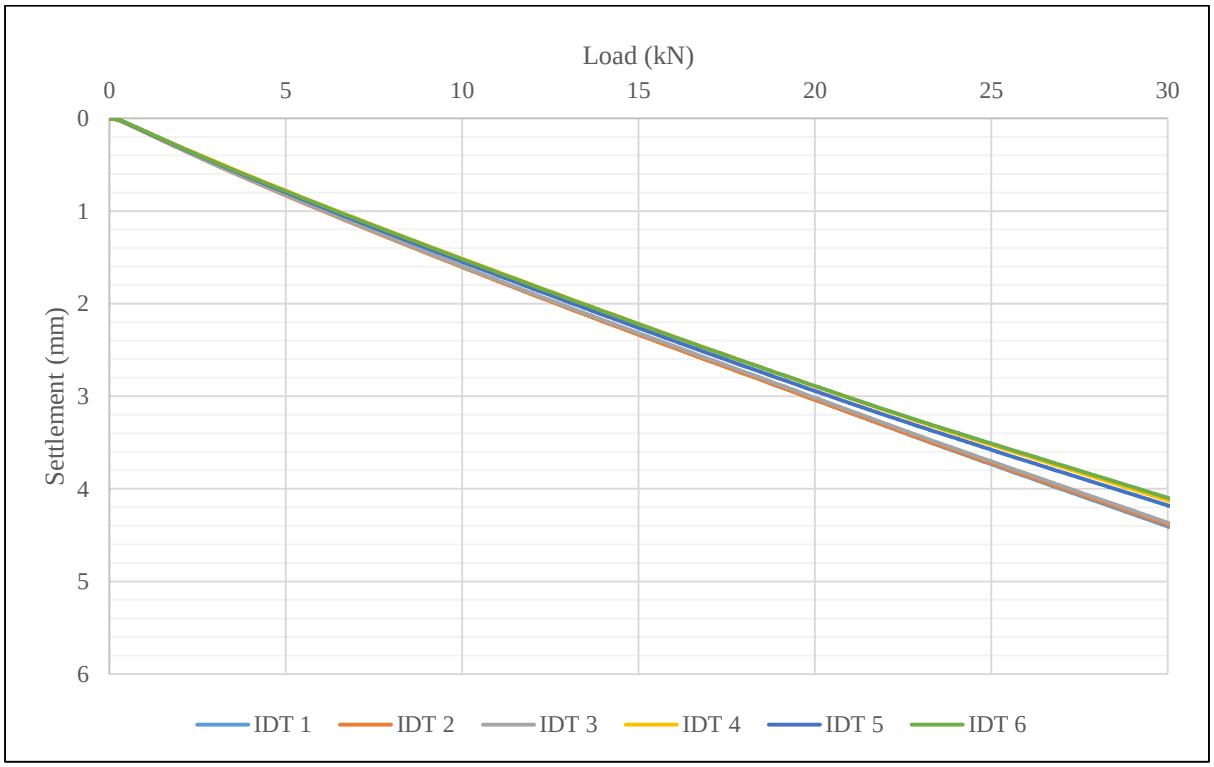

Figure C-4 Settlement data from IDT for 16 mm aluminium footing

© University of Pretoria

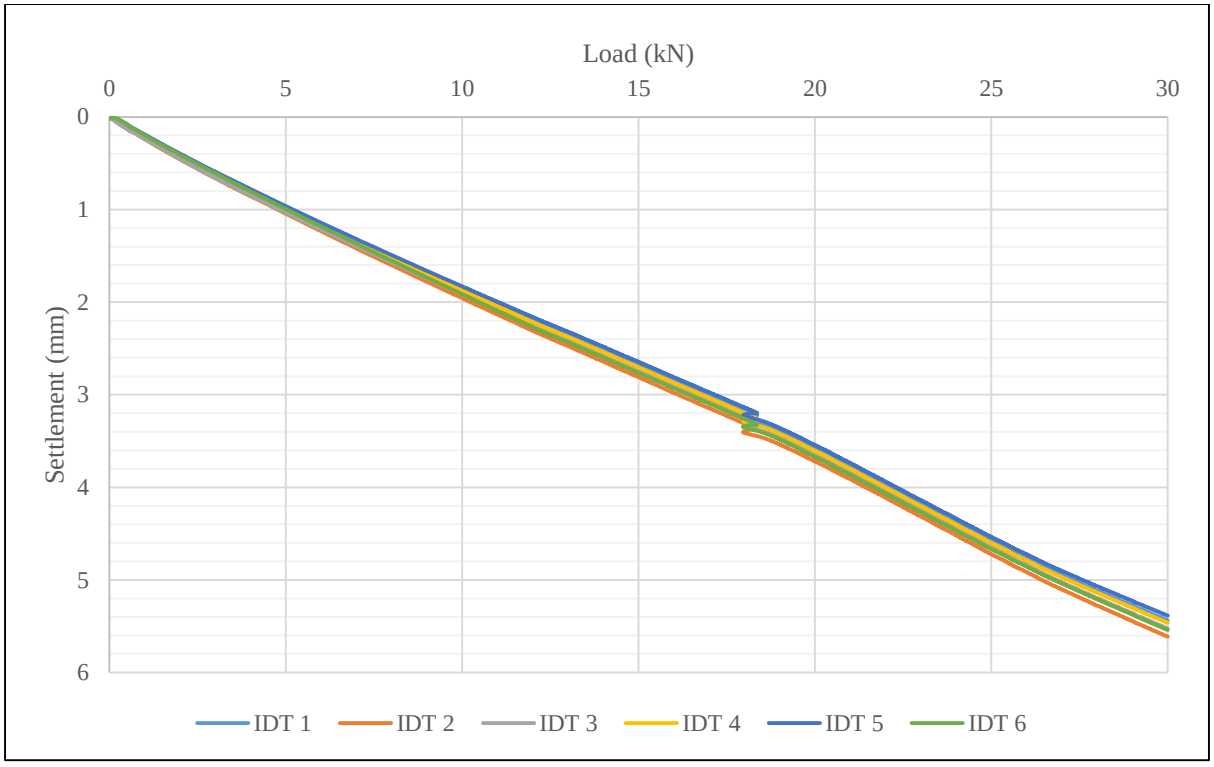

Figure C-5 Settlement data from IDT for 10 mm aluminium footing

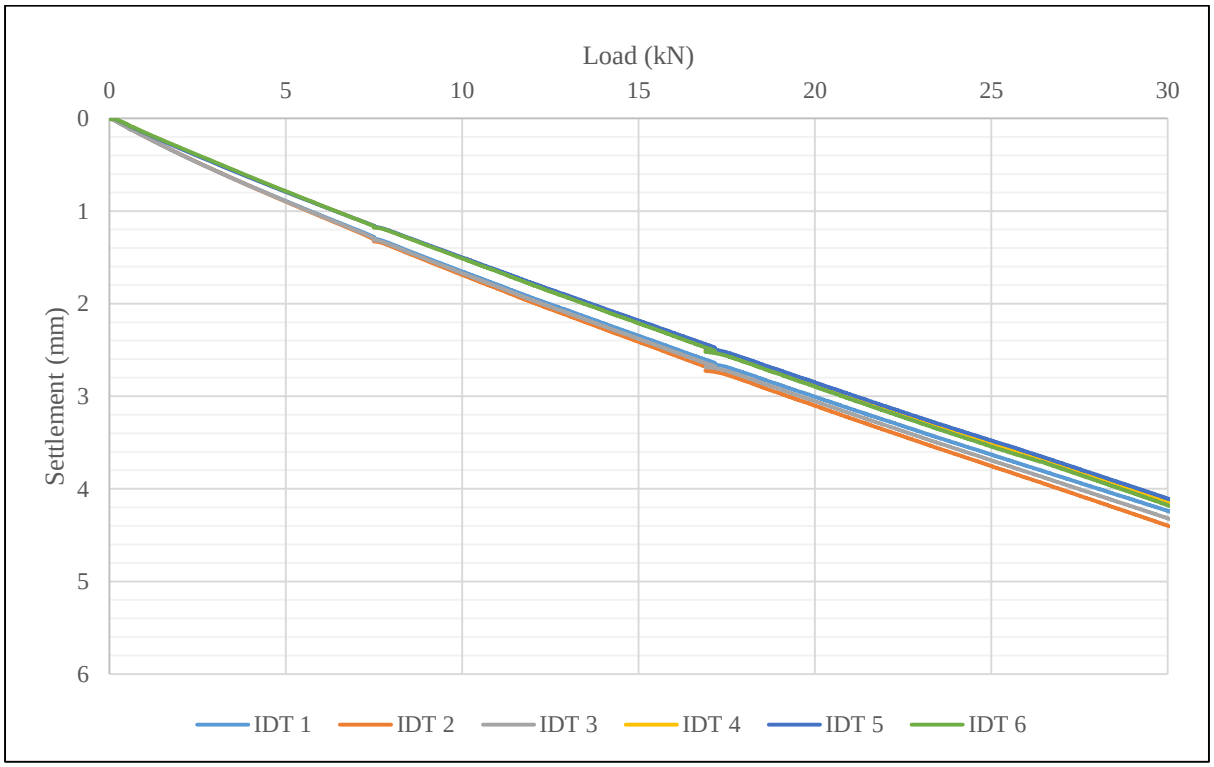

Figure C-6 Settlement data from IDT for 6.7 mm aluminium footing

© University of Pretoria

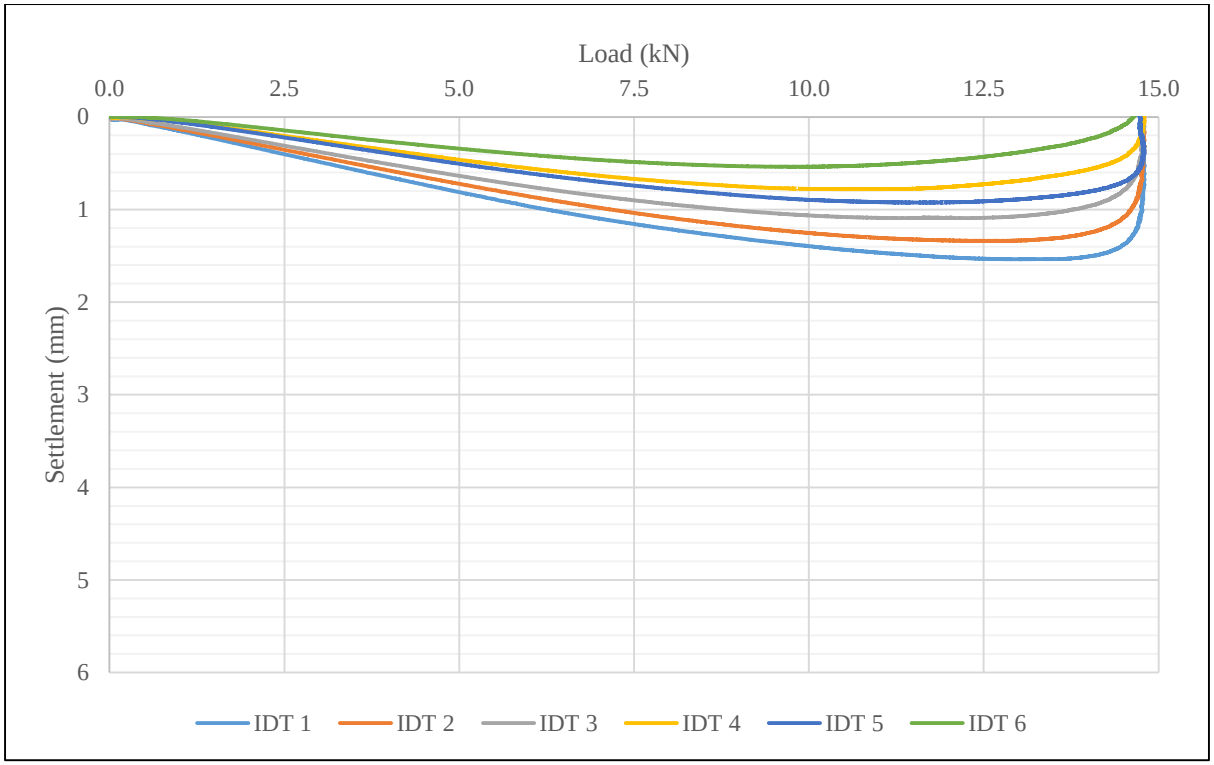

Figure C-7 Settlement data from IDT for 3 mm aluminium footing

© University of Pretoria

Appendix D PIV Settlement Data of Stiff Footings

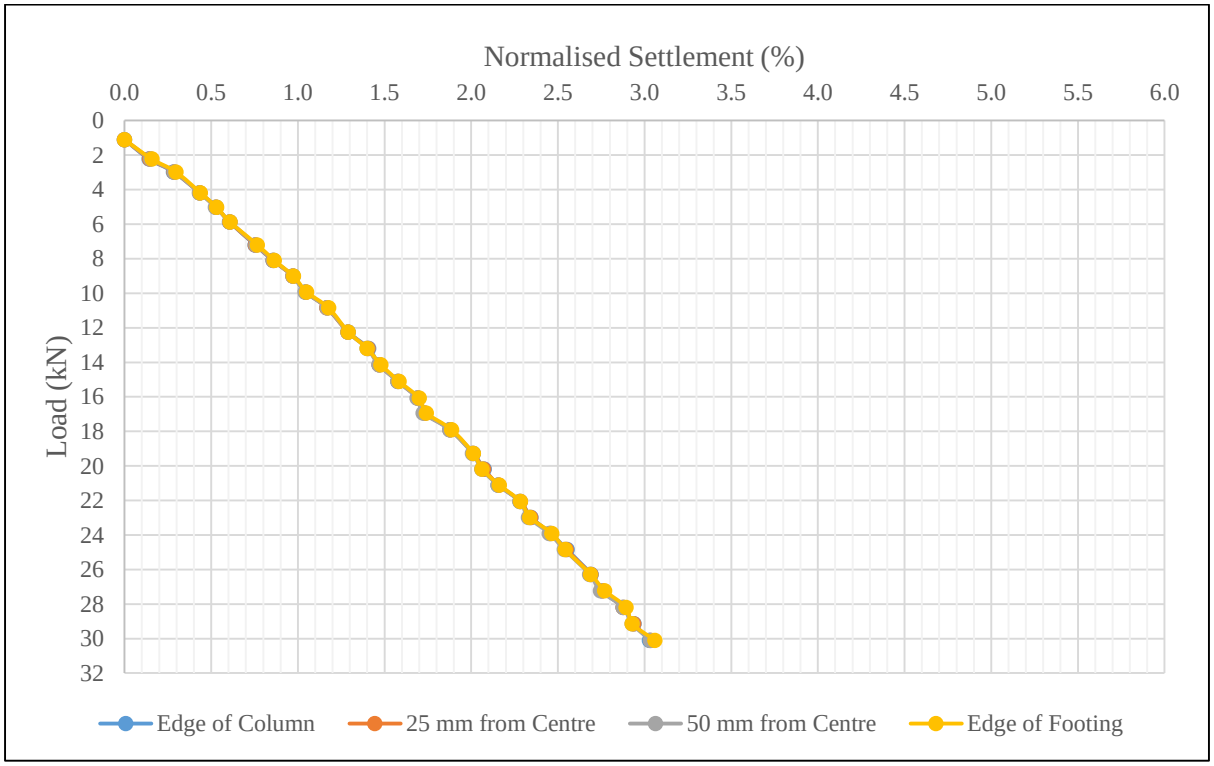

Figure D-1 Normalised settlement of 50 mm aluminium footing

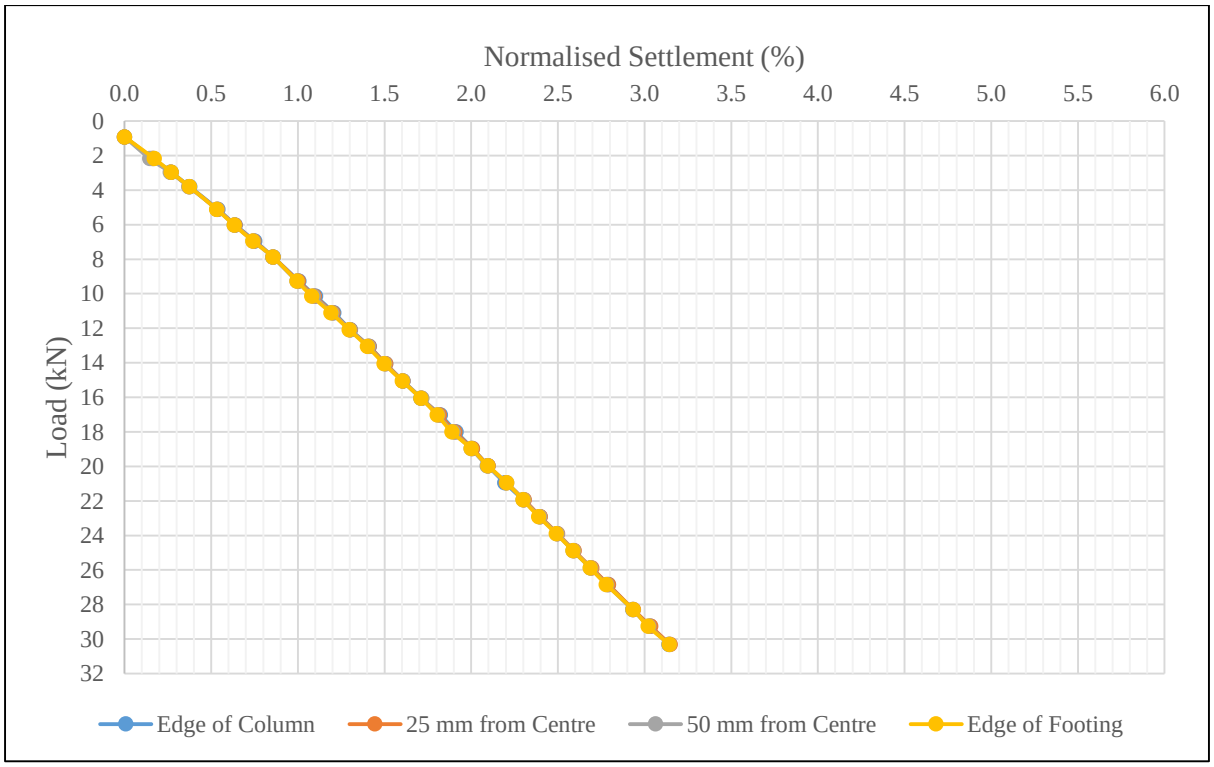

Figure D-2 Normalised settlement of 35 mm aluminium footing

© University of Pretoria

Appendix E Deflected Shapes of Stiff Footings

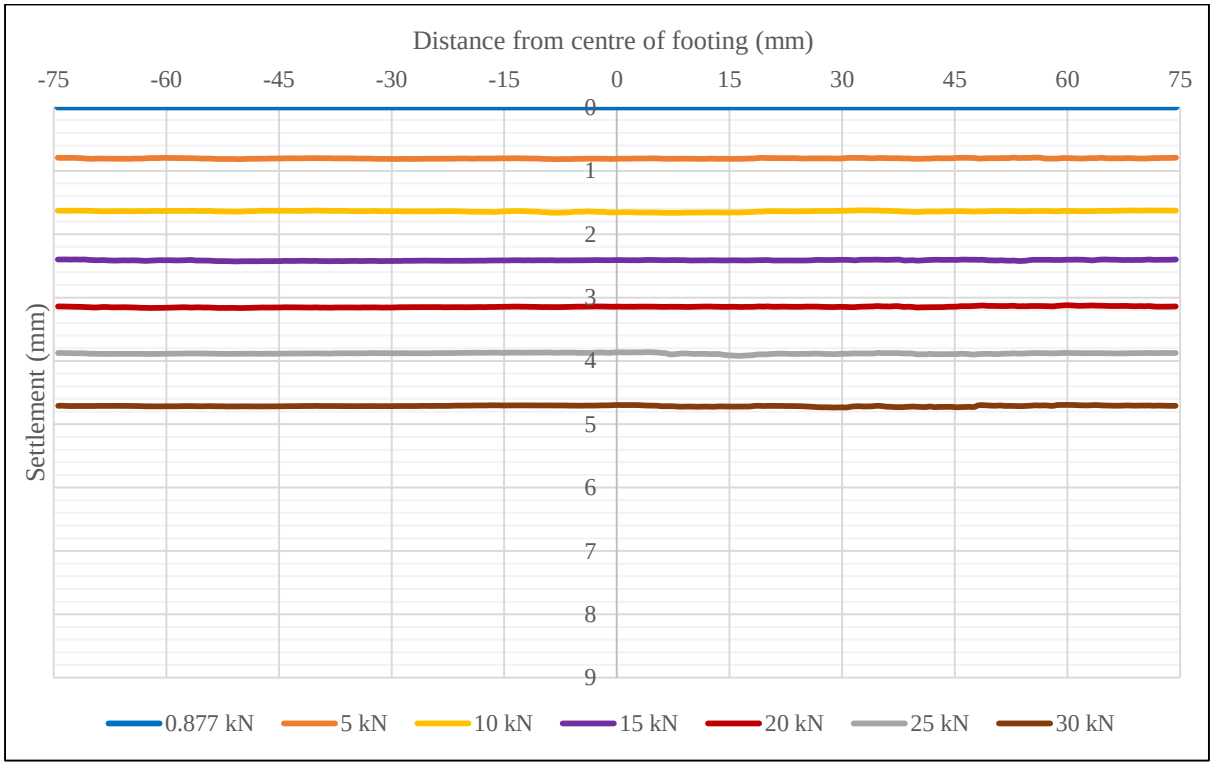

Figure E-1 Deflected shapes of 35 mm aluminium footing

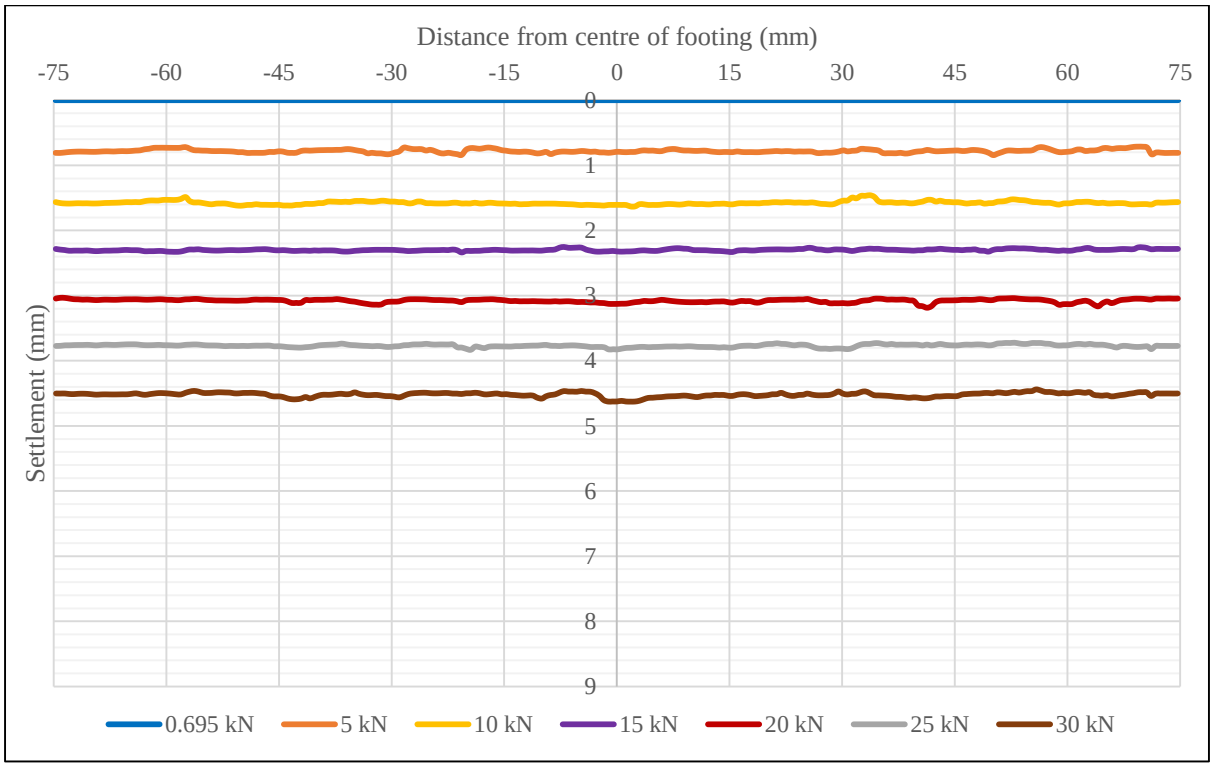

Figure E-2 Deflected shapes of 25 mm aluminium footing

© University of Pretoria

Appendix F Contact Stress Distribution beneath Stiff Footings

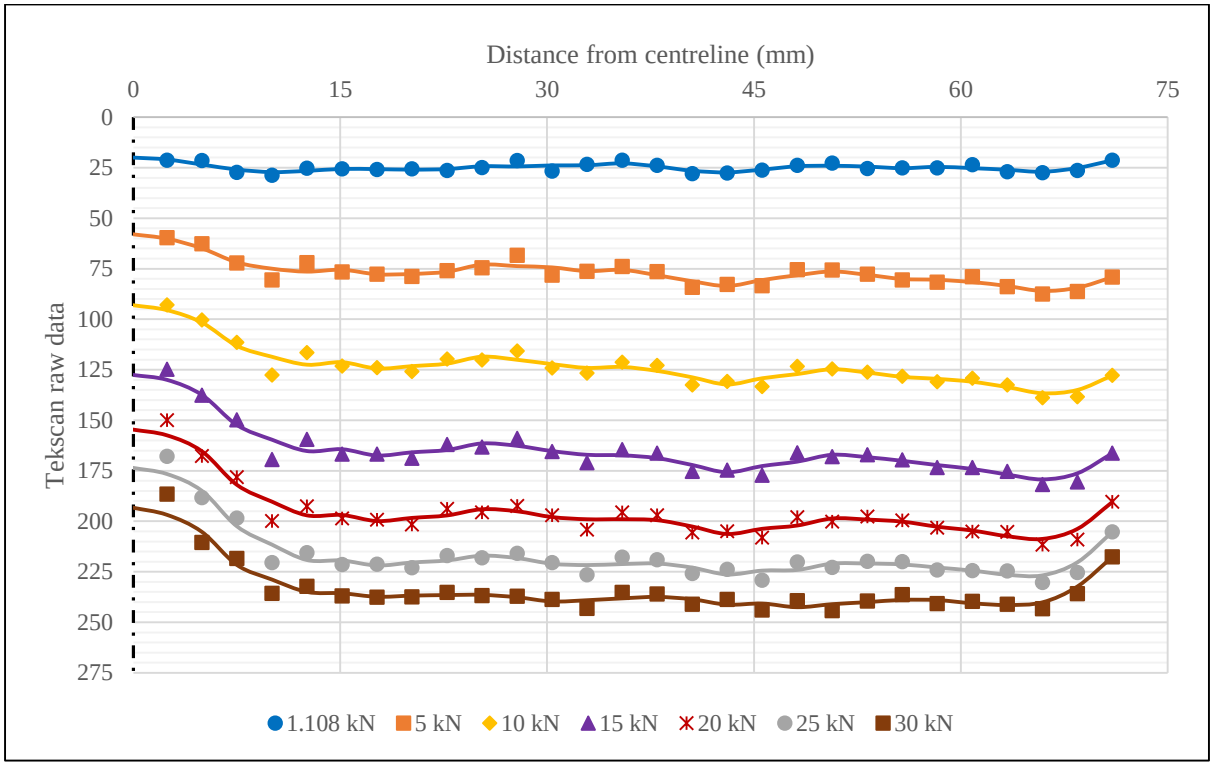

Figure F-1 Contact stress distribution from Tekscan™ data for 50 mm aluminium footing

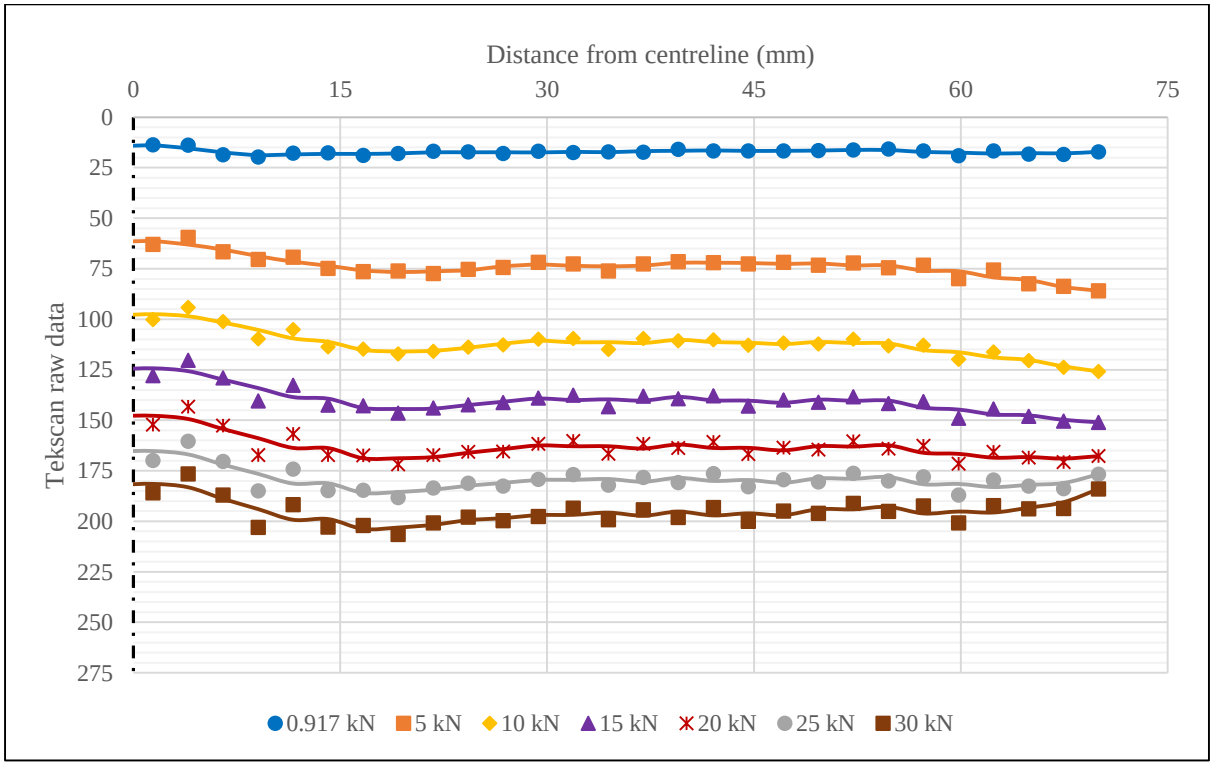

Figure F-2 Contact stress distribution from Tekscan™ data for 35 mm aluminium footing

© University of Pretoria